SEQUENTIAL METHODS FOR COUPLED GEOMECHANICS AND MULTIPHASE FLOW

A DISSERTATION
SUBMITTED TO THE DEPARTMENT OF ENERGY RESOURCES ENGINEERING
AND THE COMMITTEE ON GRADUATE STUDIES
OF STANFORD UNIVERSITY
IN PARTIAL FULFILLMENT OF THE REQUIREMENTS
FOR THE DEGREE OF
DOCTOR OF PHILOSOPHY

Jihoon Kim

February 2010

© Copyright by Jihoon Kim 2010
All Rights Reserved

I certify that I have read this dissertation and that, in my opinion, it is fully adequate in scope and quality as a dissertation for the degree of Doctor of Philosophy.

(Hamdi A. Tchelepi) Principal Adviser

I certify that I have read this dissertation and that, in my opinion, it is fully adequate in scope and quality as a dissertation for the degree of Doctor of Philosophy.

(Ruben Juanes) Co-Adviser

I certify that I have read this dissertation and that, in my opinion, it is fully adequate in scope and quality as a dissertation for the degree of Doctor of Philosophy.

(Ronaldo I. Borja)

Approved for the University Committee on Graduate Studies.

Abstract

We study sequential solution methods for coupled multiphase flow and geomechanics. Sequential methods are desirable from a software development perspective. If the sequential solution strategies have stability and convergence properties that are close to those of the fully coupled approach, they can be very competitive for solving problems of practical interest. This is because of the high investment cost associated with developing unified flow-mechanics simulators and the high computational cost of the fully coupled (i.e., simultaneous solution) method. In these sequential-implicit solution strategies, the flow and mechanics problems are solved in sequence. Implicit time discretization is used when solving each of the flow and mechanics problems. The specific details of the form of the coupling scheme and how the two problems of flow and mechanics communicate play important roles in the viability of the coupling strategy. Here, four sequential coupling methods are considered in great detail: drained, undrained, fixed-strain, and fixed-stress splits. For space discretization, we employ a finite-volume method for flow and a finite-element approach for mechanics. This space discretization yields stable solutions at early time and allows for using existing flow and mechanical simulators. The drained and undrained splits solve the mechanical problem first, whereas the fixed-strain and fixed-stress splits solve the flow problem first. The stability and convergence properties for single-phase flow are analyzed for the four sequential-implicit methods. The Von Neumann and energy methods are used to analyze the stability of the linear and nonlinear problems, respectively. The derived stability estimates indicate that the drained and fixed-strain splits, which are the obvious

splits, are, at best, conditionally stable. Moreover, their stability limit depends on the coupling strength only and is independent of time step size. On the other hand, the derived a-priori estimates indicates that the undrained and fixed-stress splits are unconditionally stable regardless of the coupling strength. All the results have been verified by performing numerical simulations for several test cases.

To analyze the convergence rates of the various coupling algorithms, we use matrix and spectral methods. The drained and fixed-strain splits can suffer from non-convergence, even when they are stable. On the other hand, the undrained split yields first-order accuracy in time for a compressible fluid, but it exhibits slow convergence rates for high coupling strength and suffers from non-convergence for purely incompressible systems (solid grains and fluid). The fixed-stress split shows first-order accuracy in time regardless of the fluid type and coupling strength, and it yields a less stiff mechanical problem. Furthermore, the fixed-stress split requires only a few iterations to converge, even for very difficult problems with strong coupling.

The stability and convergence behaviors of the four sequential methods for coupled multiphase flow and geomechanics are also analyzed using spectral and energy methods. The formulation for the flow part can be either fully implicit, or IMPES (IMplicit Pressure, Explicit Saturations). The derived a-priori estimates for the four sequential methods are similar to their single-phase counterparts. That is, the undrained and fixed-stress splits show unconditional stability, and the fixed-stress split exhibits faster convergence rates compared with the other sequential methods. Therefore, we strongly recommend the fixed-stress split with backward Euler time integration, a finite-volume scheme for flow, and a finite-element discretization for mechanics.

Acknowledgements

This thesis is made by many people who helped me with considerable effort as follows.

My deepest appreciation goes to my advisor, Prof. Hamdi A. Tchelepi in the department of energy resources engineering at Stanford. I have worked for him since 2005. For four years, I have overcome a lot of difficulty on research with which I would have been lost. Whenever I faced a problem, he always encouraged me with warm advice. He guided me to the right track, showing me valuable and critical suggestions and providing me with the freedom for various ideas. This was a great opportunity and privilege for me to work for Prof. Hamdi A. Tchelepi.

Prof. Ruben Juanes in the department of civil and environmental engineering at MIT deserves my sincere appreciation from the bottom of my heart. I have worked for him for five years since 2004 when I took the first step in the U.S. He first motivated me for coupled flow and geomechanics as the Ph.D research topic. After he moved to MIT, he has still advised me with enthusiasm all the time inviting me or visiting Stanford.

I would like to express my heartfelt thanks to Prof. Ronaldo I. Borja in the department of civil and environmental engineering at Stanford. His classes on computational geomechanics and plasticity have become critical resources for this thesis. Also, he listened to my research challenges and gave me fruitful advice on coupled flow and geomechanics at a turning point of my research.

My sincere thanks go to other members of my Ph.D committee, Prof. Mark D. Zoback and Prof. Khalid Aziz, who provided me with valuable comments.

I would like to thank Prof. Ignacio Romero in the Universidad Politecnica de Madrid

deeply. There was deep discussion on convergence analysis with him and Prof. Ruben Juanes. He helped me to deal with the problem of convergence issue providing me with the appropriate mathematical framework.

I also would like to thank Prof. Tony Settari in the University of Calgary for his simulator and for valuable discussions. He advised me enthusiastically on the current issues of reservoir geomechanics. I am grateful to Dr. Ali Fadili in Schlumberger who helped me for the initial study on coupled flow and geomechanics when I did an internship at Abingdon.

Needless to say, I am thankful to all of my colleagues at Stanford and staff in the department of energy resources engineering at Stanford. Specially, I thank my old officemates, Marco Cardoso and Qing Chen, who have shared many things for three years.

My parents, Seokwhan Kim and Sunduk Song, take my warmest thanks for their endless love and support.

My wife, Youjeong Oh, is the person who supports me all the time in my life. She is my closest friend, an enormous source of energy, and an adviser in my life. I always thank her with my heart.

This research has been supported by Foundation CMG and the SUPRI-B research group at Stanford University.

Contents

Abstract **v**

Acknowledgements **vii**

1 Introduction **1**

1.1 Coupled Flow and Mechanics 1

1.2 Solution Strategies 3

1.3 Stability of Sequential Schemes 5

1.4 Convergence of Sequential Schemes 7

1.5 Finite-Volume and Finite-Element Methods 9

1.6 Outline 10

2 Formulation **13**

2.1 Background 13

2.2 Governing Equations 14

2.3 Coupling and Constitutive Relations 15

2.3.1 Coupling of fluid, heat flow, and mechanics 15

2.3.2 Constitutive relations based on intrinsic dissipation Φ_1 18

2.4 Derivation of the Coupling Coefficients 20

2.4.1 Coupling coefficients for single-phase flow 20

2.4.2 Coupling coefficients for multi-phase flow 22

3 Stability of the Drained and Undrained Splits **27**

3.1 Mathematical Model 27

3.2 Discretization 30

3.3 Operator Splitting 33

3.3.1 Fully coupled method 34

3.3.2 Drained split 36

3.3.3 Undrained split 36

3.4 Stability Analysis for Linear Poroelasticity 37

3.4.1 Drained split 38

3.4.2 Undrained split 43

3.5 Contractivity of the Nonlinear Continuum Problem 46

3.6 Discrete Stability of the Nonlinear Problem 53

3.7 Numerical Examples 58

3.7.1 Numerical results for elasticity 58

3.7.2 Numerical results for elastoplasticity 69

4 Convergence of the Drained and Undrained Splits **81**

4.1 Error Estimation 81

4.1.1 Error estimation of the drained split by matrix algebra 81

4.1.2 Error estimation of the undrained split by matrix algebra 85

4.2 Spectral Analysis 87

4.2.1 Error amplification of the drained split 88

4.2.2 Comparison with the coupled flow and dynamics 90

4.2.3 Error amplification of the undrained split 94

4.3 Convergence Rate with Full Iterations 95

4.4 Numerical Examples 96

4.4.1 Convergence behavior for a fixed number of iterations 96

4.4.2 Convergence rate with full iterations 110

5 Fixed-strain and Fixed-stress Splits **117**

5.1 Operator Splitting . . . 117

5.1.1 Fixed-strain split . . . 118

5.1.2 Fixed-stress split . . . 118

5.1.3 Conventional reservoir simulation . . . 119

5.2 Stability Analysis for Linear Poroelasticity . . . 120

5.2.1 Fixed-strain split . . . 120

5.2.2 Fixed-stress split . . . 122

5.3 Contractivity of the Nonlinear Continuum Problem . . . 125

5.3.1 Non-contractivity of the fixed-strain split . . . 125

5.3.2 Contractivity of the fixed-stress split . . . 126

5.4 Discrete Stability of the Nonlinear Problem . . . 127

5.5 Error Estimation . . . 132

5.5.1 Error amplification of the fixed-strain split . . . 134

5.5.2 Error amplification of the fixed-stress split . . . 136

5.6 Numerical Examples . . . 139

5.6.1 Stability . . . 139

5.6.2 Convergence . . . 154

5.6.3 Effect of the deviation factor η . . . 158

6 Coupled Multiphase Flow and Geomechanics **163**

6.1 Sequential Methods for Multiphase Flow . . . 163

6.1.1 Drained split . . . 164

6.1.2 Undrained split . . . 165

6.1.3 Fixed-strain split . . . 166

6.1.4 Fixed-stress split . . . 166

6.2 Staggered Newton schemes for Multiphase Flow . . . 167

6.2.1 Convergence of FIM . . . 167

6.2.2 Drained split . . . 171

6.2.3 Undrained split . . . 173
6.2.4 Fixed-strain split . . . 174
6.2.5 Fixed-stress split . . . 176
6.3 Staggered Newton scheme with IMPES . . . 177
6.3.1 Drained split . . . 178
6.3.2 Undrained split . . . 178
6.3.3 Fixed-strain split . . . 179
6.3.4 Fixed-stress split . . . 180
6.4 Stability Analysis via the Energy Method . . . 181
6.4.1 Constitutive relations for multiphase flow and elastoplasticity . . . 181
6.4.2 Contractivity of multiphase flow . . . 182
6.4.3 Contractivity of the undrained split . . . 185
6.4.4 Contractivity of the fixed-stress split . . . 186
6.4.5 B-stability of the sequential methods . . . 187
6.4.6 B-stability of the undrained split . . . 188
6.4.7 B-stability of the fixed-stress split . . . 191
6.5 Numerical Examples with the staggered Newton methods . . . 195
6.5.1 Case 6.1—Water injection and oil production in the 1D poroelasticity 196
6.5.2 Case 6.2—Water injection and oil production in 2D with poroelasticity 200
6.6 Numerical Examples with the staggered method . . . 205

7 Conclusions **207**

7.1 Formulation of Coupled Flow and Mechanics . . . 207
7.2 Coupled Mechanics and Single-Phase flow . . . 208
7.2.1 Stability . . . 208
7.2.2 Convergence . . . 209
7.2.3 Accuracy and Efficiency . . . 210
7.3 Coupled Mechanics and Multiphase Flow . . . 210
7.4 Finite-Volume and Finite-Element Methods . . . 211

7.5 Recommendation 211

A Stability in Space **213**

A.1 Background 213

A.2 Finite-Volume and Finite-Element Methods 216

A.3 Numerical Examples 216

A.3.1 Case A.1—Terzaghi's problem 217

A.3.2 Case A.2—Two dimensional plain strain strip footing consolidation problem 219

B Miscellaneous Derivations **225**

B.1 Positive-Definite Biot's Moduli, $\mathbf{M}$ 225

B.2 Accuracy of the Fully Coupled Method 227

B.3 Drained Split in Coupled Flow and Dynamics 228

B.4 Non-Contractivity with Different Constitutive Relations 228

B.5 $\delta\phi$ for single-phase flow 231

C Constitutive Relations in Reservoir Simulation **235**

C.1 p_o, p_w, p_g formulation 235

C.2 p_o, s_w, s_g formulation 239

List of Tables

3.1 Input data for Case 3.1 59
3.2 Input data for Case 3.2 61
3.3 Input data for Case 3.3. 73
3.4 Input data for Case 3.5 78

4.1 Input data for Case 4.2 109

6.1 Input data for Case 6.1 198
6.2 Input data for Case 6.2 203

A.1 Input data for Case A.1 219
A.2 Input data for Case A.2 220

List of Figures

1.1 Schematics of the fully coupled (top) and the iteratively coupled (bottom) methods. 4

2.1 Ω_t and Ω_t^f are the geometrical volumes of the solid and fluid at time t, respectively. Even though the elementary solid system has the same fluid mass content at time t, $\Omega_t = \Omega_t^f$, the solid system does not have the same fluid mass content after time dt, $\Omega_{t+dt} \neq \Omega_{t+dt}^f$. $\boldsymbol{w}_J$ is the mass flux of fluid phase J relative to the solid skeleton (Coussy, 1995). 15

3.1 Element shape functions for displacement (left) and pressure (right) in 2-D 31

3.2 Sequential methods for flow and geomechanics. Left: drained split. Right: undrained split. 34

3.3 One-dimensional element with the finite-volume and finite-element methods. h is the grid spacing, and j is the element index 38

3.4 The characteristic equations for the drained split when $\alpha = 1$ (top), and when $\alpha = 0.5$ (bottom) 41

3.5 The characteristic equations for the undrained split when $C_0 \leq 0$ and $C_0 > 0$. 45

3.6 Top: the associative flow rule under the assumption of maximum plastic work (Coussy, 1995). Bottom: geometric interpretation of the algorithmic plastic dissipation, which corresponds to the associative flow rule (Simo and Hughes, 1998). 49

3.7 Left: the Terzaghi problem in 1D (Case 3.1). Right: 1D problem with injection and production wells (Case 3.2 and 3.4). 59

3.8 Left: Mandel's problem in 2D with elastic deformation (Case 3.3). Right: 2D problem driven by single-well production in an elasto-plastic medium (Case 3.5). 60

3.9 Case 3.1 (the Terzaghi problem). Evolution of the dimensionless pressure as a function of dimensionless time. Δp_i is the pressure rise at $t = 0$, L_z is the vertical extent of the reservoir, t is the simulation time, and c_v is the consolidation coefficient. The results from the fully coupled, drained, and undrained methods are shown. Top: coupling strength $\tau = 0.83$. Bottom: coupling strength $\tau = 1.21$. 62

3.10 Case 3.2 (1D injection–production problem). Evolution of the dimensionless pressure as a function of dimensionless time (pore volume produced). The results for the fully coupled, drained, and undrained methods are shown. Top: coupling strength $\tau = 0.83$. Bottom: coupling strength $\tau = 1.21$. . . . 64

3.11 Case 3.2 (1D injection–production problem). Results are shown for the drained split with two different coupling strengths: $\tau = 0.95$ (top), and $\tau = 1.05$ (bottom) and two very different time step sizes. The stability of the drained split is independent of the time step size. The drained split is stable if $\tau < 1$ and unstable if $\tau > 1$, regardless of the time step size. 66

3.12 1D problem with injection and production (Case 3.2). $\tau = 0.083$ is considered. Top: $\alpha = 0.5$ for both flow and mechanics. Bottom: $\alpha = 1.0$ for both flow and mechanics. 67

3.13 1D problem with injection and production (Case 3.2). The mixed time discretization ($\alpha = 0.5$ for flow and $\alpha = 1.0$ mechanics) is considered. Top: $\tau = 0.83$. Bottom: $\tau = 1.11$. 68

3.14 Case 3.3 (the Mandel problem). Evolution of the pressure at the observation point as a function of dimensionless time. Shown are the results for the fully coupled, drained, and undrained splits with different coupling strengths. Top: $\tau = 0.90$. Bottom: $\tau = 1.10$. 70

3.15 Case 3.3 (the Mandel problem). Evolution of the dimensionless vertical displacement on the top as a function of dimensionless time. Shown are the results for the fully coupled, drained, and undrained splits with different coupling strengths. Top: $\tau = 0.90$. Bottom: $\tau = 1.10$. 71

3.16 Case 3.3 (the Mandel problem). Evolution of the dimensionless horizontal displacement on the right side as a function of dimensionless time. Shown are the results for the fully coupled, drained, and undrained splits with different coupling strengths. Top: $\tau = 0.90$. Bottom: $\tau = 1.10$. 72

3.17 1D problem with injection and production with the isotropic hardening (Case 3.4). Top: the drained split is stable in plastic regime, where $\tau = 0.417$. Bottom: the drained split is unstable in the plastic regime, where $\tau = 3.41$. 75

3.18 2D problem with a production well (Case 3.5). Top: pressure history. Bottom: the history of the coupling strength. The model enters the plastic regime at $t_d \approx 0.018$. Beyond this point, the drained split becomes unstable and fails to produce a solution at all. 77

3.19 The evolution of the dimensionless pressure at the observation point vs. dimensionless time (pore volume produced) for Case 3.5 (2D production test in the elastoplastic regime). Top: schematic of the return mapping algorithm for the modified Cam-clay model. Bottom: numerical solutions using the fully coupled, drained, and undrained methods. The model enters the plastic regime at $t_d \approx 0.018$. Beyond this point, the drained split becomes unstable and fails to produce a solution at all. 80

4.1 The distribution of the error amplification factors of the drained (top) and undrained (bottom) splits with respect to pressure diffusivity χ and frequency. The coupling strength τ is 0.05. 97

4.2 The difference of the magnitude of the error amplification factors between the drained and undrained splits. 98

4.3 Case 4.1: the Terzaghi problem in one dimension (left). Case 4.2: the consolidation problem in two dimensions (right). 99

4.4 Convergence analysis of Case 4.1: pressure (top) and displacement (bottom). The coupling strength $\tau = b^2M/K_{dr}$, is 0.95. FC, Dr, and Und indicate the fully coupled, drained split, and undrained split methods, respectively. $\Delta t_d = 4c_v\Delta t/(L_z)^2$ 100

4.5 Non-convergence of the drained split with one iteration for Case 4.1: pressure (top) and displacement (bottom). 101

4.6 Convergence of the undrained split with one iteration for Case 4.1: pressure (top) and displacement (bottom). 102

4.7 Comparison between more iterations and refined time step size in the drained split for Case 4.1: pressure (top) and displacement (bottom). The coupling strength is close to one ($\tau = 0.95$). 103

4.8 Convergence analysis of pressure (top) and displacement (bottom) for a nearly incompressible fluid, where $\tau = 9.5 \times 10^4$ and $c_f = 3.5 \times 10^{-13}Pa^{-1}$. The staggered method is used. The undrained split is not convergent, showing almost zeroth-order accuracy. The fully coupled method shows first-order accuracy. 105

4.9 Spatial distributions of pressure (top) and displacement (bottom) for a nearly incompressible fluid. The undrained split produces large errors, not converging to the true solutions. 106

4.10 Convergence analysis of pressure (top) and displacement (bottom) for an incompressible fluid, where $\tau = 9.5\times10^{11} \cong \infty$ and $c_f = 3.5\times10^{-20} Pa^{-1} \cong 0$. The undrained split is not convergent, showing zeroth-order accuracy. But, the fully coupled method shows first-order accuracy. 107

4.11 Spatial distributions of pressure (top) and displacement (bottom) for an incompressible fluid. The undrained split does not converge to the true solutions. There is no pressure jump and displacement by the overburden at early time. 108

4.12 Convergence analysis of Case 4.2 on pressure (top) and displacement (bottom). $P_d = P/P_i$, $\mathbf{u}_d = \mathbf{u}/\sqrt{L_x L_z}$, and $\Delta t_d = 4\Delta t c_v / L_x^2$, where c_v is the consolidation coefficient along the horizontal direction (Abousleiman et al., 1996). 111

4.13 Non-convergence of the drained split with one iteration for Case 4.2: pressure (top) and displacement (bottom). u_x is the horizontal displacement. 112

4.14 Comparison between more iterations and refined time step size in the drained split for Case 4.2: pressure (top) and displacement (bottom). 113

4.15 Convergence of the undrained split with one iteration for Case 4.2: pressure (top) and displacement (bottom). 114

4.16 Comparison of the rate of convergence at low (top) and high χ (bottom) for Case 4.1. The coupling strength τ is 0.95. 115

4.17 Comparison of the rate of convergence at low (top) and high χ (bottom) for Case 4.2. The coupling strength τ is 0.77. 116

5.1 Iteratively coupled methods for flow and geomechanics. Left: fixed-strain split. Right: fixed-stress split. 117

5.2 Case 5.1 (the Terzaghi problem). Evolution of the dimensionless pressure as a function of dimensionless time. Shown are the results for the fully coupled method, the fixed-strain, and fixed-stress splits. Top: coupling strength $\tau =$ 0.83. Bottom: coupling strength $\tau = 1.21$. 141

5.3 Case 5.2 (1D injection–production problem). Evolution of the dimensionless pressure as a function of dimensionless time (pore volume produced). Shown are the results for the fully coupled method, the fixed-strain, and fixed-stress splits. Top: coupling strength $\tau = 0.83$. Bottom: coupling strength $\tau = 1.21$. 142

5.4 Case 5.2 (1D injection–production problem). Results are shown for the fixed-strain split, with two different coupling strengths: $\tau = 0.95$ (top), and $\tau = 1.05$ (bottom), and two very different time step sizes. The stability of the fixed-strain split is independent of time step size. The fixed-strain split is stable if $\tau < 1$ and unstable if $\tau > 1$, regardless of time step size. 144

5.5 1D problem with injection and production (Case 5.2). $K_{dr} = 1\ GPa$. $\alpha = 0.5$ for both flow and mechanics is considered. Top: $\tau = 0.83$. Bottom: $\tau = 1.11$. 145

5.6 Stability behaviors of different η's and τ's. Top: pressure history at the observation well when $\tau = 3.33$. Bottom: pressure history at the observation well when $\tau = \infty$. 146

5.7 Behavior of the undrained and fixed-stress splits for cases with high coupling strength. Top: Case 5.1 with $\tau = 16.67$. Bottom: Case 5.2 with $\tau = 12.12$. In both cases, the fixed-stress split requires one single iteration per time step to match the fully coupled solution, while many iterations are required for the undrained split. 148

5.8 Case 5.3 (the Mandel problem). Evolution of the pressure at the observation well as a function of dimensionless time. Shown are the results for the fully coupled, fixed-strain, and fixed-stress split methods. Top: $\tau = 0.90$. Bottom: $\tau = 1.10$. 150

5.9 Case 5.3 (the Mandel problem). Evolution of the dimensionless vertical displacement on the top as a function of dimensionless time. Shown are the results for the fully coupled, fixed-strain, and fixed-stress split methods. Top: $\tau = 0.90$. Bottom: $\tau = 1.10$. 151

5.10 Case 5.3 (the Mandel problem). Evolution of the dimensionless horizontal displacement on the right side as a function of dimensionless time. Shown are the results for the fully coupled, fixed-strain, and fixed-stress split methods. Top: $\tau = 0.90$. Bottom: $\tau = 1.10$. 152

5.11 2D problem with a production well (Case 5.4). Top: the history of pressure. Bottom: the history of the coupling strength. FSN and FSS indicate the fixed-strain and fixed-stress splits, respectively. The model enters the plastic regime at $t_d \approx 0.018$. Beyond this point, the fixed-strain split becomes unstable. 153

5.12 Case 5.4 (2D production problem in elastoplastic regime). Shown is the evolution of the dimensionless pressure at the observation well against dimensionless time (pore volume produced). Once the model enters the plastic regime, the fixed-strain split becomes unstable and fails to produce a solution at all. 154

5.13 Convergence analysis of Case 5.1 on pressure (top) and displacement (bottom). $\Delta t_d = 4c_v \Delta t / {L_z}^2$. FC, FSS, and FSN indicate the fully coupled, fixed-stress, and fixed-strain split methods, respectively. The fixed-strain split shows zeroth-order accuracy. But, the fixed-stress split yields first-order accuracy. 155

5.14 Non-convergence of the fixed-strain split with one iteration for Case 5.1: pressure (top) and displacement (bottom) 156

5.15 Convergence of the fixed-stress split with one iteration for Case 5.1: pressure (top) and displacement (bottom) 157

5.16 Two test cases to investigate the effect of different η's. Case 5.5: consolidation problem with constrained boundary (left picture). Case 5.6: consolidation problem with unconstrained boundary (right picture). 159

5.17 Convergence of the fixed-stress split for Case 5.5 when $K_{dr}^{est} = K_{dr}^{3D}$. Top: convergence of pressure. Bottom: pressure distribution along the vertical axis (X-Y section). $\Delta t_d = 4c_v \Delta t / L_x L_z$. 161

5.18 Pressure history at the observation well (2,5) for Case 5.6 with different deviation factors when $0.95 \times K_{dr}^{1D}$, $1.05 \times K_{dr}^{1D}$, and K_{dr}^{3D} are taken for K_{dr}^{est}. 162

6.1 The region for the linear theory. 170

6.2 Water injection and oil production. Left: coupled multiphase flow and geomechanics in a 1D poroelastic medium with overburden. Right: coupled multiphase flow and geomechanics in a 2D poroelastic medium with overburden and side burden 195

6.3 Top: pressure history at the monitoring well during simulation. Bottom: water saturation profile after simulation. $P_d = P/P_{o,i}$. 197

6.4 Convergence behaviors during iterations at $t_d = 0.08$. Top: pressure. Bottom: water saturation. $\|\cdot\|$ is the L^2 norm. 199

6.5 Pressure (top) and water saturation (bottom) distributions after simulation. 201

6.6 Top: pressure history at the monitoring well during simulation. Bottom: water saturation profile at the bottom layer after simulation. 202

6.7 Convergence behaviors during iterations at the first time step. Top: pressure. Bottom: water saturation. 204

6.8 Pressure history at the monitoring well during simulation. Top: the drained and fixed-strain splits. Bottom: the undrained and fixed-stress splits. The drained and fixed-strain splits become unstable due to water injection whereas the undrained and fixed-stress splits yield stability with good accuracy. . . 206

A.1 Left: the Terzaghi problem. Right: the two dimensional plain strain strip footing consolidation problem. 217

A.2 Case A.1 Stability of pressure at early time for Terzaghi's problem. Top: pressure distributions at early and late time by the nodal based finite element method, where linear interpolation is used for pressure and displacement (Wan, 2002). Bottom: pressure distributions at early and late time by the combined finite-volume and finite-element approach. 218

A.3 Case A.2 Dimensionless pressure (top) and vertical displacement distributions (bottom) at early time, $t_d = 3.7 \times 10^{-19}$. Note that subsidence is positive. 221

A.4 Dimensionless vertical-displacement distribution of the top layer at early time, $t_d = 3.7 \times 10^{-19}$. The left part shows large subsidence, and the subsidence decreases along the right direction. 222

A.5 Case A.2 Convergence of pressure (top) and displacement (bottom). First-order accuracy in time is observed for both pressure and displacement. . . . 223

B.1 Typical shapes of capillary pressure regarding wetting and non-wetting phases (e.g., S_w and S_g, respectively). $p_{co} = p_o - p_w$, and $p_{cg} = p_g - p_o$. The capillary pressure curves are drawn based on the work of Lenhard and Parker (1987) 226

Chapter 1

Introduction

1.1 Coupled Flow and Mechanics

The dynamics of coupled flow and mechanics are of interest in may areas of science and engineering. Coupled fluid flow and geomechanics have been dealt with in soil science and civil engineering (Biot, 1941; Park, 1983; Borja and Alarcón, 1995; Armero, 1999; Schrefler, 2004; White and Borja, 2008). Coupled mechanics and heat flow has received a great deal of attention by the mechanical engineering community (Armero and Simo, 1992). Heat can extend, or shrink bodies, and the associated thermal stresses can affect the deformation character of the structure, or porous system, of interest. In environmental engineering, fractures and faults play a critical role in subsurface CO_2 sequestration (Morris, 2009a,b). The changes in the mechanical behavior of the saturated geologic formation due to the injection of CO_2 in large quantities can affect the permeability of the medium significantly, as well as, possibly induce fractures and other leak pathways, or change the conductivity properties of existing fractures and faults in substantial ways.

In bioengineering, flow and mechanical interactions can play an important role in dictating the behavior of blood flow in soft-tissue systems, such as the brain. Since the soft tissue is viscoelastic, consolidation theory can be used to analyze the mechanical response of the tissue due to volumetric strain and media hydration (Miga et al., 1998).

Reservoir engineering is also concerned with the study of fluid flow and the mechanical response of the reservoir. Reservoir geomechanics plays a critical role in compaction drive oil recovery, subsidence, stress dependent permeability of the matrix and fractures, wellbore stability, and production of heavy oil.

Reservoir compaction can enhance oil recovery and slow the decline in the reservoir pressure during depletion, but can lead to serious damage due to surface subsidence. Field examples of the consequences of geomechanical deformation of reservoirs include the Bachaquero Post-Eocene reservoir (Merle et al., 1976), the Wilmington oil field (Kosloff et al., 1980), and the Ravena gas field, including the Venice area (Lewis and Schrefler, 1998). Stress dependent permeability behaviors are particularly significant in fractured and faulted reservoirs due to their impact on injectivity and production capacity, both locally and at field-scale (Gutierrez et al., 2001). Problems related to wellbore instability due to local changes in the stress and strain fields are a major concern and have been the subject of detailed studies (Zuluaga et al., 2007; Zoback, 2007).

Accurate modeling of coupled flow and geomechanics is necessary in order to account properly for the complex dynamics that take place. The level of activity related to numerical simulation of coupled flow and mechanics in natural geologic formations has been quite high. The research efforts span the reservoir, civil, and environmental engineering communities. Our interest here is in developing a computational framework for modeling coupled multiphase flow and geomechanics in geologic systems. The focus is on sequential implicit solution methods that can solve coupled multiphase flow and geomechanics. Specifically, we are interested in formulations that are able to resolve the complex dynamics associated with nonlinear multiphase flow and plastic deformation in geologic porous formations.

In the reservoir engineering community, the coupling strategies for flow and geomechanics have traditionally emphasized flow modeling and attempted to simplify the mechanical response. However, the problem space where proper representation of the coupling between flow and geomechanics is crucial for making engineering predictions has grown quite substantially. For this problem space, numerical simulation based on simplified, or heuristically motivated, coupling strategies is not viable.

1.2 Solution Strategies

The interactions between flow and geomechanics have been modeled using various coupling schemes (Prevost, 1997; Settari and Mourits, 1998; Settari and Walters, 2001; Mainguy and Longuemare, 2002; Minkoff et al., 2003; Thomas et al., 2003; Tran et al., 2004, 2005; Dean et al., 2006; Jha and Juanes, 2007). Coupling methods are typically classified into four types: fully coupled, iteratively coupled, explicitly coupled, and loosely coupled (Settari and Walters, 2001; Dean et al., 2006). In broad terms, the characteristics of the coupling methods are:

1. *Fully Coupled (Simultaneous Solution).* The coupled governing equations of flow and geomechanics are solved simultaneously at every time step (the top of Figure 1.1). A converged solution is obtained through iteration, typically using the Newton–Raphson method (Lewis and Sukirman, 1993; Wan et al., 2003; Jha and Juanes, 2007; Jean et al., 2007; Phillips and Wheeler, 2007a,b; Pan et al., 2009). The fully coupled approach is unconditionally stable, but requires the development of a unified flow–geomechanics simulator and can be computationally expensive. Moreover, it is quite challenging to obtain high-order time approximations using this fully implicit scheme.

2. *Iteratively Coupled (Sequential).* Either the flow, or mechanical, problem is solved first, and then the other problem is solved using the intermediate solution information (Prevost, 1997; Settari and Mourits, 1998; Settari and Walters, 2001; Mainguy and Longuemare, 2002; Thomas et al., 2003; Tran et al., 2004, 2005; Jha and Juanes, 2007; Jean et al., 2007; Wheeler and Gai, 2007; Tchonkova et al., 2008) (the bottom of Figure 1.1). This sequential procedure is iterated at each time step until the solution converges within an acceptable tolerance. The converged solution is identical to that obtained using the fully coupled approach (i.e., simultaneous solution). In principle, sequential schemes offer several advantages. One can use different domains for the flow and mechanical problems in order to deal with the boundary conditions since the details of the stress field at the reservoir boundaries can be part of the

problem (Settari and Walters, 2001; Thomas et al., 2003). Normally, the domain of the mechanical problem is larger than that for reservoir simulation.

3. *Staggered (Single-Pass Sequential).* This is a special case of the iteratively coupled method, where only one iteration is taken (Park, 1983; Zienkiewicz et al., 1988; Armero and Simo, 1992; Armero, 1999).

4. *Loosely Coupled.* The coupling between the two problems is resolved only after a certain number of flow time steps (Bevillon and Masson, 2000; Dean et al., 2006; Samier and Gennaro, 2007). This method can save computational cost compared with the other strategies, but it is less accurate and requires reliable estimates of when to update the mechanical response.

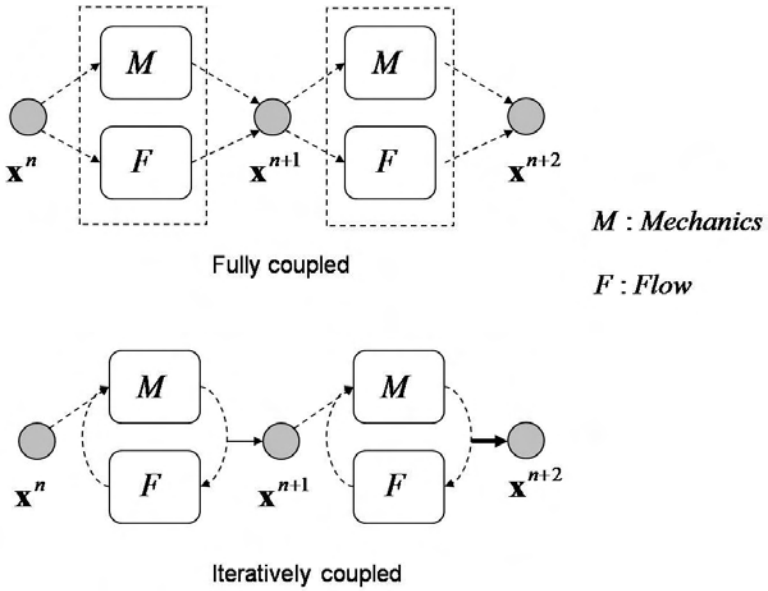

Figure 1.1: Schematics of the fully coupled (top) and the iteratively coupled (bottom) methods.

The staggered and loosely coupled methods are designed to save computational cost (Thomas et al., 2003; Dean et al., 2006). This is because fully coupled flow-mechanics simulation can be much more costly than conventional reservoir flow simulation. Given the enormous investment in software development and the high computational cost of fully

coupled flow–mechanics simulation, it is desirable to develop sequential solution methods that can be competitive with the fully coupled approach. Sequential, or staggered, solution schemes offer wide flexibility and are highly desirable from a software engineering perspective. Moreover, sequential schemes allow for using specialized numerical methods for each of the mechanics and flow problems (Felippa and Park, 1980). In a sequential solution framework, one uses separate software modules for mechanics and flow. Communication between the modules takes place using a clear, well-defined interface (Felippa and Park, 1980; Gai, 2004; Samier and Gennaro, 2007). In such a setting, the robustness and efficiency of each simulator (module) — flow and geomechanics — are available for the coupled problem. For a sequential simulation framework to be competitive in engineering practice, it must be robust across a wide range of problems and have stability and convergence properties that are similar to those enjoyed by the fully coupled method. This thesis deals with the challenge of meeting such requirements with focus on the numerical stability and convergence behaviors of sequential-implicit solution strategies.

1.3 Stability of Sequential Schemes

Significant efforts to find stable and efficient sequential methods for coupled poromechanics (or the analogous thermo-mechanics problem) have been pursued in the geotechnical and computational mechanics communities (Park, 1983; Farhat et al., 1991; Armero and Simo, 1992, 1993; Huang and Zienkiewicz, 1998; Armero, 1999; Soares, 2008). Most of the methods developed assume that the mechanical subproblem is solved first. Two sequential schemes are relevant here. One is called the drained split (the isothermal split in the thermo-elastic and thermo-plastic problems (Armero and Simo, 1992, 1993)), and the other one is the undrained split (Zienkiewicz et al., 1988; Armero, 1999; Jha and Juanes, 2007) (the adiabatic split in the thermo-elastic and thermo-plastic problems (Armero and Simo, 1992, 1993)). The drained split simply freezes the pressure during the mechanical step, thus allowing for flow to take place. Then, the computed strain and stress fields are used when solving the flow problem. Despite its simplicity, the drained split is, at best, conditionally stable. The

undrained split, on the other hand, freezes the fluid mass content when solving the mechanics problem, and then it uses the updated stress and strain fields when solving the flow problem. The undrained split has been shown to respect the dissipative character of the continuum problem, leading to unconditional stability (Armero and Simo, 1992; Armero, 1999). The undrained method can be applied to linear (Zienkiewicz et al., 1988; Huang and Zienkiewicz, 1998) and nonlinear (Armero, 1999) coupled problems of poromechanics and flow. Jha and Juanes (2007) employed the undrained scheme using a mixed finite-element method for linear poroelasticity, where the primary unknowns are pressure, velocity, and displacement. Their scheme is locally mass conservative, and enjoys good stability properties in space and time. They showed that the undrained method is well suited for reservoir simulation.

One can also solve the flow problem first and then deal with the mechanics. The obvious split, the so called fixed-strain scheme, corresponds to freezing the displacements during the solution of the flow problem. This method, however, is conditionally stable. Some sequential methods add a relaxation term to the compressibility coefficient to improve the stability and enhance the convergence rate (Bevillon and Masson, 2000; Mainguy and Longuemare, 2002; Jean et al., 2007; Settari and Mourits, 1998; Wheeler and Gai, 2007). It has been shown that this strategy yields stable numerical behavior in the case of linear poroelasticity. Gai (2004) concludes using several numerical experiences that iterative solution schemes are comparable to the fully coupled method, in terms of efficiency and accuracy. Still, there are no robust stability and convergence analyses of sequential methods of coupled flow and geomechanics, and this is especially the case for nonlinear deformation.

Even though the undrained split has been shown to be unconditionally stable, the drained split, which is conditionally stable, has not been studies as extensively. For example, Armero and Simo (1992) shows the stability limit of the drained split with a single wave number, which does not provide a sharp stability limit for practical settings. Furthermore, the algorithmic a-priori stability estimate of the undrained split for nonlinear problems has not been shown, even though Armero (1999) shows that the undrained split honors energy decay during the mechanical solution step. In order to show unconditional stability of a sequential-implicit method by the energy method, the following three steps

are necessary (Hundsdorfer and Splijer, 1981; Hairer and T́urke, 1984; Hairer, 1986; Simo, 1991; Araújo, 2004).

1. Determine whether the problem is contractive, or dissipative. An appropriate norm, or functional, is defined at this step to show the contractivity property, or energy decay.

2. Show that the operator split corresponding to the sequential method honors, at the continuum level, the contractivity property relative to the norm defined in the previous step. If the operator split is not contractive, then it is not possible to obtain an unconditionally stable solution scheme (Richtmyer and Morton, 1967).

3. When the operator split is contractive at the continuum level, one must then show contractivity at the discrete time level (B-stability) for the individual subproblems for a specific time discretization scheme (e.g., backward Euler, or midpoint rule). The algorithmic (discrete) stability properties of the individual subproblems (i.e., uncoupled) are not necessarily applicable to the B-stability of the coupled problem. This is because the natural norms associated with the subproblems may be different from the appropriate norm for the coupled problem.

1.4 Convergence of Sequential Schemes

For nonlinear problems, stability, in general, does not guarantee convergence. The fully coupled method provides first-order convergence with respect to time. On the other hand, the convergence properties of sequential schemes depend strongly on the details of the splitting strategy, the specific form and discretization schemes used for the various subproblems, and how the subproblems communicate during a time step.

For example, when an original operator $\mathcal{A}$ can be additively split as

$$\dot{\mathbf{y}}(t) = \mathcal{A}\mathbf{y}(t) = (\mathcal{A}_1 + \mathcal{A}_2)\,\mathbf{y}(t), \tag{1.1}$$

where $\mathcal{A}$ can be linear, or nonlinear, $\mathbf{y}$ is a solution vector, and $\dot{()}$ is the time derivative, we solve two subproblems in sequence as follows:

$$\underbrace{\dot{\mathbf{y}}(t) = \mathcal{A}_1\mathbf{y}(t)}_{problem\ 1} \quad and \quad \underbrace{\dot{\mathbf{y}}(t) = \mathcal{A}_2\mathbf{y}(t)}_{problem\ 2}. \tag{1.2}$$

In this case, even when one iteration is performed (i.e., a staggered method), the sequential method from Equation 1.2 is still convergent by Lie's formula (Chorin et al., 1978; Lapidus, 1981). When the operator splitting of Equation 1.2 is applied to the coupled heat flow and mechanical-dynamics, convergence with first-order accuracy in time is obtained, as long as the algorithm is stable (Armero and Simo, 1992).

In general, however, sequential methods do not guarantee convergence for a fixed number of iterations, even when they are numerically stable (Turska et al., 1994). Operator splitting of coupled flow and geomechanics can be written as:

$$\underbrace{0 = \mathcal{A}_1\mathbf{y}(t)}_{mechanics} \quad and \quad \underbrace{0 = \mathcal{A}_2(\mathbf{y}(t), \dot{\mathbf{y}}(t))}_{flow}, \tag{1.3}$$

which is different from the sequential method of Equation 1.2, where the mechanical problem is elliptic. Thus, Lie's formula cannot be applied to Equation 1.3, and it is not clear whether sequential methods are convergent for a fixed iteration number, even though they may be stable. Armero (1999) mentions that the undrained split may suffer from accuracy issues for strongly coupled problems. The convergence of sequential methods with a fixed iteration number is important, since a fixed iteration number is typically required in order to save computational resources.

Vijalapura and Govindjee (2005) propose a hybrid scheme of staggered and fully coupled methods, in which the time step size is controlled for accuracy based on the assumption that refining the time step size improves the accuracy of the staggered method. Furthermore, Vijalapura et al. (2005) investigated the order of accuracy in the index-1 differential algebraic equations because the mechanical problem in Equation 1.3 can be viewed as an

algebraic constraint (Brenan et al., 1996). They claimed that the differential algebraic equations have first-order accuracy when the first step in the algebraic equation is redundant. However, this is not applicable to the coupled flow and quasi-static mechanics because the mechanical problem is not redundant for the first time step. For example, consolidation problems are often driven by instant loading in the mechanical problem during the first time step. Rather, the work of Vijalapura et al. (2005) supports the fact that typical sequential methods can provide zeroth order accuracy in time, when the first step in the algebraic equation is not redundant.

1.5 Finite-Volume and Finite-Element Methods

Numerical experiments are performed using the finite-volume and finite-element methods (the FVM and FEM) for flow and mechanics, respectively. The benefits from this discretization strategy are as follows.

1. The choice for the discretization and the primary unknowns are practical and natural in order to make use of a reservoir simulator and a geomechanics simulator in a sequential fashion.

2. Reservoir simulation with the finite-volume method yields local mass conservation, while that with the finite-element method is not locally conservative.

3. This mixed-space discretization strategy avoids spatial oscillations at early time, which are typically encountered in consolidation problems.

There are two reasons for the early time spatial oscillations in the nodal based finite-element methods. One is the violation of the LBB condition (Fortin and Brezzi, 1991) and the other is the discontinuity of pressure at the drainage boundary. At early time, the coupled problem converges to the undrained mechanical response. The LBB condition is required to solve the incompressible mechanical problem (Fortin and Brezzi, 1991), and it must be satisfied when the fluid and solid grains are incompressible (Murad and Loula, 1992, 1994; Truty and Zimmermann, 2006; White and Borja, 2008).

Even when the LBB condition is satisfied (i.e., locking-free elements), or the fluid is compressible, the initial jump produces a pressure discontinuity at the drainage boundary, which can yield an unbounded pressure gradient. Thus, nodal based finite-element methods can produce an unbounded flux, which leads to conditional stability (i.e., lower bound on the time step size) (Vermeer and Verruijt, 1981; Ženišek, 1984). Thus, consolidation problems may involve incompatibility of the pore-pressure at the drainage boundary, which leads to a lower bound on the time step size. In these cases, a finite amount of pressure diffusion is required in order to interpolate the pressure solution reasonably accurately.

To avoid the spurious oscillations in space, an additional stabilizer can be used (Wan et al., 2003; Truty and Zimmermann, 2006; White and Borja, 2008). This approach can overcome the instability. However, an appropriate value of the control parameter must be provided. Moreover, local accuracy is sacrificed because of the additional stabilization term. The finite-volume method for flow can provide a bounded flux, thus allowing for piecewise constant approximations of the pressure field. Hence, the finite-volume approach shows stability at early time with no need for a stabilizer for compressible fluids, and it honors local mass conservation. Phillips and Wheeler (2007a) and Phillips and Wheeler (2007b) also show using a-priori error estimates and numerical experiments that mixed finite-element methods can eliminate the spatial oscillations of pressure at early time in consolidation problems, yielding stability in space.

1.6 Outline

In this thesis, we investigate the stability and convergence properties of sequential schemes for coupled flow and geomechanics. Four sequential methods are considered, namely, drained, undrained, fixed-strain, and fixed-stress splits.

In Chapter 2, we present a general framework for nonlinear formulations of coupled flow and geomechanics, and we describe the constitutive relations consistent with Biot's theory Biot (1941). The formulation integrates the approaches proposed by several researchers

(e.g., Coussy (1995), Lewis and Schrefler (1998), Borja (2006)), honoring the thermodynamics of the problem. Then, we extend the formulation to multiphase flow and transport in reservoirs.

In Chapter 3, we perform detailed stability analyses of the drained and undrained splits for coupled flow and geomechanics using the generalized midpoint time integration rule. We first employ the Von Neumann method to obtain a-priori stability estimates for the linear coupled problem. To complete the stability analysis of the undrained split for nonlinear problems (i.e., poro-elasto-plasticity), we use the energy method with the generalized midpoint rule.

In Chapter 4, we investigate the convergence properties of the drained and undrained splits. The backward Euler time discretization (i.e., implicit time integration) is used. To obtain a-priori error estimates for both the drained and undrained splitting schemes, we use matrix and spectral methods.

In Chapter 5, we perform stability analysis of sequential methods that solve the flow problem first, namely, the fixed-strain and fixed-stress splits. The fixed-strain split freezes the rate of total volumetric strain whereas the fixed-stress split freezes the rate of total volumetric stress. We perform a thorough stability analysis for poro-elasticity and poro-elasto-plasticity for single-phase flow of a slightly compressible fluid. The Von Neumann and energy methods are used to obtain the stability limits, where the generalized midpoint rule is used for time discretization. In Chapter 5, we also perform convergence analysis of the linear coupled problem. Matrix and spectral methods are used to derive a-priori error estimates of the fixed-strain and fixed-stress splits.

Chapter 6 extends the sequential coupling strategies from single-phase flow to multiphase flow. Since the sequential splits can be used in staggered Newton methods (Schrefler et al., 1997), we perform spectral analysis to analyze the convergence properties of the various splits using the backward Euler time discretization. For nonlinear operator splitting (i.e., no linearization is performed of the full problem), we perform stability analysis of the sequential implicit solution schemes using the energy method with an appropriately defined norm. In Chapter 7, we summarize our findings and suggest future work.

Chapter 2

Formulation

2.1 Background

The coupling between flow and mechanics has been studied by many authors (e.g., Biot (1941); Geertsma (1957); Biot and Willis (1957); Coussy (1995); Lewis and Schrefler (1998); Borja (2006)). Biot (1941), Geertsma (1957), and Biot and Willis (1957) develop the constitutive equations in the case of single-phase flow with a slightly compressible fluid, and they proposed appropriate laboratory tests that can determine the various coupling coefficients.

For multiphase flow, the approach by Lewis and Schrefler (1998) provides explicit expressions of the physical quantities of interest (i.e., coefficients in the governing equations), even though the formulation does not necessarily ensure complete consistency with the thermodynamic constraints when capillarity is present. Borja (2006) shows that the coupling is thermodynamically stable, examining different definitions of the effective stress, but the bulk modulus used is neither the drained, nor the undrained bulk modulus. Thus, the Biot's coefficient in Borja (2006) is different from that used by other investigators. Coussy (1995) and Coussy et al. (1998) provide thermodynamically consistent constitutive relations. Nevertheless, the coefficients of the constitutive equations (e.g., Biot's moduli) for multiphase flow are not explicitly given. For these reasons, the purpose of this chapter is to describe the

full formulation and provide expressions of the constitutive relations of coupled multiphase flow and geomechanics.

2.2 Governing Equations

The governing equations for coupled flow and reservoir geomechanics come from mass balance for flow and linear-momentum balance for mechanics. Under the quasi-static assumption for porous media displacements, the governing equation for mechanical deformation of the solid–fluid system can be written as:

$$\mathrm{Div}\,\boldsymbol{\sigma} + \rho_b \boldsymbol{g} = \mathbf{0}, \tag{2.1}$$

where $\mathrm{Div}(\cdot)$ is the divergence operator, $\boldsymbol{\sigma}$ is the Cauchy total-stress tensor, $\boldsymbol{g}$ is the gravity vector, $\rho_b = \phi\rho_f + (1-\phi)\rho_s$ is the bulk density, ρ_f is total fluid density, ρ_s is the density of the solid phase, and ϕ is the true porosity. The true porosity is defined as the ratio of the pore volume to the bulk volume in the deformed configuration.

Using the infinitesimal transformation, the fluid mass conservation equation of phase J can be expressed as

$$\frac{dm_J}{dt} + \mathrm{Div}\,\boldsymbol{w}_J = (\rho f)_J\,, \tag{2.2}$$

where $\boldsymbol{w}_J$ is the mass flux of fluid phase J (fluid mass flow rate per unit area and time) relative to the solid skeleton. dm_J/dt is the variation of fluid mass relative to the solid skeleton. From here on, we denote by $\frac{d(\cdot)}{dt}$ the change of a physical quantity $(\cdot)$ relative to the solid skeleton. ρ_J is the density of fluid phase J, and f_J is a volumetric source term of phase J.

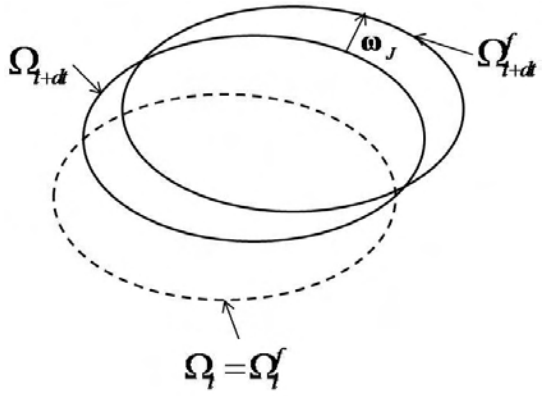

Figure 2.1: Ω_t and Ω_t^f are the geometrical volumes of the solid and fluid at time t, respectively. Even though the elementary solid system has the same fluid mass content at time t, $\Omega_t = \Omega_t^f$, the solid system does not have the same fluid mass content after time dt, $\Omega_{t+dt} \neq \Omega_{t+dt}^f$. $\boldsymbol{w}_J$ is the mass flux of fluid phase J relative to the solid skeleton (Coussy, 1995).

2.3 Coupling and Constitutive Relations

We adopt a classical continuum representation, where the fluid and solid are viewed as overlapping continua. We summarize the general coupling among mass, energy, and mechanical equilibrium based on the approach by Coussy (1995) and Coussy et al. (1998). For more generality, we include the effect of the source term in Equation 2.2.

2.3.1 Coupling of fluid, heat flow, and mechanics

The variation of internal energy of an open system with respect to time is described by the first law of thermodynamics. The infinitesimal transformation is adopted, and that allows for using the linearized strain tensor $\boldsymbol{\varepsilon}$, which can be written as

$$\boldsymbol{\varepsilon} = \mathbf{Grad}^s\, \boldsymbol{u} = \frac{1}{2}(\mathbf{Grad}\, \boldsymbol{u} + \mathbf{Grad}^t\, \boldsymbol{u}) \tag{2.3}$$

where $\boldsymbol{u}$ is the displacement vector.

$$\begin{aligned}\frac{dE}{dt} &= -\operatorname{Div}(e_J \boldsymbol{w}_J) + e_J\,(\rho f)_J - \operatorname{Div}\mathbf{q} + r + \boldsymbol{\sigma} : \dot{\boldsymbol{\varepsilon}} \\ &\quad - \operatorname{Div}\left[\left(\frac{p}{\rho}\right)_J \boldsymbol{w}_J\right] + \left(\frac{p}{\rho}\right)_J (\rho f)_J + \boldsymbol{w}\cdot\mathbf{F}, \end{aligned} \tag{2.4}$$

where $\frac{dE}{dt}$ is the change in internal energy with respect to the moving solid skeleton, e_J is the internal energy per unit mass of phase J, $\mathbf{q}$ is the heat flux, $\boldsymbol{\sigma}$ is the total stress, and $\boldsymbol{w} = \{\boldsymbol{w}_J\}$. $\dot{(\cdot)}$ denotes a time derivative. Repeated subscripts imply summation. Note that the fluid acceleration term is neglected due to the quasi-static assumption used throughout this dissertation.

In Equation 2.4, the first and second terms are the energy transported by the flow of mass, including the source term. The third and fourth terms represent the external heat provided by conduction and heat sources. The fifth term is the infinitesimal strain work. The sixth and seventh terms are the work rates of the relative mass flow, including the source term. The eighth term is the body force $\mathbf{F}$, which is normally the gravity force.

The second law of thermodynamics states that the material derivative of the entropy (i.e., the change of the total entropy) attached to any material system is greater than the external entropy supplied to the system, which is written as

$$\underbrace{\frac{dS}{dt} + \operatorname{Div}(s_J \boldsymbol{w}_J)}_{\frac{DS}{Dt}} \geq s_J\,(\rho f)_J - \operatorname{Div}\frac{\mathbf{q}}{T} + \frac{r}{T}, \tag{2.5}$$

where S is the total entropy, s_J is the internal entropy per unit mass of phase J, and $\frac{D(\cdot)}{Dt}$ is the material derivative attached to the whole material system. The first and second terms on the left of the inequality in Equation 2.5 are the entropy change observed by the motion of the solid skeleton and the entropy transported by mass flow without the source term, respectively. On the right of the inequality of Equation 2.5, the first term is the entropy transported by the fluid source; the second and third terms are the external

entropy provided by conduction and the external volume heat source.

The Helmholtz free energy (Ψ) is defined as

$$\Psi = E - TS\,. \tag{2.6}$$

Then, using Equations 2.4, 2.5, and 2.6, the fundamental inequality is obtained as

$$\underbrace{\boldsymbol{\sigma} : \dot{\boldsymbol{\varepsilon}} - g_J\left[\mathrm{Div}(\boldsymbol{w}_J) - (\rho f)_J\right] - \frac{d\Psi}{dt} - S\frac{dT}{dt}}_{\Phi_1}\ \underbrace{-\frac{\mathbf{q}}{T}\cdot\mathbf{Grad}\,T}_{\Phi_2}$$
$$\underbrace{-\boldsymbol{w}\cdot\left[\mathbf{Grad}(g_J) + s_J\,\mathbf{Grad}\,T - \mathbf{F}\right]}_{\Phi_3} \geq 0\,, \tag{2.7}$$

where g_J is the Gibbs potential per unit mass of phase J, which can be written as

$$g_J = e_J + (p/\rho)_J - Ts_J = g_J(p_J, T)\,. \tag{2.8}$$

Equation 2.7 consists of the intrinsic dissipation (Φ_1), thermal dissipation associated with heat conduction (Φ_2), and the dissipation due to mass transport (Φ_3). Applying the hypothesis that each dissipation is non-negative, we obtain

$$\Phi_1 = \boldsymbol{\sigma} : \dot{\boldsymbol{\varepsilon}} - g_J\left[\mathrm{Div}(\boldsymbol{w}_J) - (\rho f)_J\right] - \frac{d\Psi}{dt} - S\frac{dT}{dt} \geq 0, \tag{2.9}$$

$$\begin{aligned} \Phi_2 &= -\frac{\mathbf{q}}{T}\cdot\mathbf{Grad}\,T \geq 0, \\ \mathbf{q} &= -\mathbf{k}_c\cdot\mathbf{Grad}\,T, \end{aligned} \tag{2.10}$$

$$\begin{aligned} \Phi_3 &= -\left(\frac{\boldsymbol{w}}{\rho}\right)_J\cdot\left[\mathbf{Grad}(p_J) - \rho_J\mathbf{F}\right] \geq 0, \\ \left(\frac{\boldsymbol{w}}{\rho}\right)_J &= -\mathbf{k}_{p,JK}\cdot\left[\mathbf{Grad}(p_K) - \rho_K\mathbf{F}\right], \end{aligned} \tag{2.11}$$

where the heat conduction and the generalized Darcy's law (Equations 2.10 and 2.11, respectively) are obtained by employing the hypothesis of normality of the dissipative mechanisms. $\mathbf{k}_{p,JK}$ is a fourth-order symmetric positive-definite permeability tensor associated with the J and K fluid phases, where the effect of fluid viscosity is included. In typical cases, $\mathbf{k}_{p,JK}$ is zero when $J \neq K$, and $\mathbf{k}_{p,JK}$ is the effective permeability tensor when $J = K$. We typically separate the fluid viscosity from $\mathbf{k}_{p,JK}$ in Equation 2.11. $\mathbf{k}_c$ is the symmetric positive definite heat conductivity tensor.

2.3.2 Constitutive relations based on intrinsic dissipation Φ_1

The Helmholtz free energy is associated with the strain, mass, temperature, and internal variables associated with the intrinsic dissipation (e.g., plasticity). In this section, we assume elasticity, and we do not consider the internal variables associated with the intrinsic dissipation. This is because we can easily extend the description from elasticity to plasticity. For more details on elasto-plasticity, see Chapter 5 of Coussy (1995).

From Equations 2.2 and 2.9, the intrinsic dissipation can be expressed as

$$\Phi_1 = \left(\boldsymbol{\sigma} - \frac{\partial \Psi}{\partial \varepsilon}\right) : \dot{\boldsymbol{\varepsilon}} + \left(g_J - \frac{\partial \Psi}{\partial m_J}\right) \frac{dm_J}{dt} - \left(S + \frac{\partial \Psi}{\partial T}\right) \frac{dT}{dt} \geq 0. \tag{2.12}$$

In the case of elasticity, the intrinsic dissipation is zero. Since strain, mass, and temperature are independent variables, the state equations are obtained from Equation 2.12 as follows:

$$\boldsymbol{\sigma} = \frac{\partial \Psi}{\partial \varepsilon}, \;\; g_J = \frac{\partial \Psi}{\partial m_J}, \;\; S = -\frac{\partial \Psi}{\partial T} \, . \tag{2.13}$$

Differentiating Equation 2.13,

$$\delta\boldsymbol{\sigma} = \frac{\partial^2\Psi}{\partial^2\varepsilon} : \delta\varepsilon + \frac{\partial^2\Psi}{\partial\varepsilon\partial m_J}\delta m_J + \frac{\partial^2\Psi}{\partial\varepsilon\partial T}\delta T, \tag{2.14}$$

$$\delta g_J = \frac{\partial^2\Psi}{\partial\varepsilon\partial m_J} : \delta\varepsilon + \frac{\partial^2\Psi}{\partial m_J\partial m_K}\delta m_K + \frac{\partial^2\Psi}{\partial m_J\partial T}\delta T, \tag{2.15}$$

$$\text{where } \delta g_J = \frac{1}{\rho_J}\delta p + s_J\delta T,$$

$$\delta S = \frac{\partial^2\Psi}{\partial\varepsilon\partial T} : \delta\varepsilon + \frac{\partial^2\Psi}{\partial m_J\partial T}\delta m_J + \frac{\partial^2\Psi}{\partial^2 T}\delta T, \tag{2.16}$$

where δ represents the incremental form of the material derivative with respect to the solid skeleton, $d(\cdot)/dt$. Then, the constitutive relations for elasticity are obtained as follows:

$$\delta\boldsymbol{\sigma} = \mathbf{C}_{ud} : \delta\boldsymbol{\varepsilon} - M_{JK}\mathbf{b}_K\left(\frac{\delta m}{\rho}\right)_J - \mathbf{A}_q\delta T\,, \tag{2.17}$$

$$\delta p_J = M_{JK}\left(-\mathbf{b}_K : \delta\boldsymbol{\varepsilon} + \left(\frac{\delta m}{\rho}\right)_K\right) + (\rho l_q)_J\delta T\,, \tag{2.18}$$

$$\delta S = \mathbf{A}_q : \delta\boldsymbol{\varepsilon} - l_{q,J}\left(\frac{\delta m}{\rho}\right)_J + \beta_q\delta T\,, \tag{2.19}$$

where

$$\frac{\partial^2\Psi}{\partial^2\boldsymbol{\varepsilon}} = \mathbf{C}_{ud}\,,\quad \frac{\partial^2\Psi}{\partial\boldsymbol{\varepsilon}\,(\partial m/\rho)_J} = -M_{JK}\mathbf{b}_K\,,\quad \frac{\partial^2\Psi}{\partial\boldsymbol{\varepsilon}\partial T} = -\mathbf{A}_q\,,$$
$$\frac{\partial^2\Psi}{(\partial m/\rho)_J\,(\partial m/\rho)_K} = M_{JK}\,,\left(\frac{\partial^2\Psi}{(\partial m/\rho)_J\,\partial T} - s_J\right) = l_{q,J}\,,\quad \frac{\partial^2\Psi}{\partial^2 T} = \beta_q, \tag{2.20}$$

where $\mathbf{C}_{ud}$ (undrained moduli), M_{JK} (Biot moduli), $\mathbf{b}_K$ (Biot coefficient), $\mathbf{A}_q$, $l_{q,J}$, and β_q are determined from experiments. $\mathbf{b}_K$ is the second-order tensor, and becomes $b_K\mathbf{1}$ in the isotropic case, where $\mathbf{1}$ is the second-order identity tensor. When isotropic and isothermal conditions are assumed, the constitutive relations of $\delta\boldsymbol{\sigma}$, δp_J, and δS are reduced to the

coupling between mass-flow and mechanics, and we write

$$\delta\sigma = \mathbf{C}_{ud} : \delta\boldsymbol{\varepsilon} - \left(\frac{\delta m}{\rho}\right)_J M_{JK} b_K \mathbf{1}, \tag{2.21}$$

$$\delta p_J = M_{JK}\left(-b_K \delta\varepsilon_v + \left(\frac{\delta m}{\rho}\right)_K\right). \tag{2.22}$$

Equation 2.21 can be rewritten as

$$\delta\boldsymbol{\sigma} = \mathbf{C}_{dr} : \delta\boldsymbol{\varepsilon} - b_J \delta p_J \mathbf{1}, \tag{2.23}$$

where $\mathbf{C}_{dr}$ represent the drained bulk moduli. In the case of single-phase flow, the coefficients are obtained from drained and undrained experiments. For example,

$$b = 1 - \frac{K_{dr}}{K_s}, \quad \frac{1}{M} = \phi c_f + \frac{b-\phi}{K_s}, \tag{2.24}$$

where c_f is the fluid compressibility, and K_{dr} and K_s are the drained bulk modulus and the solid grain stiffness, respectively. b and M for single-phase correspond to b_J and M_{JK} for multiphase systems. In the case of multiphase flow, the Biot moduli $\mathbf{M} = \{M_{JK}\}$ and Biot coefficient $\mathbf{b} = \{b_J\}$ are not given explicitly by Coussy (1995). The subsequent sections provide appropriate expressions of $\mathbf{M}$ and $\mathbf{b}$.

2.4 Derivation of the Coupling Coefficients

2.4.1 Coupling coefficients for single-phase flow

The governing mass conservation equation for single-phase flow is

$$\frac{\partial(\rho_f \phi)}{\partial t} + \mathrm{Div}(\rho_f \phi \tilde{v_p}) = 0, \tag{2.25}$$

where $\tilde{v_p}$ is the interstitial fluid velocity. Note that Equations 2.2 and 2.25 are equivalent. Equation 2.2 is expressed using the material derivative (i.e., Lagrangian description), while

Equation 2.25 is expressed using the Eulerian description. m in Equation 2.2 is the Lagrangian density, but $\rho_f\phi$ in Equation 2.25 is the Eulerian density (Coussy, 1995). Hence, $\delta m \neq \delta\left(\rho_f\phi\right)$ due to the motion of the solid skeleton, which will be shown in Equation 2.36.

Introducing the following identity for the material derivative with respect to the solid skeleton, $d(\cdot)/dt$, (Marsden and Hughes, 1983)

$$\frac{\partial f}{\partial t} = \frac{df}{dt} - v_s \cdot \mathbf{Grad}\, f, \tag{2.26}$$

where v_s is the velocity of the solid skeleton, and f is an arbitrary function, Equation 2.25 can be rewritten as

$$\frac{d(\rho_f\phi)}{dt} - v_s \cdot \mathbf{Grad}(\rho_f\phi) + \mathrm{Div}(\rho_f\phi\tilde{v_p}) = 0. \tag{2.27}$$

Using the identity

$$\mathrm{Div}(\rho_f\phi v_s) = v_s \cdot \mathbf{Grad}(\rho_f\phi) + \rho_f\phi\,\mathrm{Div}\, v_s, \tag{2.28}$$

we obtain from Equation 2.26,

$$\frac{d(\rho_f\phi)}{dt} + \rho_f\phi\,\mathrm{Div}\, v_s + \mathrm{Div}(\rho_f v_f) = 0, \tag{2.29}$$

where $v_f = \phi(\tilde{v_p} - v_s)$ is Darcy's velocity. In order to expand the first term of Equation 2.29, we define the fluid compressibility as

$$c_f \;=\; \frac{1}{\rho_f}\frac{d\rho_f}{dp}. \tag{2.30}$$

From Appendix B.5, we have

$$\frac{d\phi}{dt} = \frac{b-\phi}{K_s}\frac{dp}{dt} + (b-\phi)\,\mathrm{Div}\, v_s, \tag{2.31}$$

where $\mathrm{Div}\, v_s \equiv d\varepsilon_v/dt$, and we define the Biot coefficient b for single phase flow as

$$b = 1 - \frac{K_{dr}}{K_s}. \tag{2.32}$$

Then, from Equations 2.30 and 2.31, Equation 2.29 can be expressed as

$$\rho_f \left\{ \left(\phi c_f + \frac{b-\phi}{K_s} \right) \frac{dp}{dt} + b \frac{d\varepsilon_v}{dt} \right\} + \mathrm{Div}(\rho_f v_f) = 0. \tag{2.33}$$

Since the first term of Equation 2.33 corresponds to the mass variation, δm, we obtain

$$\frac{\delta m}{\rho_f} = \left(\phi c_f + \frac{b-\phi}{K_s} \right) \delta p + b \delta \varepsilon_v. \tag{2.34}$$

Hence, the Biot coefficient b and the Biot modulus M are obtained as

$$b = 1 - \frac{K_{dr}}{K_s}, \quad \frac{1}{M} = \phi c_f + \frac{b-\phi}{K_s}. \tag{2.35}$$

2.4.2 Coupling coefficients for multi-phase flow

In Equation 2.2, the flux term, $\mathrm{Div}\, \boldsymbol{w}_J$, is easily expressed in terms of fluid pressures using Darcy's law, Equation 2.11. Hence, we focus on the expression of the accumulation term, dm_J/dt. We apply the same procedure used for single-phase flow. Equation 2.29 for single-phase flow yields

$$\delta m = \delta(\rho_f \phi) + \rho_f \phi \delta \varepsilon_v. \tag{2.36}$$

The Biot moduli for multiphase flow can be obtained by expanding the accumulation term in the flow equation (i.e., δm_J) as follows:

$$\begin{aligned} \delta m_J &= \delta \left((\rho S)_J \phi \right) + (\rho S)_J \phi \delta \varepsilon_v \\ &= (\rho S)_J \delta \phi + \phi \left(\rho \delta S \right)_J + \phi \left(S \delta \rho \right)_J + (\rho S)_J \phi \delta \varepsilon_v. \end{aligned} \tag{2.37}$$

For multiphase flow, we introduce the total fluid pressure, p_t (i.e., the equivalent pore pressure in Coussy (2004)). Then, the true porosity variation $\delta\phi$ in multiphase flow can be extended from that for single-phase using the total fluid pressure. Specifically, we can write

$$\begin{aligned}\delta\phi &= \frac{\partial\phi}{\partial p_t}\delta p_t + (b-\phi)\,\delta\varepsilon_v \\ &= \frac{b-\phi}{K_s}S_J\delta p_J + (b-\phi)\,\delta\varepsilon_v, \end{aligned} \tag{2.38}$$

where δp_t is assumed to be $S_J\delta p_J$ (recall that summation is implied), the validity of which will be examined in Remarks 2.2 and 2.3. Since we can define the fluid compressibility of phase J in multiphase flow, c_J, as

$$c_J = \frac{1}{\rho_J}\frac{\delta\rho_J}{\delta p_J}, \tag{2.39}$$

then, by using Equation 2.38, we can express Equation 2.37 as

$$\left(\frac{\delta m}{\rho}\right)_J = S_J\left(\frac{b-\phi}{K_s}S_J\delta p_J + b\delta\varepsilon_v\right) + \phi\delta S_J + \phi\left(Sc\delta p\right)_J. \tag{2.40}$$

In order to express δS_J in terms of δp_J, we can use the capillary relations. Typically, oil, gas, and water systems are considered. Each saturation can be expressed as

$$\begin{aligned}\delta S_o &= -\delta S_g - \delta S_w \\ &= -\frac{dS_w}{dp_{co}}\left(\delta p_o - \delta p_w\right) - \frac{dS_g}{dp_{cg}}\left(\delta p_g - \delta p_o\right)), \end{aligned} \tag{2.41}$$

$$\delta S_g = \frac{dS_g}{dp_{cg}}\left(\delta p_g - \delta p_o\right), \tag{2.42}$$

$$\delta S_w = \frac{dS_w}{dp_{co}}\left(\delta p_o - \delta p_w\right), \tag{2.43}$$

where p_{co} is the capillary pressure between oil and water, and p_{cg} is the capillary pressure

between gas and oil. Thus, the mass variation of each phase δm_J can be written as

$$\begin{aligned}
\frac{\delta m_w}{\rho_w} &= \underbrace{\left(\phi\frac{dS_w}{dp_{co}} + S_w\frac{b-\phi}{K_s}S_o\right)}_{N_{wo}}\delta p_o + \underbrace{\left(\phi S_w c_w - \phi\frac{dS_w}{dp_{co}} + S_w\frac{b-\phi}{K_s}S_w\right)}_{N_{ww}}\delta p_w \\
&+ \underbrace{S_w\frac{b-\phi}{K_s}S_g}_{N_{wg}}\delta p_g + \underbrace{S_w b}_{b_w}\delta\varepsilon_v, \qquad (2.44)\\
\frac{\delta m_o}{\rho_o} &= \underbrace{\left(\phi S_o c_o + \phi\left(-\frac{dS_w}{dp_{co}} + \frac{dS_g}{dp_{cg}}\right) + S_o\frac{b-\phi}{K_s}S_o\right)}_{N_{oo}}\delta p_o + \underbrace{\left(\phi\frac{dS_w}{dp_{co}} + S_o\frac{b-\phi}{K_s}S_w\right)}_{N_{ow}}\delta p_w \\
&+ \underbrace{\left(\phi\left(-\frac{dS_g}{dp_{cg}}\right) + S_o\frac{b-\phi}{K_s}S_g\right)}_{N_{og}}\delta p_g + \underbrace{S_o b}_{b_o}\delta\varepsilon_v, \qquad (2.45)\\
\frac{\delta m_g}{\rho_g} &= \underbrace{\left(-\phi\frac{dS_g}{dp_{cg}} + S_g\frac{b-\phi}{K_s}S_o\right)}_{N_{go}}\delta p_o + \underbrace{\left(S_g\frac{b-\phi}{K_s}S_w\right)}_{N_{gw}}\delta p_w \\
&+ \underbrace{\left(\phi S_g c_g + S_g\frac{b-\phi}{K_s}S_g + \phi\frac{dS_g}{dp_{cg}}\right)}_{N_{gg}}\delta p_g + \underbrace{S_g b}_{b_g}\delta\varepsilon_v. \qquad (2.46)
\end{aligned}$$

From Equations 2.44, 2.45, and 2.46, the Biot moduli $\mathbf{M}$ and Biot coefficient $\mathbf{b}$ can be expressed as

$$\mathbf{M}^{-1} = \mathbf{N} = \begin{pmatrix} N_{oo} & N_{ow} & N_{og} \\ N_{wo} & N_{ww} & N_{wg} \\ N_{go} & N_{gw} & N_{gg} \end{pmatrix}, \mathbf{b} = \begin{pmatrix} b_o \\ b_w \\ b_g \end{pmatrix}, \qquad (2.47)$$

where $\mathbf{N} = \mathbf{M}^{-1}$.

Remark 2.1. Note that $\mathbf{N}$ is symmetric, so that $\mathbf{M}$ is also symmetric. The symmetry of $\mathbf{M}$ is required by Equation 2.20. $\mathbf{M}$ is also positive definite as shown in Appendix B.1. The positive definiteness of $\mathbf{M}$ ensures thermodynamic stability (Coussy, 1995), which yields a well-posed problem. The well-posedness of coupled flow and geomechanics is referred to in Chapter 6.3 as contractivity.

Remark 2.2. Note that $\delta p_t \neq \delta\left(S_J p_J\right)$. If $\delta p_t = \delta\left(S_J p_J\right)$, which is used in Lewis and Sukirman (1993) and Lewis and Schrefler (1998), the constitutive relations given in Equations 2.22 and 2.23 cannot be obtained in the presence of capillarity. $\delta p_t = \delta\left(S_J p_J\right)$ cannot guarantee thermodynamic stability and well-posedness, as shown in Appendix B.4. Compare Chapter 6.3.3 with Appendix B.4 regarding the contractivity properties of coupled flow and mechanics. When p_t is assumed to be $S_J p_J$, this implies that we assume physical linearization of the total-stress from the initial (reference) state to the current state. But this assumption is not appropriate because the saturation field varies across the entire range of possible values, and that precludes linearization from the initial state to the current state.

Remark 2.3. $\delta p_t = S_J \delta p_J$, which leads to $b_J = bS_J$, honors thermodynamic stability as well as the form of the constitutive equations given by Equations 2.22 and 2.23. Only the incremental total-pressure, δp_t, is defined, since the linear model is relevant within a narrow range of variation around a reference state (Coussy, 1995). The Biot coefficient $b_J = bS_J$ matches the derivation of Coussy (1995) and Coussy et al. (1998).

Appendix C shows the formulation for the constitutive relations relevant to reservoir simulation based on the standard black-oil model, where there are two general choices for the primary variables: namely, the phase pressures p_o, p_w, and p_g, or one phase pressure and two saturations, such as p_o, S_w, and S_g.

Chapter 3

Stability of the Drained and Undrained Splits

3.1 Mathematical Model

We adopt a classical continuum representation, where the fluid and solid are viewed as overlapping continua. The physical model is based on the poro-elasticity and poro-elasto-plasticity theories (see, e.g., Coussy (1995)). In this chapter, we assume isothermal single-phase flow of a slightly compressible fluid, small deformation (i.e., infinitesimal transformations), and no stress-dependence of flow properties, such as porosity or permeability. The governing equations for coupled flow and reservoir geomechanics come from fluid mass balance and (linear) momentum balance. The governing equation for mechanical deformation of the solid–fluid system can be expressed as

$$\mathrm{Div}\,\boldsymbol{\sigma} + \rho_b \boldsymbol{g} = \mathbf{0}, \tag{3.1}$$

where a stress–strain relation must be specified for the mechanical behavior of the porous medium. Changes in total stress and fluid pressure are related to changes in strain and fluid content by Biot's theory (Biot, 1941; Geertsma, 1957; Biot and Willis, 1957; Coussy, 1995; Lewis and Schrefler, 1998; Borja, 2006). Following Coussy (1995), the poroelasticity

equations take the following form:

$$\boldsymbol{\sigma} - \boldsymbol{\sigma}_0 = \mathbf{C}_{dr} : \boldsymbol{\varepsilon} - b(p - p_0)\mathbf{1}, \tag{3.2}$$

$$\frac{1}{\rho_{f,0}}(m - m_0) = b\varepsilon_v + \frac{1}{M}(p - p_0), \tag{3.3}$$

where the linearization is applied from the reference state to the current state for single-phase flow of a slightly compressible fluid. The subscript 0 means reference state, $\mathbf{C}_{dr}$ is the rank-4 drained elasticity tensor, $\mathbf{1}$ is the rank-2 identity tensor, p is fluid pressure, m is fluid mass per unit bulk volume, M is the Biot modulus, and b is the Biot coefficient. Note that we use the convention that tensile stress is positive. Here, $\boldsymbol{\varepsilon}$ is the linearized strain tensor under the assumption of infinitesimal transformation:

$$\boldsymbol{\varepsilon} = \mathbf{Grad}^s\, \boldsymbol{u} = \frac{1}{2}(\mathbf{Grad}\, \boldsymbol{u} + \mathbf{Grad}^t\, \boldsymbol{u}). \tag{3.4}$$

Note that we also have (Coussy, 1995)

$$\frac{1}{M} = \phi_0 c_f + \frac{b - \phi_0}{K_s}, \tag{3.5}$$

$$b = 1 - \frac{K_{dr}}{K_s}, \tag{3.6}$$

where c_f is the fluid compressibility $(1/K_f)$, K_f is the bulk modulus of the fluid. Again, the subscript 0 means reference state. It is convenient to express the strain and stress tensors in terms of their volumetric and deviatoric parts,

$$\boldsymbol{\varepsilon} = \frac{1}{3}\varepsilon_v \mathbf{1} + \boldsymbol{e}, \tag{3.7}$$

$$\boldsymbol{\sigma} = \sigma_v \mathbf{1} + \boldsymbol{s}, \tag{3.8}$$

where $\varepsilon_v = \mathrm{tr}\boldsymbol{\varepsilon}$ is the volumetric strain (the trace of the strain tensor), $\boldsymbol{e}$ is the deviatoric part of the strain tensor, $\sigma_v = \frac{1}{3}\mathrm{tr}\boldsymbol{\sigma}$ is the volumetric (mean) total stress, and $\boldsymbol{s}$ is the deviatoric total stress tensor.

The fluid mass conservation equation is

$$\frac{dm}{dt} + \text{Div}\, \boldsymbol{w} = \rho_{f,0} f, \tag{3.9}$$

where $\boldsymbol{w}$ is the fluid mass flux (fluid mass flow rate per unit area and time) relative to the solid skeleton, and f is a volumetric source term. Using Equation 3.3, we write Equation 3.9 in terms of pressure and volumetric strain as follows:

$$\frac{1}{M}\frac{\partial p}{\partial t} + b\frac{\partial \varepsilon_v}{\partial t} + \text{Div}\, \frac{\boldsymbol{w}}{\rho_{f,0}} = f. \tag{3.10}$$

By noting the relation between volumetric stress and strain,

$$(\sigma_v - \sigma_{v,0}) + b(p - p_0) = K_{dr}\varepsilon_v, \tag{3.11}$$

we write Equation 3.10 in terms of pressure and volumetric (mean) total stress,

$$\left(\frac{1}{M} + \frac{b^2}{K_{dr}}\right)\frac{\partial p}{\partial t} + \frac{b}{K_{dr}}\frac{\partial \sigma_v}{\partial t} + \text{Div}\, \frac{\boldsymbol{w}}{\rho_{f,0}} = f. \tag{3.12}$$

The two equivalent expressions of the flow problem (Equations 3.10 and 3.12) are useful in explaining the relationship between reservoir flow simulation and geomechanical coupling. The fluid velocity $\boldsymbol{v} = \boldsymbol{w}/\rho_{f,0}$ is given by Darcy's law:

$$\boldsymbol{v} = -\frac{1}{B_f}\frac{\boldsymbol{k}}{\mu}(\mathbf{Grad}\, p - \rho_f \boldsymbol{g}), \tag{3.13}$$

where $\boldsymbol{k}$ is the absolute permeability tensor, μ is fluid viscosity, and $B_f = \rho_{f,0}/\rho_f$ is the so-called formation volume factor of the fluid (Aziz and Settari, 1979).

To complete the mathematical description of the coupled flow and geomechanics problem, we need to specify initial and boundary conditions. For the flow problem we consider the boundary conditions $p = \bar{p}$ (prescribed pressure) on Γ_p, and $\boldsymbol{v} \cdot \boldsymbol{n} = \bar{v}$ (prescribed volumetric flux) on Γ_v, where $\boldsymbol{n}$ is the outward unit normal to the boundary, $\partial\Omega$. We assume that $\Gamma_p \cap \Gamma_v = \emptyset$, and $\Gamma_p \cup \Gamma_v = \partial\Omega$.

The boundary conditions for the mechanical problem are $\boldsymbol{u} = \bar{\boldsymbol{u}}$ (prescribed displacement) on Γ_u and $\boldsymbol{\sigma} \cdot \boldsymbol{n} = \bar{\boldsymbol{t}}$ (prescribed traction) on Γ_σ. Again, we assume $\Gamma_u \cap \Gamma_\sigma = \emptyset$, and $\Gamma_u \cup \Gamma_\sigma = \partial\Omega$.

The initial displacements and strains are, by definition, equal to zero. The initial condition of the coupled problem is $p|_{t=0} = p_0$ and $\boldsymbol{\sigma}|_{t=0} = \boldsymbol{\sigma}_0$. The initial stress field must satisfy mechanical equilibrium.

3.2 Discretization

The finite-volume method is widely used by the reservoir simulation community (Aziz and Settari, 1979), whereas most numerical models in geotechnical engineering and thermomechanics use nodal-based finite-element discretizations (Zienkiewicz et al., 1988; Lewis and Sukirman, 1993; Lewis and Schrefler, 1998; Armero and Simo, 1992; Armero, 1999; Wan et al., 2003; White and Borja, 2008). In the finite-volume method for the flow problem, the pressure is located at the cell (grid block) center. In the nodal-based finite-element method for the mechanical problem, the displacement vector is located at vertices (Hughes, 1987). This space discretization has the following characteristics: local mass conservation at the element level, a continuous displacement field, which allows for tracking the deformation, and convergent approximations with the lowest order discretization (Jha and Juanes, 2007). Since we assume slightly compressible fluid flow, the given space discretization provides a stable pressure field at early time (Phillips and Wheeler, 2007a,b), while for nodal based finite element methods, spurious pressure oscillations are identified for the equal-order approximations of pressure and displacement (e.g., piecewise continuous interpolation) and incompressible fluid flow (Vermeer and Verruijt, 1981; Murad and Loula, 1992, 1994; White and Borja, 2008). Stabilization techniques to deal with spurious pressure oscillations have been studied by several authors (Murad and Loula, 1992, 1994; Wan, 2002; Wan et al., 2003; Truty and Zimmermann, 2006; White and Borja, 2008). Refer to Appendix A. for further discussion on the finite-volume and finite-element methods.

Let the domain be partitioned into nonoverlapping elements (grid blocks), $\Omega = \cup_{j=1}^{n_e} \Omega_j$,

where n_e is the number of elements. Let $\mathcal{Q} \subset L^2(\Omega)$ and $\mathcal{U} \subset (H^1(\Omega))^d$ (where $d = 2, 3$ is the number of space dimensions), be the functional spaces of the solution for pressure, p, and displacements, $\boldsymbol{u}$. Let $\mathcal{Q}_0$ and $\mathcal{U}_0$ be the corresponding spaces for the test functions φ and $\boldsymbol{\eta}$, for flow and mechanics, respectively (Jha and Juanes, 2007). Let $\mathcal{Q}_h$, $\mathcal{Q}_{h,0}$, $\mathcal{U}_h$ and $\mathcal{U}_{h,0}$ be the corresponding finite-dimensional subspaces. Then the discrete approximation of the weak form of the governing equations 3.1 and 3.9 becomes: find $(\boldsymbol{u}_h, p_h) \in \mathcal{U}_h \times \mathcal{Q}_h$ such that

$$\int_\Omega \mathbf{Grad}^s \boldsymbol{\eta}_h : \boldsymbol{\sigma}_h \, d\Omega = \int_\Omega \boldsymbol{\eta}_h \cdot \rho_b \boldsymbol{g} \, d\Omega + \int_{\Gamma_\sigma} \boldsymbol{\eta}_h \cdot \bar{\boldsymbol{t}} \, d\Gamma \quad \forall \boldsymbol{\eta}_h \in \mathcal{U}_{h,0}, \tag{3.14}$$

$$\frac{1}{\rho_{f,0}} \int_\Omega \varphi_h \frac{dm_h}{dt} \, d\Omega + \int_\Omega \varphi_h \operatorname{Div} \boldsymbol{v}_h \, d\Omega = \int_\Omega \varphi_h f \, d\Omega, \quad \forall \varphi_h \in \mathcal{Q}_{h,0}. \tag{3.15}$$

The pressure and displacement fields are approximated as follows:

$$p_h = \sum_{j=1}^{n_{\text{elem}}} \varphi_j P_j, \tag{3.16}$$

$$\boldsymbol{u}_h = \sum_{b=1}^{n_{\text{node}}} \eta_b \boldsymbol{U}_b, \tag{3.17}$$

where n_{node} is the number of nodes, P_j are the element pressures, and $\boldsymbol{U}_b$ are the displacement vectors at the element nodes (vertices).

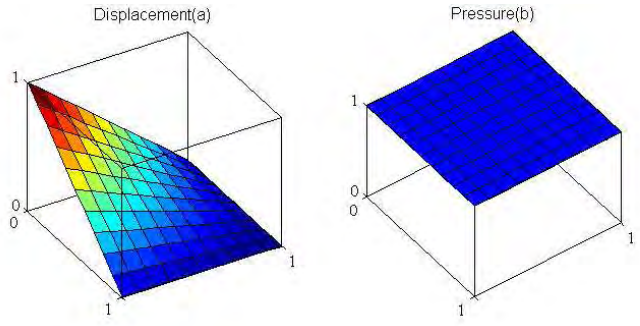

Figure 3.1: Element shape functions for displacement (left) and pressure (right) in 2-D

We restrict our analysis to pressure shape functions that are piecewise constant, so

that φ_j takes a constant value of 1 over element j and 0 at all other elements (Figure 3.1 right plot). Therefore, Equation 3.15 can be interpreted as a mass conservation statement, element-by-element. The second term can be integrated by parts to arrive at the sum of integral fluxes, $V_{h,ij}$, between element i and its adjacent elements j:

$$\int_\Omega \varphi_i \operatorname{Div} \boldsymbol{v}_h \, d\Omega = -\int_{\partial\Omega_i} \boldsymbol{v}_h \cdot \boldsymbol{n}_i \, d\Gamma = -\sum_{j=1}^{n_{\text{face}}} \int_{\Gamma_{ij}} \boldsymbol{v}_h \cdot \boldsymbol{n}_i \, d\Gamma = -\sum_{j=1}^{n_{\text{face}}} V_{h,ij}. \tag{3.18}$$

The inter-element flux can be evaluated using a two-point or a multipoint flux approximation (Aavatsmark, 2002).

The interpolation functions for the displacement vectors are the usual C^0-continuous isoparametric functions, such that η_b takes a value of 1 at node b, and 0 at all other nodes (the left of Figure 3.1). Inserting the interpolation from Equations 3.16–3.17, and testing Equations 3.14–3.15 against each individual shape function, the semi-discrete finite-element/finite-volume equations can be written as

$$\int_\Omega \boldsymbol{B}_a^T \boldsymbol{\sigma}_h \, d\Omega = \int_\Omega \eta_a \rho_b \boldsymbol{g} \, d\Omega + \int_{\Gamma_\sigma} \eta_a \bar{\boldsymbol{t}} \, d\Gamma \quad \forall a = 1, \ldots, n_{\text{node}}, \tag{3.19}$$

$$\int_{\Omega_i} \frac{1}{M} \frac{dP_i}{dt} \, d\Omega + \int_{\Omega_i} b \frac{d\varepsilon_v}{dt} \, d\Omega - \sum_{j=1}^{n_{\text{face}}} V_{h,ij} = \int_{\Omega_i} f \, d\Omega, \quad \forall i = 1, \ldots, n_{\text{elem}}. \tag{3.20}$$

The matrix $\boldsymbol{B}_a$ is the linearized strain operator, which in 2D takes the form

$$\boldsymbol{B}_a = \begin{bmatrix} \partial_x \eta_a & 0 \\ 0 & \partial_y \eta_a \\ \partial_y \eta_a & \partial_x \eta_a \end{bmatrix}. \tag{3.21}$$

The stress and strain tensors are expressed in compact engineering notation (Hughes, 1987). For example, in 2D,

$$\boldsymbol{\sigma}_h = \begin{bmatrix} \sigma_{h,xx} \\ \sigma_{h,yy} \\ \sigma_{h,xy} \end{bmatrix}, \qquad \boldsymbol{\varepsilon}_h = \begin{bmatrix} \varepsilon_{h,xx} \\ \varepsilon_{h,yy} \\ 2\varepsilon_{h,xy} \end{bmatrix}. \tag{3.22}$$

The stress–strain relation for linear poroelasticity takes the form:

$$\boldsymbol{\sigma}_h = \boldsymbol{\sigma}'_h - bp_h\mathbf{1}, \qquad \delta\boldsymbol{\sigma}'_h = \boldsymbol{D}_{ps}\delta\boldsymbol{\varepsilon}_h, \tag{3.23}$$

where $\boldsymbol{\sigma}'$ is the effective stress tensor, and $\boldsymbol{D}_{ps}$ is the elasticity matrix which, for 2D plane strain conditions, can be written as

$$\boldsymbol{D}_{ps} = \frac{E(1-\nu)}{(1+\nu)(1-2\nu)} \begin{bmatrix} 1 & \frac{\nu}{1-\nu} & \frac{\nu}{1-\nu} \\ \frac{\nu}{1-\nu} & 1 & \frac{\nu}{1-\nu} \\ \frac{\nu}{1-\nu} & \frac{\nu}{1-\nu} & 1 \end{bmatrix}, \tag{3.24}$$

where E is the Young modulus, and ν is the Poisson ratio.

The coupled equations that describe quasi-static poromechanics form an elliptic–parabolic system. A fully discrete system of equations can be obtained by further discretizing in time the mass accumulation term in Equations 3.19–3.20. We use the generalized mid-point rule for time discretization.

3.3 Operator Splitting

The fully coupled method solves the equations of flow and mechanics simultaneously and obtains a converged solution through iteration, typically using the Newton-Raphson method (Lewis and Sukirman, 1993; Wan et al., 2003; Jha and Juanes, 2007; Jean et al., 2007). The fully coupled method is unconditionally stable, but requires high computational cost and the development of a unified simulator for flow and mechanics. It is thus desirable to develop solution methods that have stability properties comparable to the fully coupled approach, but that are computationally more efficient and easier to implement. Sequential solution methods offer such a possibility. With sequential methods, we can employ separate flow and mechanics simulators.

There are two representative sequential strategies, in which one solves the mechanical problem first. One is the drained split shown in the left diagram of Figure 3.2. The other

is the undrained split shown on the right diagram of Figure 3.2.

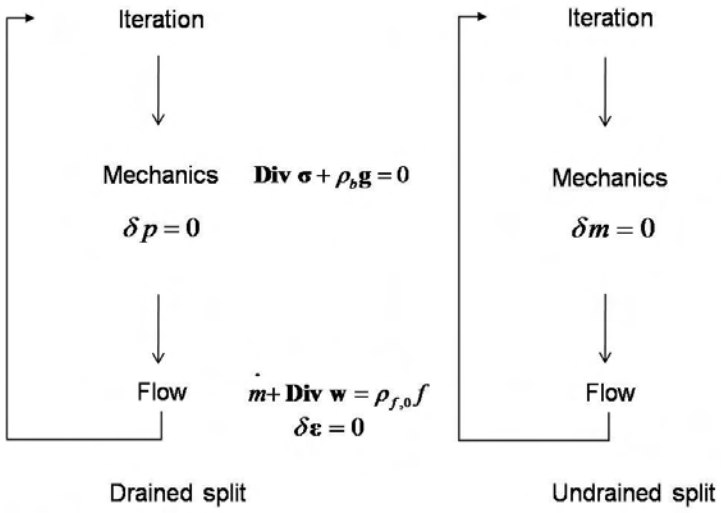

Figure 3.2: Sequential methods for flow and geomechanics. Left: drained split. Right: undrained split.

3.3.1 Fully coupled method

Let us denote by $\mathcal{A}$ the operator of the original problem (Equations 3.1 and 3.9). The discrete approximation of this operator corresponding to the fully coupled method can be represented as:

$$\begin{bmatrix} \boldsymbol{u}^n \\ \boldsymbol{p}^n \end{bmatrix} \xrightarrow{\mathcal{A}_{fc}} \begin{bmatrix} \boldsymbol{u}^{n+1} \\ \boldsymbol{p}^{n+1} \end{bmatrix}, \quad \text{where} \quad \mathcal{A}_{fc} : \begin{cases} \operatorname{Div} \boldsymbol{\sigma} + \rho_b \boldsymbol{g} = \boldsymbol{0}, \\ \dot{m} + \operatorname{Div} \boldsymbol{w} = \rho_{f,0} f, \end{cases} \tag{3.25}$$

where $\dot{(\,)}$ denotes the material time derivative with respect to the solid skeleton, $d(\,)/dt$. Using the backward Euler time discretization in Equations 3.19 and 3.20, the residual form

of the fully-discrete coupled equations is:

$$\boldsymbol{R}_a^u = \int_\Omega \boldsymbol{B}_a^T \boldsymbol{\sigma}_h^{n+1}\, d\Omega - \int_\Omega \eta_a \rho_b^{n+1} \boldsymbol{g}\, d\Omega - \int_{\Gamma_\sigma} \eta_a \bar{\boldsymbol{t}}^{n+1}\, d\Gamma \quad \forall a = 1, \ldots, n_{\text{node}}, \tag{3.26}$$

$$R_i^p = \int_{\Omega_i} \frac{1}{M}(P_i^{n+1} - P_i^n)\, d\Omega + \int_{\Omega_i} b(\varepsilon_v^{n+1} - \varepsilon_v^n)\, d\Omega - \Delta t \sum_{j=1}^{n_{\text{face}}} V_{h,ij}^{n+1} - \Delta t \int_{\Omega_i} f^{n+1}\, d\Omega$$

$$\forall i = 1, \ldots, n_{\text{elem}}. \tag{3.27}$$

where $\boldsymbol{R}_a^u$ and R_i^p are the residuals for mechanics (node a) and flow (element i), respectively. The superscript n indicates the time level. The set of Equations 3.26–3.27 is to be solved for the nodal displacements $\boldsymbol{u}^{n+1} = \{\boldsymbol{U}_b^{n+1}\}$ and element pressures $\boldsymbol{p}^{n+1} = \{P_j^{n+1}\}$ (a total of $d \times n_{\text{node}} + n_{\text{elem}}$ unknowns). Given an approximation of the solution $(\boldsymbol{u}^{n+1,(k)}, \boldsymbol{p}^{n+1,(k)})$, where (k) denotes the iteration level, Newton's method leads to the following system of Equations for the corrections:

$$\underbrace{\begin{bmatrix} \boldsymbol{K} & -\boldsymbol{L}^T \\ \boldsymbol{L} & \boldsymbol{F} \end{bmatrix}}_{\boldsymbol{J}} \begin{bmatrix} \delta\boldsymbol{u} \\ \delta\boldsymbol{p} \end{bmatrix}^{n+1,(k)} = - \begin{bmatrix} \boldsymbol{R}^u \\ \boldsymbol{R}^p \end{bmatrix}^{n+1,(k)}, \tag{3.28}$$

where $\boldsymbol{J}$ is the Jacobian matrix, $\boldsymbol{K}$ is the stiffness matrix, $\boldsymbol{L}$ is the coupling poromechanics matrix, and $\boldsymbol{F} = \boldsymbol{Q} + \Delta t \boldsymbol{T}$ is the flow matrix ($\boldsymbol{Q}$ is the compressibility matrix, and $\boldsymbol{T}$ the transmissibility matrix). The entries of the different matrices are:

$$\boldsymbol{K}_{ab} = \int_\Omega \boldsymbol{B}_a^T \boldsymbol{D}_{ps} \boldsymbol{B}_b\, d\Omega, \tag{3.29}$$

$$\boldsymbol{L}_{ib} = \int_\Omega \varphi_i b (\mathbf{Grad}\, \eta_b)^T\, d\Omega, \tag{3.30}$$

$$Q_{ij} = \int_\Omega \varphi_i M^{-1} \varphi_j\, d\Omega, \tag{3.31}$$

and T_{ij} is the transmissibility between grid blocks i and j. The fully coupled method computes the Jacobian matrix $\boldsymbol{J}$, and determines $\delta\boldsymbol{u}$ and $\delta\boldsymbol{p}$ simultaneously, iterating until convergence.

3.3.2 Drained split

In the drained split, the solution is obtained sequentially by first solving the mechanics problem, and then the flow problem. The pressure field is frozen when the mechanical problem is solved. The drained-split approximation of the operator $\mathcal{A}$ can be written as

$$\begin{bmatrix} \boldsymbol{u}^n \\ \boldsymbol{p}^n \end{bmatrix} \xrightarrow{\mathcal{A}^u_{dr}} \begin{bmatrix} \boldsymbol{u}^{n+1} \\ \boldsymbol{p}^n \end{bmatrix} \xrightarrow{\mathcal{A}^p_{dr}} \begin{bmatrix} \boldsymbol{u}^{n+1} \\ \boldsymbol{p}^{n+1} \end{bmatrix}, \quad \text{where} \quad \begin{cases} \mathcal{A}^u_{dr} : \operatorname{Div} \boldsymbol{\sigma} + \rho_b \boldsymbol{g} = \boldsymbol{0}, \ \delta p = 0, \\ \mathcal{A}^p_{dr} : \dot{m} + \operatorname{Div} \boldsymbol{w} = \rho_{f,0} f, \ \dot{\boldsymbol{\varepsilon}} : \text{prescribed}, \end{cases} \tag{3.32}$$

where the superscript n indicates the time level. One solves the mechanical problem with no pressure change, thus allowing the fluid to drain. Then, the fluid flow problem is solved with a frozen displacement field.

3.3.3 Undrained split

In contrast to the drained split, the undrained split uses a different pressure predictor for the mechanical problem, which is computed by imposing that the fluid mass in each grid block remains constant during the mechanical step ($\delta m = 0$). The original operator $\mathcal{A}$ is split as follows:

$$\begin{bmatrix} \boldsymbol{u}^n \\ \boldsymbol{p}^n \end{bmatrix} \xrightarrow{\mathcal{A}^u_{ud}} \begin{bmatrix} \boldsymbol{u}^{n+1} \\ \boldsymbol{p}^* \end{bmatrix} \xrightarrow{\mathcal{A}^p_{ud}} \begin{bmatrix} \boldsymbol{u}^{n+1} \\ \boldsymbol{p}^{n+1} \end{bmatrix}, \quad \text{where} \quad \begin{cases} \mathcal{A}^u_{ud} : \operatorname{Div} \boldsymbol{\sigma} + \rho_b \boldsymbol{g} = \boldsymbol{0}, \ \delta m = 0, \\ \mathcal{A}^p_{ud} : \dot{m} + \operatorname{Div} \boldsymbol{w} = \rho_{f,0} f, \ \dot{\boldsymbol{\varepsilon}} : \text{prescribed}. \end{cases} \tag{3.33}$$

The undrained strategy allows the pressure to change locally when the mechanical problem is solved. From Equation 3.3, the undrained condition ($\delta m = 0$) yields

$$0 = b\delta\varepsilon_v + \frac{1}{M}\delta p, \tag{3.34}$$

and the pressure is updated locally in each element using

$$p^* = p^n - bM(\varepsilon_v^{n+1} - \varepsilon_v^n). \tag{3.35}$$

For the mechanical problem, Equation 3.2 with the generalized midpoint rule at $t_{n+\alpha}$ is discretized as follows:

$$\begin{aligned} \boldsymbol{\sigma}^{n+\alpha} - \boldsymbol{\sigma}_0 &= \mathbf{C}_{dr} : \boldsymbol{\varepsilon}^{n+\alpha} - b(p^{n+\alpha} - p_0)\mathbf{1}, \\ p^{n+\alpha} &= \alpha p^* + (1-\alpha)p^n \,, \end{aligned} \tag{3.36}$$

where $\alpha \in (0, 1]$. After substituting Equation 3.35 in Equation 3.36, the mechanical problem can be expressed in terms of displacements using the undrained bulk modulus, $\mathbf{C}_{ud} = \mathbf{C}_{dr} + b^2 M \mathbf{1} \otimes \mathbf{1}$. The additional computational cost is negligible because the calculation of $\boldsymbol{p}^*$ is explicit. However, we have a stiff mechanical problem due to the undrained constraint, which requires a more robust linear solver compared with the mechanical problem associated with the drained split.

3.4 Stability Analysis for Linear Poroelasticity

We employ the Von Neumann method to analyze the stability of sequential schemes, which is frequently used for stability analysis of linear (or linearized versions of) problems (e.g., Strikwerda (2004), Wan et al. (2005), Miga et al. (1998)). Miga et al. (1998) show that the fully coupled method for the coupled flow and mechanics problem is unconditionally stable for $\alpha \geq 0.5$. The governing equations of coupled flow and geomechanics in one dimension without source terms are

$$\frac{\partial}{\partial x}\left(K_{dr}\frac{\partial u}{\partial x} - bp\right) = 0 \text{ (for mechanics)}\,, \tag{3.37}$$

$$\frac{1}{M}\frac{\partial p}{\partial t} + b\frac{\partial}{\partial t}\frac{\partial u}{\partial x} - \frac{k}{\mu}\frac{\partial^2 p}{\partial x^2} = 0 \text{ (for flow)}\,, \tag{3.38}$$

where $\frac{\partial u}{\partial x}$ is ε_{xx}, which is equal to ε_v.

3.4.1 Drained split

From the generalized midpoint rule, we have for Equations 3.19 and 3.20

$$\boldsymbol{\sigma}_h^{n+\alpha} = (1-\alpha)\boldsymbol{\sigma}_h^n + \alpha\boldsymbol{\sigma}_h^{n+1}, \tag{3.39}$$

$$V_h^{n+\alpha} = (1-\alpha)V_h^n + \alpha V_h^{n+1}. \tag{3.40}$$

Based on the finite-volume and finite-element methods, the one-dimensional space discretization is shown in Figure 3.3.

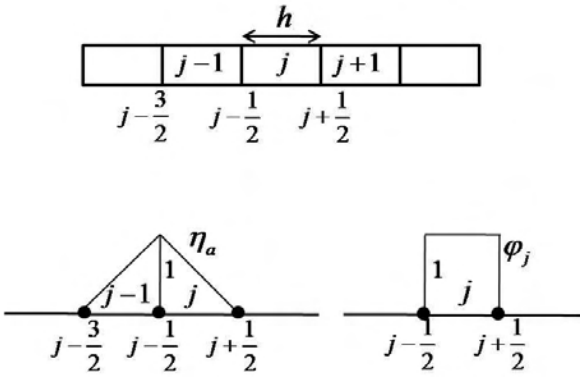

Figure 3.3: One-dimensional element with the finite-volume and finite-element methods. h is the grid spacing, and j is the element index

The drained split freezes the variation of the pressure, so that

$$P^{n+\alpha} = P^n. \tag{3.41}$$

Full discretization in one dimension yields

$$-(\frac{K_{dr}}{h}U_{j-\frac{3}{2}}^{n+\alpha} - 2\frac{K_{dr}}{h}U_{j-\frac{1}{2}}^{n+\alpha} + \frac{K_{dr}}{h}U_{j+\frac{1}{2}}^{n+\alpha}) - b(P_{j-1}^n - P_j^n) = 0, \tag{3.42}$$

$$\begin{aligned}&\frac{h}{M}\frac{P_j^{n+1}-P_j^n}{\Delta t} + \frac{bh}{\Delta t}[(-\frac{U_{j-\frac{1}{2}}^{n+1} - U_{j+\frac{1}{2}}^{n+1}}{h}) + (\frac{U_{j-\frac{1}{2}}^{n} - U_{j+\frac{1}{2}}^{n}}{h})]\\ &-\frac{k_p}{\mu h}\left(P_{j-1}^{n+\alpha} - 2P_j^{n+\alpha} + P_{j+1}^{n+\alpha}\right) = 0,\end{aligned} \tag{3.43}$$

where k_p is the permeability, $U^{n+\alpha} = \alpha U^{n+1} + (1-\alpha)U^n$ and $P^{n+\alpha} = \alpha P^{n+1} + (1-\alpha)P^n$. Introducing solutions of the form $U_j^n = \gamma^n e^{ij\theta}\hat{U}$ and $P_j^n = \gamma^n e^{ij\theta}\hat{P}$ (Strikwerda, 2004), where γ is the amplification factor, $e^{(\cdot)} = \exp(\cdot)$, $i = \sqrt{-1}$, and $\theta \in [-\pi, \pi]$, we have

$$\begin{bmatrix} U_j^n \\ P_j^n \end{bmatrix} = \gamma^n e^{ij\theta} \begin{bmatrix} \hat{U} \\ \hat{P} \end{bmatrix}. \tag{3.44}$$

Substituting Equation 3.44 into Equations 3.42 and 3.43, we obtain

$$\mathbf{G}_{dr} \begin{bmatrix} \hat{U} \\ \hat{P} \end{bmatrix} = \begin{bmatrix} 0 \\ 0 \end{bmatrix}, \tag{3.45}$$

where $\mathbf{G}_{dr} =$

$$\begin{bmatrix} \frac{K_{dr}}{h}((1-\alpha)+\alpha\gamma)2(1-\cos\theta) & b2i\sin\frac{\theta}{2} \\ b(\gamma-1)2i\sin\frac{\theta}{2} & \frac{h}{M}(\gamma-1) + \frac{k_p\Delta t}{\mu h}((1-\alpha)+\alpha\gamma)2(1-\cos\theta) \end{bmatrix}.$$

$\det(\mathbf{G}_{dr}) = 0$, where det is the determinant, is required since the matrix needs to be singular (e.g., Armero and Simo (1992)). The characteristic equation from $\det \mathbf{G}_{dr} = 0$ is written as

$$\begin{aligned} F_{dr}^{\alpha}(\gamma) &= \left(\frac{K_{dr}}{M}\alpha + K_{dr}\frac{k_p\Delta t}{\mu h^2}\alpha^2 2(1-\cos\theta)\right)\gamma^2 \\ &+ \left(\frac{K_{dr}}{M}(1-2\alpha) + K_{dr}\frac{k\Delta t}{\mu h^2}(1-\alpha)\alpha 4(1-\cos\theta) + b^2\right)\gamma \\ &- \left(\frac{K_{dr}}{M}(1-\alpha) - K_{dr}\frac{k_p\Delta t}{\mu h^2}(1-\alpha)^2 2(1-\cos\theta) + b^2\right) = 0. \end{aligned} \tag{3.46}$$

For linear stability, we must have (Hughes, 1987)

(i) $\max(|\gamma|) < 1$ or

(ii) $\max(|\gamma|) = 1$, where the γ's are distinct for all values of θ.

The backward Euler ($\alpha = 1$) and midpoint ($\alpha = 1/2$) time discretizations are frequently

used.

For the backward Euler scheme, $\alpha = 1$, Equation 3.46 reduces to

$$F_{dr}^{\alpha=1}(\gamma) = \left(\frac{K_{dr}}{M} + K_{dr}\frac{k_p\Delta t}{\mu h^2}2(1-\cos\theta)\right)\gamma^2 + \left(-\frac{K_{dr}}{M} + b^2\right)\gamma - b^2 = 0. \tag{3.47}$$

Since the constant term of Equation 3.47, $-b^2$, is negative, the stability condition becomes $\max(|\gamma|) \leq 1$, which yields $F_{dr}^{\alpha=1}(\gamma = 1) \geq 0$ and $F_{dr}^{\alpha=1}(\gamma = -1) \geq 0$, where the γ' s are real (the top of Figure 3.4). When $\gamma = 1$ and -1,

$$F_{dr}^{\alpha=1}(\gamma = 1) = K_{dr}\frac{k_p\Delta t}{\mu h^2}2(1-\cos\theta) \geq 0, \tag{3.48}$$

$$F_{dr}^{\alpha=1}(\gamma = -1) = 2\frac{K_{dr}}{M} - 2b^2 \geq 0. \tag{3.49}$$

The condition such that Equations 3.48 and 3.49 are satisfied for all θ is

$$\tau \equiv \frac{b^2 M}{K_{dr}} \leq 1, \tag{3.50}$$

where τ is referred to as the *coupling strength*, and it is given by the ratio of the bulk stiffness of the fluid and solid skeleton. We can extend the stability analysis from one to multiple dimensions easily. This is because the coupling between flow and mechanics is due to the volumetric response, which is a scalar quantity. It follows that K_{dr} in one dimension is the constrained modulus, K_{dr} in the two dimensional plane-strain case is $\frac{1}{4}\mathbf{1}_2^T\boldsymbol{D}_{ps}\mathbf{1}_2$, and K_{dr} in three dimensions is the drained bulk modulus, which is $\frac{1}{9}\mathbf{1}_3^T\boldsymbol{D}_{dr}\mathbf{1}_3$. These expressions are based on matrix-vector notation (Hughes, 1987), where $\mathbf{1}_2^T = [1,1,0]$, $\mathbf{1}_3^T = [1,1,1,0,0,0]$, $\boldsymbol{D}_{ps}$ is a 3×3 matrix given in Equation 3.24, and $\boldsymbol{D}_{dr}$ is a 6×6 matrix involving the drained moduli (Hughes, 1987). Let K_{dr}^{1D}, K_{dr}^{2D}, and K_{dr}^{3D} be the K_{dr}'s in one, two, and three dimensions for convenience, respectively, which will be used in Chapter 5.

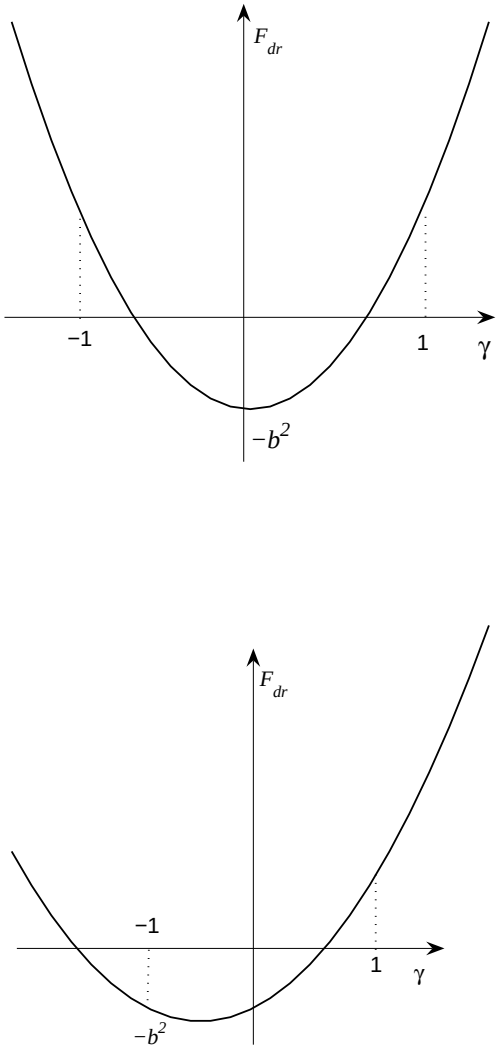

Figure 3.4: The characteristic equations for the drained split when $\alpha = 1$ (top), and when $\alpha = 0.5$ (bottom)

In this way, the coupling strength can be extended to multi-dimensional elasto-plasticity:

$$\tau = \frac{b^2 M}{\frac{1}{9}\mathbf{1}_3^T \boldsymbol{D}_{ep} \mathbf{1}_3}, \tag{3.51}$$

where $\boldsymbol{D}_{ep}$ is the elastoplastic tangent moduli (in compact engineering notation) in three dimensions.

For the midpoint rule ($\alpha = 0.5$), Equation 3.46 reduces to

$$\begin{aligned} F_{dr}^{\alpha=0.5}(\gamma) &= \left(\frac{1}{2}\frac{K_{dr}}{M} + \frac{K_{dr}}{2}\frac{k k_p \Delta t}{\mu h^2}(1-\cos\theta)\right)\gamma^2 + \left(K_{dr}\frac{k_p \Delta t}{\mu h^2}(1-\cos\theta) + b^2\right)\gamma \\ &\quad - \left(\frac{1}{2}\frac{K_{dr}}{M} - \frac{K_{dr}}{2}\frac{k_p \Delta t}{\mu h^2}(1-\cos\theta) + b^2\right) = 0. \end{aligned} \tag{3.52}$$

From the characteristic equation $F_{dr}^{\alpha=0.5}(\gamma)$,

$$F_{dr}^{\alpha=0.5}(\gamma=-1) = -2b^2 < 0\,, \tag{3.53}$$

$$F_{dr}^{\alpha=0.5}(\gamma=1) = K_{dr}\frac{k_p \Delta t}{\mu h^2} 2(1-\cos\theta) \geq 0, \tag{3.54}$$

which implies the roots (γ) of Equation 3.52 are real and distinct. One of the roots is inside the interval [-1, 1], and the other is outside (the bottom of Figure 3.4). Then $\max(|\gamma|) > 1$. Thus, the drained split with the midpoint rule is unconditionally unstable.

Remark 3.1. For the backward Euler time discretization, $\alpha = 1$, the stability condition of the drained split is independent of time step size, which implies that the problem with $\tau > 1$ cannot be overcome by reducing the time step size. Also, it shows that the drained split will suffer from oscillatory behavior even in the stable domain, since one γ is negative (Strikwerda, 2004).

Remark 3.2. In Armero and Simo (1992), the backward Euler time discretization is adopted in the mechanical problem, while the midpoint rule is used for the flow problem. Nodal-based finite element methods are used for the spatial discretization of both flow and

geomechanics. This mixed time discretization yields the following amplification factors:

$$\gamma = 1, \quad \frac{-b^2(1+\cos\theta)}{\left(\frac{2K_{dr}}{3M}(2+\cos\theta) + \frac{k_p\Delta t}{\mu h^2}2(1-\cos\theta)\right)}, \tag{3.55}$$

from which the stability condition is $\tau \leq 1$, which is the same as the backward Euler discretization with finite-volume (for flow) and finite-element (for mechanics) methods. Moreover, this stability condition is sharper than that proposed by Armero and Simo (1992), which is

$$2\frac{k_p\Delta t M}{\mu h^2} \geq \left(\tau - \frac{4}{3}\right). \tag{3.56}$$

Equation 3.50 clearly satisfies Equation 3.56. The mixed time discretization with the finite-volume and finite-element methods also yields the same stability criterion as the backward Euler time discretization.

3.4.2 Undrained split

The undrained split freezes the variation of fluid mass during the mechanical problem, which from Equations 3.35 and 3.36 leads to

$$P^{n+\alpha} = -\alpha b M \Delta\boldsymbol{\varepsilon}^n + P^n, \tag{3.57}$$

where $\Delta\boldsymbol{\varepsilon}^n = \boldsymbol{\varepsilon}^{n+1} - \boldsymbol{\varepsilon}^n$. Then the discretization of the undrained split becomes

$$\begin{aligned} - \quad & \frac{K_{dr}}{h}(U^{n+\alpha}_{j-\frac{3}{2}} - 2U^{n+\alpha}_{j-\frac{1}{2}} + U^{n+\alpha}_{j+\frac{1}{2}}) - \alpha\frac{b^2M}{h}\Big((U^{n+1}_{j-\frac{3}{2}} - 2U^{n+1}_{j-\frac{1}{2}} + U^{n+1}_{j+\frac{1}{2}}) \\ & -(U^{n}_{j-\frac{3}{2}} - 2U^{n}_{j-\frac{1}{2}} + U^{n}_{j+\frac{1}{2}})\Big) - b(P^n_{j-1} - P^n_j) = 0, \end{aligned} \tag{3.58}$$

$$\frac{h}{M}\frac{P_j^{n+1}-P_j^n}{\Delta t}+\frac{bh}{\Delta t}\left[(-\frac{U_{j-\frac{1}{2}}^{n+1}-U_{j+\frac{1}{2}}^{n+1}}{h})+(\frac{U_{j-\frac{1}{2}}^{n}-U_{j+\frac{1}{2}}^{n}}{h})\right]$$
$$-\frac{k_p}{\mu h}\left(P_{j-1}^{n+\alpha}-2P_j^{n+\alpha}+P_{j+1}^{n+\alpha}\right)=0. \tag{3.59}$$

Substituting Equation 3.44 into Equations 3.58 and 3.59, we obtain

$$\mathbf{G}_{ud}\begin{bmatrix}\hat{U}\\ \hat{P}\end{bmatrix}=\begin{bmatrix}0\\0\end{bmatrix}, \tag{3.60}$$

where $\mathbf{G}_{ud}=$

$$\begin{bmatrix}\left(\frac{K_{dr}}{h}((1-\alpha)+\alpha\gamma)\right. & b2i\sin\frac{\theta}{2}\\ \left.+\alpha\frac{b^2M}{h}(\gamma-1)\right)2(1-\cos\theta) & \\ b(\gamma-1)2i\sin\frac{\theta}{2} & \frac{h}{M}(\gamma-1)\\ & +\frac{k_p\Delta t}{\mu h}((1-\alpha)+\alpha\gamma)2(1-\cos\theta)\end{bmatrix}.$$

Applying $\det(\mathbf{G}_{ud})=0$,

$$\begin{aligned}&F_{ud}^{\alpha}(\gamma)\\ &=\underbrace{\left(\frac{K_{dr}}{M}\alpha+\alpha b^2+(K_{dr}+b^2M)\alpha^2\frac{k_p\Delta t}{\mu h^2}2(1-\cos\theta)\right)}_{C_2}\gamma^2\\ &+\underbrace{\left(\frac{K_{dr}}{M}(1-2\alpha)+(K_{dr}2(1-\alpha)+b^2M(1-2\alpha))\alpha\frac{k_p\Delta t}{\mu h^2}2(1-\cos\theta)+(1-2\alpha)b^2\right)}_{C_1}\gamma\\ &+\underbrace{\left(-\frac{K_{dr}}{M}(1-\alpha)-(\alpha b^2M-(1-\alpha)K_{dr})(1-\alpha)\frac{k_p\Delta t}{\mu h^2}2(1-\cos\theta)-(1-\alpha)b^2\right)}_{C_0}=0.\end{aligned} \tag{3.61}$$

When $0.5 \leq \alpha \leq 1$,

$$
\begin{aligned}
&F_{ud}^{\alpha}(\gamma = 1) = K_{dr}\frac{k_p \Delta t}{\mu h^2} 2(1 - \cos\theta) \geq 0, \\
&F_{ud}^{\alpha}(\gamma = -1) \\
&\quad = (2\alpha - 1)\left(2\frac{K_{dr}}{M} + 2b^2 + \left(2\alpha b^2 M + (2\alpha - 1)K_{dr}\right)\frac{k_p \Delta t}{\mu h^2} 2(1 - \cos\theta)\right) \geq 0.
\end{aligned}
\tag{3.62}
$$

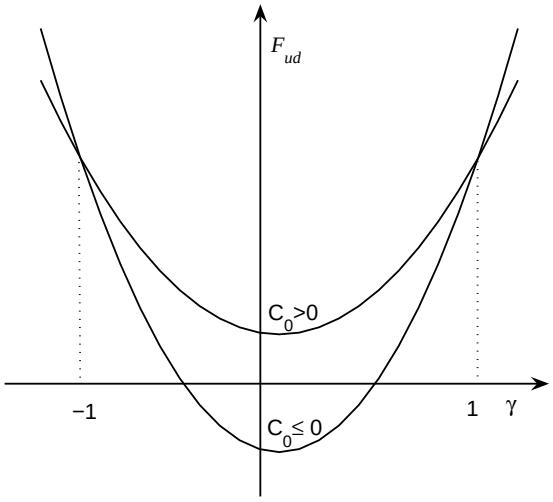

Figure 3.5: The characteristic equations for the undrained split when $C_0 \leq 0$ and $C_0 > 0$.

From Equation 3.61, C_2 is always positive. If $C_0 \leq 0$, then $max(|\gamma|) \leq 1$, as shown in Figure 3.5. If $C_0 > 0$, then $C_0/C_2 \leq 1$, which provides $(|\gamma_1\gamma_2|) \leq 1$, is required to ensure that $max(|\gamma|) \leq 1$ because the γ's are complex conjugates. Then $C_0 > 0$ and $C_0/C_2 \leq 1$ (or equivalently $C_0 \leq C_2$), and we have

$$
\frac{K_{dr}}{M} + b^2 + \left((2\alpha - 1)K_{dr} + \alpha b^2 M\right)\frac{k_p \Delta t}{\mu h^2} 2(1 - \cos\theta) \geq 0, \tag{3.63}
$$

which is true for all θ. Therefore, the undrained split is unconditionally stable for $0.5 \leq \alpha \leq 1$. The unconditional stability for $0.5 \leq \alpha \leq 1$ is also valid for the nonlinear problem,

which will be shown via the energy method in the next section.

Remark 3.3. When the backward Euler scheme is used for mechanics and the midpoint rule is used for flow, the undrained split is still unconditionally stable by the Von Neumann method.

3.5 Contractivity of the Nonlinear Continuum Problem

In this section, we study the contractivity of the coupled continuum problem, and whether the dissipative character of the coupled problem is inherited by the drained and undrained splits. The results of this section are not new, and they simply re-state the findings of Armero (1999).

The constitutive equations between the mechanics and the flow for elastoplasticity under isothermal conditions can be written as (Coussy, 1995)

$$\boldsymbol{\sigma} - \boldsymbol{\sigma}_0 = \mathbf{C}_{dr} : (\boldsymbol{\varepsilon} - \boldsymbol{\varepsilon}_p) - b(p - p_0)\mathbf{1}, \tag{3.64}$$

$$\frac{1}{\rho_{f,0}}(m - m_0) - \phi_p = b(\varepsilon_v - \varepsilon_{p,v}) + \frac{1}{M}(p - p_0), \tag{3.65}$$

where $\boldsymbol{\varepsilon}_p$ is the linearized plastic strain tensor, $\varepsilon_{p,v} = \mathrm{tr}\,(\boldsymbol{\varepsilon}_p)$, and ϕ_p is the plastic porosity. The elastic strain, $\boldsymbol{\varepsilon}_e$, is defined as $\boldsymbol{\varepsilon} - \boldsymbol{\varepsilon}_p$, and $\varepsilon_{e,v} = \mathrm{tr}\,(\boldsymbol{\varepsilon}_e)$. The plastic porosity and plastic strain can be related to each other by assuming that $\dot{\phi}_p = \beta\dot{\varepsilon}_{p,v}$. Here, we assume that $\beta = b$ (Armero, 1999), which yields

$$\delta\phi_p = b\delta\varepsilon_{p,v}. \tag{3.66}$$

Note that when the solid grains are incompressible, $\beta = b = 1$.

The natural norm to study the contractivity of the coupled problem is defined as

$$\begin{aligned} \|\zeta\|_{\mathcal{T}}^2 &= \frac{1}{2}\int_\Omega \left(\boldsymbol{\sigma'} : \mathbf{C}_{dr}^{-1}\boldsymbol{\sigma'} + \kappa \cdot \mathbf{H}^{-1}\kappa + \frac{1}{M}p^2\right) d\Omega, \qquad (3.67) \\ \mathcal{T} &:= \left\{\zeta := (\boldsymbol{\sigma'}, \kappa, p) \in \mathrm{S} \times \mathrm{R}^{\mathrm{n_{int}}} \times \mathrm{R} : \ {\sigma'}_{ij} \in L^2(\Omega), \right. \\ &\qquad \left. \kappa_i \in L^2(\Omega),\ p \in L^2(\Omega)\right\}, \qquad (3.68) \end{aligned}$$

where ${\sigma'}_{ij}$ and κ_i are the components of $\boldsymbol{\sigma'}$ and κ, respectively. κ is a vector of the stress-like plastic internal variable - the hardening force. n_{dim} is the dimension of the domain Ω, and n_{int} is the dimension of κ. $\mathrm{S} = \mathrm{R}^{(\mathrm{n_{dim}}+1)\mathrm{n_{dim}}/2}$ is the vector space of symmetric rank-two tensors. Note that $p \in L^2(\Omega)$, since we use the finite-volume method for flow. $\mathbf{H}$ is a hardening modulus matrix, yielding

$$\kappa - \kappa_0 = -\mathbf{H} \cdot \xi, \qquad (3.69)$$

where $\mathbf{H}$ is positive-definite, and ξ is a vector of the strain-like plastic internal variable (Coussy, 1995).

For the norm in Equation 3.67, the first and second terms correspond to the complementary Helmholtz free energy norm for the uncoupled mechanical problem, where the effective stress $\boldsymbol{\sigma'}$ is used in Equation 3.67, and the third term is the weighted $L^2(\Omega)$ norm in the flow problem (Simo, 1991).

In the mechanical problem with elastoplasticity, we have the global version of the maximal plastic work (maximal plastic dissipation), written as

$$\int_\Omega \left((\boldsymbol{\pi}' - \boldsymbol{\sigma'}) : \dot{\boldsymbol{\varepsilon}}_p + (\boldsymbol{\eta} - \boldsymbol{\kappa}) \cdot \dot{\boldsymbol{\xi}}\right) d\Omega \leq 0\,, \quad {}^{\forall}(\boldsymbol{\pi}', \boldsymbol{\eta}) \in \mathcal{E}\,, \qquad (3.70)$$

where $\boldsymbol{\pi}'$ and $\boldsymbol{\eta}$ are effective stress and hardening force, respectively. The generalized elastic domain $\mathcal{E}$ is defined as

$$\mathcal{E} := \left\{\Sigma := (\boldsymbol{\sigma'}, \kappa) \in \mathrm{S} \times \mathrm{R}^{\mathrm{n_{int}}} : f_Y(\boldsymbol{\sigma'}, \kappa) \leq 0\right\}, \qquad (3.71)$$

where $\mathcal{E}$ contains the origin $(\mathbf{0}, \mathbf{0})$, and f_Y is the yield surface, which is assumed to be a convex function. $\Sigma = (\sigma', \kappa)$ is a generalized effective stress constrained to lie within the elastic domain. The bilinear form $\ll \cdot, \cdot \gg$ is defined as

$$\ll \Sigma,\, \Pi \gg \;\; = \;\; \int \big(\boldsymbol{\sigma'} \mathbf{C}_{dr}^{-1} \boldsymbol{\pi}' + \boldsymbol{\kappa} \cdot \mathbf{H}^{-1} \boldsymbol{\eta}\big) d\Omega \,, \tag{3.72}$$

which forms the norm as $2\,\|\Sigma\|_{\mathcal{E}}^2 = \ll \Sigma, \Sigma \gg$. The top of Figure 3.6 shows the associative flow rule based on maximum plastic dissipation.

To show the contractivity of the coupled problem, let $(\mathbf{u}_0,\ p_0,\ \boldsymbol{\xi}_0)$ and $(\tilde{\mathbf{u}}_0,\ \tilde{p}_0,\ \tilde{\xi}_0)$ be two arbitrary initial conditions and let $(\mathbf{u},\ p,\ \xi)$ and $(\tilde{\mathbf{u}},\ \tilde{p},\ \tilde{\xi})$ be the corresponding solutions, yielding $(\boldsymbol{\sigma'},\ m,\ \kappa,\ \boldsymbol{\varepsilon}_p)$ and $(\tilde{\boldsymbol{\sigma}}',\ \tilde{m},\ \tilde{\kappa},\ \tilde{\boldsymbol{\varepsilon}_p})$, respectively. By subtracting the two solutions, we obtain

$$\begin{bmatrix} d\mathbf{u}^n \\ dp^n \end{bmatrix} \xrightarrow{\mathcal{A}_{fc}} \begin{bmatrix} d\mathbf{u}^{n+1} \\ dp^{n+1} \end{bmatrix}, \quad \text{where} \quad \mathcal{A}_{fc} : \begin{cases} \text{Div}\, d\boldsymbol{\sigma} = \mathbf{0}, \\ \dot{dm} + \text{Div}\, d\boldsymbol{w} = 0, \end{cases} \tag{3.73}$$

where $d(\cdot) = (\cdot) - \tilde{(\cdot)}$. Equation 3.73 has homogeneous boundary conditions with no source terms. From Equations 3.64, 3.65, and 3.69, $d\boldsymbol{\sigma}$, dm, and $d\kappa$ can be expressed as

$$d\boldsymbol{\sigma} = \mathbf{C}_{dr} : (d\boldsymbol{\varepsilon} - d\boldsymbol{\varepsilon}_p) - b dp \mathbf{1}, \tag{3.74}$$

$$\frac{dm}{\rho_{f,0}} = b d\varepsilon_v + \frac{1}{M} dp, \tag{3.75}$$

$$d\kappa = -\mathbf{H} \cdot d\xi, \tag{3.76}$$

where $d\phi_p = b d\varepsilon_{p,v}$ is used in Equation 3.75. From Equation 3.70, we obtain

$$\int_\Omega \Big((\tilde{\boldsymbol{\sigma}}' - \boldsymbol{\sigma}') : \dot{\boldsymbol{\varepsilon}_p} + (\tilde{\kappa} - \kappa) \cdot \dot{\xi} \Big) d\Omega \le 0 \,, \quad \text{Choosing } (\boldsymbol{\pi}, \eta) = (\tilde{\boldsymbol{\sigma}}', \tilde{\kappa}), \tag{3.77}$$

$$\int_\Omega \big((\boldsymbol{\sigma}' - \tilde{\boldsymbol{\sigma}}') : \dot{\tilde{\boldsymbol{\varepsilon}}}_p + (\kappa - \tilde{\kappa}) \cdot \dot{\tilde{\xi}} \big) d\Omega \le 0 \,, \quad \text{Choosing } (\boldsymbol{\pi}, \eta) = (\boldsymbol{\sigma}', \kappa). \tag{3.78}$$

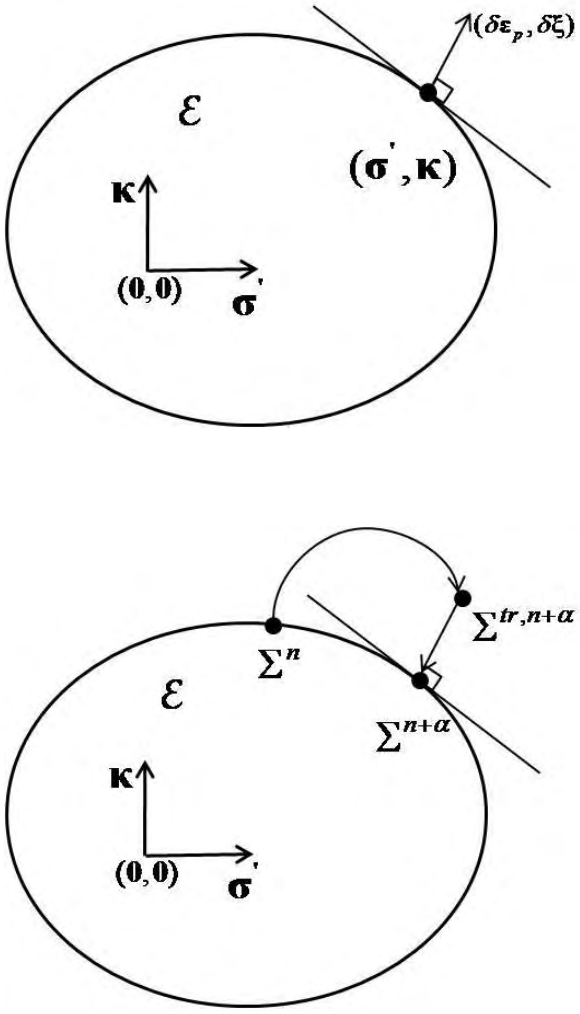

Figure 3.6: Top: the associative flow rule under the assumption of maximum plastic work (Coussy, 1995). Bottom: geometric interpretation of the algorithmic plastic dissipation, which corresponds to the associative flow rule (Simo and Hughes, 1998).

Adding Equations 3.77 and 3.78,

$$\int_{\Omega} \left(d\boldsymbol{\sigma'} : d\dot{\boldsymbol{\varepsilon}}_p + d\kappa \cdot d\dot{\xi} \right) d\Omega \geq 0 \,. \tag{3.79}$$

From Equation 3.67, we have

$$\begin{aligned} \|d\zeta\|_{\mathcal{T}}^2 &= \frac{1}{2} \int_{\Omega} \left(d\boldsymbol{\sigma'} : \mathbf{C}_{dr}^{-1} d\boldsymbol{\sigma'} + d\kappa \cdot \mathbf{H}^{-1} d\kappa + \frac{1}{M} dp^2 \right) d\Omega, \qquad (3.80) \\ &= \frac{1}{2} \int_{\Omega} \left(d\boldsymbol{\varepsilon}_e : \mathbf{C}_{dr} d\boldsymbol{\varepsilon}_e + d\xi \cdot \mathbf{H} d\xi + M \left(\frac{dm_e}{\rho_{f,0}} - b d\varepsilon_{e,v} \right)^2 \right) d\Omega, \\ &= \|d\chi\|_{\mathcal{N}}^2 \,, \end{aligned}$$

where we define the norm of $\|\chi\|_{\mathcal{N}}$ as

$$\|\chi\|_{\mathcal{N}}^2 = \frac{1}{2} \int_{\Omega} \left(\boldsymbol{\varepsilon}_e : \mathbf{C}_{dr} \boldsymbol{\varepsilon}_e + \xi \cdot \mathbf{H} \xi + M \left(\frac{m_e}{\rho_{f,0}} - b\varepsilon_{e,v} \right)^2 \right) d\Omega, \tag{3.81}$$

$$\begin{aligned} \mathcal{N} := \big\{ &\chi := (\boldsymbol{\varepsilon_e}, \xi, m_e) \in \mathrm{S} \times \mathrm{R}^{\mathrm{n_{int}}} \times \mathrm{R} : \, \varepsilon_{e_{ij}} \in L^2(\Omega), \\ &\xi_i \in L^2(\Omega), \, m_e \in L^2(\Omega) \big\} \,, \end{aligned} \tag{3.82}$$

where $\varepsilon_{e_{ij}}$ and ξ_i are the components of $\boldsymbol{\varepsilon_e}$ and ξ, respectively. Equation 3.81 originates from the Helmholtz free energy (Coussy, 1995). Let us denote $\|d\chi\|_{\mathcal{N}}^2$ by Ψ^d for convenience.

Then, the coupled problem has the following contractivity property,

$$\begin{aligned}
\frac{d\Psi^d}{dt} &= \frac{\partial \Psi^d}{\partial d\boldsymbol{\varepsilon}_e} : d\dot{\boldsymbol{\varepsilon}}_e + \frac{\partial \Psi^d}{\partial d\xi} \cdot d\dot{\xi} + \frac{\partial \Psi^d}{\partial dm_e} d\dot{m}_e \\
&= \int_\Omega \left[d\boldsymbol{\sigma}' : d\dot{\boldsymbol{\varepsilon}}_e - M \left(\frac{dm_e}{\rho_{f,0}} - b d\varepsilon_{e,v} \right) b d\varepsilon_{e,v} \right. \\
&\quad \left. - d\kappa \cdot d\dot{\xi} + \frac{M}{\rho_{f,0}} \left(\frac{dm_e}{\rho_{f,0}} - b\varepsilon_{e,v} \right) d\dot{m}_e \right] d\Omega \\
&= \int_\Omega \left[d\boldsymbol{\sigma} : d\dot{\boldsymbol{\varepsilon}} + \frac{dp}{\rho_{f,0}} d\dot{m} \right] d\Omega - \underbrace{\int_\Omega \left[d\boldsymbol{\sigma}' : d\dot{\boldsymbol{\varepsilon}}_p + d\kappa \cdot d\dot{\xi} \right] d\Omega}_{D_p^d} \\
&= \int_\Omega \left[d\boldsymbol{\sigma} : d\dot{\boldsymbol{\varepsilon}} - dp \, \mathrm{Div}(d\boldsymbol{v}) \right] d\Omega - D_p^d \quad (\text{from Equation 3.73}) \\
&= -\int_\Omega d\boldsymbol{v} \cdot \mu \mathbf{k}^{-1} d\boldsymbol{v} d\Omega - D_p^d \leq 0, \quad \left(\because \int_\Omega d\boldsymbol{\sigma} : d\dot{\boldsymbol{\varepsilon}} d\Omega = 0 \ \text{from Equation 3.73} \right)
\end{aligned} \tag{3.83}$$

where $(\dot{\cdot})$ is the time derivative, and $D_p^d \geq 0$ from Equation 3.79. From Darcy's law,

$$d\boldsymbol{v} = -\frac{\mathbf{k}}{\mu} \mathbf{Grad}\, dp, \quad dv_i \in H\,(div, \Omega), \tag{3.84}$$

where dv_i is the component of $d\boldsymbol{v}$. Equation 3.83 yields

$$\|\chi(t) - \tilde{\chi}(t)\|_{\mathcal{N}} \leq \|\chi_0 - \tilde{\chi}_0\|_{\mathcal{N}}\,, \tag{3.85}$$

which indicates that the coupled problem is contractive relative to the norm $\|\cdot\|_{\mathcal{N}}$. Thus, Equations 3.67 and 3.81 are the appropriate norms to show the contractivity.

From Equation 3.81, the stability of the displacement field requires $\|\mathbf{H}\| > 0$ for bounded $\|\varepsilon_p\|$. Thus, the stability of the displacement field is not guaranteed for perfect plasticity, $(\|\mathbf{H}\| = 0)$.

We now investigate whether the drained and undrained splits are contractive. Introducing two arbitrary initial conditions and taking similar steps to the fully coupled method,

the drained split can be expressed as

$$\begin{bmatrix} d\mathbf{u}^n \\ dp^n \end{bmatrix} \xrightarrow{\mathcal{A}^u_{dr}} \begin{bmatrix} d\mathbf{u}^{n+1} \\ dp^n \end{bmatrix} \xrightarrow{\mathcal{A}^p_{dr}} \begin{bmatrix} d\mathbf{u}^{n+1} \\ dp^{n+1} \end{bmatrix}, \quad \text{where} \quad \begin{cases} \mathcal{A}^u_{dr} : \operatorname{Div} d\boldsymbol{\sigma} = \mathbf{0},\ \delta(dp) = 0, \\ \mathcal{A}^p_{dr} : d\dot{m} + \operatorname{Div} d\boldsymbol{w} = \mathbf{0}, \\ \quad d\dot{\boldsymbol{\varepsilon}} = \mathbf{0},\ d\dot{\boldsymbol{\varepsilon}}_p = \mathbf{0},\ d\dot{\boldsymbol{\xi}} = \mathbf{0}, \end{cases} \tag{3.86}$$

which has homogeneous boundary conditions with no source terms. Since $\dot{\boldsymbol{\varepsilon}}$, $\dot{\boldsymbol{\varepsilon}}_p$, and $\dot{\boldsymbol{\xi}}$ are prescribed, they are not affected by the perturbation of the initial condition, yielding $d\dot{\boldsymbol{\varepsilon}} = \mathbf{0}$, $d\dot{\boldsymbol{\varepsilon}}_p = \mathbf{0}$, and $d\dot{\boldsymbol{\xi}} = \mathbf{0}$. When we solve the mechanical problem $\mathcal{A}^u_{dr}$ by the drained split, we have,

$$\begin{aligned} \frac{d\Psi^d}{dt} &= \int_\Omega \left[d\boldsymbol{\sigma} : \dot{d\boldsymbol{\varepsilon}} + \frac{dp}{\rho_{f,0}} \dot{dm} \right] d\Omega - \underbrace{\int_\Omega \left[d\boldsymbol{\sigma}' : \dot{d\boldsymbol{\varepsilon}}_p + \boldsymbol{\kappa} \cdot \dot{d\boldsymbol{\xi}} \right] d\Omega}_{D^d_p} \\ &= \int_\Omega \left[d\boldsymbol{\sigma} : \dot{d\boldsymbol{\varepsilon}} + \frac{dp}{\rho_{f,0}} b \dot{d\varepsilon}_v \right] d\Omega - D^d_p \ \ (\text{from } \delta(dp) = 0) \\ &= \int_\Omega \frac{dp}{\rho_{f,0}} b \dot{d\varepsilon}_v d\Omega - D^d_p \not\leq 0 \ \ (\text{from } \operatorname{Div} d\boldsymbol{\sigma} = \mathbf{0}) \ . \end{aligned} \tag{3.87}$$

Equation 3.87 proves that the drained split is not contractive when we solve the mechanical problem. This non-contractivity of the drained split has been pointed out by Armero and Simo (1992) and Armero (1999).

Then, when we solve the flow problem $\mathcal{A}^p_{dr}$ by the drained split, we have

$$\begin{aligned} \frac{d\Psi^d}{dt} &= \int_\Omega \left[d\boldsymbol{\sigma} : \dot{d\boldsymbol{\varepsilon}} + \frac{dp}{\rho_{f,0}} \dot{dm} \right] d\Omega - \underbrace{\int_\Omega \left[d\boldsymbol{\sigma}' : \dot{d\boldsymbol{\varepsilon}}_p + d\boldsymbol{\kappa} \cdot \dot{d\boldsymbol{\xi}} \right] d\Omega}_{D_p} \\ &= \int_\Omega -dp \operatorname{Div}(d\boldsymbol{v}) d\Omega \ \ \left(\because d\dot{\boldsymbol{\varepsilon}} = \mathbf{0},\ d\dot{\boldsymbol{\varepsilon}}_p = \mathbf{0},\ d\dot{\boldsymbol{\xi}} = \mathbf{0} \right) \\ &= -\int_\Omega d\boldsymbol{v} \cdot \mu \mathbf{k}^{-1} d\boldsymbol{v} d\Omega \leq 0. \end{aligned} \tag{3.88}$$

For the undrained split, we have

$$\begin{bmatrix} d\mathbf{u}^n \\ dp^n \end{bmatrix} \xrightarrow{\mathcal{A}^u_{ud}} \begin{bmatrix} d\mathbf{u}^{n+1} \\ dp^* \end{bmatrix} \xrightarrow{\mathcal{A}^p_{ud}} \begin{bmatrix} d\mathbf{u}^{n+1} \\ dp^{n+1} \end{bmatrix}, \quad \text{where} \quad \begin{cases} \mathcal{A}^u_{ud} : \operatorname{Div} \boldsymbol{d\sigma} = \mathbf{0},\ \delta dm = 0, \\ \mathcal{A}^p_{ud} : \dot{dm} + \operatorname{Div} d\boldsymbol{w} = \mathbf{0}, \\ \quad \dot{d\boldsymbol{\varepsilon}} = \mathbf{0},\ \dot{d\boldsymbol{\varepsilon}_p} = \mathbf{0},\ \dot{d\boldsymbol{\xi}} = \mathbf{0}, \end{cases} \tag{3.89}$$

which has homogeneous boundary conditions with no source terms. When we solve the mechanical problem $\mathcal{A}^u_{ud}$ by the undrained split, we have

$$\begin{aligned} \frac{d\Psi^d}{dt} &= \int_\Omega \left[d\boldsymbol{\sigma} : \dot{d\boldsymbol{\varepsilon}} + \frac{dp}{\rho_{f,0}} \dot{dm} \right] d\Omega - \underbrace{\int_\Omega \left[d\boldsymbol{\sigma'} : \dot{d\boldsymbol{\varepsilon}_p} + d\boldsymbol{\kappa} \cdot \dot{d\boldsymbol{\xi}} \right] d\Omega}_{D^d_p \geq 0} \\ &= \int_\Omega d\boldsymbol{\sigma} : \dot{d\boldsymbol{\varepsilon}} d\Omega - D^d_p \\ &= -D^d_p \leq 0. \end{aligned} \tag{3.90}$$

Note that the operator for flow in the undrained split is the same as that in the drained split, $\mathcal{A}^p_{ud}$ is the same as $\mathcal{A}^p_{dr}$. Thus, the undrained split satisfies the contractivity condition for both mechanics and flow.

3.6 Discrete Stability of the Nonlinear Problem

As shown in the previous section (Armero, 1999), the undrained split honors the dissipative properties of the coupled problem. But, we need to find which algorithm (i.e. time integration technique) provides unconditional stability - so called B-stability. By B-stability we mean the discrete counterpart of contractivity (Simo, 1991; Simo and Govindjee, 1991; Simo and Hughes, 1998), i.e.,

$$\left\| d\chi^{n+1} \right\|_{\mathcal{N}} \leq \| d\chi^n \|_{\mathcal{N}} \quad \forall n. \tag{3.91}$$

Since the drained split does not guarantee contractivity, it cannot provide an unconditionally stable solution algorithm. So, we study the undrained split further. We solve the mechanical problem first with a return mapping algorithm for poro-elasto-plasticity. For return mapping, we adopt the generalized midpoint rule described by Simo and Taylor (1986), Simo (1991), and Simo and Govindjee (1991), where we enforce the consistency condition of the return mapping at $t_{n+\alpha}$. This return mapping algorithm yields unconditional stability for $0.5 \leq \alpha \leq 1$ in the uncoupled elastoplastic mechanical problem. In contrast, the return mapping algorithm by Ortiz and Popov (1985) enforces the consistency condition of the return mapping at t_{n+1}, which yields unconditional stability only for $\alpha = 1$, the backward Euler time discretization, in the uncoupled mechanical problem (Simo and Hughes, 1998).

From the return mapping algorithm with the generalized midpoint rule, we obtain the discrete counterpart of Equation 3.70 as

$$\ll \Sigma^{tr,n+\alpha} - \Sigma^{n+\alpha},\ \Pi - \Sigma^{n+\alpha} \gg \leq 0 \quad {}^{\forall}\Pi \in \mathcal{E}\,, \tag{3.92}$$

where $\mathcal{E}$ contains the origin $(\mathbf{0}, \mathbf{0})$. $\Sigma = (\sigma', \kappa)$ is a generalized effective stress constrained to lie within the elastic domain $(\mathcal{E})$, and $\Sigma^{tr,n+\alpha}$ from the elastic trial step is defined as $(\boldsymbol{\sigma'}^n + \alpha \mathbf{C}_{dr} \Delta\varepsilon^n, \kappa^n)$. $\Pi = (\boldsymbol{\pi}', \boldsymbol{\eta})$ is a generalized stress. The bottom of Figure 3.6 shows a geometric interpretation of Equation 3.92.

Let $(\mathbf{u}^n,\ p^n,\ \boldsymbol{\xi}^n)$ and $(\tilde{\mathbf{u}}^n,\ \tilde{p}^n,\ \tilde{\xi}^n)$ be two arbitrary solutions at time t_n, yielding $(\boldsymbol{\sigma'}^n,\ m^n,\ \kappa^n,\ \boldsymbol{\varepsilon}_p^n)$ and $(\tilde{\boldsymbol{\sigma}}'^n,\ \tilde{m}^n,\ \tilde{\kappa}^n,\ \tilde{\boldsymbol{\varepsilon}}_p{}^n)$, respectively. Then Equation 3.89 with the generalized midpoint rule yields

$$\mathrm{Div}\, d\boldsymbol{\sigma}^{n+\alpha} = \mathbf{0}, \quad \Delta dm = 0, \tag{3.93}$$

where $d\boldsymbol{\sigma}^{n+\alpha} = \boldsymbol{\sigma}^{n+\alpha} - \tilde{\boldsymbol{\sigma}}^{n+\alpha}$. From Equation 3.92, we obtain

$$\ll \Sigma^{tr,n+\alpha} - \Sigma^{n+\alpha},\ \tilde{\Sigma}^{n+\alpha} - \Sigma^{n+\alpha} \gg \leq 0 \quad \left(\text{Choosing } \Pi = \tilde{\Sigma}^{\mathrm{n}+\alpha}\right), \tag{3.94}$$

$$\ll \tilde{\Sigma}^{tr,n+\alpha} - \tilde{\Sigma}^{n+\alpha},\ \Sigma^{n+\alpha} - \tilde{\Sigma}^{n+\alpha} \gg \leq 0 \quad \left(\text{Choosing } \Pi = \Sigma^{\mathrm{n}+\alpha}\right). \tag{3.95}$$

Adding Equations 3.94 and 3.95,

$$\begin{aligned} &\ll d\Sigma^n - d\Sigma^{n+\alpha},\ -d\Sigma^{n+\alpha} \gg \\ &+ \ll (\alpha \mathbf{C}_{dr} \Delta d\varepsilon^n, 0),\ (-d\boldsymbol{\sigma}'^{n+\alpha}, -d\boldsymbol{\kappa}^{n+\alpha}) \gg \leq 0\,, \end{aligned} \tag{3.96}$$

where again $d(\cdot) = (\cdot) - \tilde{(\cdot)}$, (e.g., $\Delta d\varepsilon^n = \Delta\varepsilon^n - \Delta\tilde{\varepsilon}^n$). The first term of Equation 3.96 can be written as

$$\begin{aligned} &\ll d\Sigma^n - d\Sigma^{n+\alpha},\ -d\Sigma^{n+\alpha} \gg \\ &= - \ll \alpha(d\Sigma^n - d\Sigma^{n+1}),\ d\Sigma^{n+1/2} + \left(\alpha - \frac{1}{2}\right)\left(d\Sigma^{n+1} - d\Sigma^n\right) \gg \\ &= \alpha\left(\left\|d\Sigma^{n+1}\right\|_{\mathcal{E}}^2 - \|d\Sigma^n\|_{\mathcal{E}}^2\right) + \alpha\,(2\alpha - 1)\left\|d\Sigma^{n+1} - d\Sigma^n\right\|_{\mathcal{E}}^2\,, \end{aligned} \tag{3.97}$$

where $\Sigma^{n+1/2} = (\Sigma^n + \Sigma^{n+1})/2$. The second term of Equation 3.96 can be written as

$$\begin{aligned} &\ll (\alpha \mathbf{C}_{dr} \Delta d\varepsilon^n, 0),\ (-d\boldsymbol{\sigma}'^{n+\alpha}, -d\kappa^{n+\alpha}) \gg \\ &= -\int_\Omega \alpha \Delta d\varepsilon^n : d\boldsymbol{\sigma}'^{n+\alpha} d\Omega \\ &= -\alpha \int_\Omega \Delta d\varepsilon^n : (d\boldsymbol{\sigma}^{n+\alpha} + b dp^{n+\alpha}\mathbf{1}) d\Omega \\ &= -\alpha \int_\Omega \Delta d\varepsilon^n : b dp^{n+\alpha}\mathbf{1} d\Omega \\ &\qquad \left(\because \int_\Omega \Delta d\varepsilon^n : d\boldsymbol{\sigma}^{n+\alpha} d\Omega = 0 \text{ from Equation 3.93}\right) \\ &= \alpha \int_\Omega \frac{1}{M}(dp^{n+1} - dp^n) dp^{n+\alpha} d\Omega \\ &\qquad \left(\because b\Delta d\varepsilon^n : \mathbf{1} = -\frac{1}{M}(dp^{n+1} - dp^n) \text{ from } \Delta dm = 0\right) \\ &= \alpha \frac{1}{2M}(\left\|dp^{n+1}\right\|_{L^2}^2 - \|dp^n\|_{L^2}^2) + \alpha\,(2\alpha - 1)\,\frac{1}{2M}\left\|dp^{n+1} - dp^n\right\|_{L^2}^2\,, \end{aligned} \tag{3.98}$$

where $\|\cdot\|_{L^2}$ is the L^2 norm. From Equation 3.96,

$$\alpha\left(\left\|d\Sigma^{n+1}\right\|_{\mathcal{E}}^2-\|d\Sigma^n\|_{\mathcal{E}}^2+\frac{1}{2M}(\left\|dp^{n+1}\right\|_{L^2}^2-\|dp^n\|_{L^2}^2)\right)$$
$$+\alpha\left(2\alpha-1\right)\left(\left\|d\Sigma^{n+1}-d\Sigma^n\right\|_{\mathcal{E}}^2+\frac{1}{2M}\left\|dp^{n+1}-dp^n\right\|_{L^2}^2\right)\leq 0\,. \tag{3.99}$$

From Equation 3.99, when we solve the mechanical problem, the evolution of the norm at the discrete time level satisfies

$$\begin{aligned}
&\left\|d\chi^{n+1}\right\|_{\mathcal{N}}^2-\|d\chi^n\|_{\mathcal{N}}^2\\
&=\left\|d\zeta^{n+1}\right\|_{\mathcal{T}}^2-\|d\zeta^n\|_{\mathcal{T}}^2\\
&=\left\|d\Sigma^{n+1}\right\|_{\mathcal{E}}^2+\frac{1}{2M}\left\|dp^{n+1}\right\|_{L^2}^2-\|d\Sigma^n\|_{\mathcal{E}}^2-\frac{1}{2M}\|dp^n\|_{L^2}^2\\
&\leq-(2\alpha-1)\left(\left\|d\Sigma^{n+1}-d\Sigma^n\right\|_{\mathcal{E}}^2+\frac{1}{2M}\left\|dp^{n+1}-dp^n\right\|_{L^2}^2\right),
\end{aligned} \tag{3.100}$$

which indicates that the stability condition of Equation 3.91 is satisfied during the mechanical step if $0.5\leq\alpha\leq 1$.

Remark 3.4. Equation 3.98 contains terms associated with pressure, which is characteristic of the coupled problem. Equation 3.98 is identically zero in the uncoupled mechanical problem (Simo, 1991).

After the mechanical problem is solved, we deal with the flow problem. Equation 3.89 yields

$$\frac{1}{M}\frac{dp^{n+1}-dp^n}{\Delta t}+\mathrm{Div}(d\boldsymbol{v}^{n+\alpha})=0, \tag{3.101}$$
$$\Delta d\boldsymbol{\varepsilon}=\mathbf{0},\Delta d\boldsymbol{\varepsilon}_p=\mathbf{0},\ \Delta d\boldsymbol{\xi}=\mathbf{0}. \tag{3.102}$$

Integrating over the domain and using the generalized midpoint rule, Equation 3.101 yields

$$\begin{aligned}
&\int_\Omega dp^{n+\alpha}\frac{1}{M}\frac{(dp^{n+1}-dp^n)}{\Delta t}d\Omega \\
&= \int_\Omega \mathbf{Grad}\, dp^{n+\alpha} d\boldsymbol{v}^{n+\alpha} d\Omega \\
&= -\int_\Omega d\boldsymbol{v}^{n+\alpha}\cdot\mu\mathbf{k}^{-1}d\boldsymbol{v}^{n+\alpha}d\Omega \quad \left(\because \mathbf{Grad}\, dp^{n+\alpha} = -\mu\mathbf{k}^{-1}d\boldsymbol{v}^{n+\alpha}\right).
\end{aligned} \tag{3.103}$$

Equation 3.102 implies that

$$\left\|d\Sigma^{n+1}\right\|^2_{\mathcal{E}} = \|d\Sigma^n\|^2_{\mathcal{E}}\,. \tag{3.104}$$

We introduce the following identity

$$\begin{aligned}
&\int_\Omega dp^{n+\alpha}\frac{1}{M}\left(dp^{n+1}-dp^n\right)d\Omega \\
&= \frac{1}{2M}(\left\|dp^{n+1}\right\|^2_{L^2} - \|dp^n\|^2_{L^2}) + (2\alpha-1)\,\frac{1}{2M}\left\|dp^{n+1}-dp^n\right\|^2_{L^2}.
\end{aligned} \tag{3.105}$$

Then, from Equations 3.103 – 3.105, the evolution of the norm during the flow step is written as

$$\begin{aligned}
&\left\|d\chi^{n+1}\right\|^2_{\mathcal{N}} - \|d\chi^n\|^2_{\mathcal{N}} \\
&= \left\|d\zeta^{n+1}\right\|^2_{\mathcal{T}} - \|d\zeta^n\|^2_{\mathcal{T}} \\
&= \frac{1}{2M}(\left\|dp^{n+1}\right\|^2_{L^2} - \|dp^n\|^2_{L^2}) \\
&= -(2\alpha-1)\,\frac{1}{2M}\left\|dp^{n+1}-dp^n\right\|^2_{L^2} - \Delta t\int_\Omega d\boldsymbol{v}^{n+\alpha}\cdot\mu\mathbf{k}^{-1}d\boldsymbol{v}^{n+\alpha}d\Omega,
\end{aligned} \tag{3.106}$$

where the stability condition is $0.5 \leq \alpha \leq 1$. From Equation 3.106, the stability condition during the flow step is identical to the uncoupled problem, where the proper norm to show stability is a weighted L^2 norm of the pressure (Thomée, 2006; Simo, 1991). From Equations 3.100 and 3.106, the B-stability condition of the undrained split is $0.5 \leq \alpha \leq 1$.

3.7 Numerical Examples

We use five test cases to compare the various coupling strategies.

Case 3.1 The Terzaghi problem in a 1D linear poroelastic medium (the left picture in Figure 3.7). The driving mechanical force is provided by the overburden.

Case 3.2 Injection and production in a 1D poroelastic medium. The driving force is due to injection and production (the right picture in Figure 3.7).

Case 3.3 The Mandel problem in a 2D elastic medium. The driving force is provided by the side burden (the left picture in Figure 3.8).

Case 3.4 Injection and production in a 1D poro-elasto-plastic medium with isotropic hardening. The driving force is due to injection and production (the right picture in Figure 3.7).

Case 3.5 Fluid production in 2D with elasto-plastic behavior described by the modified Cam-clay model. The compaction of the reservoir occurs due to production (the right picture in Figure 3.8).

The numerical results are based on *one iteration* per time step (i.e., staggered method) unless noted explicitly otherwise.

3.7.1 Numerical results for elasticity

Case 3.1—The Terzaghi problem

We have drainage boundaries for flow at the top and bottom, where the boundary fluid pressure is $P_{bc} = 2.125\ MPa$. The overburden is $\bar{\sigma} = 2 \times 2.125\ MPa$ at the top, and a no-displacement boundary condition is applied to the bottom. The domain has 20 grid blocks. The length of the domain is $L_z = 40\ m$ with grid spacing $\Delta z = 2\ m$. The bulk density of the porous medium is $\rho_b = 2400\ kg\ m^{-1}$. Initial fluid pressure is $P_i = 2.125\ MPa$. Fluid density and viscosity are $\rho_{f,0} = 1000\ kg\ m^{-1}$ and $\mu = 1.0\ cp$, respectively. Permeability is

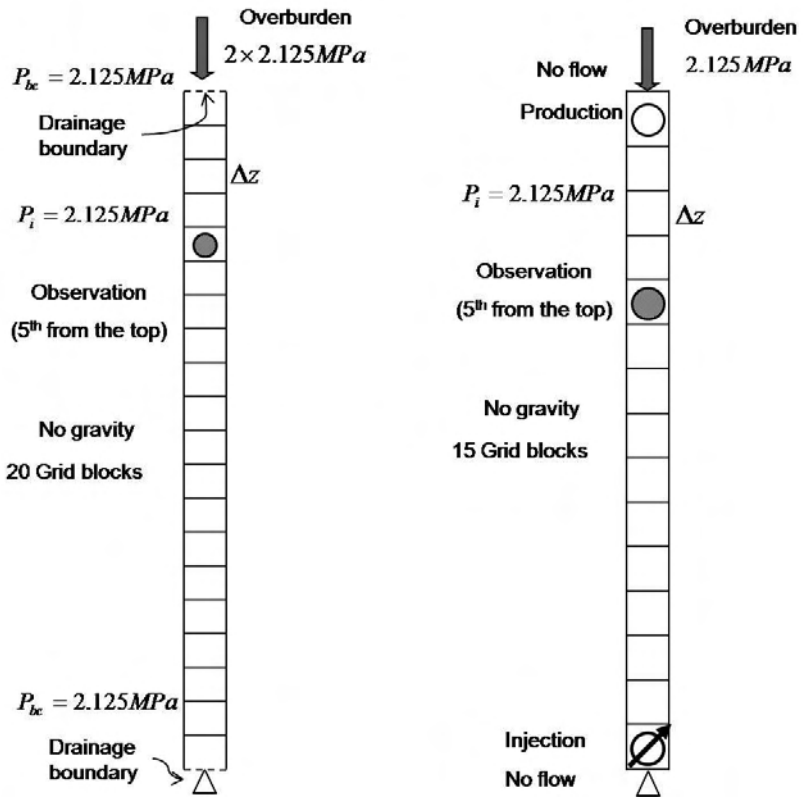

Figure 3.7: Left: the Terzaghi problem in 1D (Case 3.1). Right: 1D problem with injection and production wells (Case 3.2 and 3.4).

Table 3.1: Input data for Case 3.1

Property	Value
Permeability (k_p)	50 md
Porosity (ϕ_0)	0.3
Biot coefficient (b)	1.0
Drained (constrained) modulus (K_{dr})	100 MPa
Bulk density (ρ_b)	2400 kg m^{-3}
Fluid density ($\rho_{f,0}$)	1000 kg m^{-3}
Fluid viscosity (μ)	1.0 cp
Initial pressure (P_i)	2.125 MPa
Boundary pressure (P_{bc})	2.125 MPa
Overburden ($\bar{\sigma}$)	2×2.125 MPa
Grid spacing (Δz)	2 m

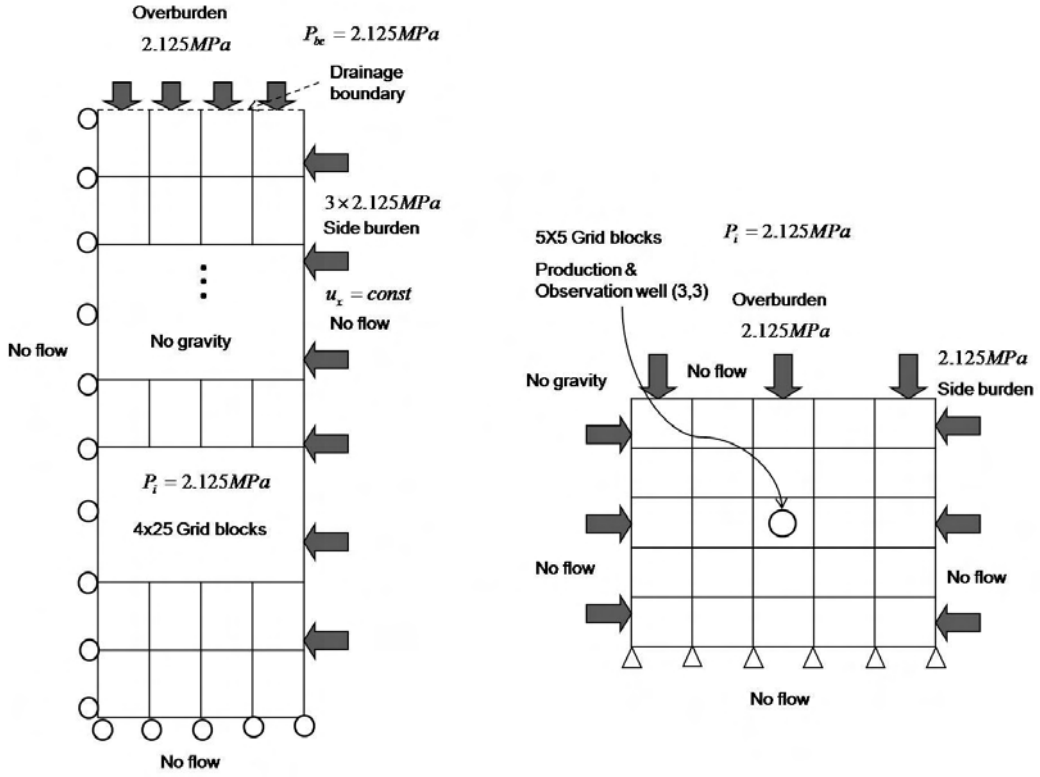

Figure 3.8: Left: Mandel's problem in 2D with elastic deformation (Case 3.3). Right: 2D problem driven by single-well production in an elasto-plastic medium (Case 3.5).

Table 3.2: Input data for Case 3.2

Property	Value
Permeability (k_p)	50 md
Porosity (ϕ_0)	0.3
Drained (constrained) modulus (K_{dr})	100 MPa
Biot coefficient (b)	1.0
Bulk density (ρ_b)	2400 $\mathrm{kg\,m^{-3}}$
Fluid density ($\rho_{f,0}$)	1000 $\mathrm{kg\,m^{-3}}$
Fluid viscosity (μ)	1.0 cp
Injection rate (Q_{inj})	100 $\mathrm{kg\,day^{-1}}$
Production rate (Q_{prod})	100 $\mathrm{kg\,day^{-1}}$
Boundary pressure (P_{bc})	2.125 MPa
Overburden ($\bar{\sigma}$)	2.125 MPa
Grid spacing (Δz)	10 m

$k_p = 50\ md$, porosity is $\phi_0 = 0.3$, the constrained modulus is $K_{dr} = 100\ MPa$, and the Biot coefficient is $b = 1.0$. No production and injection of fluid is applied. An observation well is located at the fifth grid block from the top. Gravity is neglected. The Biot modulus is left unspecified to test the performance of the drained and undrained splits for different values of the coupling strength, τ, in Equation 3.50. The numerical values of the parameters for Case 3.1 are also listed in Table 3.1. We determine the pressure and displacement fields, using the fully coupled method with very small time step size in order to minimize the temporal error.

Figures 3.9 shows the results of the numerical experiments, as well as, the reference analytical solution. The backward Euler time discretization is used. Both sequential methods are stable for $\tau = 0.83 < 1$ (Figs. 3.9 (top)). The drained split, however, is unstable for $\tau = 1.21 > 1$ (Figs. 3.9 (bottom)). On the other hand, the undrained split is stable for $\tau = 1.21 > 1$ (Figs. 3.9 (bottom)). Even in the region of stability, the drained split produces wildly oscillatory solutions, which is in agreement with the predictions from the Von Neumann stability analysis. The validity of the simulations is supported by the agreement between the (stable) numerical solutions and the analytical solution to the problem (see, e.g., (Wang, 2000)).

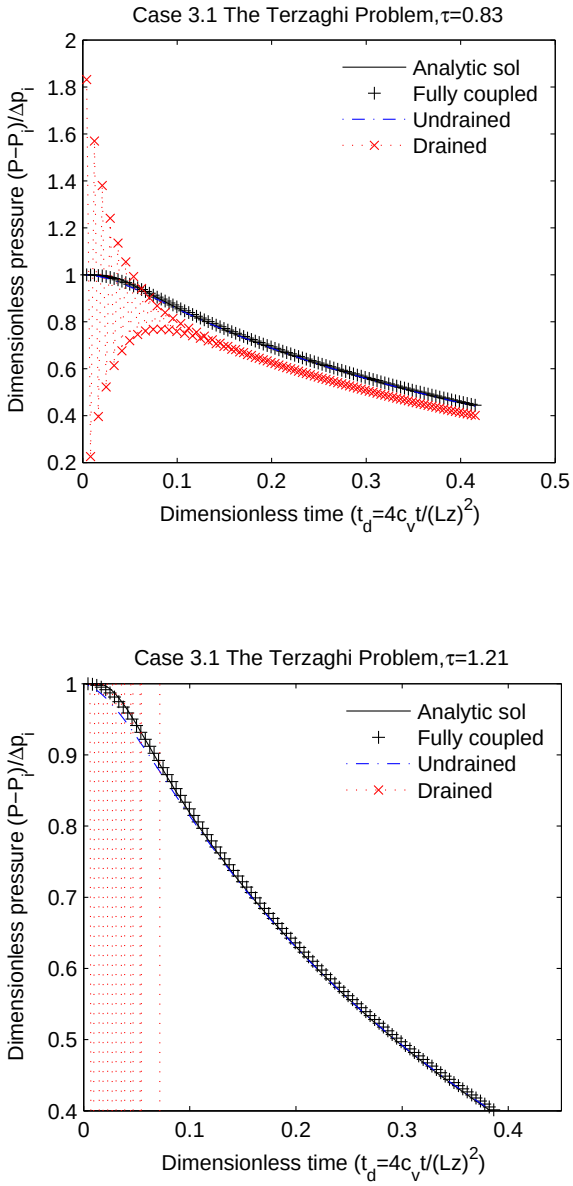

Figure 3.9: Case 3.1 (the Terzaghi problem). Evolution of the dimensionless pressure as a function of dimensionless time. Δp_i is the pressure rise at $t = 0$, L_z is the vertical extent of the reservoir, t is the simulation time, and c_v is the consolidation coefficient. The results from the fully coupled, drained, and undrained methods are shown. Top: coupling strength $\tau = 0.83$. Bottom: coupling strength $\tau = 1.21$.

Case 3.2—1D fluid injection and production

For Case 3.2, dilation and compaction occur around the injection and production wells. The total subsidence is zero because the injection rate $Q_{inj} = 100\ kg\ day^{-1}$ is the same as the production rate $Q_{prod} = 100\ kg\ day^{-1}$, and the domain is homogeneous with 15 grid blocks. The length of the domain is $L_z = 150\ m$ with grid spacing $\Delta z = 10\ m$. The overburden is $\bar{\sigma} = 2.125\ MPa$ and a no-displacement boundary condition is used at the bottom of the domain. The bulk density of the porous medium is $\rho_b = 2400\ kg\ m^{-1}$. The initial fluid pressure is $P_i = 2.125\ MPa$, and the fluid density and viscosity are $\rho_{f,0} = 1000\ kg\ m^{-1}$ and $\mu = 1.0\ cp$, respectively. Permeability is $k_p = 50\ md$, porosity is $\phi_0 = 0.3$, the constrained modulus is $K_{dr} = 100\ MPa$, and the Biot coefficient is $b = 1.0$. The observation well is located at the fifth grid block from the top. A no-flow boundary condition is applied at the top and bottom. There is no gravity in the domain. The Biot modulus is left unspecified for different values of the coupling strength τ. The data for Case 3.2 are also given in Table 3.2.

The results are shown in Figures 3.10, where the backward Euler time discretization is used. The results support the same conclusion as those of Case 3.1. When the coupling strength, τ, is less than one, all sequential methods are stable. But, when τ is greater than one, the drained split is unstable, and produces oscillatory solutions even when it is stable (in this case, the oscillations are small). Most importantly, the results confirm that the undrained split is stable and nonoscillatory regardless of the coupling strength.

Independence of stability limit on time step size for the drained split

Figure 3.11 shows that the stability limit for the drained split is independent of the time step size. Two time step sizes are considered: $\Delta t_d = 4.4 \times 10^{-2}$ and $\Delta t_d = 4.4 \times 10^{-5}$. The drained split is stable for both time step sizes when the coupling strength is less than one ($\tau = 0.95$, Fig. 3.11(top)). The drained split is unstable for both time step sizes when the coupling strength is greater than one ($\tau = 1.05$, Fig. 3.11(bottom)). The stability of the drained split is not improved by reducing the time step size, in agreement with our theoretical analysis. Therefore, physical problems with large coupling strength ($\tau > 1$)

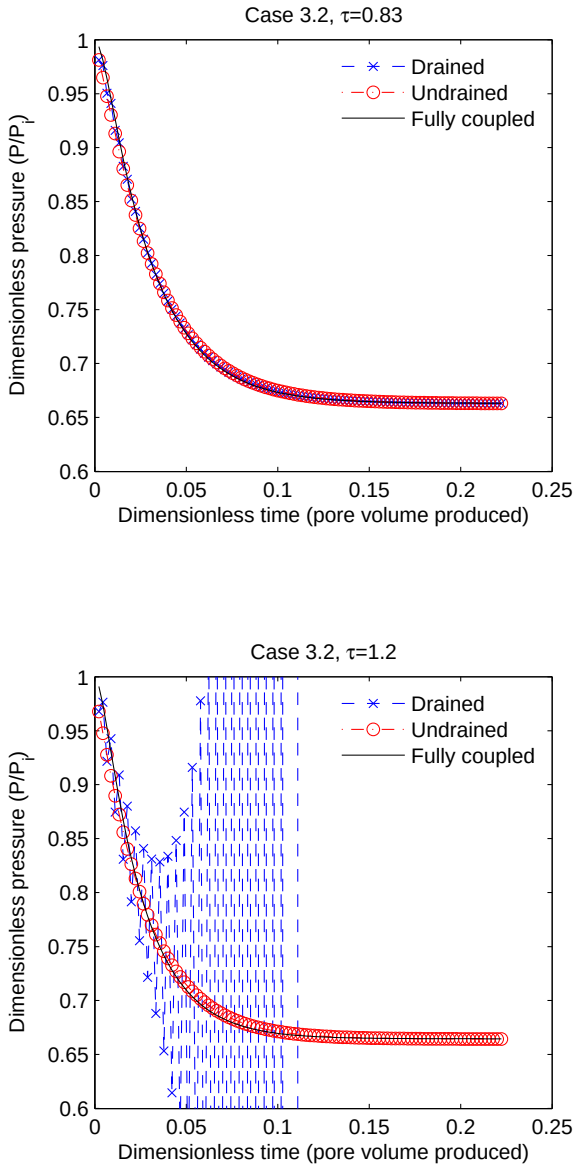

Figure 3.10: Case 3.2 (1D injection–production problem). Evolution of the dimensionless pressure as a function of dimensionless time (pore volume produced). The results for the fully coupled, drained, and undrained methods are shown. Top: coupling strength $\tau = 0.83$. Bottom: coupling strength $\tau = 1.21$.

cannot be solved by the drained split. The sharpness of the stability estimate is also valid in multidimensional problems, and this is shown later when we study Case 3.3.

The results from Figures 3.9–3.11 indicate that the stability criterion of Equation 3.50 is quite sharp. The drained split yields severe oscillatory behaviors even when it is stable, which is expected due to the presence of a negative amplification factor.

Other time discretization schemes

We investigate the midpoint time discretization ($\alpha = 0.5$ for both mechanics and flow) and the mixed time discretization ($\alpha = 1.0$ for mechanics and $\alpha = 0.5$ for flow). Here, $K_{dr} = 1GPa$ and other data are the same as Table 3.2. Figure 3.12 shows the stability behaviors of the midpoint ($\alpha = 0.5$) and backward Euler ($\alpha = 1.0$) time discretizations for a very low coupling strength $\tau = 0.083$. The drained split is unstable even though the coupling is very weak (see the top figure), whereas the undrained split is stable.

In Figure 3.13, the mixed time discretization is applied to the mechanics ($\alpha = 1.0$) and flow ($\alpha = 0.5$). When the coupling strength is less than one, both the drained and undrained split are stable. On the other hand, the drained split is unstable when the coupling strength is 1.11, while the undrained split is stable. Therefore, the numerical results support all stability estimates obtained from the Von Neumann method.

Case 3.3—The Mandel problem

Mandel's problem is commonly used to show the validity of simulators for coupled flow and geomechanics. A description and analytical solution to the Mandel problem is presented in Abousleiman et al. (1996).

For this case, the homogeneous domain has dimensions of $0.02\ m \times 100\ m$ discretized using 4×25 grid blocks. The domain has an overburden $\bar{\sigma} = 2 \times 2.125\ MPa$ at the top, no-horizontal displacement boundary on the left side, and no vertical displacement boundary at the bottom. The right side has a side burden $\bar{\sigma_h} = 3 \times 2.125\ MPa$, where we impose constant horizontal displacement. The bulk density of the porous medium is $\rho_b = 2400\ kg\ m^{-1}$. Initial fluid pressure is $P_i = 2.125\ MPa$. Fluid density and viscosity

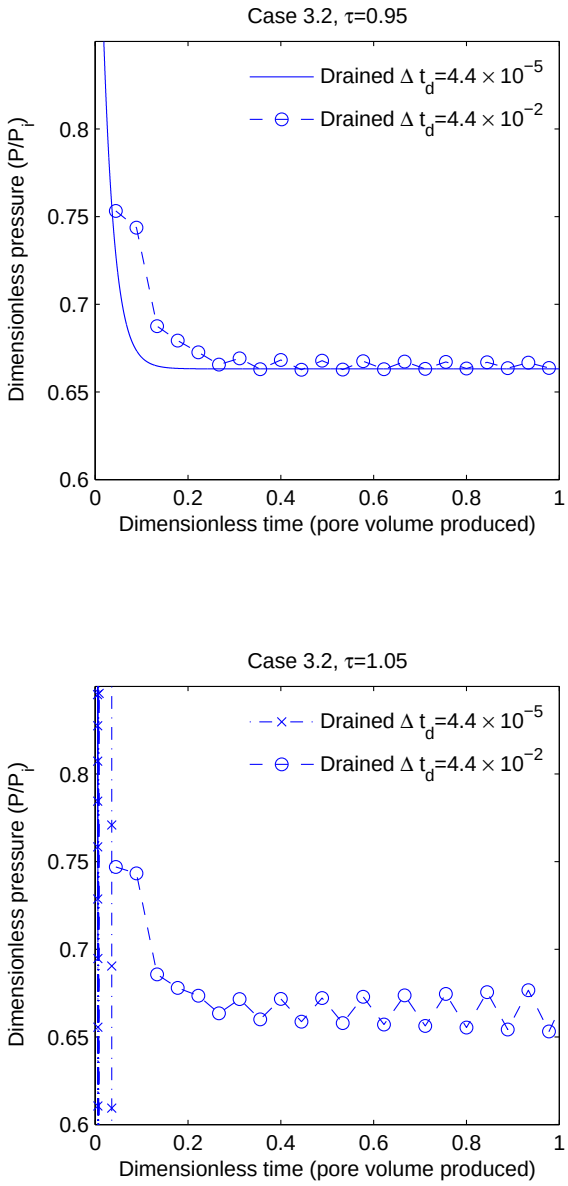

Figure 3.11: Case 3.2 (1D injection–production problem). Results are shown for the drained split with two different coupling strengths: $\tau = 0.95$ (top), and $\tau = 1.05$ (bottom) and two very different time step sizes. The stability of the drained split is independent of the time step size. The drained split is stable if $\tau < 1$ and unstable if $\tau > 1$, regardless of the time step size.

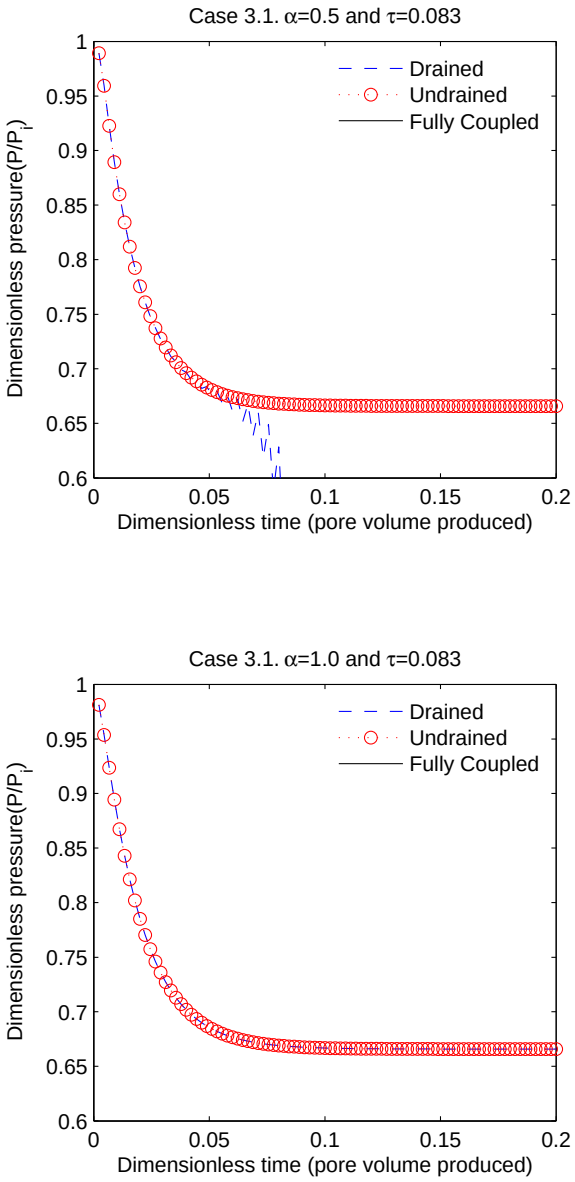

Figure 3.12: 1D problem with injection and production (Case 3.2). $\tau = 0.083$ is considered. Top: $\alpha = 0.5$ for both flow and mechanics. Bottom: $\alpha = 1.0$ for both flow and mechanics.

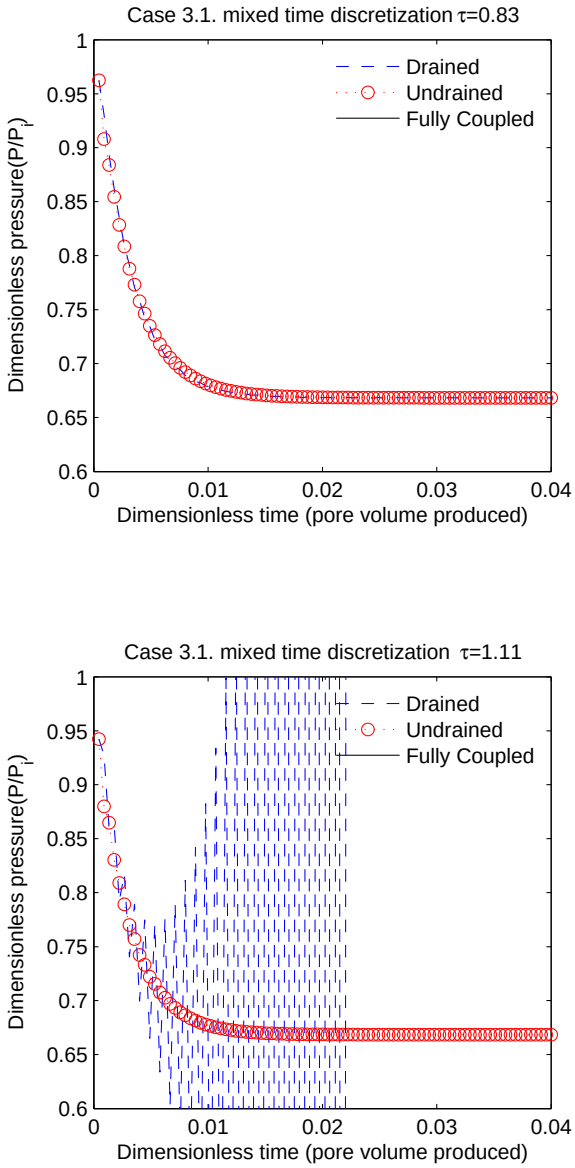

Figure 3.13: 1D problem with injection and production (Case 3.2). The mixed time discretization ($\alpha = 0.5$ for flow and $\alpha = 1.0$ mechanics) is considered. Top: $\tau = 0.83$. Bottom: $\tau = 1.11$.

are $\rho_{f,0} = 1000\ kg\ m^{-1}$ and $\mu = 1.0\ cp$, respectively. Permeability is $k_p = 50\ md$, and porosity is $\phi_0 = 0.3$. Young's modulus is $E = 2.9\ GPa$, and Poisson's ratio is $\nu = 0.0$. The Biot coefficient is $b = 1.0$. An observation well is located at the lower left corner (1,25). We have a drainage boundary for flow at the top, where the boundary fluid pressure is $P_{bc} = 2.125\ MPa$. A no-flow boundary condition is applied to both sides and the bottom. Gravity is neglected. The Biot modulus can be determined from the different values of the coupling strength τ, which are used for the various numerical tests. The input parameters are listed in Table 3.3.

Figure 3.14 shows that the drained split (the top figure) is stable when τ is less than one, while it is unstable when τ is greater than one (the bottom figure). Furthermore, severe oscillations are observed even though the drained split is stable. Due to the oscillations, the early time solution is not computed properly in the drained split even though the late time solution converges to the analytical results. On the other hand, the undrained split shows unconditional stability and yields a monotonic solution that matches the analytical solution for all time.

The *Mandel–Cryer effect*, where a rise in the pressure during early time is observed, can be captured accurately by the undrained split. The solutions from the fully coupled method and the undrained split are in good agreement with the analytical solution.

Figures 3.15 and 3.16 show the vertical and horizontal displacements, respectively. The drained split suffers from severe oscillations in the displacements, even though it is stable (top figures). But, when the drained split violates the stability condition, it shows instability (bottom figures). In contrast, the fully coupled and undrained methods are stable regardless of the coupling strength, and they agree with the analytical solutions.

3.7.2 Numerical results for elastoplasticity

We investigate the behavior of sequential solution methods for nonlinear poro-elasto-plastic problems. We compare the numerical solutions using a one-pass strategy (i.e., staggered method) with our a-priori stability estimates for the drained and undrained splits. After we investigate the sequential schemes with the staggered method, we perform full iterations

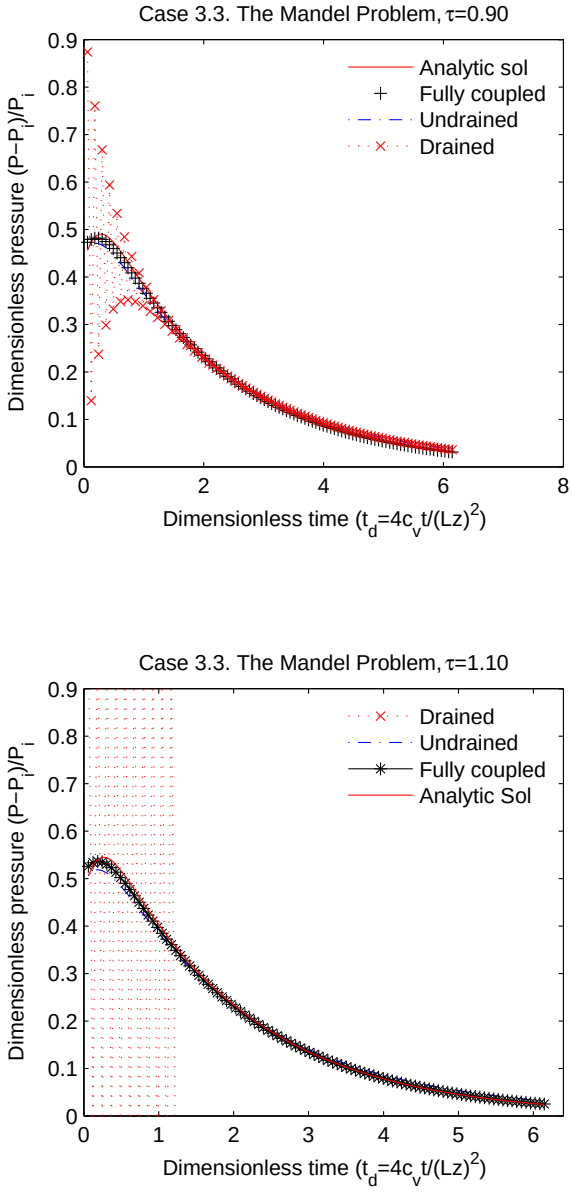

Figure 3.14: Case 3.3 (the Mandel problem). Evolution of the pressure at the observation point as a function of dimensionless time. Shown are the results for the fully coupled, drained, and undrained splits with different coupling strengths. Top: $\tau = 0.90$. Bottom: $\tau = 1.10$.

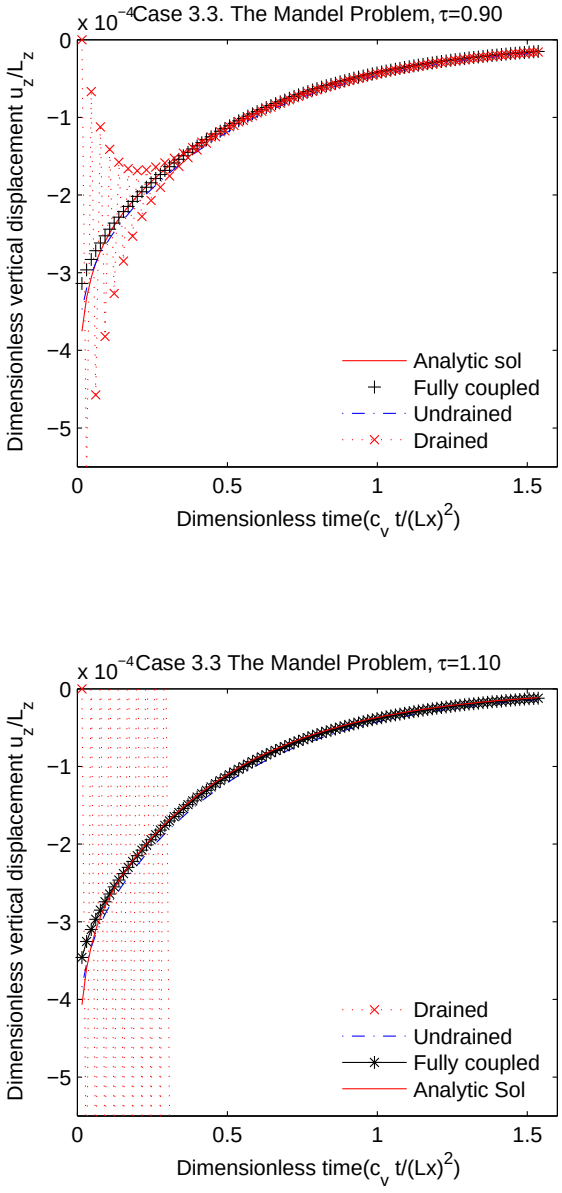

Figure 3.15: Case 3.3 (the Mandel problem). Evolution of the dimensionless vertical displacement on the top as a function of dimensionless time. Shown are the results for the fully coupled, drained, and undrained splits with different coupling strengths. Top: $\tau = 0.90$. Bottom: $\tau = 1.10$.

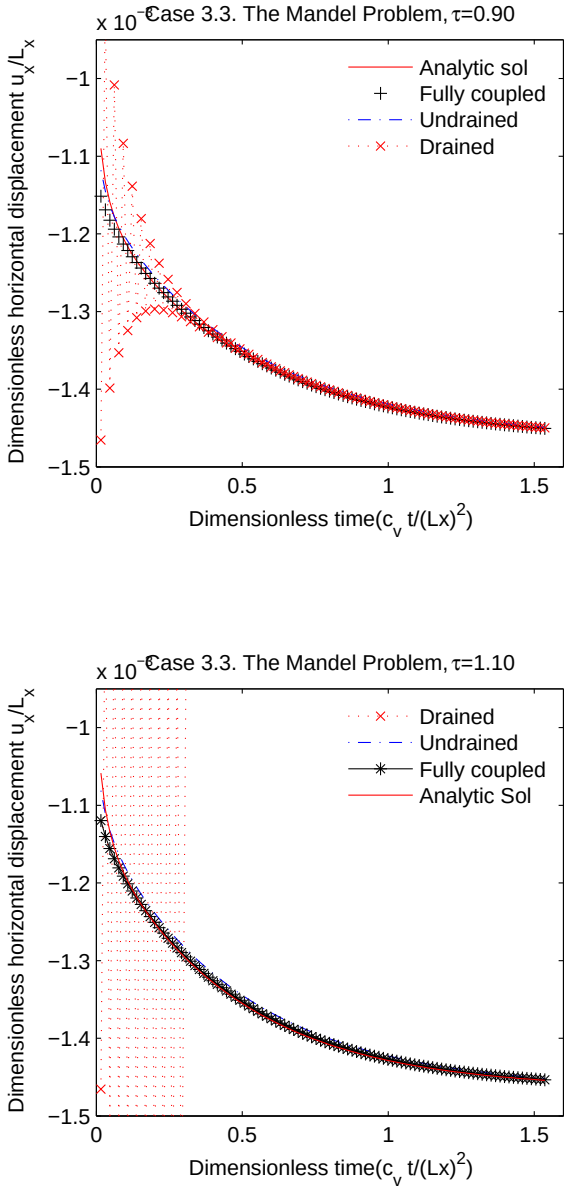

Figure 3.16: Case 3.3 (the Mandel problem). Evolution of the dimensionless horizontal displacement on the right side as a function of dimensionless time. Shown are the results for the fully coupled, drained, and undrained splits with different coupling strengths. Top: $\tau = 0.90$. Bottom: $\tau = 1.10$.

Table 3.3: Input data for Case 3.3.

Property	Value
Permeability (k_p)	50 md
Porosity (ϕ_0)	0.3
Young modulus (E)	2900 MPa
Poisson ratio (ν)	0
Biot coefficient (b)	1.0
Bulk density (ρ_b)	2400 $\mathrm{kg\,m^{-3}}$
Fluid density ($\rho_{f,0}$)	1000 $\mathrm{kg\,m^{-3}}$
Fluid viscosity (μ)	1.0 cp
Initial pressure (P_i)	2.125 MPa
Boundary pressure (P_{bc})	2.125 MPa
Side burden	3×2.125 MPa
Overburden ($\bar{\sigma}$)	2.125 MPa
Grid spacing (Δx)	0.005 m
Grid spacing (Δz)	2.0 m
Grid	4×25

for the nonlinear poroelastoplastic problem after linearization, where we use the drained and undrained splits as preconditioning methods for the fully coupled Jacobian (i.e., the staggered Newton schemes (Schrefler et al., 1997)). The backward Euler scheme is used for time discretization.

We adopt the associative plasticity formulation (Simo, 1991; Simo and Hughes, 1998; Coussy, 1995). For Case 3.4, the yield function f_Y is given by

$$f_Y = \left|\boldsymbol{\sigma}'\right| - (\boldsymbol{\sigma}'_Y + H\,|\dot{\varepsilon}_p|) = 0, \tag{3.107}$$

where H is the hardening modulus. For Case 3.5, The yield function f_Y of the modified Cam-clay model (Borja and Lee, 1990; Borja, 1991) is

$$f_Y = \frac{q'^2}{M^2_{\mathrm{mcc}}} + \sigma'_v(\sigma'_v - p_{co}) = 0, \tag{3.108}$$

where q' is the deviatoric effective stress, σ'_v is the volumetric effective stress, M_{mcc} is the slope of the critical state line, and p_{co} is the preconsolidation pressure. The parameter λ is the virgin compression index, and κ is the swell index. A schematic of the return mapping

for the modified Cam-clay model is shown in the top picture of Figure 3.19 (refer to Borja and Lee (1990); Borja (1991) for more details).

Case 3.4—1D fluid injection and production in elastoplasticity

The constrained modulus is $K_{dr} = 1\ GPa$ and the Biot modulus is $M = 83.3\ MPa$. The hardening moduli are unspecified for the numerical tests. The other data and geometry of the domain are the same as in Case 3.2. The coupling strength τ is 0.083 when the mechanical problem is elastic. An iterative staggered method is used, whereby. Each iteration involves solving two problems in sequence, such that each problem is solved implicitly. So, for a given time step, a single-pass strategy would entail solving the first sub-problem implicitly (subject to a given tolerance), updating the appropriate terms to set up the second problem, and finally solving the second problem implicitly. We then move to the next time step. In the iterative approach, the implicit-implicit solution sequence is repeated until convergence.

Figure 3.17 shows the numerical results for Case 3.4. On the top figure, the yield stress and hardening modulus are $\boldsymbol{\sigma}'_Y = 1.5\ MPa$ and $H = 250\ MPa$, respectively. This condition yields a coupling strength less than one for plasticity, $\tau = 0.417$. The drained split is stable in the elastic regime, since the coupling strength is less than one. After the simulation enters the plastic regime, at about $t_d = 0.05$, the drained split is still stable, shown on the top of Figure 3.17, because the coupling strength is still less than one.

The case that the yield stress and hardening modulus are $\boldsymbol{\sigma}'_Y = 1.5\ MPa$ and $H = 25\ MPa$, respectively, is shown in Figure 3.17 (bottom). These conditions yield a coupling strength greater than one for plasticity, $\tau = 3.41$. The bottom figure shows that the drained split is unstable in the plastic regime because the coupling strength is higher than one. This supports the a-priori stability estimates from the Von Neumann method. Moreover, the instability of the drained split cannot be fixed by tuning the time step size, since the stability limit is independent of the time step size. However, the undrained split is stable regardless of the coupling strength, as shown in Figure 3.17.

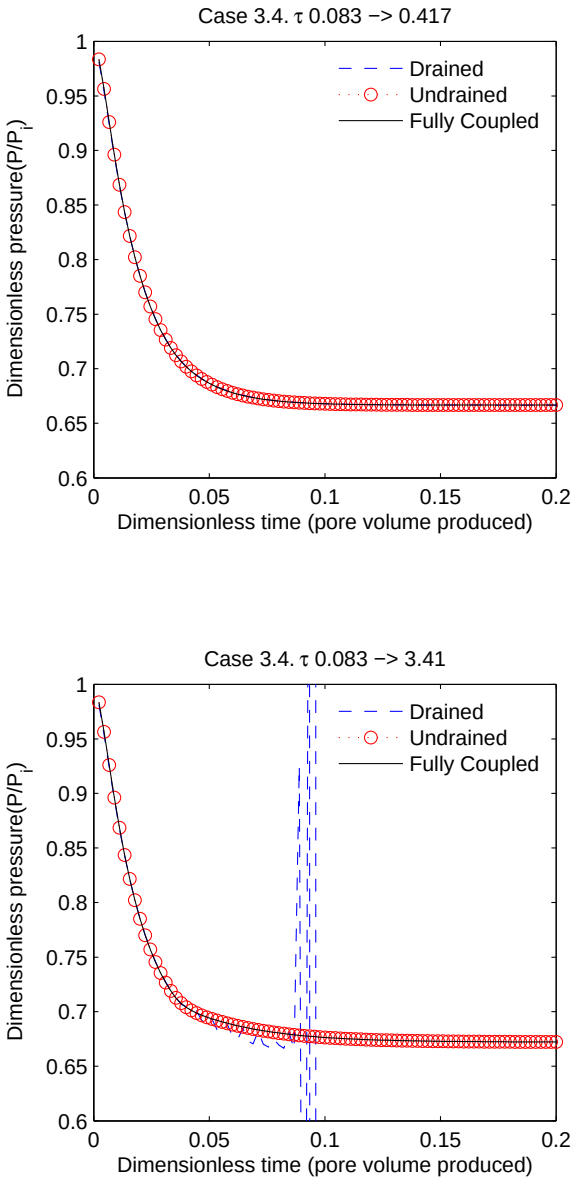

Figure 3.17: 1D problem with injection and production with the isotropic hardening (Case 3.4). Top: the drained split is stable in plastic regime, where $\tau = 0.417$. Bottom: the drained split is unstable in the plastic regime, where $\tau = 3.41$.

Case 3.5—Fluid production scenario in 2D with elastoplasticity

The dimensions of the domain are $50\ m \times 50\ m$ with 5×5 grid blocks under the plane strain mechanical conditions. The domain is homogeneous with an overburden $\bar{\sigma} = 2.125\ MPa$, side burden $\bar{\sigma_h} = 2.125\ MPa$ on both sides, and no-vertical and no-horizontal displacement boundary at the bottom. The bulk density of the porous medium is $\rho_b = 2400\ kg\ m^{-1}$. Initial fluid pressure is $P_i = 2.125\ MPa$. Fluid density and viscosity are $\rho_{f,0} = 1000\ kg\ m^{-1}$ and $\mu = 1.0\ cp$, respectively. Permeability is $k_p = 50\ md$, and porosity is $\phi_0 = 0.3$. Young's modulus is $E = 350\ MPa$, and Poisson's ratio is $\nu = 0.35$. The Biot coefficient is $b = 1.0$. For the modified Cam-clay model, the virgin compression index is $\lambda = 0.37$, the swell index is $\kappa = 0.054$, the critical state slope is $M_{mcc} = 1.4$, and the preconsolidation pressure is $p_{co,0} = -1.0\ MPa$, where tensile stress is positive. The production and observation wells are located at the center of the domain (3,3). The production rate is $Q_{prod} = 1000\ kg\ day^{-1}$. A no-flow boundary condition is applied to the domain. There is no gravity in the domain. The input parameters for Case 3.5 are listed in Table 3.4.

Figure 3.18 shows that the drained split is not stable in the plastic regime, even though it is stable in the elastic regime. This is because at around $t_d \approx 0.018$, we reach the plastic regime and the coupling strength increases beyond one. On the other hand, the undrained split is stable in the plastic regime. Note that there is a small difference between the undrained-split and the fully coupled results, and this is due to using a single iteration. As the figure indicates, when two iterations are used, the solution from the undrained split is quite close to the fully coupled results.

Staggered Newton schemes for Case 3.5

The staggered Newton method has the following solution procedure (Schrefler et al., 1997).

1. Linearize the flow and mechanical problems.

2. Given the linearized coupled system, solve the flow and mechanical problems in a sequential way.

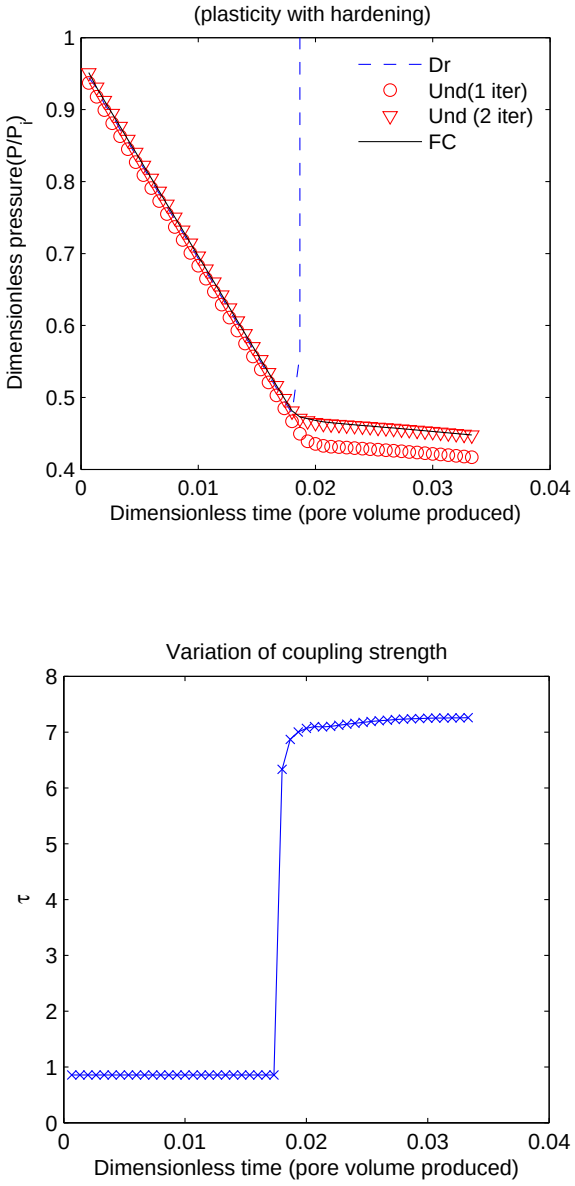

Figure 3.18: 2D problem with a production well (Case 3.5). Top: pressure history. Bottom: the history of the coupling strength. The model enters the plastic regime at $t_d \approx 0.018$. Beyond this point, the drained split becomes unstable and fails to produce a solution at all.

Table 3.4: Input data for Case 3.5

Property	Value
Permeability (k)	50 md
Porosity (ϕ_0)	0.3
Young modulus (E)	350 MPa
Poisson ratio (ν)	0.35
Biot coefficient (b)	1.0
Bulk density (ρ_b)	2400 $\mathrm{kg\,m^{-3}}$
Fluid density ($\rho_{f,0}$)	1000 $\mathrm{kg\,m^{-3}}$
Fluid viscosity (μ)	1.0 cp
Virgin compression index (λ)	0.37
Swell index (κ)	0.054
Critical state slope (M_{mcc})	1.4
Preconsolidation pressure ($p_{co,0}$)	-1.0 MPa
Initial pressure (p_0)	2.125 MPa
Side burden ($\bar{\sigma}_h$)	2.125 MPa
Overburden ($\bar{\sigma}$)	2.125 MPa
Grid spacing (Δx)	10 m
Grid spacing (Δz)	10 m
Grid	5×5

3. Perform a return mapping to determine the plastic internal variables and algorithmic tangent moduli.

4. Update the solutions and variables at the current iteration level, and reevaluate the residuals for flow and mechanics.

5. Take Steps 1–4 until the solutions are converged for a given tolerance.

Thus, we take full iterations in the staggered Newton method after linearization, whereas in the previous tests we take one iteration with the staggered method before linearization. Figure 3.19 shows that the drained split is stable during the early-time elastic regime, which has a weak coupling strength ($\tau < 1$). However, when plasticity is reached, the solution by the drained method is no longer stable because the coupling strength increases dramatically. It is clear that when the coupling strength increases beyond unity, the solution by the drained split becomes unstable (Figures 3.19). No solution by the drained split is possible after plasticity. On the other hand, the fully coupled and undrained methods provide stable

results well into the plastic regime, as shown in Figure 3.19.

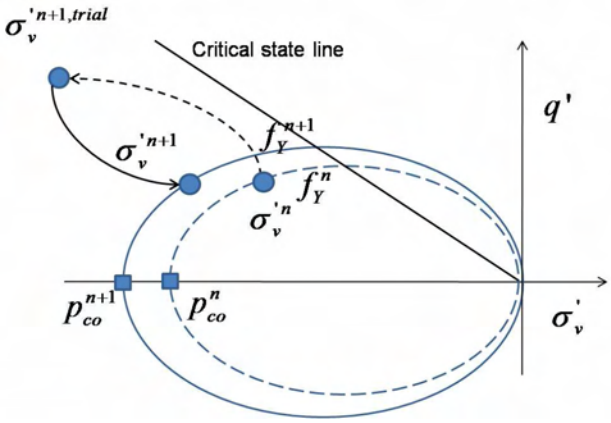

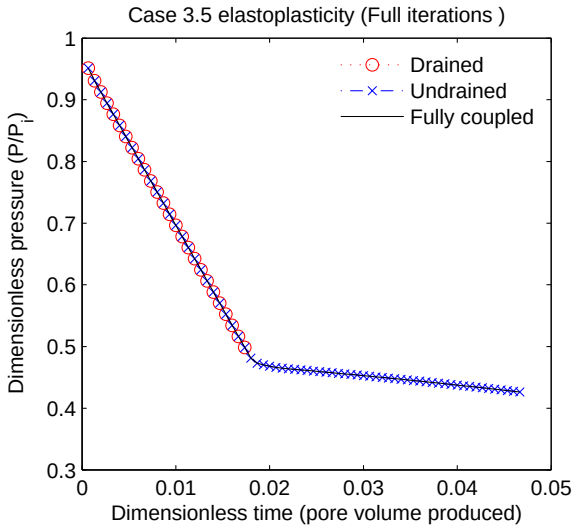

Figure 3.19: The evolution of the dimensionless pressure at the observation point vs. dimensionless time (pore volume produced) for Case 3.5 (2D production test in the elastoplastic regime). Top: schematic of the return mapping algorithm for the modified Cam-clay model. Bottom: numerical solutions using the fully coupled, drained, and undrained methods. The model enters the plastic regime at $t_d \approx 0.018$. Beyond this point, the drained split becomes unstable and fails to produce a solution at all.

Chapter 4

Convergence of the Drained and Undrained Splits

4.1 Error Estimation

Sequential implicit solution schemes for coupled geomechanics and flow entail solutions of two implicit problems, one for mechanics and one for flow, in sequence. In such schemes, one often performs a single pass or a few iterations, and it is crucial to assess the convergence behavior of the sequential coupling strategy. In this Chapter, two sequential schemes are investigated: the drained and undrained splits. The backward Euler time discretization is used, and the linear coupled problem is considered for simplicity. We employ matrix and spectral methods to analyze the behavior of the error as a function of iteration.

4.1.1 Error estimation of the drained split by matrix algebra

For a sequential solution strategy, we can write

$$\begin{aligned} \left\| \mathbf{e}_{ts}^{n+1,n_{iter}} \right\| &\leq \left\| \mathbf{x}_t^{n+1} - \mathbf{x}_f^{n+1} \right\| + \left\| \mathbf{x}_f^{n+1} - \mathbf{x}_s^{n+1,n_{iter}} \right\| \\ &= \mathbf{O}(\Delta t) + \left\| \mathbf{x}_f^{n+1} - \mathbf{x}_s^{n+1,n_{iter}} \right\|, \end{aligned} \tag{4.1}$$

where $\mathbf{e}_{ts}$ is the error between the true solution and the numerical solutions from the sequential method, and $\|\cdot\|$ is an appropriate norm (e.g., L^2 norm). $\mathbf{e}_{fs}^{n+1} = \mathbf{x}_f^{n+1} - \mathbf{x}_s^{n+1,n_{iter}}$ is the error between the fully coupled and sequential methods, n is the time step, and n_{iter} is the iteration number within a time step, and $\mathbf{x}_f^t = [\mathbf{u}^t,\ \mathbf{p}^t]$. The subscripts f and s (i.e., $(\cdot)_f$ and $(\cdot)_s$) denote the fully coupled and sequential methods, respectively, the subscript t (i.e., $(\cdot)_t$) denotes the true solution. If $\|\mathbf{e}_{fs}\|$ is $\mathbf{O}(\Delta t^m)$, where $m > 0$, the numerical scheme is convergent (Strikwerda, 2004). If $\|\mathbf{e}_{fs}\|$ is $\mathbf{O}(1)$, the numerical scheme is not convergent. In Appendix B.2, we show that $\left\|\mathbf{x}_t^{n+1} - \mathbf{x}_f^{n+1}\right\|$ has $\mathbf{O}(\Delta t)$ with the backward Euler time discretization.

For the fully coupled method, the algebraic form of the coupled problem is written as

$$\underbrace{\begin{bmatrix} \mathbf{K} & -\mathbf{L^t} \\ \mathbf{L} & \mathbf{F} \end{bmatrix}}_{\mathbf{A}} \begin{bmatrix} \mathbf{u} \\ \mathbf{p} \end{bmatrix}^{n+1} - \underbrace{\begin{bmatrix} \mathbf{0} & \mathbf{0} \\ \mathbf{L} & \mathbf{Q} \end{bmatrix}}_{\mathbf{B}} \begin{bmatrix} \mathbf{u} \\ \mathbf{p} \end{bmatrix}^{n} = \underbrace{\begin{bmatrix} \mathbf{f_u} \\ \mathbf{f_p} \end{bmatrix}}_{\mathbf{f}}^{n+1},$$

$$\mathbf{x} = \begin{bmatrix} \mathbf{u} \\ \mathbf{p} \end{bmatrix}, \quad \mathbf{F} = \mathbf{Q} + \Delta t \mathbf{T}, \tag{4.2}$$

where $\mathbf{K}$ is the stiffness matrix with the drained moduli, and $\mathbf{F}$ is composed of $\mathbf{Q}$ and $\mathbf{T}$ (Lewis and Schrefler, 1998). $\mathbf{Q}$ is the fluid compressibility matrix, which includes the Biot modulus, and $\mathbf{T}$ is the transmissibility matrix of the flow problem. $\mathbf{L}$ is associated with the coupling (Biot) coefficient. $\mathbf{u}$ and $\mathbf{p}$ are the displacement and pressure, respectively. The drained split decomposes the matrix $\mathbf{A}$ into

$$\begin{bmatrix} \mathbf{K} & \mathbf{0} \\ \mathbf{L} & \mathbf{F} \end{bmatrix} \begin{bmatrix} \mathbf{u} \\ \mathbf{p} \end{bmatrix}^{n+1,k+1} - \begin{bmatrix} \mathbf{0} & \mathbf{L}^t \\ \mathbf{0} & \mathbf{0} \end{bmatrix} \begin{bmatrix} \mathbf{u} \\ \mathbf{p} \end{bmatrix}^{n+1,k} - \begin{bmatrix} \mathbf{0} & \mathbf{0} \\ \mathbf{L} & \mathbf{Q} \end{bmatrix} \begin{bmatrix} \mathbf{u} \\ \mathbf{p} \end{bmatrix}^{n} = \begin{bmatrix} \mathbf{f_u} \\ \mathbf{f_p} \end{bmatrix}^{n+1}, \tag{4.3}$$

where k is the iteration index. From Equations 4.2 and 4.3, the errors of pressure and

displacement between the fully coupled method and drained split are written as

$$
\begin{aligned}
&\begin{bmatrix} \mathbf{e}_{fs,\mathbf{u}} \\ \mathbf{e}_{fs,\mathbf{p}} \end{bmatrix}^{n+1,k+1} \\
&= \begin{bmatrix} \mathbf{K} & \mathbf{0} \\ \mathbf{L} & \mathbf{F} \end{bmatrix}^{-1} \left(\begin{bmatrix} \mathbf{0} & \mathbf{L}^t \\ \mathbf{0} & \mathbf{0} \end{bmatrix} \begin{bmatrix} \mathbf{e}_{fs,\mathbf{u}} \\ \mathbf{e}_{fs,\mathbf{p}} \end{bmatrix}^{n+1,k} + \begin{bmatrix} \mathbf{0} & \mathbf{0} \\ \mathbf{L} & \mathbf{Q} \end{bmatrix} \begin{bmatrix} \mathbf{e}_{fs,\mathbf{u}} \\ \mathbf{e}_{fs,\mathbf{p}} \end{bmatrix}^{n} \right) \\
&= \begin{bmatrix} \mathbf{K}^{-1} & \mathbf{0} \\ -\mathbf{F}^{-1}\mathbf{L}\mathbf{K}^{-1} & \mathbf{F}^{-1} \end{bmatrix} \left(\begin{bmatrix} \mathbf{0} & \mathbf{L}^t \\ \mathbf{0} & \mathbf{0} \end{bmatrix} \begin{bmatrix} \mathbf{e}_{fs,\mathbf{u}} \\ \mathbf{e}_{fs,\mathbf{p}} \end{bmatrix}^{n+1,k} \right. \\
&\quad \left. + \begin{bmatrix} \mathbf{0} & \mathbf{0} \\ \mathbf{L} & \mathbf{Q} \end{bmatrix} \begin{bmatrix} \mathbf{e}_{fs,\mathbf{u}} \\ \mathbf{e}_{fs,\mathbf{p}} \end{bmatrix}^{n} \right) \\
&= \underbrace{\begin{bmatrix} \mathbf{0} & \mathbf{K}^{-1}\mathbf{L}^t \\ \mathbf{0} & -\mathbf{F}^{-1}\mathbf{L}\mathbf{K}^{-1}\mathbf{L}^t \end{bmatrix}}_{\mathbf{D}} \begin{bmatrix} \mathbf{e}_{fs,\mathbf{u}} \\ \mathbf{e}_{fs,\mathbf{p}} \end{bmatrix}^{n+1,k} + \underbrace{\begin{bmatrix} \mathbf{0} & \mathbf{0} \\ \mathbf{F}^{-1}\mathbf{L} & \mathbf{F}^{-1}\mathbf{Q} \end{bmatrix}}_{\mathbf{H}} \begin{bmatrix} \mathbf{e}_{fs,\mathbf{u}} \\ \mathbf{e}_{fs,\mathbf{p}} \end{bmatrix}^{n},
\end{aligned}
\tag{4.4}
$$

where $\mathbf{e}_{fs} = \begin{bmatrix} \mathbf{e}_{fs,\mathbf{u}} \\ \mathbf{e}_{fs,\mathbf{p}} \end{bmatrix}$, and $\mathbf{e}_{fs}^{n} = \mathbf{e}_{fs}^{n,n_{iter}}$. Then $\mathbf{e}_{fs}^{n+1,n_{iter}}$ can be written as

$$
\begin{aligned}
\mathbf{e}_{fs}^{n+1,n_{iter}} &= \mathbf{D}^{n_{iter}}\mathbf{e}^{n+1,0} + \sum_{l=1}^{n_{iter}} \mathbf{D}^{l-1}\mathbf{H}\mathbf{e}_{fs}^{n,n_{iter}} \\
&= \mathbf{D}^{n_{iter}}(\mathbf{x}_f^{n+1} - \mathbf{x}_f^{n}) + \underbrace{(\mathbf{D}^{n_{iter}} + \sum_{l=1}^{n_{iter}} \mathbf{D}^{l-1}\mathbf{H})}_{\mathbf{S}} \mathbf{e}_{fs}^{n,n_{iter}},
\end{aligned}
\tag{4.5}
$$

where $\mathbf{e}^{n+1,0}$ is written as $(\mathbf{x}_f^{n+1} - \mathbf{x}_f^{n}) + (\mathbf{x}_f^{n} - \mathbf{x}_s^{n,n_{iter}})$. By recursion, $\mathbf{e}^{n+1,n_{iter}}$ is expressed in terms of the initial error $\mathbf{e}_{fs}^{0,0}$, $\mathbf{D}^{n_{iter}}$, and $\mathbf{S}$ as

$$
\mathbf{e}_{fs}^{n+1,n_{iter}} = \sum_{l=0}^{n} \mathbf{D}^{n_{iter}}\mathbf{S}^{l}(\mathbf{x}_f^{n+1-l} - \mathbf{x}_f^{n-l}) + \mathbf{S}^{n+1}\mathbf{e}_{fs}^{0,0}. \tag{4.6}
$$

To achieve stability, we must have $\|\mathbf{S}\| \leq 1$ and $\|\mathbf{D}^{n_{iter}}\| \leq 1$ (Turska et al., 1994). For convergence analysis, we assume no initial error, such that $\mathbf{e}_{fs}^{0,0} = \left\|\mathbf{x}_f^0 - \mathbf{x}_s^{0,0}\right\| = 0$. By the triangular inequality

$$\begin{aligned}
\left\|\mathbf{e}_{fs}^{n+1,n_{iter}}\right\| &\leq \|\mathbf{D}^{n_{iter}}\| \sum_{l=0}^{n} \left\|\mathbf{x}_f^{n+1-l} - \mathbf{x}_f^{n-l}\right\| \\
&\leq \|\mathbf{D}^{n_{iter}}\| \sum_{l=0}^{n} M_1 \Delta t \\
&= \|\mathbf{D}^{n_{iter}}\| \, M_1 t_{n+1} \qquad (4.7) \\
&\quad (\because \ \mathbf{x}_f^{n+1} = \mathbf{x}_f^n + O(\Delta t) \text{ from the Taylor expansion}),
\end{aligned}$$

where M_1 is a positive constant independent of time step size, and t_n is the simulation time up to the nth time step. Thus, $\left\|\mathbf{e}_{fs}^{n+1,n_{iter}}\right\| = O(1)$ when $\|\mathbf{D}\| = O(1)$. As the time step size goes to zero, we have

$$\lim_{\Delta t \to 0} \|\mathbf{D}\| \neq 0.$$

which yields $\|\mathbf{D}\| = O(1)$ in Equation 4.4. Non-convergence of the drained split for a fixed number of iterations was originally anticipated by Turska et al. (1994). They pointed out that $\|\mathbf{D}\| = O(1)$ implies non-convergence, whereas $\|\mathbf{D}\| = O(\Delta t)$ shows convergence.

$\|\mathbf{D}\| = O(1)$ is also obtained from the error amplification factor as shown in the next section. Thus, the drained split with a fixed iteration number is not convergent. In particular, the drained split can show severe non-convergence problems as $\|\mathbf{D}\|$ approaches one, which is the stability limit of the drained split.

Remark 4.1. Turska et al. (1994) and Turska and Schrefler (1993) indicate that $\|\mathbf{D}\| \leq 1$ for convergence of sequential methods during iterations and $\|\mathbf{S}\| \leq 1$ for stability of sequential methods. Here, we define convergence as global convergence of a numerical solution, and stability as the condition for bounding the numerical errors. Hence, we require

that $\|\mathbf{D}\| \leq 1$ and $\|\mathbf{S}\| \leq 1$ for stability, and $\lim_{\Delta t \to 0} \|\mathbf{D}\| = 0$ for convergence.

4.1.2 Error estimation of the undrained split by matrix algebra

In the undrained split, the matrix $\mathbf{A}$ of Equation 4.2 is decomposed into

$$\begin{bmatrix} \mathbf{K} + \mathbf{L}^t\mathbf{Q}^{-1}\mathbf{L} & \mathbf{0} \\ \mathbf{L} & \mathbf{F} \end{bmatrix} \begin{bmatrix} \mathbf{u} \\ \mathbf{p} \end{bmatrix}^{n+1,k+1} - \begin{bmatrix} \mathbf{L}^t\mathbf{Q}^{-1}\mathbf{L} & \mathbf{L}^t \\ \mathbf{0} & \mathbf{0} \end{bmatrix} \begin{bmatrix} \mathbf{u} \\ \mathbf{p} \end{bmatrix}^{n+1,k} - \begin{bmatrix} \mathbf{0} & \mathbf{0} \\ \mathbf{L} & \mathbf{Q} \end{bmatrix} \begin{bmatrix} \mathbf{u} \\ \mathbf{p} \end{bmatrix}^{n} = \begin{bmatrix} \mathbf{f_u} \\ \mathbf{f_p} \end{bmatrix}^{n+1}. \tag{4.8}$$

Let $\mathbf{K}_{ud} = \mathbf{K} + \mathbf{L}^t\mathbf{Q}^{-1}\mathbf{L}$. Then the errors can be expressed as

$$\begin{aligned}
&\begin{bmatrix} \mathbf{e}_{fs,\mathbf{u}} \\ \mathbf{e}_{fs,\mathbf{p}} \end{bmatrix}^{n+1,k+1} \\
&= \begin{bmatrix} \mathbf{K}_{ud} & \mathbf{0} \\ \mathbf{L} & \mathbf{F} \end{bmatrix}^{-1} \left(\begin{bmatrix} \mathbf{L}^t\mathbf{Q}^{-1}\mathbf{L} & \mathbf{L}^t \\ \mathbf{0} & \mathbf{0} \end{bmatrix} \begin{bmatrix} \mathbf{e}_{fs,\mathbf{u}} \\ \mathbf{e}_{fs,\mathbf{p}} \end{bmatrix}^{n+1,k} + \begin{bmatrix} \mathbf{0} & \mathbf{0} \\ \mathbf{L} & \mathbf{Q} \end{bmatrix} \begin{bmatrix} \mathbf{e}_{fs,\mathbf{u}} \\ \mathbf{e}_{fs,\mathbf{p}} \end{bmatrix}^{n} \right) \\
&= \begin{bmatrix} \mathbf{K}_{ud}^{-1} & \mathbf{0} \\ -\mathbf{F}^{-1}\mathbf{L}\mathbf{K}_{ud}^{-1} & \mathbf{F}^{-1} \end{bmatrix} \left(\begin{bmatrix} \mathbf{L}^t\mathbf{Q}^{-1}\mathbf{L} & \mathbf{L}^t \\ \mathbf{0} & \mathbf{0} \end{bmatrix} \begin{bmatrix} \mathbf{e}_{fs,\mathbf{u}} \\ \mathbf{e}_{fs,\mathbf{p}} \end{bmatrix}^{n+1,k} \right. \\
&\quad \left. + \begin{bmatrix} \mathbf{0} & \mathbf{0} \\ \mathbf{L} & \mathbf{Q} \end{bmatrix} \begin{bmatrix} \mathbf{e}_{fs,\mathbf{u}} \\ \mathbf{e}_{fs,\mathbf{p}} \end{bmatrix}^{n} \right) \\
&= \underbrace{\begin{bmatrix} \mathbf{K}_{ud}^{-1}\mathbf{L}^t\mathbf{Q}^{-1}\mathbf{L} & \mathbf{K}_{ud}^{-1}\mathbf{L}^t \\ -\mathbf{F}^{-1}\mathbf{L}\mathbf{K}_{ud}^{-1}\mathbf{L}^t\mathbf{Q}^{-1}\mathbf{L} & -\mathbf{F}^{-1}\mathbf{L}\mathbf{K}_{ud}^{-1}\mathbf{L}^t \end{bmatrix}}_{\mathbf{D}_{ud}} \begin{bmatrix} \mathbf{e}_{fs,\mathbf{u}} \\ \mathbf{e}_{fs,\mathbf{p}} \end{bmatrix}^{n+1,k} \\
&\quad + \begin{bmatrix} \mathbf{0} & \mathbf{0} \\ \mathbf{F}^{-1}\mathbf{L} & \mathbf{F}^{-1}\mathbf{Q} \end{bmatrix} \begin{bmatrix} \mathbf{e}_{fs,\mathbf{u}} \\ \mathbf{e}_{fs,\mathbf{p}} \end{bmatrix}^{n}.
\end{aligned} \tag{4.9}$$

From the first row of Equation 4.9, we have

$$\begin{aligned}\mathbf{e}_{fs,\mathbf{u}}^{n+1,k+1} &= \mathbf{K}_{ud}^{-1}\mathbf{L}^t\mathbf{Q}^{-1}\mathbf{L}\mathbf{e}_{fs,\mathbf{u}}^{n+1,k} + \mathbf{K}_{ud}^{-1}\mathbf{L}^t\mathbf{e}_{fs,\mathbf{p}}^{n+1,k} \\ &= \mathbf{K}_{ud}^{-1}\mathbf{L}^t(\mathbf{Q}^{-1}\mathbf{L}\mathbf{e}_{fs,\mathbf{u}}^{n+1,k} + \mathbf{e}_{fs,\mathbf{p}}^{n+1,k}). \end{aligned} \tag{4.10}$$

$\mathbf{F}^{-1}\mathbf{L}$ times the first row of Equation 4.9 plus the second row of Equation 4.9 yields

$$\mathbf{F}^{-1}\mathbf{L}\mathbf{e}_{fs,\mathbf{u}}^{n+1,k+1} + \mathbf{e}_{fs,\mathbf{p}}^{n+1,k+1} = \mathbf{F}^{-1}\mathbf{L}\mathbf{e}_{fs,\mathbf{u}}^{n} + \mathbf{F}^{-1}\mathbf{Q}\mathbf{e}_{fs,\mathbf{p}}^{n}. \tag{4.11}$$

Note that $\mathbf{F} \to \mathbf{Q}$ as $\Delta t \to 0$ since $\lim_{\Delta t \to 0} \{\Delta t \mathbf{T}\} = \mathbf{0}$ in Equations 4.2. Using Equations 4.10 and 4.11, the pressure error, $\mathbf{e}_{fs,\mathbf{p}}$, becomes

$$\begin{aligned}&\lim_{\Delta t \to 0} \mathbf{e}_{fs,\mathbf{p}}^{n+1,k+1} \\ &= \lim_{\Delta t \to 0} \left(-\mathbf{F}^{-1}\mathbf{L}\mathbf{e}_{fs,\mathbf{u}}^{n+1,k+1} + \mathbf{F}^{-1}\mathbf{L}\mathbf{e}_{fs,\mathbf{u}}^{n} + \mathbf{F}^{-1}\mathbf{Q}\mathbf{e}_{fs,\mathbf{p}}^{n}\right) \quad \text{(from Equation 4.11)} \\ &= -\mathbf{Q}^{-1}\mathbf{L}\underbrace{\mathbf{K}_{ud}^{-1}\mathbf{L}^t(\mathbf{Q}^{-1}\mathbf{L}\mathbf{e}_{fs,\mathbf{u}}^{n} + \mathbf{Q}^{-1}\mathbf{Q}\mathbf{e}_{fs,\mathbf{p}}^{n})}_{\text{from Equation 4.10}} + \mathbf{Q}^{-1}\mathbf{L}\mathbf{e}_{fs,\mathbf{u}}^{n} + \mathbf{Q}^{-1}\mathbf{Q}\mathbf{e}_{fs,\mathbf{p}}^{n} \\ &= (\mathbf{I} - \mathbf{Q}^{-1}\mathbf{L}\mathbf{K}_{ud}^{-1}\mathbf{L}^t)(\mathbf{Q}^{-1}\mathbf{L}\mathbf{e}_{fs,\mathbf{u}}^{n} + \mathbf{e}_{fs,\mathbf{p}}^{n}). \end{aligned} \tag{4.12}$$

As the time step size is refined to zero, Equation 4.11 yields

$$\lim_{\Delta t \to 0} \left(\mathbf{F}^{-1}\mathbf{L}\mathbf{e}_{fs,\mathbf{u}}^{n+1,k+1} + \mathbf{e}_{fs,\mathbf{p}}^{n+1,k+1}\right) = \mathbf{Q}^{-1}\mathbf{L}\mathbf{e}_{fs,\mathbf{u}}^{n} + \mathbf{e}_{fs,\mathbf{p}}^{n}. \tag{4.13}$$

From Equation 4.13, the displacement error, $\mathbf{e}_{fs,\mathbf{u}}$, in Equation 4.10, using $\lim_{\Delta t \to 0} \mathbf{F} = \mathbf{Q}$, becomes

$$\begin{aligned}\lim_{\Delta t \to 0} \mathbf{e}_{fs,\mathbf{u}}^{n+1,k+1} &= \lim_{\Delta t \to 0} \mathbf{K}_{ud}^{-1}\mathbf{L}^t(\mathbf{Q}^{-1}\mathbf{L}\mathbf{e}_{fs,\mathbf{u}}^{n+1,k} + \mathbf{e}_{fs,\mathbf{p}}^{n+1,k}) \\ &= \mathbf{K}_{ud}^{-1}\mathbf{L}^t(\mathbf{Q}^{-1}\mathbf{L}\mathbf{e}_{fs,\mathbf{u}}^{n} + \mathbf{e}_{fs,\mathbf{p}}^{n}). \end{aligned} \tag{4.14}$$

Then, from Equations 4.12 and 4.14, the displacement and pressure errors become

$$\begin{bmatrix} \mathbf{e}_{fs,\mathbf{u}} \\ \mathbf{e}_{fs,\mathbf{p}} \end{bmatrix}^{n+1,k+1} \xrightarrow{\Delta t \to 0} \underbrace{\begin{bmatrix} \mathbf{K}_{ud}^{-1}\mathbf{L}^t\mathbf{Q}^{-1}\mathbf{L} & \mathbf{K}_{ud}^{-1}\mathbf{L}^t \\ (\mathbf{I}-\mathbf{Q}^{-1}\mathbf{L}\mathbf{K}_{ud}^{-1}\mathbf{L}^t)\mathbf{Q}^{-1}\mathbf{L} & \mathbf{I}-\mathbf{Q}^{-1}\mathbf{L}\mathbf{K}_{ud}^{-1}\mathbf{L}^t \end{bmatrix}}_{\mathbf{E}_{ud}} \begin{bmatrix} \mathbf{e}_{fs,\mathbf{u}} \\ \mathbf{e}_{fs,\mathbf{p}} \end{bmatrix}^{n}. \tag{4.15}$$

By recursion and the assumption $\mathbf{e}_{fs}^{0,0} = 0$, $\mathbf{e}_{fs}^{n+1,n_{iter}}$, we can write

$$\lim_{\Delta t \to 0} \left\| \mathbf{e}_{fs}^{n+1,n_{iter}} \right\| = \left\| \mathbf{E}_{ud}\mathbf{e}_{fs}^{n,n_{iter}} \right\| \leq \|\mathbf{E}_{ud}\|^n \left\| \mathbf{e}_{fs}^{0} \right\| = 0. \tag{4.16}$$

Equation 4.16 implies that the undrained split yields convergence as the time step size is refined. Therefore, the undrained split is convergent with a fixed iteration number. We can also show convergence of the undrained split if $\|\mathbf{D}_{ud}\| = O(\Delta t)$, since $\|\mathbf{D}_{ud}\|$ corresponds to $\|\mathbf{D}\|$ in Equation 4.7. The next section investigates $\|\mathbf{D}_{ud}\|$ by spectral analysis. These results are easy to explain. As the time step size goes to zero the physical system approaches the undrained condition, and the undrained split converges to the fully coupled method regardless of how many iterations are taken.

Remark 4.2. Convergence of the undrained split is restricted to a (slightly) compressible system (i.e., compressible fluid or solid grains). When both the fluid and solid grains are incompressible, $\mathbf{Q} = \mathbf{0}$. As a result, $\mathbf{K}_{ud}^{-1}$ does not exist, and Equation 4.16 is not valid for incompressible systems.

4.2 Spectral Analysis

The matrix algebra approach is generic to analyze convergence, but it provides less sharp information for the order of accuracy. In the previous sections, $\|\mathbf{D}\|$ and $\|\mathbf{D}_{ud}\|$ are the key parameters for convergence. In order to investigate $\|\mathbf{D}\|$ and $\|\mathbf{D}_{ud}\|$ further, we perform analysis of the error amplification for one-dimensional problems based on the finite-volume

and finite-element methods adopted for flow and mechanics, respectively. The error estimates can be extended to multiple dimensions because the coupling between flow and mechanics is based on the volumetric response, which is a scalar quantity.

In the fully coupled method with the backward Euler time discretization, we have

$$-(\frac{K_{dr}}{h}U^{n+1}_{j-\frac{3}{2}} - 2\frac{K_{dr}}{h}U^{n+1}_{j-\frac{1}{2}} + \frac{K_{dr}}{h}U^{n+1}_{j+\frac{1}{2}}) - b(P^{n+1}_{j-1} - P^{n+1}_{j}) = 0, \tag{4.17}$$

$$\begin{aligned}&\frac{h}{M}\frac{P^{n+1}_j - P^n_j}{\Delta t} + \frac{bh}{\Delta t}[(-\frac{U^{n+1}_{j-\frac{1}{2}} - U^{n+1}_{j+\frac{1}{2}}}{h}) + (\frac{U^n_{j-\frac{1}{2}} - U^n_{j+\frac{1}{2}}}{h})]\\ &-\frac{k_p}{\mu h}\left(P^{n+1}_{j+1} - 2P^{n+1}_j + P^{n+1}_{j-1}\right) = 0,\end{aligned} \tag{4.18}$$

where k_p denotes permeability.

4.2.1 Error amplification of the drained split

The drained split treats the pressure term P^{n+1} in Equation 4.17 explicitly as $P^{n+1,k}$, which is obtained from the previous iteration (k^{th}) step. The other variables in Equations 4.17 and 4.18 are treated implicitly as $U^{n+1,k+1}$ and $P^{n+1,k+1}$, which are unknown at the present $(k+1)^{th}$ step. Then the discretized equations for flow and mechanics by the drained split are written as

$$\begin{aligned}&-\left(\frac{K_{dr}}{h}U^{n+1,k+1}_{j-\frac{3}{2}} - 2\frac{K_{dr}}{h}U^{n+1,k+1}_{j-\frac{1}{2}} + \frac{K_{dr}}{h}U^{n+1,k+1}_{j+\frac{1}{2}}\right)\\ &-b(P^{n+1,k}_{j-1} - P^{n+1,k}_{j}) = 0,\end{aligned} \tag{4.19}$$

$$\begin{aligned}&\frac{h}{M}\frac{P^{n+1,k+1}_j - P^n_j}{\Delta t} + \frac{bh}{\Delta t}[(-\frac{U^{n+1,k+1}_{j-\frac{1}{2}} - U^{n+1,k+1}_{j+\frac{1}{2}}}{h}) + (\frac{U^n_{j-\frac{1}{2}} - U^n_{j+\frac{1}{2}}}{h})]\\ &-\frac{k_p}{\mu h}\left(P^{n+1,k+1}_{j+1} - 2P^{n+1,k+1}_j + P^{n+1,k+1}_{j-1}\right) = 0.\end{aligned} \tag{4.20}$$

Let $e^k_u = U^{n+1} - U^{n+1,k}$ and $e^k_P = P^{n+1} - P^{n+1,k}$, where U^{n+1} and P^{n+1} are the solutions

from the fully coupled method, and $U^{n+1,k}$ and $P^{n+1,k}$ are those from the sequential methods at the kth iteration step. Let $e_P^{n,n_{iter}}$ and $e_U^{n,n_{iter}}$ be the difference between the solutions from the fully coupled and sequential methods at t_n for pressure and displacement, respectively. Subtracting Equations 4.19 and 4.20 from Equations 4.17 and 4.18, respectively, gives

$$-\frac{K_{dr}}{h}e_{U_{j-\frac{3}{2}}}^{k+1} + 2\frac{K_{dr}}{h}e_{U_{j-\frac{1}{2}}}^{k+1} - \frac{K_{dr}}{h}e_{U_{j+\frac{1}{2}}}^{k+1} - b(e_{P_{j-1}}^{k} - e_{P_j}^{k}) = 0, \tag{4.21}$$

$$\begin{aligned}&\frac{h}{M}\frac{e_{P_j}^{k+1}}{\Delta t} + b\frac{h}{\Delta t}(-\frac{e_{U_{j-\frac{1}{2}}}^{k+1} - e_{U_{j+\frac{1}{2}}}^{k+1}}{h}) - \frac{k_p}{\mu}\frac{1}{h}(e_{P_{j+1}}^{k+1} - 2e_{P_j}^{k+1} + e_{P_{j-1}}^{k+1})\\ &-\frac{h}{M}\frac{e_{P_j}^{n,n_{iter}}}{\Delta t} - b\frac{h}{\Delta t}(-\frac{e_{U_{j-\frac{1}{2}}}^{n,n_{iter}} - e_{U_{j+\frac{1}{2}}}^{n,n_{iter}}}{h}) = 0.\end{aligned} \tag{4.22}$$

We set $e_P^{n,n_{iter}}$ and $e_U^{n,n_{iter}}$ to zero in order to investigate $\|\mathbf{D}\|$ in Equation 4.4 only. This implies that we drop the second term in Equation 4.4. Introducing errors of the form $e_{U_j}^k = \gamma_e^k e^{i(j)\theta}\hat{e_U}$ and $e_{P_j}^k = \gamma_e^k e^{i(j)\theta}\hat{e_P}$, where γ_e is the amplification factor of error, $e^{(\cdot)} = \exp(\cdot)$, $i = \sqrt{-1}$, and $\theta \in [-\pi, \pi]$, we obtain from Equations 4.21 and 4.22

$$\underbrace{\begin{bmatrix} \frac{K_{dr}}{h}2\gamma_e(1-\cos\theta) & b2i\sin\frac{\theta}{2} \\ b\gamma_e 2i\sin\frac{\theta}{2} & [\frac{1}{M}h + \frac{k_p\Delta t}{\mu}\frac{1}{h}2(1-\cos\theta)]\gamma_e \end{bmatrix}}_{\mathbf{B_{dr}}} \begin{bmatrix} \hat{e_U^k} \\ \hat{e_P^k} \end{bmatrix} = \begin{bmatrix} 0 \\ 0 \end{bmatrix}. \tag{4.23}$$

Since the matrix $\mathbf{B_{dr}}$ is required to be singular (i.e., $\det \mathbf{B_{dr}} = 0$), this leads to

$$\gamma_e = 0,\ -\frac{b^2}{K_{dr}\left(\frac{1}{M} + \chi 2(1-\cos\theta)\right)},\quad \chi = \frac{k_p\Delta t}{\mu h^2}. \tag{4.24}$$

The γ_e is equivalent to the eigenvalue of the error amplification matrix $\mathbf{G}$ defined by

$$\begin{bmatrix} e_{U_j}^{k+1} \\ e_{P_j}^{k+1} \end{bmatrix} = \mathbf{G}\begin{bmatrix} e_{U_j}^{k} \\ e_{P_j}^{k} \end{bmatrix}. \tag{4.25}$$

The two γ_e's in Equation 4.24 are distinct, then $\mathbf{G}$ can be decomposed as $\mathbf{G} = \mathbf{P\Lambda P^{-1}}$

(Strang, 1988), where $\Lambda = \text{diag}\{\gamma_{e,1}, \gamma_{e,2}\}$ and $\mathbf{P}$ is an invertible matrix. When a fixed iteration number, $k = n_{iter}$, is used, the error estimate of the drained split is

$$\left\| \mathbf{e}_{fs}^{n+1,n_{iter}} \right\| \leq (max|\gamma_e|)^{n_{iter}} \left\| \mathbf{e}_{fs}^{n+1,0} \right\|, \tag{4.26}$$

where $\mathbf{e}_{fs}^{n+1,0} = \mathbf{x}_f^{n+1} - \mathbf{x}_s^{n,n_{iter}}$. Thus, $(max|\gamma_e|)$ is equivalent to $\|\mathbf{D}\|$.

Remark 4.3. From Equation 4.7, $\mathbf{e}_{fs}^{n,n_{iter}}$ does not disappear even though Δt approaches zero, because $(max|\gamma_e|)^{n_{iter}}$ does not approach zero (i.e., $O(1)$). Thus, the drained split with a fixed number of iterations is not convergent. Non-convergence of the drained split becomes severe when $max|\gamma_e|$ approaches one, which is also the same as the stability limit.

Remark 4.4. $\|\mathbf{D}\|$ is less than one if $max|\gamma_e| \leq 1$ for all θ, which yields the stability condition of the drained split during iterations. In order to have $max|\gamma_e| \leq 1$ for all θ in Equation 4.24, the stability condition is $\tau = b^2 M/K_{dr} \leq 1$, where τ is the coupling strength. This stability condition has been obtained by the Von Neumann method in Chapter 3.

4.2.2 Comparison with the coupled flow and dynamics

The governing equations of the coupled flow and dynamics are given, for example, in Armero and Simo (1992) as

$$\text{Div}\,\boldsymbol{\sigma} + \rho_b \boldsymbol{g} = \rho_b \ddot{\mathbf{u}}, \tag{4.27}$$

$$\dot{m} + \text{Div}\,\boldsymbol{w} = \rho_{f,0} f, \tag{4.28}$$

where $\ddot{()}$ is the second-order time derivative. Denote $\dot{\mathbf{u}}$ by $\mathbf{v}_k$, which is the rate of the solid skeleton displacement. Then, Equations 4.27 and 4.28 can be expressed as

$$\dot{\xi} = \mathcal{A}\xi + \mathbf{s}, \tag{4.29}$$

where

$$\xi = \begin{pmatrix} \mathbf{u} \\ \mathbf{v}_k \\ p \end{pmatrix}, \quad \mathcal{A}\xi = \begin{pmatrix} \mathbf{v}_k \\ \frac{1}{\rho_b}\operatorname{Div}(\mathbf{C}_{dr} : \boldsymbol{\varepsilon} - bp\mathbf{1}) \\ M \operatorname{Div} \frac{\boldsymbol{k}_p}{\mu} \mathbf{Grad}\, p - bM\, \mathbf{Grad}^s\, \mathbf{v}_k : \mathbf{1} \end{pmatrix},$$

$$\mathbf{s} = \begin{pmatrix} 0 \\ \frac{1}{\rho_b} \operatorname{Div} bp_0\mathbf{1} + \boldsymbol{g} \\ -M \operatorname{Div} \frac{\boldsymbol{k}}{\mu}\rho_f \boldsymbol{g} + f \end{pmatrix}. \tag{4.30}$$

When we discretize Equation 4.29 in one dimension, assuming a linear homogeneous equation with homogeneous boundary conditions, we obtain

$$U^{n+1}_{j-\frac{1}{2}} - U^n_{j-\frac{1}{2}} = \Delta t V^{n+1}_{j-\frac{1}{2}}, \tag{4.31}$$

$$V^{n+1}_{j-\frac{1}{2}} - V^n_{j-\frac{1}{2}} = \frac{\Delta t K_{dr}}{\rho_b h^2}\left(U^{n+1}_{j-\frac{3}{2}} - 2U^{n+1}_{j-\frac{1}{2}} + U^{n+1}_{j+\frac{1}{2}}\right) + \frac{\Delta t b}{\rho_b h}\left(P^{n+1}_{j-1} - P^{n+1}_j\right) \tag{4.32}$$

$$P^{n+1}_j - P^n_j = \frac{\Delta t M k_p}{\mu h^2}\left(P^{n+1}_{j-1} - 2P^{n+1}_j + P^{n+1}_{j+1}\right) + \frac{\Delta t M b}{h}\left(V^{n+1}_{j-\frac{1}{2}} - V^{n+1}_{j+\frac{1}{2}}\right), \tag{4.33}$$

where $V = \dot{U}$, and we use the finite-volume method for flow and finite-element method for mechanics for space discretization, and the backward Euler method for time discretization. Then, applying the fully coupled and drained split methods to Equations 4.31, 4.32, and 4.33 and following the same procedure of the previous section, we obtain the following error equations

$$e^{k+1}_{U_{j-\frac{1}{2}}} = \Delta t e^{k+1}_{V_{j-\frac{1}{2}}}, \tag{4.34}$$

$$e^{k+1}_{V_{j-\frac{1}{2}}} = \frac{\Delta t K_{dr}}{\rho_b h^2}\left(e^{k+1}_{U_{j-\frac{3}{2}}} - 2e^{k+1}_{U_{j-\frac{1}{2}}} + e^{k+1}_{U_{j+\frac{1}{2}}}\right) + \frac{\Delta t b}{\rho_b h}\left(e^k_{P_{j-1}} - e^k_{P_j}\right) \tag{4.35}$$

$$e^{k+1}_{P_j} = \frac{\Delta t M k_p}{\mu h^2}\left(e^{k+1}_{P_{j-1}} - 2e^{k+1}_{P_j} + e^{k+1}_{P_{j+1}}\right) + \frac{\Delta t M b}{h}\left(e^{k+1}_{V_{j-\frac{1}{2}}} - e^{k+1}_{V_{j+\frac{1}{2}}}\right), \tag{4.36}$$

where $e^k_V = V^{n+1} - V^{n+1,k}$, and we assume the difference between the solutions from the fully coupled and sequential methods at t_n to be zero, as in the previous section. Introducing

errors of the form $e^k_{U_j} = \gamma^k_e e^{i(j)\theta} e\hat{}_U$, $e^k_{V_j} = \gamma^k_e e^{i(j)\theta} e\hat{}_V$, and $e^k_{P_j} = \gamma^k_e e^{i(j)\theta} e\hat{}_P$, we obtain

$$\underbrace{\begin{bmatrix} \gamma_e & -\Delta t\gamma_e & 0 \\ \frac{\Delta t K_{dr}}{\rho_b h^2} 2(1-\cos\theta)\gamma_e & \gamma_e & \frac{\Delta t b}{\rho_b h} 2i \sin\frac{\theta}{2} \\ 0 & \frac{\Delta t M b}{h} 2i \sin\frac{\theta}{2}\gamma_e & \gamma_e + \frac{\Delta t M k_p}{\mu h^2} 2(1-\cos\theta)\gamma_e \end{bmatrix}}_{\mathbf{B^*_{dr}}} \begin{bmatrix} e\hat{}_U \\ e\hat{}_V \\ e\hat{}_P \end{bmatrix} = \begin{bmatrix} 0 \\ 0 \\ 0 \end{bmatrix}. \tag{4.37}$$

From $\det(\mathbf{B^*_{dr}}) = 0$, the error amplification factors of the coupled flow and dynamics for the drained split are given by

$$\gamma_e = 0, \quad -\frac{\frac{\Delta t^2 M b^2}{\rho_b h^2} 2(1-\cos\theta)}{\left(1 + \frac{\Delta t^2 K_{dr}}{\rho_b h^2} 2(1-\cos\theta)\right)\left(1 + \frac{\Delta t M k_p}{\mu h^2} 2(1-\cos\theta)\right)}. \tag{4.38}$$

Equation 4.38 indicates that

$$\lim_{\Delta t \to 0} max\,|\gamma_e| = 0. \tag{4.39}$$

When we follow a similar procedure for the drained split in coupled flow and statics (Equations 4.5 – 4.7) and add $\mathbf{v}_k$ to the unknowns, convergence is obtained for the drained split of the coupled flow and dynamics from Equations 4.1 and 4.39 because $\lim_{\Delta t \to 0} \left\| \mathbf{e}^{n+1}_{fs} \right\| = 0$. As explained by Armero and Simo (1992), when we use the staggered method (i.e., one iteration), convergence and first-order accuracy can be directly estimated by Lie's formula (Chorin et al., 1978; Lapidus, 1981), written as

$$\lim_{n \to \infty} \left[\exp(\mathcal{A}_1 t/n)\exp(\mathcal{A}_2 t/n)\right]^n = \exp\left[(\mathcal{A}_1 + \mathcal{A}_2)t\right], \tag{4.40}$$

because Equation 4.29 is split by the drained split as

$$\dot{\xi} = \mathcal{A}_1 \xi + \mathbf{s}_1, \;\; \dot{\xi} = \mathcal{A}_2 \xi + \mathbf{s}_2, \tag{4.41}$$

where

$$\mathcal{A}_1\xi = \begin{pmatrix} \mathbf{v}_k \\ \frac{1}{\rho_b}\,\mathrm{Div}(\mathbf{C}_{dr} : \boldsymbol{\varepsilon} - bp\mathbf{1}) \\ 0 \end{pmatrix}, \quad \mathbf{s}_1 = \begin{pmatrix} 0 \\ \frac{1}{\rho_b}\,\mathrm{Div}\, bp_0\mathbf{1} + \boldsymbol{g} \\ 0 \end{pmatrix}, \tag{4.42}$$

$$\mathcal{A}_2\xi = \begin{pmatrix} 0 \\ 0 \\ M\,\mathrm{Div}\,\frac{\boldsymbol{k}_p}{\mu}\,\mathbf{Grad}\,p - bM\,\mathbf{Grad}^s\,\mathbf{v}_k : \mathbf{1} \end{pmatrix}, \tag{4.43}$$

$$\mathbf{s}_2 = \begin{pmatrix} 0 \\ 0 \\ -M\,\mathrm{Div}\,\frac{\boldsymbol{k}_p}{\mu}\rho_f\boldsymbol{g} + f \end{pmatrix}. \tag{4.44}$$

Equation 4.40 implies that the product formula of the operator splitting converges to the original operator as the time step size goes to zero. Thus, the drained split of the coupled flow and dynamics is convergent, whereas the drained split of the coupled flow and statics is not convergent, especially close to the stability limit.

Remark 4.5. Similar to coupled flow and statics in Remark 4.4, $max|\gamma_e| \leq 1$ for all θ in Equation 4.38 provides a necessary condition for stability in the coupled flow and dynamics. Consider the undrained limit corresponding to $k_p = 0$ in order to compare with the stability estimate of thermoelasticity in Armero and Simo (1992). Then, the stability condition becomes (see Appendix B.2)

$$\left\{2a_s\frac{\Delta t}{h}\right\}^2(\tau - 1) \leq 1, \tag{4.45}$$

where $a_s^2 = \frac{K_{dr}}{\rho_b}$, and a_s is the speed of sound (Hughes, 1987). Equation 4.45 has a similar form to that of Armero and Simo (1992). The slight difference between the two is due to the different space and time discretization. In contrast to coupled flow and statics, we

obtain dependence on the time step size for stability of the drained split in coupled flow and dynamics. From Equation 4.45, $\tau \leq 1$ can only provide stability as the mechanical problem approaches the elliptic limit (i.e., $\rho_b \to 0$, which yields $a_s \to \infty$), which is identical to the stability condition of coupled flow and statics. Furthermore, since one of the error amplification factors is negative, we may observe oscillations during iterations for the drained split in coupled flow and dynamics.

Remark 4.6. Even when both the fluid and solid grains are incompressible, $\lim_{\Delta t \to 0} max\,|\gamma_e| = 0$. Hence, in contrast to coupled flow and statics, refining the time step size can recover stability and first-order accuracy for an incompressible problem, implying convergence.

4.2.3 Error amplification of the undrained split

The undrained split solves the mechanical problem while freezing fluid mass content for each grid block. Then Equation 4.19 is replaced by

$$\begin{aligned} &-\frac{K_{ud}}{h}(U^{n+1,k+1}_{j-\frac{3}{2}} - 2U^{n+1,k+1}_{j-\frac{1}{2}} + U^{n+1,k+1}_{j+\frac{1}{2}}) + \frac{b^2 M}{h}(U^{n+1,k}_{j-\frac{3}{2}} - 2U^{n+1,k}_{j-\frac{1}{2}} + U^{n+1,k}_{j+\frac{1}{2}}) \\ &-b(P^{n+1,k}_{j-1} - P^{n+1,k}_{j}) = 0\,, \end{aligned} \tag{4.46}$$

where $K_{ud} = K_{dr} + b^2 M$. The flow equation of the undrained split is the same as Equation 4.20. Subtracting Equation 4.46 from Equation 4.17, we obtain

$$\begin{aligned} &-\frac{K_{ud}}{h}(e^{k+1}_{U_{j-\frac{3}{2}}} - 2e^{k+1}_{U_{j-\frac{1}{2}}} + e^{k+1}_{U_{j+\frac{1}{2}}}) + \frac{b^2 M}{h}(e^{k}_{U_{j-\frac{3}{2}}} - 2e^{k}_{U_{j-\frac{1}{2}}} + e^{k}_{U_{j+\frac{1}{2}}}) \\ &-b(e^{k}_{P_{j-1}} - e^{k}_{P_j}) = 0. \end{aligned} \tag{4.47}$$

The error equation for flow is the same as Equation 4.22. Introducing errors of the form

$e^k_{U_j} = \gamma_e^k e^{i(j)\theta} \hat{e_U}$ and $e^k_{P_j} = \gamma_e^k e^{i(j)\theta} \hat{e_P}$, Equations 4.47 and 4.22 yield

$$\underbrace{\begin{bmatrix} (\frac{K_{dr}+b^2M}{h}\gamma_e - \frac{b^2M}{h})2(1-\cos\theta) & b2i\sin\frac{\theta}{2} \\ b\gamma_e 2i\sin\frac{\theta}{2} & [\frac{1}{M}h + \frac{k_p\Delta t}{\mu}\frac{1}{h}2(1-\cos\theta)]\gamma_e \end{bmatrix}}_{\mathbf{B_{ud}}} \begin{bmatrix} \hat{e^k_U} \\ \hat{e^k_P} \end{bmatrix} = \begin{bmatrix} 0 \\ 0 \end{bmatrix}. \tag{4.48}$$

From $\det \mathbf{B_{ud}} = 0$, the error amplification factors of the undrained split are obtained as

$$\gamma_e = 0, \ \frac{b^2\chi M 2(1-\cos\theta)}{(K_{dr}+b^2M)\left(\frac{1}{M}+2\chi(1-\cos\theta)\right)}. \tag{4.49}$$

From Equation 4.49, when Δt is refined, $max\,|\gamma_e|$ approaches zero. Since $\|\mathbf{D}_{ud}\| = max\,|\gamma_e|$, $\mathbf{e}^n_{fs}$ disappears when the time step size is refined even though a fixed iteration number is used, including one iteration. Hence, the undrained split is convergent with a fixed number of iterations for a compressible system, yielding first-order accuracy.

Remark 4.7. We obtain first-order accuracy for the undrained split only for a compressible system. From Equation 4.49, if the fluid and solid grains become incompressible, we have $M \to \infty$ and $max\,|\gamma_e| = 1$ regardless of time step size. Thus, we expect severe reductions of accuracy if the system is incompressible ($M = \infty$), or nearly incompressible ($M \approx \infty$).

Remark 4.8. The undrained split is always stable during iterations, since $max\,|\gamma_e| \leq 1$ and γ_e's are distinct. Global unconditional stability is rigorously shown in Chapter 3.

4.3 Convergence Rate with Full Iterations

Solutions of sequential methods become the same as the fully coupled method when full iterations are performed if the solutions are stable and convergent during iterations. Then, the next question is which sequential method is more efficient in terms of the rate of convergence when full iterations are performed. The error amplification factors, shown in Equations 4.24

and 4.49, are appropriate tools for estimating the rate of convergence: Smaller magnitudes indicate faster rates of convergence (Schrefler et al., 1997).

The top and bottom plots of Figure 4.1 show the error amplification factors from Equations 4.24 and 4.49, respectively, for a coupling strength τ of 0.05. The absolute value of the error amplification factor of the drained split, $|\gamma_{e,dr}|$, decreases with respect to χ in Equation 4.24, where χ is pressure diffusivity. Hence, high (pressure) diffusive conditions (e.g., high permeability and large time step size) are favorable to the drained split in terms of the rate of convergence. However, $|\gamma_{e,ud}|$ of the undrained split increases with respect to χ, which implies that the undrained split can show better rates of convergence under less (pressure) diffusive conditions (e.g., low permeability and small time step size). Figure 4.2 shows the difference between the magnitude of the two amplification factors, $|\gamma_{e,ud}| - |\gamma_{e,dr}|$. When the difference is negative, the undrained split shows a better rate of convergence compared with the drained split. On the other hand, when the difference is positive, the drained split shows better rates of convergence. From Figure 4.2, it is anticipated that the drained split can be faster than the undrained split for high χ, but the undrained split can be faster than the drained split for low χ.

4.4 Numerical Examples

4.4.1 Convergence behavior for a fixed number of iterations

We introduce two test cases in order to study the error propagation of the fully coupled, drained, and undrained methods. Cases 4.1 and 4.2 are one and two dimensional consolidation problems.

Case 4.1 One-dimensional consolidation problem in a linear poroelastic medium, the Terzaghi problem (the left picture in Figure 4.3).

Case 4.2 Two-dimensional consolidation problem in a linear poroelastic medium (the right picture in Figure 4.3).

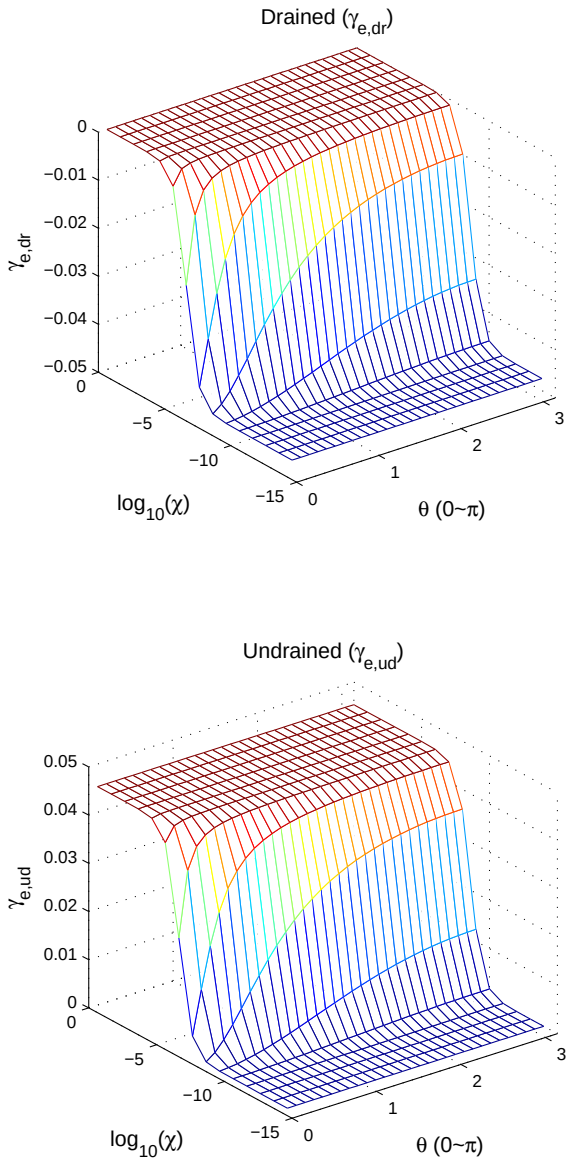

Figure 4.1: The distribution of the error amplification factors of the drained (top) and undrained (bottom) splits with respect to pressure diffusivity χ and frequency. The coupling strength τ is 0.05.

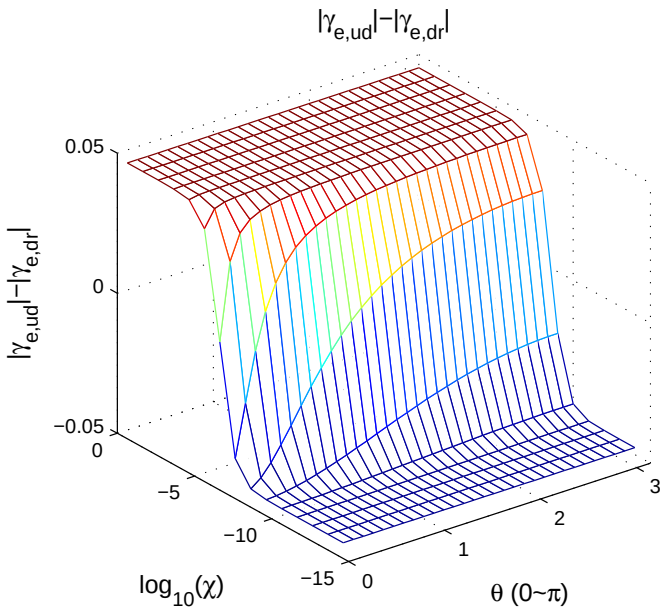

Figure 4.2: The difference of the magnitude of the error amplification factors between the drained and undrained splits.

The true (reference) solutions are computed using the fully coupled method with very small time step sizes to minimize the temporal error. For space discretization, we employ the finite-volume and finite-element methods for flow and mechanics, respectively. The analytical solution is available for Case 1. The reference solution matches the analytical solution within tight error tolerances.

Case 4.1—The Terzaghi problem

We reuse Case 3.1 in Chapter 3. The coupling strength τ is 0.95 where $c_f = 3.5 \times 10^{-8} Pa^{-1}$. The other data are the same as those for Case 3.1.

For Case 3.1, Figure 4.4 illustrates the errors between the true and numerical solutions from the drained, undrained, and fully coupled methods with respect to time step size when a fixed number of iterations is performed. The errors of dimensionless pressure and displacement are measured by the L^2 norm. The undrained and fully coupled methods are convergent when a staggered method is used. As the time step size is refined, the errors

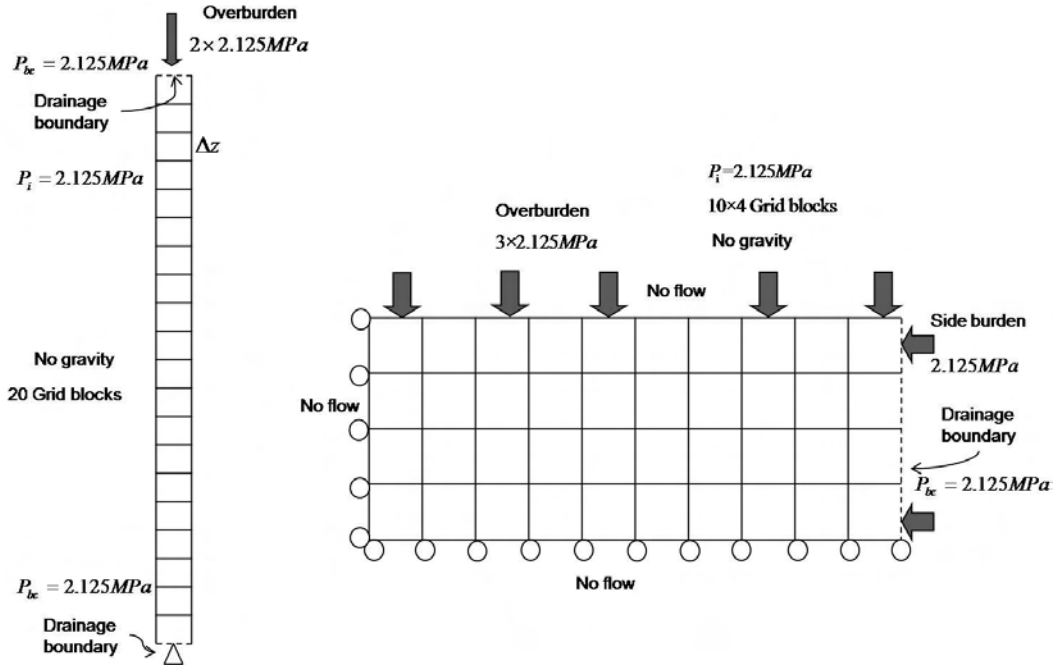

Figure 4.3: Case 4.1: the Terzaghi problem in one dimension (left). Case 4.2: the consolidation problem in two dimensions (right).

decrease as $O(\Delta t)$. This confirms that the undrained and fully coupled methods have $O(\Delta t)$ accuracy in time. However, the drained split does not show convergence. In particular, one iteration of the drained split yields zeroth-order accuracy, which supports the a-priori error estimate. Figures 4.5 and 4.6 show the spatial distributions of pressure and displacement by the drained and undrained splits, respectively. As the time step size is refined, the drained split with one iteration does not converge to the true solution, but to a different solution, even though the distributions of pressure and displacement look plausible. On the other hand, the undrained spit with one iteration converges to the true solution. When even iteration numbers are used, the drained split shows better convergence in time, whereas odd iteration numbers show less accurate solutions.

Figure 4.7 shows a comparison between taking more iterations for a fixed time step and refining the time step size under the same computational cost for the drained split. Performing more iterations is a better strategy for the drained split than refining the time

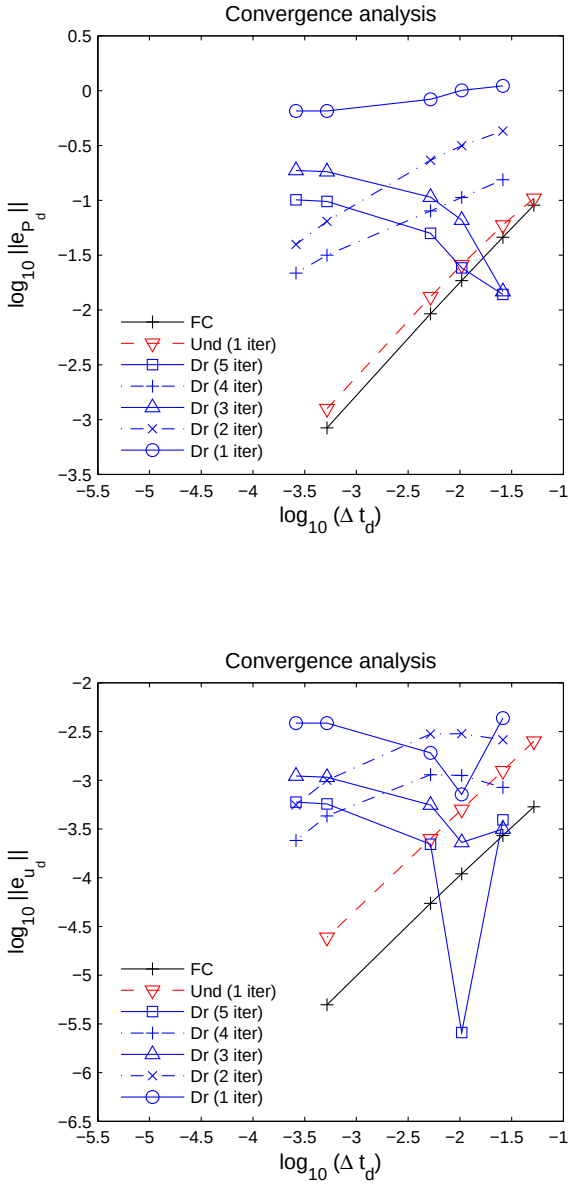

Figure 4.4: Convergence analysis of Case 4.1: pressure (top) and displacement (bottom). The coupling strength $\tau = b^2 M/K_{dr}$, is 0.95. FC, Dr, and Und indicate the fully coupled, drained split, and undrained split methods, respectively. $\Delta t_d = 4c_v \Delta t/(L_z)^2$

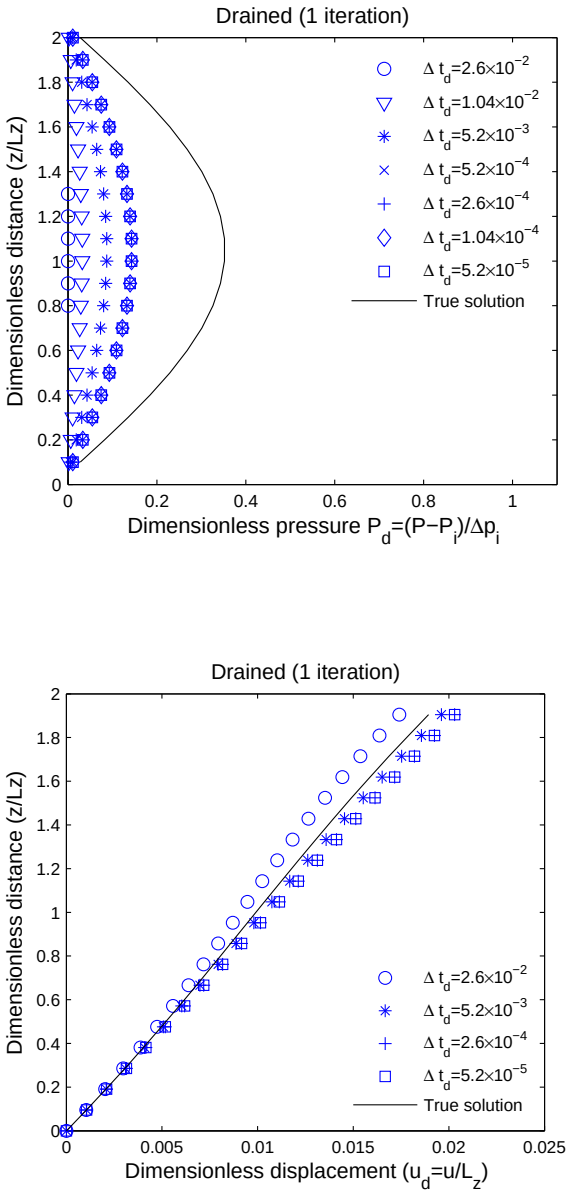

Figure 4.5: Non-convergence of the drained split with one iteration for Case 4.1: pressure (top) and displacement (bottom).

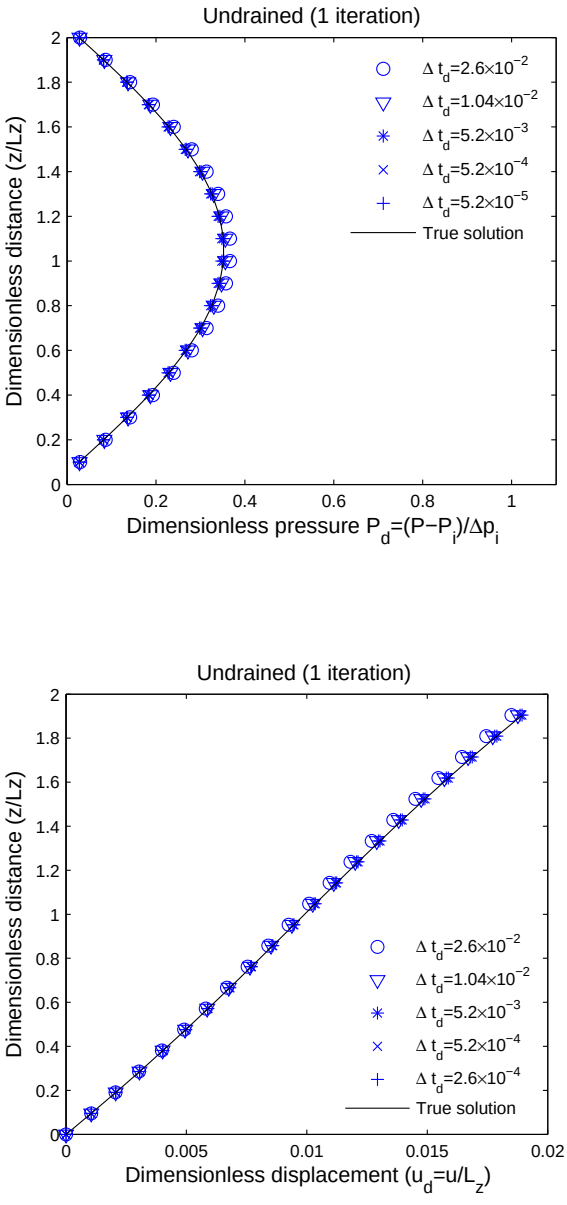

Figure 4.6: Convergence of the undrained split with one iteration for Case 4.1: pressure (top) and displacement (bottom).

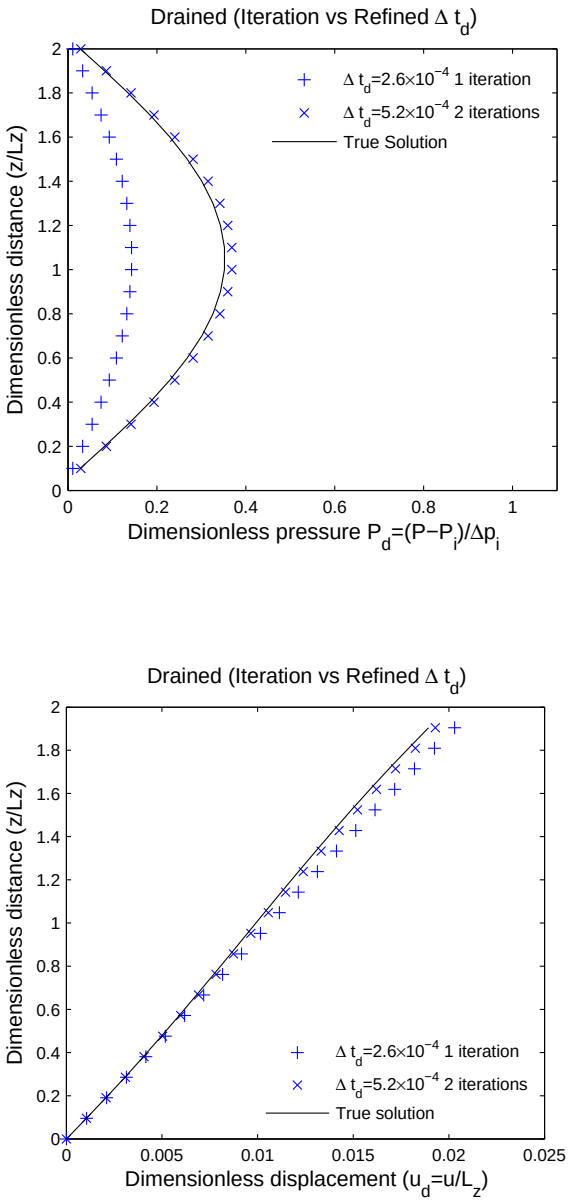

Figure 4.7: Comparison between more iterations and refined time step size in the drained split for Case 4.1: pressure (top) and displacement (bottom). The coupling strength is close to one ($\tau = 0.95$).

step size, showing improved convergence. However, from Figure 4.4, the undrained split yields better accuracy when the time step size is refined than when more iterations are performed. Hence, refining the time step size is a better strategy for the undrained split than performing more iterations for a given time step size.

Non-convergence of the undrained split

From Equation 4.49, we expect convergence problems of the undrained split if a system is incompressible, or nearly incompressible. In Figure 4.8, we observe zeroth order accuracy for pressure and displacement for the nearly incompressible fluid, $c_f = 3.5 \times 10^{-13} Pa^{-1}$. Figure 4.9 shows clearly that the solutions by the undrained split do not converge to the true solutions. Non-convergence of the undrained split becomes severe when the fluid is incompressible, $c_f \cong 0$. Figure 4.10 shows zeroth-order accuracy for pressure and displacement as well. In Figure 4.11, there is no change in both pressure and displacement. So, we have no change in the volumetric strain, ε_v, when we solve the mechanical problem because the undrained bulk modulus is infinite due to the incompressible fluid. Thus, there is no update of the volumetric strain in the flow problem, resulting in no pressure changes. So, we cannot solve the coupled problem because the flow and mechanical problems are not communicating properly.

Case 4.2—Two-dimensional consolidation problem

Case 4.2 is an example of two-dimensional consolidation, where the coupling strength approaches one ($\tau \approx 1 < 1$ where $c_f = 2.30 \times 10^{-9} Pa^{-1}$). The dimension of the domain is $20\ m \times 0.02\ m$ with 10×4 grid blocks under the plane strain mechanical condition. The domain is homogeneous with an overburden $\bar{\sigma} = 3 \times 2.125\ MPa$ at the top, no horizontal displacement boundary on the left side, the side burden $\bar{\sigma_h} = 2.125\ MPa$ on the right side, and no vertical displacement boundary at the bottom. The bulk density of the porous medium is $\rho_b = 2400\ kg\ m^{-1}$. Initial fluid pressure is $P_i = 2.125\ MPa$. Fluid density and viscosity are $\rho_{f,0} = 1000\ kg\ m^{-1}$ and $\mu = 1.0\ cp$, respectively. Permeability is $k_p = 5\ md$, and porosity is $\phi_0 = 0.3$. Young's modulus is $E = 2.9\ GPa$, and Poisson's ratio is $\nu = 0$.

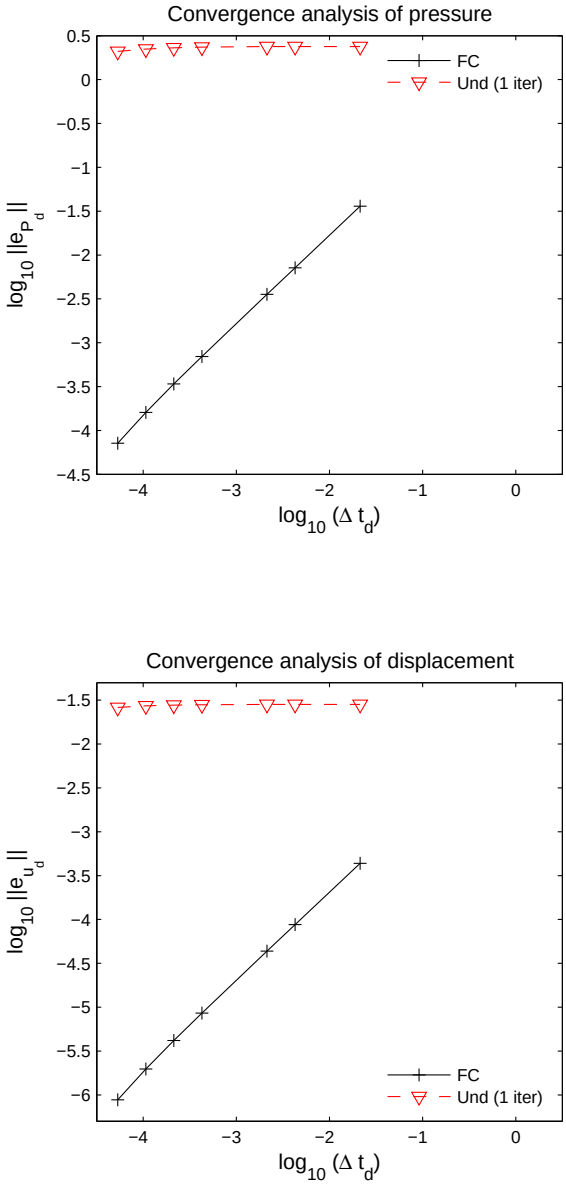

Figure 4.8: Convergence analysis of pressure (top) and displacement (bottom) for a nearly incompressible fluid, where $\tau = 9.5 \times 10^4$ and $c_f = 3.5 \times 10^{-13} Pa^{-1}$. The staggered method is used. The undrained split is not convergent, showing almost zeroth-order accuracy. The fully coupled method shows first-order accuracy.

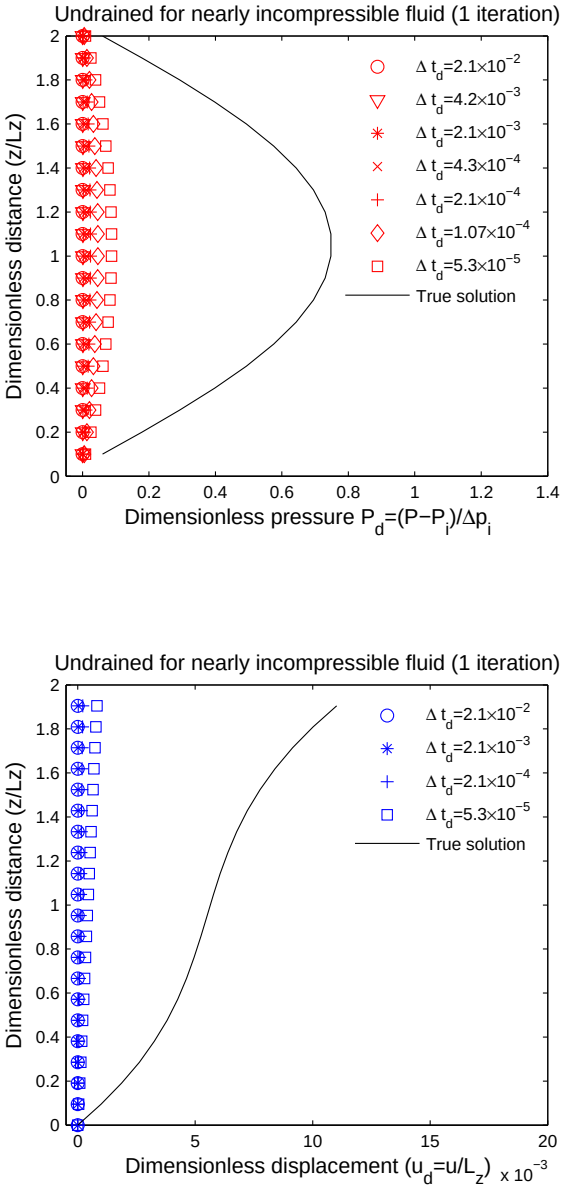

Figure 4.9: Spatial distributions of pressure (top) and displacement (bottom) for a nearly incompressible fluid. The undrained split produces large errors, not converging to the true solutions.

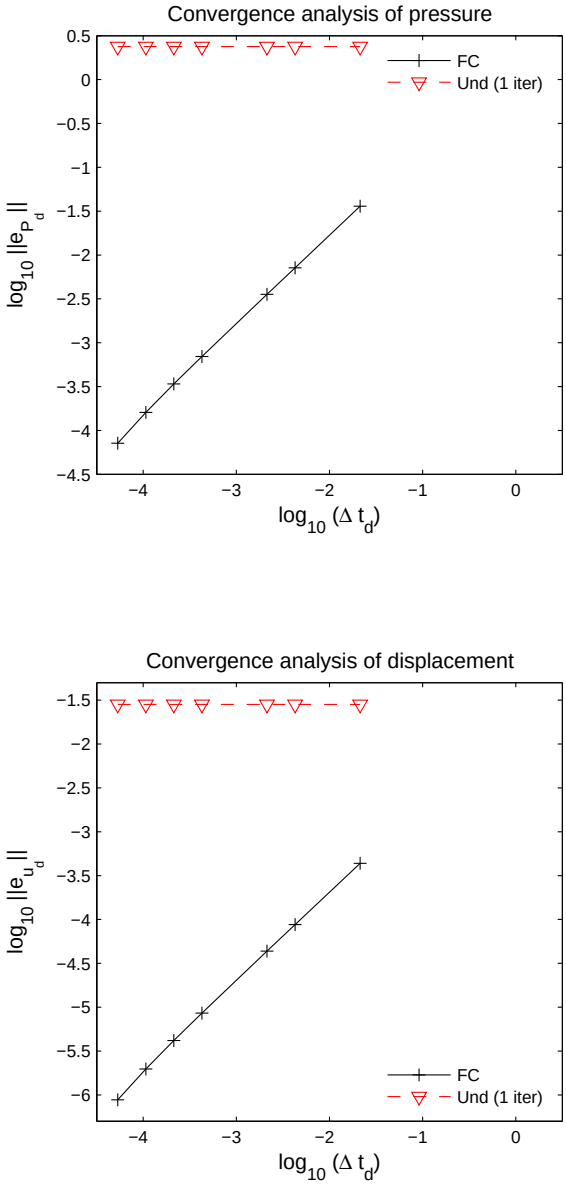

Figure 4.10: Convergence analysis of pressure (top) and displacement (bottom) for an incompressible fluid, where $\tau = 9.5 \times 10^{11} \cong \infty$ and $c_f = 3.5 \times 10^{-20} Pa^{-1} \cong 0$. The undrained split is not convergent, showing zeroth-order accuracy. But, the fully coupled method shows first-order accuracy.

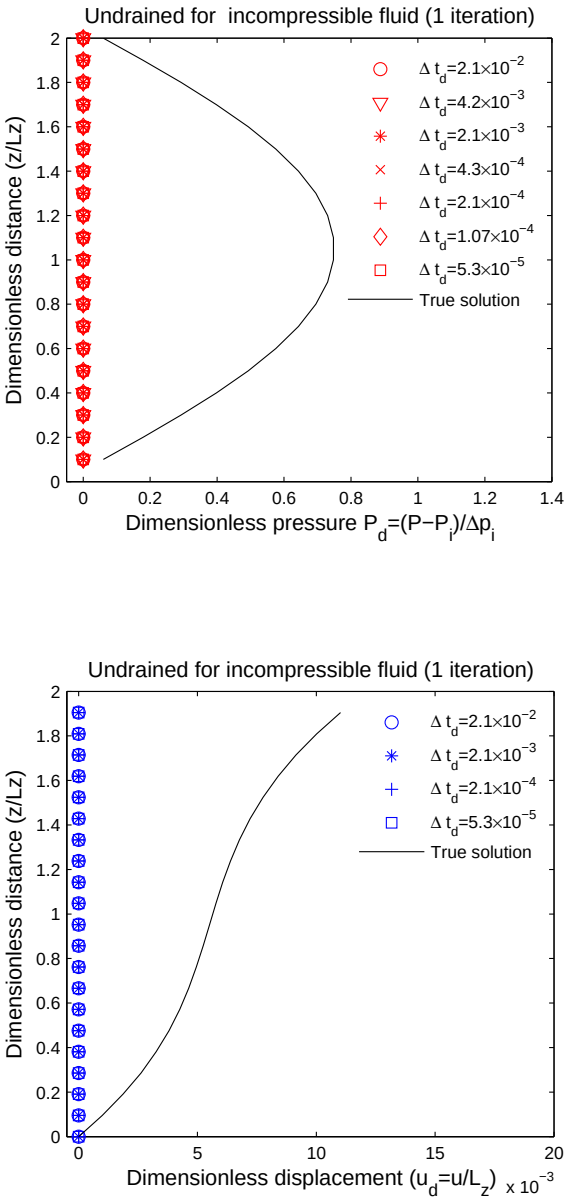

Figure 4.11: Spatial distributions of pressure (top) and displacement (bottom) for an incompressible fluid. The undrained split does not converge to the true solutions. There is no pressure jump and displacement by the overburden at early time.

The Biot coefficient is $b = 1.0$. We have a drainage boundary for flow on the right side where the boundary fluid pressure is $P_{bc} = 2.125\ MPa$. No-flow boundary conditions are applied at the left side, top, and bottom, and there is no gravity. The input data are also listed in Table 4.1.

Table 4.1: Input data for Case 4.2

Property	Value
Porosity (ϕ_0)	0.3
Young modulus (E)	2.9 GPa
Poisson ratio (ν)	0.0
Biot coefficient (b)	1.0
Bulk density (ρ_b)	2400 kg m^{-3}
Fluid density ($\rho_{f,0}$)	1000 kg m^{-3}
Permeability (k)	5 md
Initial pressure (P_i)	2.125 MPa
Overburden ($\bar{\sigma}$)	3×2.125 MPa
Side burden ($\bar{\sigma_h}$)	2.125 MPa
Boundary pressure (P_{bc})	2.125 MPa
Grid spacing (Δx)	2 m
Grid spacing (Δz)	0.005 m
Grid	10×4

Since the layer is very thin, the fluid flows mainly along the horizontal direction. Figure 4.12 shows the convergence behaviors of the drained and undrained splits for Case 4.2 when one iteration is performed. The drained split shows zeroth order accuracy in time, but the undrained split shows first-order accuracy ($O(\Delta t)$). Non-convergence of the drained split can be clearly identified in Figure 4.13, showing the distributions of pressure (the top figure) and horizontal displacement (the bottom figure) of the top layer. The solutions by the drained split with one iteration do not converge to the true solutions showing significant errors even though the distributions look plausible. Thus, refining the time step size cannot improve the accuracy of the solutions by the drained split with one iteration. In contrast, performing iterations for a fixed time step size improves the accuracy. Figure 4.14 compares a large time step size with more iterations ($\Delta t_d = 2.06 \times 10^{-3}$, 10 iterations) with a small time step size and one iteration ($\Delta t_d = 2.06 \times 10^{-4}$, one iteration). The two simulations

have the same computational cost. $\Delta t_d = 2.06 \times 10^{-3}$ with 10 iterations provides higher accuracy matching the true solutions compared with $\Delta t_d = 2.06 \times 10^{-4}$ with one iteration. In the undrained split, Figure 4.15 shows that the results with one iteration converge to the true solutions.

4.4.2 Convergence rate with full iterations

We reuse Cases 4.1 and 4.2 to study the rate of convergence with full iterations. For Case 4.1, Figure 4.16 shows the variation of the maximum absolute values of the residuals with respect to the number of iterations under low (the top figure) and high (the bottom figure) pressure diffusion conditions. The coupling strength τ is 0.95, where $c_f = 3.5 \times 10^{-8} Pa^{-1}$. As shown in Figure 4.16, the drained split yields a fast convergence rate for the large time step size $\Delta t = 0.1$ day and high permeability $k_p = 50000$ md (the bottom figure). But, the undrained split shows better rate of convergence for the small time step size $\Delta t = 0.01$ day and low permeability $k_p = 500$ md (the top figure). These results support the a-priori estimates from Equations 4.24 and 4.49. Furthermore, the estimates and numerical results for the drained split support the observation in Schrefler et al. (1997) that large time step size can reduce the spectral norm of the error amplification matrix for the drained split when used in a staggered Newton scheme.

In Case 4.2, the coupling strength τ is 0.77 with $c_f = 3.0 \times 10^{-9} Pa^{-1}$. We perform two tests with low and high diffusion of pressure. For low pressure diffusion (i.e. low χ), the permeability and time step size are $k_p = 5$ md and $\Delta t = 5 \times 10^{-4}$ day, respectively. Figure 4.17 (the top figure) shows that the rate of convergence for the undrained split is faster than the drained split in the case of low pressure diffusion. In contrast, the bottom in Figure 4.17 shows that the rate of convergence for the drained split is faster than the undrained split when pressure is highly diffusive, where the permeability and time step size are $k_p = 500$ md and $\Delta t = 0.01$ day, respectively.

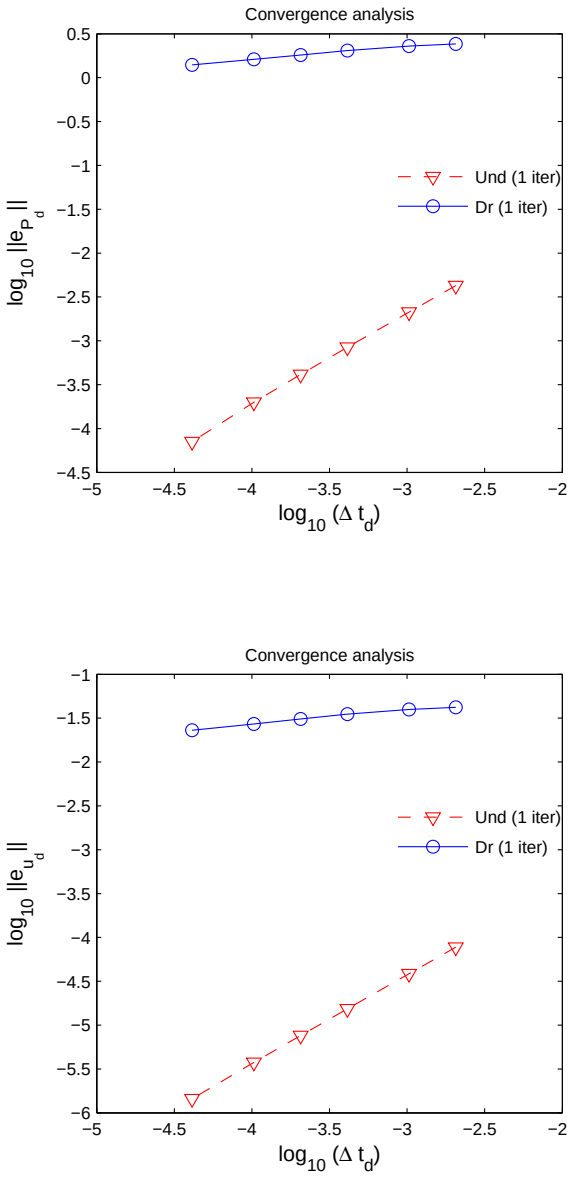

Figure 4.12: Convergence analysis of Case 4.2 on pressure (top) and displacement (bottom). $P_d = P/P_i$, $\mathbf{u}_d = \mathbf{u}/\sqrt{L_x L_z}$, and $\Delta t_d = 4\Delta t c_v / L_x^2$, where c_v is the consolidation coefficient along the horizontal direction (Abousleiman et al., 1996).

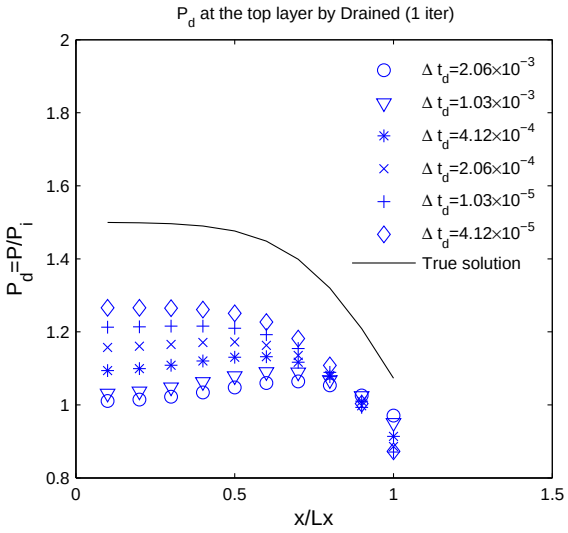

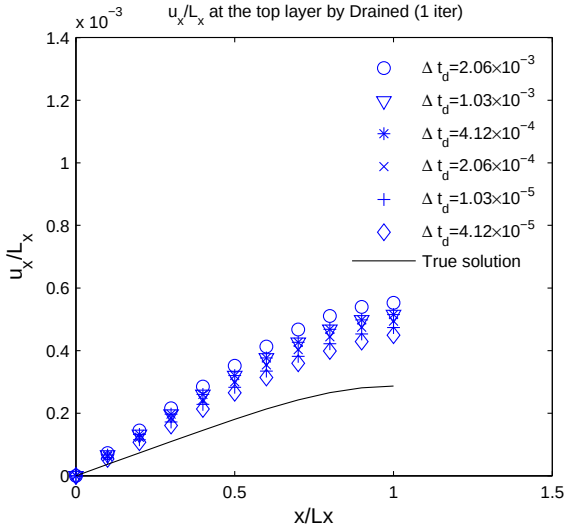

Figure 4.13: Non-convergence of the drained split with one iteration for Case 4.2: pressure (top) and displacement (bottom). u_x is the horizontal displacement.

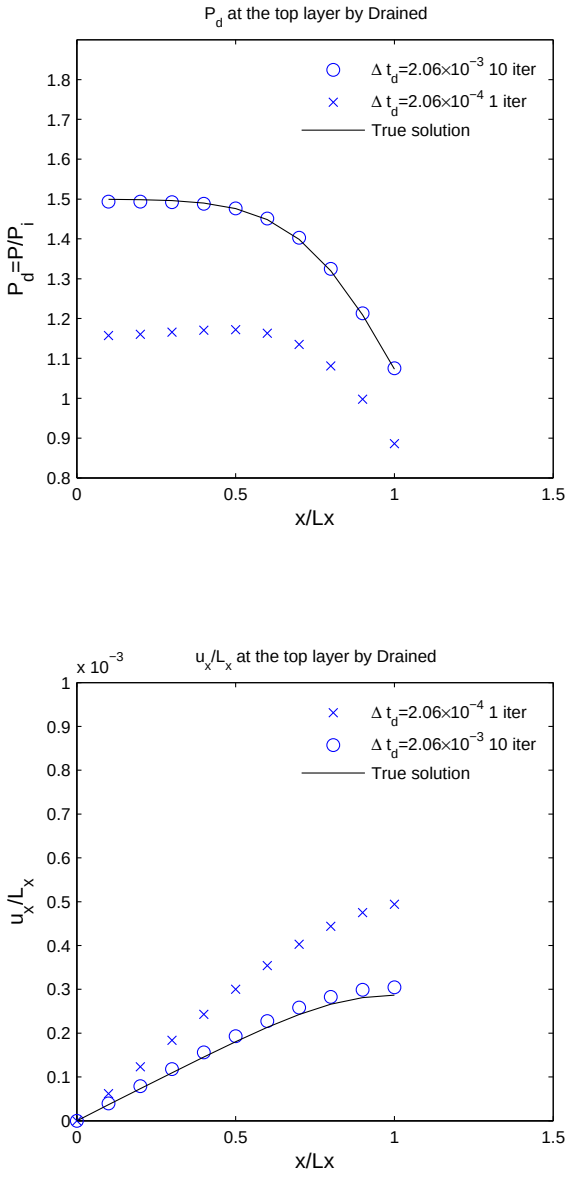

Figure 4.14: Comparison between more iterations and refined time step size in the drained split for Case 4.2: pressure (top) and displacement (bottom).

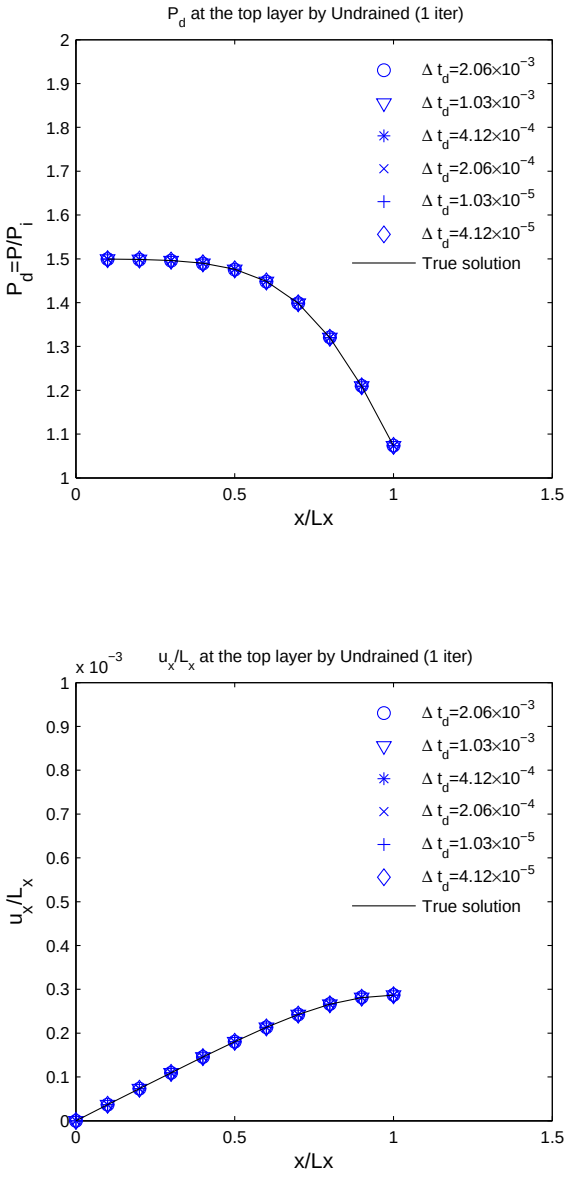

Figure 4.15: Convergence of the undrained split with one iteration for Case 4.2: pressure (top) and displacement (bottom).

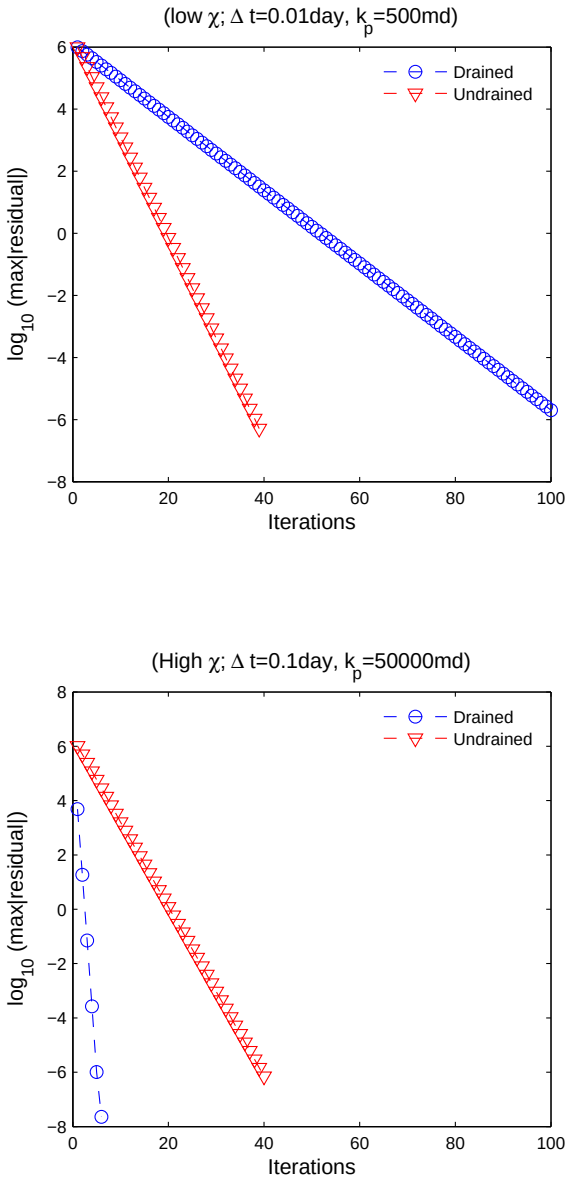

Figure 4.16: Comparison of the rate of convergence at low (top) and high χ (bottom) for Case 4.1. The coupling strength τ is 0.95.

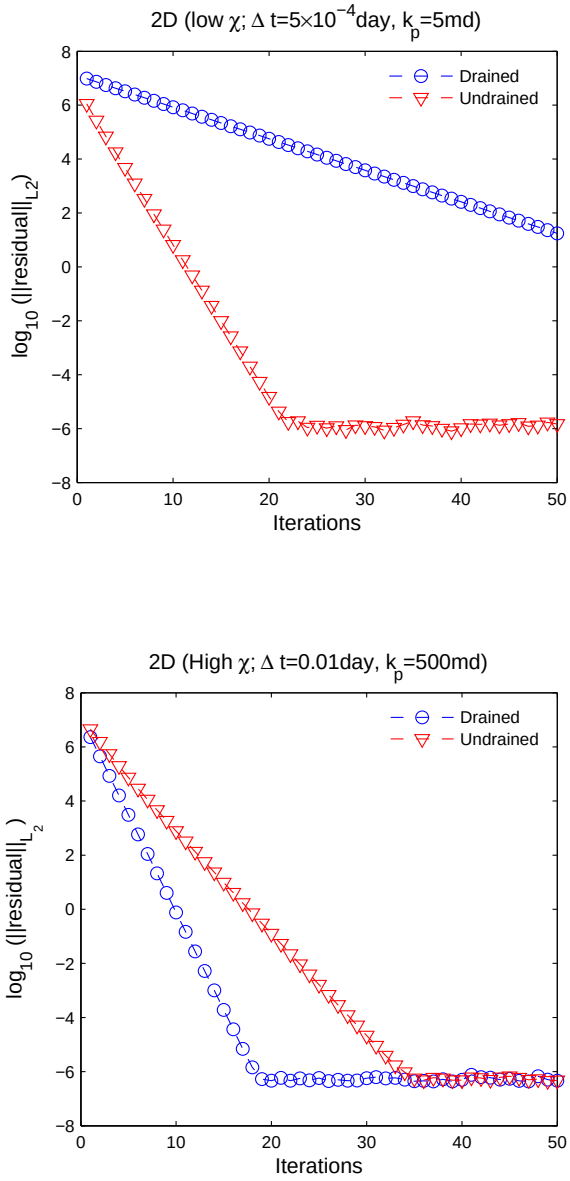

Figure 4.17: Comparison of the rate of convergence at low (top) and high χ (bottom) for Case 4.2. The coupling strength τ is 0.77.

Chapter 5

Fixed-strain and Fixed-stress Splits

5.1 Operator Splitting

There are two representative sequential implicit methods when the flow problem is solved implicitly first, followed by implicit solution of the mechanical problem, namely the fixed-strain and fixed-stress splits. The left and right diagrams of Figure 5.1 illustrate the solution procedures by the fixed-strain and fixed-stress splits, respectively.

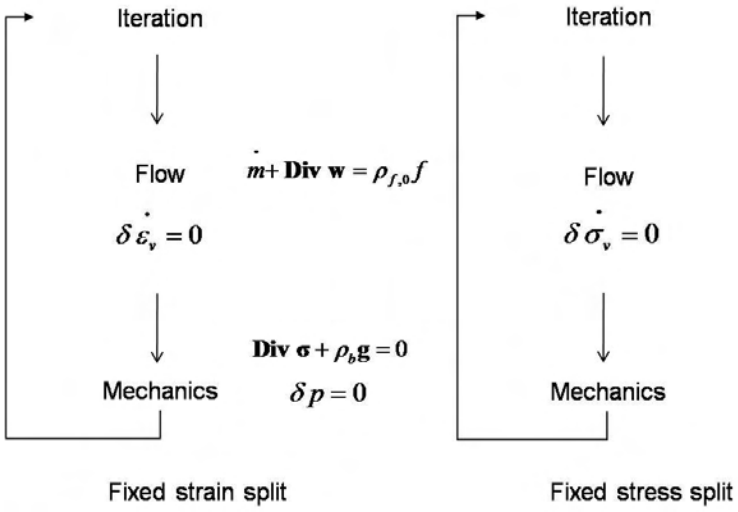

Figure 5.1: Iteratively coupled methods for flow and geomechanics. Left: fixed-strain split. Right: fixed-stress split.

5.1.1 Fixed-strain split

For the fixed-strain approach, the original operator $\mathcal{A}$ is split as follows.

$$\begin{bmatrix} \boldsymbol{u}^n \\ \boldsymbol{p}^n \end{bmatrix} \xrightarrow{\mathcal{A}^p_{sn}} \begin{bmatrix} \boldsymbol{u}^* \\ \boldsymbol{p}^{n+1} \end{bmatrix} \xrightarrow{\mathcal{A}^u_{sn}} \begin{bmatrix} \boldsymbol{u}^{n+1} \\ \boldsymbol{p}^{n+1} \end{bmatrix}, \quad \text{where} \quad \begin{cases} \mathcal{A}^p_{sn} : \dot{m} + \operatorname{Div} \boldsymbol{w} = \rho_{f,0} f, \ \delta\dot{\varepsilon}_v = 0, \\ \mathcal{A}^u_{sn} : \operatorname{Div} \boldsymbol{\sigma} + \rho_b \boldsymbol{g} = \boldsymbol{0}, \ p: \text{ prescribed}, \end{cases} \tag{5.1}$$

where we solve the flow problem first using implicit time discretization, followed by solution of the mechanical problem using an appropriate implicit time discretization scheme. In the fixed-strain split, $\delta\dot{\varepsilon}_v = 0$ means that the volumetric strain term $b\dot{\varepsilon}_v$ in the accumulation term for the flow problem (Equation 3.10) is evaluated explicitly. We first solve the flow problem while freezing the rate of the strain everywhere (i.e., $\delta\dot{\varepsilon}_v = 0$). Then we solve the mechanical problem. Note that the pressure is prescribed when we solve the mechanical problem because we determine the pressure at t_{n+1} from the previous flow problem. It is worth noting that the mechanical problem uses the drained rock properties, and that the pressure corrections act as "loads" (Settari and Mourits, 1998).

5.1.2 Fixed-stress split

In this scheme, the flow problem is solved first while freezing the rate of the total mean stress ($\delta\dot{\sigma}_v = 0$). That is, the volumetric stress term $(b/K_{dr})\dot{\sigma}_v$ in the accumulation term of Equation 3.12 is evaluated explicitly when solving the flow problem.

The original operator $\mathcal{A}$ is split as follows:

$$\begin{bmatrix} \boldsymbol{u}^n \\ \boldsymbol{p}^n \end{bmatrix} \xrightarrow{\mathcal{A}^p_{ss}} \begin{bmatrix} \boldsymbol{u}^* \\ \boldsymbol{p}^{n+1} \end{bmatrix} \xrightarrow{\mathcal{A}^u_{ss}} \begin{bmatrix} \boldsymbol{u}^{n+1} \\ \boldsymbol{p}^{n+1} \end{bmatrix}, \quad \text{where} \quad \begin{cases} \mathcal{A}^p_{ss} : \dot{m} + \operatorname{Div} \boldsymbol{w} = \rho_{f,0} f, \ \delta\dot{\sigma}_v = 0, \\ \mathcal{A}^u_{ss} : \operatorname{Div} \boldsymbol{\sigma} + \rho_b \boldsymbol{g} = \boldsymbol{0}, \ p: \textit{ prescribed}. \end{cases} \tag{5.2}$$

The initial conditions of $\mathcal{A}^p_{ss}$ are determined from the initial time conditions of the original coupled problem, which satisfy

$$\operatorname{Div} \dot{\sigma}_{t=0} = 0\,, \quad \operatorname{Div} \sigma_{t=0} = 0. \tag{5.3}$$

We fix the rate of the entire stress tensor field during the flow problem, where flow does not affect the shear stress field (i.e., $\delta\dot{\boldsymbol{\sigma}} = \mathbf{0}$). In the fixed *mean*-stress split, no full matrix inversion or multiplication is required, since the rate of mean stress is kept constant by introducing the term b^2/K_{dr} locally in each element (see Equation 3.12).

In elastoplasticity, b^2/K_{dr} is evaluated from the tangent moduli $\mathbf{C}_{ep}$ (e.g. $b^2/K_{dr} = \frac{1}{9}\mathbf{1}^t\mathbf{D}_{ep}\mathbf{1}$, where $\mathbf{D}_{ep}$ is the matrix notation of $\mathbf{C}_{ep}$ in three dimensions). When b^2/K_{dr} is treated explicitly and evaluated at t_n, the return mapping is not required due to the use of $\mathbf{C}_{ep}^n$ even though plastic dissipation is considered during the flow step. Furthermore, it is not necessary to calculate the displacement and stress at the intermediate step because the quasi-static mechanical problem is elliptic and the intermediate displacement and stress fields are not needed. Thus, the computational cost of the fixed-stress split is the same as that of the fixed-strain split. Once the flow problem is solved, both splitting schemes solve the same mechanical problem.

5.1.3 Conventional reservoir simulation

In traditional reservoir simulation, the pressure equation is given by

$$(\phi_0 c_f + \phi_0 c_p)\frac{\partial p}{\partial t} + \operatorname{Div} \boldsymbol{v} = f, \tag{5.4}$$

where c_p is the pore-volume compressibility. The pore-volume compressibility is not an intrinsic property of the rock, since it depends on the deformation scenario and the boundary conditions of the coupled problem. It is used in traditional reservoir simulation as a simplified way to account for changes in the state of stress and strain in the reservoir (Settari and Mourits, 1998; Settari and Walters, 2001). From Equations 3.5, 3.10, and 5.4, the fixed-strain split takes $\phi_0 c_p|_{sn}$ as $(b-\phi_0)/K_s$ and uses $b\dot{\varepsilon}_v$ as a correction source term due to mechanical effects. Similarly, from Equations 3.5, 3.12, and 5.4, the fixed-stress split takes $\phi_0 c_p|_{ss} = (b-\phi_0)/K_s + b^2/K_{dr}$ and uses $b/K_{dr}\dot{\sigma}_v$ as a correction source term from the mechanical solution. The expression for the pore compressibility associated with the fixed-stress split coincides with the one proposed by Settari and Mourits (1998) (albeit for

linear poroelasticity only). Other values of c_p could be used in order to enhance the stability and convergence of sequential schemes, and this has been studied, in the context of linear poroelasticity, by Bevillon and Masson (2000), and Mainguy and Longuemare (2002).

In order to properly account for geomechanical effects, a correction needs to be included as a source term. This source term is known as *porosity correction*, $\dot{\Phi}$ (Settari and Mourits, 1998; Mainguy and Longuemare, 2002) and takes the following two equivalent expressions:

$$\dot{\Phi} = \left(\phi_0 c_p + \frac{\phi_0 - b}{K_s}\right)\dot{p} - b\dot{\varepsilon}_v \qquad \text{(from Equation 3.10)}, \tag{5.5}$$

$$= \left(\phi_0 c_p + \frac{\phi_0}{K_s} - \frac{b}{K_{dr}}\right)\dot{p} - \left(\frac{1}{K_{dr}} - \frac{1}{K_s}\right)\dot{\sigma}_v \qquad \text{(from Equation 3.12)}. \tag{5.6}$$

Even though the pore-volume compressibility has been recognized as a stabilization term, a complete stability analysis and comparison study of sequential methods including plasticity is lacking. In the next section, we analyze the stability and accuracy of the two sequential implicit methods presented here.

5.2 Stability Analysis for Linear Poroelasticity

We use the Von Neumann method to analyze the stability of the fixed-strain and fixed-stress splits.

5.2.1 Fixed-strain split

Using the generalized mid-point rule, we can express the total stress $\boldsymbol{\sigma}_h$ and velocity V_h in the discretized space as

$$\boldsymbol{\sigma}_h^{n+\alpha} = (1-\alpha)\boldsymbol{\sigma}_h^n + \alpha\boldsymbol{\sigma}_h^{n+1}\,, \tag{5.7}$$

$$V_h^{n+\alpha} = (1-\alpha)V_h^n + \alpha V_h^{n+1}. \tag{5.8}$$

Figure 3.3 shows the one dimensional spatial discretization. The fixed-strain split freezes

the variation of the strain rate, that is

$$\Delta\varepsilon^n = \Delta\varepsilon^{n-1}. \tag{5.9}$$

Full discretization in one dimension yields

$$\frac{h}{M}\frac{\Delta P_j^n}{\Delta t} + \frac{bh}{\Delta t}(-\frac{\Delta U_{j-\frac{1}{2}}^{n-1} - \Delta U_{j+\frac{1}{2}}^{n-1}}{h}) - \frac{k_p}{\mu h}\left(P_{j-1}^{n+\alpha} - 2P_j^{n+\alpha} + P_{j+1}^{n+\alpha}\right) = 0, \tag{5.10}$$

$$-(\frac{K_{dr}}{h}U_{j-\frac{3}{2}}^{n+\alpha} - 2\frac{K_{dr}}{h}U_{j-\frac{1}{2}}^{n+\alpha} + \frac{K_{dr}}{h}U_{j+\frac{1}{2}}^{n+\alpha}) - b(P_{j-1}^{n+\alpha} - P_j^{n+\alpha}) = 0. \tag{5.11}$$

Introducing solutions of the form $U_j^n = \gamma^n e^{i(j)\theta}\hat{U}$ and $P_j^n = \gamma^n e^{i(j)\theta}\hat{P}$, where γ is the amplification factor, $e^{(\cdot)} = \exp(\cdot)$, $i = \sqrt{-1}$, and $\theta \in [-\pi, \pi]$, we have

$$\begin{bmatrix} U_j^n \\ P_j^n \end{bmatrix} = \gamma^n \begin{bmatrix} e^{i(j)\theta}\hat{U} \\ e^{i(j)\theta}\hat{P} \end{bmatrix}. \tag{5.12}$$

Substituting Equation 5.12 into Equations 5.10 and 5.11, we obtain

$$\underbrace{\begin{bmatrix} \frac{1}{M}h(\gamma-1)\gamma + \frac{k_p\Delta t}{\mu h}2((1-\alpha)+\alpha\gamma)\gamma(1-\cos\theta) & b(\gamma-1)2i\sin\frac{\theta}{2} \\ b2i\sin\frac{\theta}{2} & \frac{K_{dr}}{h}2(1-\cos\theta) \end{bmatrix}}_{\mathbf{G}_{sn}} \begin{bmatrix} \hat{P} \\ \hat{U} \end{bmatrix} = \begin{bmatrix} 0 \\ 0 \end{bmatrix}. \tag{5.13}$$

Since the matrix needs to be singular, $\det \mathbf{G}_{sn} = 0$. Then the characteristic equation is obtained and can be written as

$$\begin{aligned} F_{sn}^{\alpha}(\gamma) &= \left(\frac{K_{dr}}{M} + K_{dr}\frac{k_p\Delta t}{\mu h^2}\alpha 2(1-\cos\theta)\right)\gamma^2 \\ &\quad + \left(-\frac{K_{dr}}{M} + K_{dr}\frac{k_p\Delta t}{\mu h^2}(1-\alpha)2(1-\cos\theta) + b^2\right)\gamma - b^2 = 0. \end{aligned} \tag{5.14}$$

Note that the constant term of $F^{\alpha}_{sn}(\gamma)$, $-b^2$, is negative, so one root is positive and the one is negative. The condition for linear stability is $\max(|\gamma|) \leq 1$, which is obtained for $F^{\alpha}_{sn}(\gamma = 1) \geq 0$ and $F^{\alpha}_{sn}(\gamma = -1) \geq 0$. From Equation 5.14, we get

$$F^{\alpha}_{sn}(\gamma = 1) = \frac{k_p \Delta t}{\mu h^2} \alpha 2(1 - \cos\theta) \geq 0\,, \tag{5.15}$$

$$F^{\alpha}_{dr}(\gamma = -1) = 2\frac{K_{dr}}{M} + (2\alpha - 1)K_{dr}\frac{k_p \Delta t}{\mu h^2} 2(1 - \cos\theta) - 2b^2 \geq 0. \tag{5.16}$$

Equation 5.15 is valid for all θ. Equation 5.16 is valid for all θ depending on the weight α, as follows:

$$\text{For } 0.5 \leq \alpha \leq 1: \qquad \tau = \frac{b^2 M}{K_{dr}} \leq 1\,, \tag{5.17}$$

$$\text{For } 0 < \alpha < 0.5: \qquad \tau = \frac{b^2 M}{K_{dr}} \leq 1 \text{ and } \Delta t \leq (\frac{K_{dr}}{M} - b^2)\frac{\mu h^2}{2(1 - 2\alpha)K_{dr} k_p}. \tag{5.18}$$

Equation 5.17 indicates that the stability of the fixed-strain split depends on the coupling strength only and is independent of time step size, when $0.5 \leq \alpha \leq 1$. In the case that $0 < \alpha < 0.5$, we obtain an additional condition for stability with restriction on the time step size. Since one of the γ's is negative, oscillation is anticipated even when the fixed-strain split is stable.

Remark 5.1. For the backward Euler time discretization, $\alpha = 1$, the characteristic equation of the fixed-strain split (Equation 5.14) is identical to that of the drained split. Notice, however, that the fixed-strain split with the midpoint rule $\alpha = 0.5$ is conditionally stable, even though the drained split with the midpoint rule is unconditionally unstable.

5.2.2 Fixed-stress split

The fixed-stress split freezes the variation of the total stress rate, which yields

$$\Delta\varepsilon^n = \frac{b}{K_{dr}}(\Delta P^n - \Delta P^{n-1}) + \Delta\varepsilon^{n-1}. \tag{5.19}$$

Then the discrete form of the fixed-stress split becomes

$$\left(\frac{1}{M}+\frac{b^2}{K_{dr}}\right)h\frac{\Delta P_j^n}{\Delta t}-\frac{b^2}{K_{dr}}h\frac{\Delta P_j^{n-1}}{\Delta t}+\frac{bh}{\Delta t}(-\frac{\Delta U_{j-\frac{1}{2}}^{n-1}-\Delta U_{j+\frac{1}{2}}^{n-1}}{h})$$
$$-\frac{k_p}{\mu h}\left(P_{j-1}^{n+\alpha}-2P_j^{n+\alpha}+P_{j+1}^{n+\alpha}\right)=0, \tag{5.20}$$

$$-(\frac{K_{dr}}{h}U_{j-\frac{3}{2}}^{n+\alpha}-2\frac{K_{dr}}{h}U_{j-\frac{1}{2}}^{n+\alpha}+\frac{K_{dr}}{h}U_{j+\frac{1}{2}}^{n+\alpha})-b(P_{j-1}^{n+\alpha}-P_j^{n+\alpha})=0. \tag{5.21}$$

Substituting Equation 5.12 into Equations 5.20 and 5.21, we obtain

$$\mathbf{G}_{ss}\begin{bmatrix}\hat{P}\\ \hat{U}\end{bmatrix}=\begin{bmatrix}0\\0\end{bmatrix}, \tag{5.22}$$

where $\mathbf{G}_{ss}=$

$$\begin{bmatrix}\left(\left(\frac{1}{M}+\frac{b^2}{K_{dr}}\right)\gamma-\frac{b^2}{K_{dr}}\right)h(\gamma-1)+\frac{k_p\Delta t}{\mu h}2((1-\alpha)+\alpha\gamma)\gamma(1-\cos\theta) & b(\gamma-1)2i\sin\frac{\theta}{2}\\ b2i\sin\frac{\theta}{2} & \frac{K_{dr}}{h}2(1-\cos\theta)\end{bmatrix}.$$

Applying $\det\mathbf{G}_{ss}=0$

$$\gamma=0,\ \frac{\left(\frac{1}{M}+\frac{b^2}{K_{dr}}\right)-\frac{k_p\Delta t}{\mu h^2}(1-\alpha)2(1-\cos\theta)}{\left(\frac{1}{M}+\frac{b^2}{K_{dr}}\right)+\frac{k_p\Delta t}{\mu h^2}\alpha 2(1-\cos\theta)}. \tag{5.23}$$

The condition of linear stability yields

$$\text{For } 0.5\le\alpha\le 1: \qquad \text{Unconditionally stable}, \tag{5.24}$$
$$\text{For } 0<\alpha<0.5: \qquad \Delta t\le\frac{\mu h^2}{2(1-2\alpha)k_p}\left(\frac{1}{M}+\frac{b^2}{K_{dr}}\right). \tag{5.25}$$

Hence, the fixed-stress split is unconditionally stable when $0.5\le\alpha\le 1$. For $0<\alpha<0.5$, the time step size is limited for stability. When $\alpha=1$, the γ's are non-negative, which indicates non-oscillatory behavior. The amplification factors γ's in Equation 5.23 are

different from those for the undrained split. Interestingly, they are identical to those for the fully coupled method.

Remark 5.2. When the mechanical problem has complicated boundary conditions in multiple dimensions, we might not obtain the exact local value of K_{dr} in the flow problem of Equation 5.20 for the fixed-stress split. Let K_{dr}^{est} be an estimated local K_{dr}. We define $\eta = K_{dr}/K_{dr}^{est}$ as the deviation factor between the true and estimated local drained bulk moduli. Then, following the same procedure of the Von Neumann method with the backward Euler time discretization, we obtain the condition for the linear stability as

$$\eta \geq \frac{1}{2}\left(1 - \frac{1}{\tau}\right), \tag{5.26}$$

where one of the amplification factors is negative if $\eta < 1$, but all the amplification factors are positive if $\eta > 1$. From Equation 5.26, $\eta \geq 0.5$ provides unconditional stability for linear problems.

Suppose we use $K_{dr}^{est} = K_{dr}^{3D}$ for incompressible fluid and solid grains when the true K_{dr} is K_{dr}^{1D}. In this case, $\tau = \infty$ and $\eta = 3(1-\nu)/(1+\nu)$, where ν is Poisson's ratio. Since $0 \leq \nu \leq 0.5$, $1.0 \leq \eta \leq 3.0$, which gives unconditional stability with monotonic behavior. On the other hand, we obtain $\eta = (1+\nu)/3(1-\nu)$ where we use $K_{dr}^{est} = K_{dr}^{1D}$ while the true K_{dr} is K_{dr}^{3D}. In this case, instabilities may occur because $0.33 \leq \eta \leq 1.0$ (e.g., $\eta = 0.33$ when $\nu = 0.0$), and we may lead to oscillatory behaviors, even though the scheme is stable. Hence, a less stiff K_{dr}^{est} than the true K_{dr} yields unconditional stability with monotonicity because it guarantees $1.0 \leq \eta \leq 3.0$. Thus, it is appropriate to choose K_{dr}^{1D}, K_{dr}^{2D}, and K_{dr}^{3D} as K_{dr}^{est}'s for one, two, and three dimensional problems, respectively.

5.3 Contractivity of the Nonlinear Continuum Problem

5.3.1 Non-contractivity of the fixed-strain split

The coupled problem is contractive relative to the norms $\|\cdot\|_{\mathcal{N}}$ and $\|\cdot\|_{\mathcal{T}}$, as shown in Chapter 3. We investigate whether the fixed-strain split is contractive, or not. We consider two arbitrary initial conditions as we did in Chapter 3. The fixed-strain split can be written as

$$\begin{bmatrix} d\boldsymbol{u}^n \\ d\boldsymbol{p}^n \end{bmatrix} \xrightarrow{\mathcal{A}^p_{sn}} \begin{bmatrix} d\boldsymbol{u}^* \\ d\boldsymbol{p}^{n+1} \end{bmatrix} \xrightarrow{\mathcal{A}^u_{sn}} \begin{bmatrix} d\boldsymbol{u}^{n+1} \\ d\boldsymbol{p}^{n+1} \end{bmatrix}, \quad \text{where} \quad \begin{cases} \mathcal{A}^p_{sn} : \dot{dm} + \operatorname{Div} d\boldsymbol{v} = 0,\ \delta\dot{d\varepsilon}_v = 0, \\ \mathcal{A}^u_{sn} : \operatorname{Div} \boldsymbol{d\sigma} = \boldsymbol{0},\ dp = 0 \\ \quad \Rightarrow \quad \operatorname{Div} \boldsymbol{d\sigma'} = \boldsymbol{0}. \end{cases} \tag{5.27}$$

Equation 5.27 has homogeneous boundary conditions with no source terms. Since the pressure in the mechanical problem is prescribed, the pressure is not affected by perturbations of the initial condition, thus $dp = 0$. When solving the flow problem, $\mathcal{A}^p_{sn}$, we obtain

$$\begin{aligned} \frac{d\,\|d\chi\|^2_{\mathcal{N}}}{dt} &= \frac{\partial \|d\chi\|^2_{\mathcal{N}}}{\partial d\boldsymbol{\varepsilon}_e} : \dot{d\boldsymbol{\varepsilon}}_e + \frac{\partial \|d\chi\|^2_{\mathcal{N}}}{\partial d\xi} \cdot \dot{d\xi} + \frac{\partial \|d\chi\|^2_{\mathcal{N}}}{\partial dm_e} \dot{dm}_e \\ &= \int_\Omega \left[d\boldsymbol{\sigma'} : \dot{d\boldsymbol{\varepsilon}}_e - d\kappa \cdot \dot{d\xi} - M\left(\frac{dm_e}{\rho_{f,0}} - b d\varepsilon_{e,v}\right) b \dot{d\varepsilon}_{e,v} \right. \\ &\quad \left. + \frac{M}{\rho_{f,0}}\left(\frac{dm_e}{\rho_{f,0}} - b\varepsilon_{e,v}\right) \dot{dm}_e \right] d\Omega \\ &= \int_\Omega \left[d\boldsymbol{\sigma} : \dot{d\boldsymbol{\varepsilon}} + \frac{dp}{\rho_{f,0}} \dot{dm} \right] d\Omega - \underbrace{\int_\Omega \left[d\boldsymbol{\sigma'} : \dot{d\boldsymbol{\varepsilon}}_p + d\boldsymbol{\kappa} \cdot \dot{d\boldsymbol{\xi}} \right] d\Omega}_{D^d_p \geq 0} \\ &= \int_\Omega \left[d\boldsymbol{\sigma} : \dot{d\boldsymbol{\varepsilon}} - d\boldsymbol{v} \cdot \mathbf{k}^{-1} \mu d\boldsymbol{v} \right] d\Omega - D^d_p \not\leq 0, \\ &\quad \left(\dot{dm} = -d\boldsymbol{v} \cdot \mathbf{k}^{-1} \mu d\boldsymbol{v} \ \text{from Equation 5.27} \right) \end{aligned} \tag{5.28}$$

where $\boldsymbol{v} \in [H(div, \Omega)]^{n_{dim}}$. Note that we consider maximum plastic dissipation, $D^d_p \geq 0$, when solving the flow problem.

From Equation 5.28, the fixed-strain split does not inherit the contractivity relative to the norm $\|\cdot\|_{\mathcal{N}}$ at the stage of $\mathcal{A}^p_{sn}$. As a result, the fixed-strain split is not contractive with respect to the full problem.

When solving the mechanical problem after the flow problem, $\mathcal{A}^u_{sn}$, we obtain

$$\begin{aligned}
\frac{d\,\|d\chi\|^2_{\mathcal{N}}}{dt} &= \int_\Omega \left[d\boldsymbol{\sigma}' : \dot{d\boldsymbol{\varepsilon}}_e - d\kappa \cdot \dot{d\xi} + \frac{1}{M} dp \dot{dp} \right] d\Omega \\
&= \int_\Omega d\boldsymbol{\sigma}' : \dot{d\boldsymbol{\varepsilon}} d\Omega - \underbrace{\int_\Omega \left[d\boldsymbol{\sigma}' : \dot{d\boldsymbol{\varepsilon}}_p + d\boldsymbol{\kappa} \cdot \dot{d\boldsymbol{\xi}} \right] d\Omega}_{D^d_p \geq 0} \quad (\text{from } \dot{dp} = 0) \\
&= -D^d_p \leq 0, \qquad (5.29) \\
&\quad \left(\int_\Omega d\boldsymbol{\sigma}' : \dot{d\boldsymbol{\varepsilon}} d\Omega = 0 \ \text{ from Equation 5.27} \right).
\end{aligned}$$

5.3.2 Contractivity of the fixed-stress split

Again we consider two arbitrary initial conditions and study the contractivity of the fixed-stress split. In the fixed-stress split, the original operator $\mathcal{A}$ is decomposed as follows:

$$\begin{bmatrix} d\boldsymbol{u}^n \\ d\boldsymbol{p}^n \end{bmatrix} \xrightarrow{\mathcal{A}^p_{ss}} \begin{bmatrix} d\boldsymbol{u}^* \\ d\boldsymbol{p}^{n+1} \end{bmatrix} \xrightarrow{\mathcal{A}^u_{ss}} \begin{bmatrix} d\boldsymbol{u}^{n+1} \\ d\boldsymbol{p}^{n+1} \end{bmatrix}, \quad \text{where} \quad \begin{cases} \mathcal{A}^p_{ss} : \dot{dm} + \operatorname{Div} d\boldsymbol{v} = 0, \ \delta \dot{d\sigma}_v = 0, \\ \mathcal{A}^u_{ss} : \operatorname{Div} d\boldsymbol{\sigma} = \boldsymbol{0}, \ dp = 0, \\ \quad \Rightarrow \quad \operatorname{Div} d\boldsymbol{\sigma}' = \boldsymbol{0}, \end{cases} \tag{5.30}$$

which has homogeneous boundary conditions with no source terms. Note that $\delta \dot{d\sigma}_v = 0$ is equivalent to $\delta \dot{d\boldsymbol{\sigma}} = \boldsymbol{0}$ in $\mathcal{A}^p_{ss}$, since pressure variations affect the volumetric stress, not the shear stress. Using Equation 5.3, the initial conditions of $\mathcal{A}^p_{ss}$ in Equation 5.30 become

$$\operatorname{Div} \dot{d\boldsymbol{\sigma}}_{t=0} = 0, \ \operatorname{Div} d\boldsymbol{\sigma}(t)_{t=0} = 0. \tag{5.31}$$

First, we show the contractivity of the fixed-stress split when solving the flow problem $\mathcal{A}^p_{ss}$. In $\mathcal{A}^p_{ss}$ of Equation 5.30, $\delta \dot{d\boldsymbol{\sigma}} = \boldsymbol{0}$ yields $\dot{d\boldsymbol{\sigma}}(t) - \dot{d\boldsymbol{\sigma}}_{t=0} = \boldsymbol{0}$. Combining this result

with the initial condition in Equation 5.31_1, we have

$$\mathrm{Div}\, d\dot{\boldsymbol{\sigma}}(t) = \mathrm{Div}\, d\dot{\boldsymbol{\sigma}}_{t=0} = 0. \tag{5.32}$$

Since the divergence operator Div is not a function of time under the infinitesimal transformation, $\mathrm{Div}\, d\dot{\boldsymbol{\sigma}}(t) = \partial_t \mathrm{Div}\, d\boldsymbol{\sigma}(t)$. Then Equations 5.31 and 5.32 lead to

$$\mathrm{Div}\, d\boldsymbol{\sigma}(t) = \mathrm{Div}\, d\boldsymbol{\sigma}(t)_{t=0} = 0. \tag{5.33}$$

Equation 5.33 and the homogeneous boundary condition yield

$$\int_\Omega d\boldsymbol{\sigma} : d\dot{\boldsymbol{\varepsilon}} d\Omega = 0. \tag{5.34}$$

The contractivity of the fixed-stress split is shown as

$$\begin{aligned} \frac{d\left\|d\chi\right\|_{\mathcal{N}}^2}{dt} &= \int_\Omega \left[d\boldsymbol{\sigma} : d\dot{\boldsymbol{\varepsilon}} + \frac{dp}{\rho_{f,0}} d\dot{m} \right] d\Omega - \underbrace{\int_\Omega \left[d\boldsymbol{\sigma}' : d\dot{\boldsymbol{\varepsilon}}_p + d\boldsymbol{\kappa} \cdot d\dot{\boldsymbol{\xi}} \right] d\Omega}_{D_p^d \geq 0} \\ &= -\int_\Omega d\boldsymbol{v} \cdot \mathbf{k}^{-1} \mu d\boldsymbol{v} d\Omega - D_p^d \leq 0 \;\; (\text{from Equation 5.34}) \,. \end{aligned} \tag{5.35}$$

Thus, the fixed-stress scheme is contractive relative to the norm $\|\cdot\|_{\mathcal{N}}$ when solving the flow problem. Since the mechanical problem in the fixed-stress split, A_{ss}^u, is the same as that in the fixed-strain split, A_{sn}^u, the fixed-stress split satisfies contractivity in the norm $\|\cdot\|_{\mathcal{N}}$ when solving the mechanical problem as indicated by Equation 5.29.

5.4 Discrete Stability of the Nonlinear Problem

The fixed-strain split is not contractive and cannot provide unconditional stability. Thus, we only investigate what time integration scheme can provide unconditional stability for the fixed-stress split. Let $(\mathbf{u}^n,\ p^n,\ \boldsymbol{\xi}^n)$ and $(\tilde{\mathbf{u}}^n,\ \tilde{p}^n,\ \tilde{\xi}^n)$ be two arbitrary solutions at time t_n, yielding $(\boldsymbol{\sigma}'^n,\ m^n,\ \kappa^n,\ \boldsymbol{\varepsilon}_p^n)$ and $(\tilde{\boldsymbol{\sigma}}'^n,\ \tilde{m}^n,\ \tilde{\kappa}^n,\ \tilde{\boldsymbol{\varepsilon}}_p^{\,n})$, respectively.

We employ B-stability for unconditional stability of the nonlinear problem, which is expressed as

$$\left\|d\chi^{n+1}\right\|_{\mathcal{N}} \leq \left\|d\chi^{n}\right\|_{\mathcal{N}}. \tag{5.36}$$

First, we show B-stability when solving the flow problem. We solve the flow problem first based on the maximum plastic work, for which we adopt the generalized midpoint rule described in Simo (1991) and Simo and Govindjee (1991). The algorithmic maximum plastic work is written as

$$\begin{aligned} &\ll d\Sigma^{n} - d\Sigma^{n+\alpha},\ -d\Sigma^{n+\alpha} \gg \\ &+ \ll (\alpha \mathbf{C}_{dr} \Delta d\varepsilon^{n}, 0),\ (-d\boldsymbol{\sigma}'^{n+\alpha}, -d\boldsymbol{\kappa}^{n+\alpha}) \gg \leq 0, \end{aligned} \tag{5.37}$$

where again $d(\cdot) = (\cdot) - (\tilde{\cdot})$, (e.g. $\Delta d\varepsilon^{n} = \Delta\varepsilon^{n} - \Delta\tilde{\varepsilon}^{n}$). The flow problem A^{p}_{ss} also has the constraint of $\delta d\dot{\boldsymbol{\sigma}} = \mathbf{0}$, expressed as

$$d\boldsymbol{\sigma}^{n+1} - d\boldsymbol{\sigma}^{n} = d\boldsymbol{\sigma}^{n} - d\boldsymbol{\sigma}^{n-1} = \cdots = d\boldsymbol{\sigma}^{1} - d\boldsymbol{\sigma}^{0} \tag{5.38}$$

The discrete counterpart of the initial conditions in Equation 5.31 yields

$$\mathrm{Div}\left(d\boldsymbol{\sigma}^{1} - d\boldsymbol{\sigma}^{0}\right) = 0,\ \ \mathrm{Div}\, d\boldsymbol{\sigma}^{0} = 0. \tag{5.39}$$

From Equations 5.38 and 5.39, we obtain

$$\mathrm{Div}\, d\boldsymbol{\sigma}^{n+1} = \mathrm{Div}\, d\boldsymbol{\sigma}^{n} = \cdots = 0, \tag{5.40}$$

which yields

$$\mathrm{Div}\, d\boldsymbol{\sigma}^{n+\alpha} = 0. \tag{5.41}$$

Combining Equation 5.41 with the homogeneous boundary condition in $\mathcal{A}_{ss}^{p}$ of Equation 5.30, we obtain

$$\int_{\Omega} d\boldsymbol{\sigma}^{n+\alpha} : \Delta d\boldsymbol{\varepsilon}^{n} d\Omega = 0. \tag{5.42}$$

The first term in Equation 5.37 can be expressed as

$$\begin{aligned} &\ll d\Sigma^{n} - d\Sigma^{n+\alpha},\ -d\Sigma^{n+\alpha} \gg \\ &= - \ll \alpha(d\Sigma^{n} - d\Sigma^{n+1}),\ d\Sigma^{n+1/2} + \left(\alpha - \frac{1}{2}\right)\left(d\Sigma^{n+1} - d\Sigma^{n}\right) \gg \\ &= \alpha\left(\left\|d\Sigma^{n+1}\right\|_{\mathcal{E}}^{2} - \left\|d\Sigma^{n}\right\|_{\mathcal{E}}^{2}\right) + \alpha\left(2\alpha - 1\right)\left\|d\Sigma^{n+1} - d\Sigma^{n}\right\|_{\mathcal{E}}^{2}, \end{aligned} \tag{5.43}$$

where $\Sigma^{n+1/2} = (\Sigma^{n} + \Sigma^{n+1})/2$.

The second term of Equation 5.37 can be written as

$$\begin{aligned} &\ll (\alpha \mathbf{C}_{dr} \Delta d\varepsilon^{n}, 0),\ (-d\boldsymbol{\sigma}'^{n+\alpha}, -d\kappa^{n+\alpha}) \gg \\ &= -\int \alpha \Delta d\varepsilon^{n} : d\boldsymbol{\sigma}'^{n+\alpha} d\Omega \\ &= -\alpha \int \Delta d\varepsilon^{n} : (d\boldsymbol{\sigma}^{n+\alpha} + b dp^{n+\alpha}\mathbf{1}) d\Omega \\ &= -\alpha \int \Delta d\varepsilon_{v}^{n} b dp^{n+\alpha} d\Omega \quad \text{(from Equation 5.42)}. \end{aligned} \tag{5.44}$$

From Equations 5.43 and 5.44, Equation 5.37 yields

$$\left(\left\|d\Sigma^{n+1}\right\|_{\mathcal{E}}^{2} - \left\|d\Sigma^{n}\right\|_{\mathcal{E}}^{2}\right) + (2\alpha - 1)\left\|d\Sigma^{n+1} - d\Sigma^{n}\right\|_{\mathcal{E}}^{2} - \int \Delta d\varepsilon_{v}^{n} b dp^{n+\alpha} d\Omega \leq 0. \tag{5.45}$$

From the flow equation of A_{ss}^{p}, we obtain

$$\int dp^{n+\alpha}\left(\frac{1}{M}\frac{dp^{n+1} - dp^{n}}{\Delta t} + b\frac{d\varepsilon_{v}^{n+1} - d\varepsilon_{v}^{n}}{\Delta t} + \mathrm{Div}(d\boldsymbol{v}^{n+\alpha})\right) d\Omega = 0. \tag{5.46}$$

Using the following identity,

$$\begin{aligned}&\int_\Omega dp^{n+\alpha}\frac{1}{M}\left(dp^{n+1}-dp^n\right)d\Omega\\&=\frac{1}{2M}(\left\|dp^{n+1}\right\|_{L^2}^2-\|dp^n\|_{L^2}^2)+(2\alpha-1)\frac{1}{2M}\left\|dp^{n+1}-dp^n\right\|_{L^2}^2,\end{aligned}\tag{5.47}$$

Equation 5.46 yields

$$\begin{aligned}&\frac{1}{2M}\left(\left\|dp^{n+1}\right\|_{L^2}^2-\|dp^n\|_{L^2}^2\right)=\\&-(2\alpha-1)\frac{1}{2M}\left\|dp^{n+1}-dp^n\right\|_{L^2}^2-\int dp^{n+\alpha}b\Delta d\varepsilon_v^n d\Omega\\&-\Delta t\int d\boldsymbol{v}^{n+\alpha}\cdot{\mathbf{k}_p}^{-1}\mu d\boldsymbol{v}^{n+\alpha}d\Omega,\end{aligned}\tag{5.48}$$

where $dp^{n+\alpha}=-\mu\mathbf{k}^{-1}d\boldsymbol{v}^{n+\alpha}$ from Darcy's law.

Then, when we solve the flow problem by the fixed-stress split, the evolution of the norm $\|\cdot\|_{\mathcal{N}}$ at the discrete time level is shown from Equations 5.45 and 5.48 as

$$\begin{aligned}&\left\|d\chi^{n+1}\right\|_{\mathcal{N}}-\|d\chi^n\|_{\mathcal{N}}\\&=\left\|d\Sigma^{n+1}\right\|_{\mathcal{E}}^2+\frac{1}{2M}\left\|dp^{n+1}\right\|_{L^2}^2-\|d\Sigma^n\|_{\mathcal{E}}^2-\frac{1}{2M}\|dp^n\|_{L^2}^2\\&\le-(2\alpha-1)\left(\left\|d\Sigma^{n+1}-d\Sigma^n\right\|_{\mathcal{E}}^2+\frac{1}{2M}\left\|dp^{n+1}-dp^n\right\|_{L^2}^2\right)\\&\quad-\Delta t\int d\boldsymbol{v}^{n+\alpha}\cdot{\mathbf{k}_p}^{-1}\mu d\boldsymbol{v}^{n+\alpha}d\Omega\,,\end{aligned}\tag{5.49}$$

from which the condition for unconditional stability is $0.5\le\alpha\le1$.

Remark 5.3 The return mapping with maximum plastic dissipation is required in order to treat b^2/K_{dr} implicitly in the flow problem. In this case, the flow problem would be iterated according to the updated b^2/K_{dr} by the return mapping. However, the implicit treatment of b^2/K_{dr} leads to considerable computational cost due to iterations in the flow problem. Hence, as described in Section 4.2, we treat b^2/K_{dr} explicitly (i.e., the previous time step). Accordingly, the return mapping is not required when solving the flow problem,

leading to the same computational cost as the fixed-strain split. Then, the return mapping is used only when solving the mechanical problem.

After we solve the flow problem, the discrete stability for mechanics A^u_{ss} is examined for the following problem.

$$\text{Div}\, d\boldsymbol{\sigma}^{n+\alpha} = \mathbf{0},\ dp^{n+\alpha} = 0 \quad \Rightarrow \quad \text{Div}\, d\boldsymbol{\sigma}'^{n+\alpha} = \mathbf{0}. \tag{5.50}$$

Equation 5.37 is applied again with maximum plastic dissipation. Under A^u_{ss}, the first term of Equation 5.37 is the same as Equation 5.43, and the second term of Equation 5.37 is written as

$$\begin{aligned} &\ll (\alpha \mathbf{C}_{dr} \Delta d\varepsilon^n, 0),\ (-d\boldsymbol{\sigma}'^{n+\alpha}, -d\kappa^{n+\alpha}) \gg \\ &= -\int \alpha \Delta d\varepsilon^n : d\boldsymbol{\sigma}'^{n+\alpha} d\Omega = 0 \ \ (\text{from Equation 5.50})\,. \end{aligned} \tag{5.51}$$

From Equations 5.37, 5.43, and 5.51, the algorithmic dissipation is given by

$$\left(\left\| d\Sigma^{n+1} \right\|^2_{\mathcal{E}} - \left\| d\Sigma^n \right\|^2_{\mathcal{E}} \right) + (2\alpha - 1) \left\| d\Sigma^{n+1} - d\Sigma^n \right\|^2_{\mathcal{E}} \leq 0. \tag{5.52}$$

From Equation 5.47, $dp^{n+\alpha} = 0$ in Equation 5.50 provides

$$\frac{1}{2M} (\left\| dp^{n+1} \right\|^2_{L^2} - \left\| dp^n \right\|^2_{L^2}) = -\,(2\alpha - 1)\, \frac{1}{2M} \left\| dp^{n+1} - dp^n \right\|^2_{L^2}. \tag{5.53}$$

Using Equations 5.52 and 5.53, the evolution of the norm $\|d\chi\|_{\mathcal{N}}$ for A^u_{ss} is written as

$$\begin{aligned} &\left\| d\chi^{n+1} \right\|_{\mathcal{N}} - \left\| d\chi^n \right\|_{\mathcal{N}} \\ &= \left\| d\Sigma^{n+1} \right\|^2_{\mathcal{E}} + \frac{1}{2M} \left\| dp^{n+1} \right\|^2_{L^2} - \left\| d\Sigma^n \right\|^2_{\mathcal{E}} - \frac{1}{2M} \left\| dp^n \right\|^2_{L^2} \\ &\leq -\,(2\alpha - 1) \left(\left\| d\Sigma^{n+1} - d\Sigma^n \right\|^2_{\mathcal{E}} + \frac{1}{2M} \left\| dp^{n+1} - dp^n \right\|^2_{L^2} \right), \end{aligned} \tag{5.54}$$

from which the condition for unconditional stability of A^u_{ss} is $0.5 \leq \alpha \leq 1$. Therefore,

unconditional stability (i.e., B-stability) for the fixed-stress split is achieved when $0.5 \leq \alpha \leq 1$.

5.5 Error Estimation

Stable sequential schemes yield the same solution as the fully coupled method when full iterations are taken and the sequential schemes are convergent. In practice, we take a fixed number of iterations due to limited computational resources. In this situation, first-order accuracy in time is desired. For example, in coupled flow and dynamics, the staggered method can preserve first-order accuracy in time based on Lie's formula (Armero and Simo, 1992; Chorin et al., 1978; Lapidus, 1981). However, when a fixed number of iterations is performed, typical sequential methods do not guarantee convergence (Turska et al., 1994). The drained split shows non-convergence under a fixed number of iterations for a slightly compressible fluid, whereas the undrained split shows convergence. But, the undrained split is not convergent when both the fluid and the solid grains are incompressible. To determine the convergence properties of the fixed-strain and fixed-stress splits, we employ matrix algebra and spectral analysis as we did in Chapter 3. The linear coupled problem is considered here for simplicity. We use the finite volume and finite element methods for flow and mechanics, respectively, and the backward Euler time discretization. The procedures of the error estimation for the fixed-strain and fixed-stress splits are quite similar to those of the drained and undrained splits used in Chapter 3.

The error associated with a sequential method can be decomposed into two terms as

$$\begin{aligned} \left\| \mathbf{e}_{ts}^{n+1,n_{iter}} \right\| &\leq \left\| \mathbf{x}_t^{n+1} - \mathbf{x}_f^{n+1} \right\| + \left\| \mathbf{x}_f^{n+1} - \mathbf{x}_s^{n+1,n_{iter}} \right\| \\ &= \mathbf{O}(\Delta t) + \left\| \mathbf{x}_f^{n+1} - \mathbf{x}_s^{n+1,n_{iter}} \right\|. \end{aligned} \tag{5.55}$$

Using the fully coupled method, the problem is written as

$$\underbrace{\begin{bmatrix} \mathbf{F} & \mathbf{L} \\ -\mathbf{L^t} & \mathbf{K} \end{bmatrix}}_{\mathbf{A}} \begin{bmatrix} \mathbf{p} \\ \mathbf{u} \end{bmatrix}^{n+1} - \underbrace{\begin{bmatrix} \mathbf{L} & \mathbf{Q} \\ \mathbf{0} & \mathbf{0} \end{bmatrix}}_{\mathbf{B}} \begin{bmatrix} \mathbf{p} \\ \mathbf{u} \end{bmatrix}^{n} = \underbrace{\begin{bmatrix} \mathbf{f_p} \\ \mathbf{f_u} \end{bmatrix}}_{\mathbf{f}}^{n+1}, \tag{5.56}$$

$$\mathbf{x} = \begin{bmatrix} \mathbf{p} \\ \mathbf{u} \end{bmatrix}, \ \mathbf{F} = \mathbf{Q} + \Delta t \mathbf{T},$$

Sequential methods decompose the matrix $\mathbf{A}$ into

$$\begin{bmatrix} \mathbf{F}+\mathbf{R} & \mathbf{0} \\ -\mathbf{L^t} & \mathbf{K} \end{bmatrix} \begin{bmatrix} \mathbf{p} \\ \mathbf{u} \end{bmatrix}^{n+1,k+1} - \begin{bmatrix} \mathbf{R} & -\mathbf{L} \\ \mathbf{0} & \mathbf{0} \end{bmatrix} \begin{bmatrix} \mathbf{p} \\ \mathbf{u} \end{bmatrix}^{n+1,k}$$
$$- \begin{bmatrix} \mathbf{L} & \mathbf{Q} \\ \mathbf{0} & \mathbf{0} \end{bmatrix} \begin{bmatrix} \mathbf{p} \\ \mathbf{u} \end{bmatrix}^{n} = \begin{bmatrix} \mathbf{f_p} \\ \mathbf{f_u} \end{bmatrix}^{n+1}, \tag{5.57}$$

where $\mathbf{R}$ is the relaxation matrix in a sequential method. $\mathbf{R}$ depends on the specific sequential method used. Subtracting Equation 5.57 from Equation 5.56, the errors of pressure and displacement are written as

$$\begin{aligned} \begin{bmatrix} \mathbf{e}_{fs,\mathbf{p}} \\ \mathbf{e}_{fs,\mathbf{u}} \end{bmatrix}^{n+1,k+1} &= \begin{bmatrix} \mathbf{F}+\mathbf{R} & \mathbf{0} \\ -\mathbf{L}^t & \mathbf{K} \end{bmatrix}^{-1} \left(\begin{bmatrix} \mathbf{R} & -\mathbf{L} \\ \mathbf{0} & \mathbf{0} \end{bmatrix} \begin{bmatrix} \mathbf{e}_{fs,\mathbf{p}} \\ \mathbf{e}_{fs,\mathbf{u}} \end{bmatrix}^{n+1,k} \right. \\ &\quad \left. + \begin{bmatrix} \mathbf{L} & \mathbf{Q} \\ \mathbf{0} & \mathbf{0} \end{bmatrix} \begin{bmatrix} \mathbf{e}_{fs,\mathbf{p}} \\ \mathbf{e}_{fs,\mathbf{u}} \end{bmatrix}^{n} \right) \\ &= \underbrace{\begin{bmatrix} (\mathbf{F}+\mathbf{R})^{-1} & \mathbf{0} \\ \mathbf{K}^{-1}\mathbf{L}^t(\mathbf{F}+\mathbf{R})^{-1} & \mathbf{K}^{-1} \end{bmatrix}}_{\mathbf{M}} \left(\underbrace{\begin{bmatrix} \mathbf{R} & -\mathbf{L} \\ \mathbf{0} & \mathbf{0} \end{bmatrix}}_{\mathbf{N}} \begin{bmatrix} \mathbf{e}_{fs,\mathbf{p}} \\ \mathbf{e}_{fs,\mathbf{u}} \end{bmatrix}^{n+1,k} \right. \\ &\quad \left. + \begin{bmatrix} \mathbf{L} & \mathbf{Q} \\ \mathbf{0} & \mathbf{0} \end{bmatrix} \begin{bmatrix} \mathbf{e}_{fs,\mathbf{p}} \\ \mathbf{e}_{fs,\mathbf{u}} \end{bmatrix}^{n} \right). \end{aligned} \tag{5.58}$$

Let $\mathbf{D} = \mathbf{MN}$ and $\mathbf{H} = \mathbf{MB}$, respectively. Then we obtain

$$\begin{aligned} \mathbf{e}_{fs}^{n+1,n_{iter}} &= \mathbf{D}^{n_{iter}}\mathbf{e}^{n+1,0} + \sum_{l=1}^{n_{iter}} \mathbf{D}^{l-1}\mathbf{H}\mathbf{e}_{fs}^{n,n_{iter}} \\ &= \mathbf{D}^{n_{iter}}(\mathbf{x}_f^{n+1} - \mathbf{x}_f^n) + \underbrace{(\mathbf{D}^{n_{iter}} + \sum_{l=1}^{n_{iter}} \mathbf{D}^{l-1}\mathbf{H})}_{\mathbf{S}}\,\mathbf{e}_{fs}^{n,n_{iter}}. \end{aligned} \tag{5.59}$$

Equation 5.59 has the same form as the drained split shown in Chapter 3 even though the components of $\mathbf{D}$ and $\mathbf{S}$ are different from those of the drained split because of the relaxation matrix $\mathbf{R}$. As discussed in Chapter 3, convergence of sequential methods requires $\|\mathbf{D}\|$ to be $O(\Delta t^m)$, where $m > 0$. We investigate $\|\mathbf{D}\|$ for the fixed-strain and fixed-stress splits in the next section using the spectral method.

5.5.1 Error amplification of the fixed-strain split

We perform one-dimensional spectral analysis for error amplification. By the fully coupled method with backward Euler time discretization, we have

$$\begin{aligned} &\frac{h}{M}\frac{P_j^{n+1} - P_j^n}{\Delta t} + \frac{bh}{\Delta t}[(-\frac{U_{j-\frac{1}{2}}^{n+1} - U_{j+\frac{1}{2}}^{n+1}}{h}) + (\frac{U_{j-\frac{1}{2}}^{n} - U_{j+\frac{1}{2}}^{n}}{h})] \\ &-\frac{k_p}{\mu h}\left(P_{j-1}^{n+1} - 2P_j^{n+1} + P_{j+1}^{n+1}\right) = 0, \end{aligned} \tag{5.60}$$

$$-(\frac{K_{dr}}{h}U_{j-\frac{3}{2}}^{n+1} - 2\frac{K_{dr}}{h}U_{j-\frac{1}{2}}^{n+1} + \frac{K_{dr}}{h}U_{j+\frac{1}{2}}^{n+1}) - b(P_{j-1}^{n+1} - P_j^{n+1}) = 0. \tag{5.61}$$

The fixed-strain split treats the displacement term U^{n+1} in Equation 5.60 explicitly as $U^{n+1,k}$, which is obtained from the previous iteration (k^{th}) step. The other variables in Equations 5.60 and 5.61 are treated implicitly as $U^{n+1,k+1}$ and $P^{n+1,k+1}$.

Then, the discretized equations by the fixed-strain split are written as

$$\frac{h}{M}\frac{P_j^{n+1,k+1}-P_j^n}{\Delta t}+\frac{bh}{\Delta t}\left((-\frac{U_{j-\frac{1}{2}}^{n+1,k}-U_{j+\frac{1}{2}}^{n+1,k}}{h})+(\frac{U_{j-\frac{1}{2}}^{n}-U_{j+\frac{1}{2}}^{n}}{h})\right)$$
$$-\frac{k_p}{\mu h}\left(P_{j-1}^{n+1,k+1}-2P_j^{n+1,k+1}+P_{j+1}^{n+1,k+1}\right)=0. \tag{5.62}$$

$$-(\frac{K_{dr}}{h}U_{j-\frac{3}{2}}^{n+1,k+1}-2\frac{K_{dr}}{h}U_{j-\frac{1}{2}}^{n+1,k+1}+\frac{K_{dr}}{h}U_{j+\frac{1}{2}}^{n+1,k+1})$$
$$-b(P_{j-1}^{n+1,k+1}-P_j^{n+1,k+1})=0. \tag{5.63}$$

Subtracting Equations 5.62 and 5.63 from Equations 5.60 and 5.61, respectively,

$$\frac{h}{M}\frac{e_{P_j}^{k+1}}{\Delta t}+\frac{bh}{\Delta t}(-\frac{e_{U_{j-\frac{1}{2}}}^{k}-e_{U_{j+\frac{1}{2}}}^{k}}{h})-\frac{k_p}{\mu}\frac{1}{h}(e_{P_{j-1}}^{k+1}-2e_{P_j}^{k+1}+e_{P_{j+1}}^{k+1})$$
$$-\frac{h}{M}\frac{e_{P_j}^{n,n_{iter}}}{\Delta t}+\frac{bh}{\Delta t}(\frac{e_{U_{j-\frac{1}{2}}}^{n,n_{iter}}-e_{U_{j+\frac{1}{2}}}^{n,n_{iter}}}{h})=0, \tag{5.64}$$

$$-\frac{K_{dr}}{h}e_{U_{j-\frac{3}{2}}}^{k+1}+2\frac{K_{dr}}{h}e_{U_{j-\frac{1}{2}}}^{k+1}-\frac{K_{dr}}{h}e_{U_{j+\frac{1}{2}}}^{k+1}-b(e_{P_{j-1}}^{k+1}-e_{P_j}^{k+1})=0. \tag{5.65}$$

Then, we neglect $e_P^{n,n_{iter}}$ and $e_U^{n,n_{iter}}$ in Equation 5.64, assuming that P^n and U^n in Equation 5.62 are the same as those in Equation 5.60, because our purpose is to investigate $\|\mathbf{D}\|$ in Equation 5.59. Then, we introduce errors of the form $e_{U_j}^k=\gamma_e^k e^{i(j)\theta}\hat{e_U}$ and $e_{P_j}^k=\gamma_e^k e^{i(j)\theta}\hat{e_P}$, where γ_e is the error amplification factor, $e^{(\cdot)}=\exp(\cdot)$, $i=\sqrt{-1}$, and $\theta\in[-\pi,\pi]$. From Equations 5.64 and 5.65, we obtain

$$\underbrace{\begin{bmatrix} \frac{h}{M}\gamma_e+\frac{k_p\Delta t}{\mu}\frac{1}{h}2\gamma_e(1-\cos\theta) & b2i\sin\frac{\theta}{2} \\ \gamma_e b2i\sin\frac{\theta}{2} & \gamma_e\frac{K_{dr}}{h}2(1-\cos\theta)\end{bmatrix}}_{\mathbf{B}_{sn}}\begin{bmatrix}\hat{e_P^k}\\ \hat{e_U^k}\end{bmatrix}=\begin{bmatrix}0\\0\end{bmatrix}. \tag{5.66}$$

Since the matrix is required to be singular, $\det \mathbf{B}_{sn} = 0$, which leads to

$$\gamma_e = 0,\ -\frac{b^2}{K_{dr}\left(\frac{1}{M} + \chi 2(1-\cos\theta)\right)},\quad \chi = \frac{k_p \Delta t}{\mu h^2}. \tag{5.67}$$

The γ_e's are equivalent to the eigenvalues of the error amplification matrix $\mathbf{G}$ defined by

$$\begin{bmatrix} e_{P_j}^{k+1} \\ e_{U_j}^{k+1} \end{bmatrix} = \mathbf{G} \begin{bmatrix} e_{P_j}^{k} \\ e_{U_j}^{k} \end{bmatrix}. \tag{5.68}$$

The two γ_e's in Equation 5.67 are distinct, and $\mathbf{G}$ can be decomposed as $\mathbf{G} = \mathbf{P}\mathbf{\Lambda}\mathbf{P}^{-1}$ (Hughes, 1987), where $\Lambda = \text{diag}\{\gamma_{e,1},\ \gamma_{e,2}\}$, as shown in Chapter 4. By recursion and Equation 5.68, the fixed-strain split yields

$$\left\|\mathbf{e}^{n+1,n_{iter}}\right\| \leq (max|\gamma_e|)^{n_{iter}} \left\|\mathbf{e}^{n+1,0}\right\|, \tag{5.69}$$

where $\mathbf{e}^{n+1,0} = \mathbf{x}_f^{n+1} - \mathbf{x}_s^{n,n_{iter}}$. From Equation 5.67, we obtain

$$\lim_{\Delta t \to 0} max|\gamma_e| = \frac{b^2 M}{K_{dr}} (\neq 0), \tag{5.70}$$

which yields $\|\mathbf{D}\| = O(1)$. Therefore, as Δt approaches zero, $\mathbf{e}_{fs}^n$ does not disappear, and the fixed-strain split with a fixed number of iterations is not a convergent scheme. Non-convergence is severe when $\|\mathbf{D}\|$ approaches unity, which is the stability limit. $\|\mathbf{D}\| \leq 1$ is also a necessary condition for stability (Turska et al., 1994), which yields $|\gamma_e| \leq 1$. The stability requirement is that the coupling strength should be less than one, which is the same as Equation 5.17.

5.5.2 Error amplification of the fixed-stress split

When we consider a fixed number of iterations for the fixed-stress split, the constraint of the fixed-stress rate becomes

$$\sigma_v^{n+1,k+1} = \sigma_v^{n+1,k}. \tag{5.71}$$

The fixed-stress split solves the flow problem using Equation 5.71, which is written as

$$\varepsilon_v^{n+1,k+1} = \varepsilon_v^{n+1,k} + \frac{b}{K_{dr}}(P^{n+1,k+1} - P^{n+1,k}). \tag{5.72}$$

Then Equation 5.62 is replaced by

$$\begin{aligned}
&\left(\frac{h}{M} + \frac{hb^2}{K_{dr}}\right)\frac{P_j^{n+1,k+1} - P_j^n}{\Delta t} - \frac{hb^2}{K_{dr}}\frac{P_j^{n+1,k} - P_j^n}{\Delta t} \\
&+\frac{bh}{\Delta t}\left((-\frac{U_{j-\frac{1}{2}}^{n+1,k} - U_{j+\frac{1}{2}}^{n+1,k}}{h}) + (\frac{U_{j-\frac{1}{2}}^{n} - U_{j+\frac{1}{2}}^{n}}{h})\right) \\
&-\frac{k_p}{\mu h}\left(P_{j-1}^{n+1,k+1} - 2P_j^{n+1,k+1} + P_{j+1}^{n+1,k+1}\right) = 0.
\end{aligned} \tag{5.73}$$

The flow equation of the fixed-stress split is the same as Equation 5.63. Subtracting Equation 5.73 from Equation 5.60 and assuming again that P^n and U^n in Equation 5.73 are the same as those in Equation 5.60, we obtain the error equation for flow as

$$\begin{aligned}
&\left(\frac{h}{M} + \frac{hb^2}{K_{dr}}\right)\frac{e_{P_j}^{k+1}}{\Delta t} - \frac{hb^2}{K_{dr}}\frac{e_{P_j}^{k}}{\Delta t} + \frac{bh}{\Delta t}(-\frac{e_{U_{j-\frac{1}{2}}}^{k} - e_{U_{j+\frac{1}{2}}}^{k}}{h}) \\
&-\frac{k_p}{\mu}\frac{1}{h}(e_{P_{j-1}}^{k+1} - 2e_{P_j}^{k+1} + e_{P_{j+1}}^{k+1}) = 0.
\end{aligned} \tag{5.74}$$

The error equation for mechanics is the same as Equation 5.65. Introducing errors of the form $e_{U_j}^k = \gamma_e^k e^{i(j)\theta}\hat{e_U}$ and $e_{P_j}^k = \gamma_e^k e^{i(j)\theta}\hat{e_P}$, Equations 5.74 and 5.65 yield

$$\underbrace{\begin{bmatrix} \left(\frac{1}{M}h + \frac{hb^2}{K_{dr}}\right)\gamma_e - \frac{hb^2}{K_{dr}} + \frac{k_p\Delta t}{\mu h}2\gamma_e(1-\cos\theta) & b2i\sin\frac{\theta}{2} \\ \gamma_e b2i\sin\frac{\theta}{2} & \gamma_e\frac{K_{dr}}{h}2(1-\cos\theta) \end{bmatrix}}_{\mathbf{B}_{ss}} \begin{bmatrix} \hat{e_P^k} \\ \hat{e_U^k} \end{bmatrix} = \begin{bmatrix} 0 \\ 0 \end{bmatrix}. \tag{5.75}$$

From $\det \mathbf{B}_{ss} = 0$, the error amplification factors for the fixed-stress split are obtained

as

$$\gamma_e = 0. \tag{5.76}$$

Then $\mathbf{G}$ can be expressed using a similarity transform as $\mathbf{G} = \mathbf{PJP^{-1}}$, (Strang, 1988), where

$$\mathbf{J} = \begin{bmatrix} 0 & 1 \\ 0 & 0 \end{bmatrix}. \tag{5.77}$$

Since $\gamma_{ss}^e = 0$, the fixed-stress split is a convergent scheme with a fixed number of iterations. Furthermore, for the linear coupled flow-geomechanics problem, exactly two iterations of the fixed-stress scheme are needed to converge to the fully coupled solution because $\mathbf{G}^2 = \mathbf{PJ}^2\mathbf{P}^{-1} = \mathbf{0}$. This assumes that the local K_{dr} is estimated exactly in the flow problem.

Remark 5.4. The local K_{dr} may not be estimated exactly in the flow problem when complex boundary conditions are present, as pointed out in Remark 5.2. Introducing the deviation factor η and following the same procedure of the spectral method described in Chapter 4, we obtain

$$\gamma_e = 0, \quad \frac{b^2\,(\eta - 1)}{\frac{K_{dr}}{M} + \eta b^2 + K_{dr}\chi 2(1 - cos\theta)}, \tag{5.78}$$

$$\lim_{\Delta t \to 0} max|\gamma_e| = \frac{|\eta - 1|}{\frac{1}{\tau} + \eta}. \tag{5.79}$$

Even though $\lim_{\Delta t \to 0} max|\gamma_e| \neq 0$, $max|\gamma_e|$ is much smaller than one because $1 \leq \eta \leq 3$, where we follow the dimension-based estimation for K_{dr}^{est} explained after Remark 5.2. Hence, $\|\mathbf{e}_{fs}\|$ decreases exponentially as we increase the number of time steps and reduce the time step size. Hence, first-order accuracy in time is obtained eventually.

Remark 5.5. If a fluid and solid grains are incompressible, $\tau = \infty$, Equation 5.79 yields

$$\lim_{\Delta t \to 0} max|\gamma_e| \quad = \quad \frac{|\eta - 1|}{\eta}. \tag{5.80}$$

If η approaches 0.5 or ∞, we have $\lim_{\Delta t \to 0} max|\gamma_e| \approx 1$, and one may suspect non-convergence even though the fixed-stress split is stable. However, in contrast to the undrained split, the fixed-stress split shows convergence for incompressibility of a fluid and solid grains because $max|\gamma_e|$ is much smaller than one if $1 \leq \eta \leq 3$, as explained in Remark 5.4.

5.6 Numerical Examples

We perform numerical experiments in order to investigate the stability and convergence behaviors. We use four test cases to study the stability. The backward Euler time integration is chosen for time discretization unless noted otherwise. The Terzaghi problem is used as a test case for convergence. We use two test cases to study the effect of the deviation factor η.

5.6.1 Stability

We reuse the same four test cases from Chapter 3, which are re-stated here for convenience.

Case 5.1 The Terzaghi problem in a 1D linear poroelastic medium, same as Case 3.1. The driving mechanical force is provided by the overburden.

Case 5.2 Injection and production in a 1D poroelastic medium, same as Case 3.2. The driving force is due to injection and production.

Case 5.3 The Mandel problem in a 2D elastic medium, same as Case 3.3. The driving force is provided by the side burden.

Case 5.4 Fluid production in 2D with elastoplastic behavior described by the modified Cam-clay model, same as Case 3.5. The compaction of the reservoir occurs due to production.

The first three cases assume linear poroelastic behavior. The numerical results are based on a one-pass (implicit-implicit) strategy per time step (i.e., staggered method) unless noted explicitly otherwise.

Case 5.1—The Terzaghi problem

The numerical values of the parameters for Case 5.1 are the same as Case 3.1. The Biot modulus M is left unspecified to test the performance of the fixed-strain and fixed-stress splits for different values of the coupling strength τ.

Figure 5.2 shows the results of the numerical experiments. Both sequential methods are stable for $\tau = 0.83 < 1$ (Figure 5.2 (top)). The fixed-strain split, however, is unstable for $\tau = 1.21 > 1$ (Figure 5.2 (bottom)). On the other hand, the fixed-stress split is stable for $\tau = 1.21 > 1$ (Figure 5.2 (bottom)). Even in the region of stability, the fixed-strain split produces wildly oscillatory solutions, in agreement with the predictions of the Von Neumann stability analysis.

Case 5.2—1D fluid injection and production

The parameter values for Case 5.2 are the same as Case 3.2, and the Biot modulus M is left unspecified as for Case 5.1. Figure 5.3 shows the results from the numerical simulations, which support the same conclusion as in Case 5.1. When the coupling strength, τ, is less than one, both sequential methods are stable. The fixed-strain split is unstable when τ is greater than one, and it produces an oscillatory solution even when it is stable (in this case, the oscillations are relatively small). On the other hand, the fixed-stress split is stable and nonoscillatory in all cases.

Independence of stability limit on time step size for the fixed-strain split

Equation 5.17 indicates that the stability limit for the fixed-strain split is independent of time step size when $0.5 \leq \alpha \leq 1.0$. Two time step sizes are considered: $\Delta t_d = 4.4 \times 10^{-2}$ and $\Delta t_d = 4.4 \times 10^{-5}$. The fixed-strain split is stable for both time step sizes when the

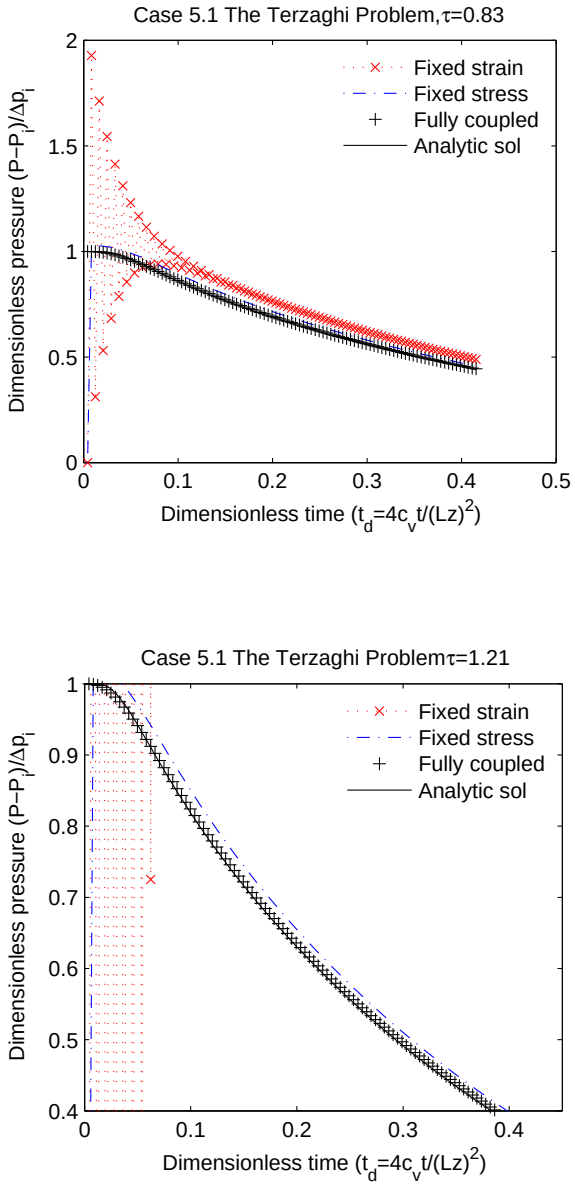

Figure 5.2: Case 5.1 (the Terzaghi problem). Evolution of the dimensionless pressure as a function of dimensionless time. Shown are the results for the fully coupled method, the fixed-strain, and fixed-stress splits. Top: coupling strength $\tau = 0.83$. Bottom: coupling strength $\tau = 1.21$.

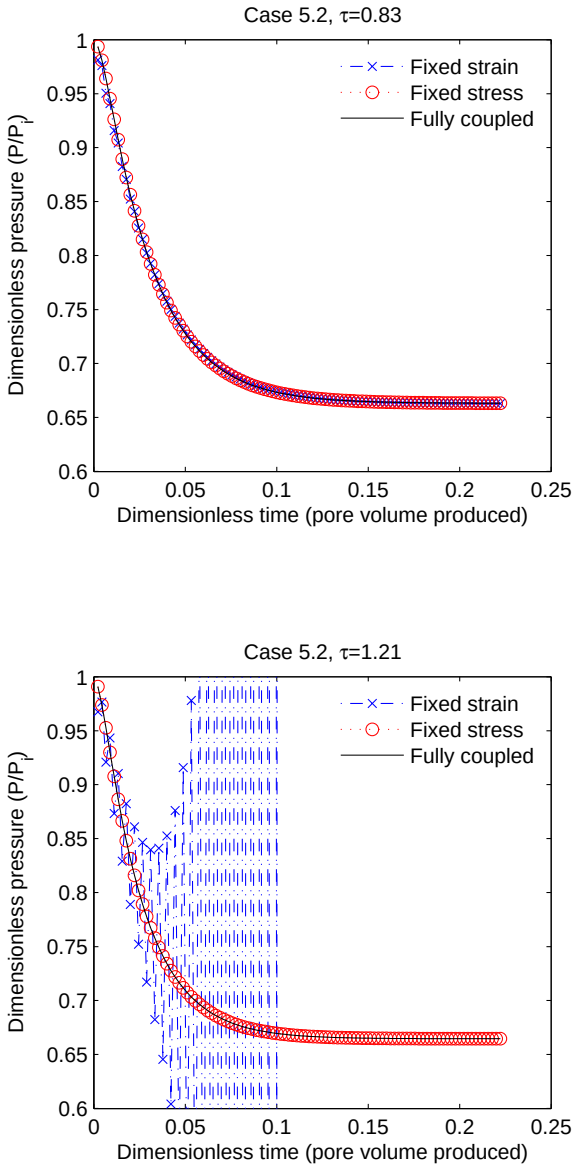

Figure 5.3: Case 5.2 (1D injection–production problem). Evolution of the dimensionless pressure as a function of dimensionless time (pore volume produced). Shown are the results for the fully coupled method, the fixed-strain, and fixed-stress splits. Top: coupling strength $\tau = 0.83$. Bottom: coupling strength $\tau = 1.21$.

coupling strength is less than one ($\tau = 0.95$, Fig. 5.4 (top)). The stability of the fixed-strain split is not improved by reducing the time step size. Thus, physical problems with large coupling strength ($\tau > 1$) cannot be solved by the fixed-strain split (Fig. 5.4 (bottom)).

The results from Figures 5.2–5.4 indicate that the stability criterion of the fixed-strain split is quite sharp. The fixed-strain split yields severe oscillatory behaviors even in its stability range, which is explained by the negative amplification factor.

Midpoint rule for time integration

We consider the midpoint rule for time discretization ($\alpha = 0.5$ for both mechanics and flow). Here, $K_{dr} = 1\ GPa$ and the other data are the same as Case 5.2. Figure 5.5 shows the stability behaviors for $\alpha = 0.5$ when $\tau = 0.83$ (top) and $\tau = 1.11$ (bottom). The fixed-strain split is stable when $\tau < 1$ whereas it is unstable when $\tau > 1$, which supports our a-priori stability estimates from the Von Neumann method. Furthermore, while the drained split with the midpoint rule is unconditionally unstable, as shown in Chapter 3, the fixed-strain split with the midpoint rule is conditionally stable. The fixed-stress split, however, is unconditionally stable when $\tau \geq 1$, as shown in the bottom plot of Figure 5.5. This supports the a-priori stability estimate in Equations 5.17 and 5.24.

The deviation factor η

We use Case 5.2 with the backward Euler time discretization in order to validate the stability estimate of Equation 5.26, where $\tau = 3.33$ and $\tau = \infty$. From Equation 5.26, the stability condition becomes $\eta \geq 0.35$ for $\tau = 3.33$ and $\eta \geq 0.5$ for $\tau = \infty$. Figure 5.6 shows the pressure history with respect to time for $\tau = 3.33$ and $\tau = \infty$. On the top of Figure 5.6, $\eta = 0.33$ leads to instability, but $\eta = 0.37$ yields a stable solution when $\tau = 3.33$. The bottom of Figure 5.6 also shows that $\eta = 0.48$ causes instability whereas $\eta = 0.52$ leads to stability when $\tau = \infty$. Figure 5.6 supports the fact that the stability estimate of Equation 5.26 is quite sharp.

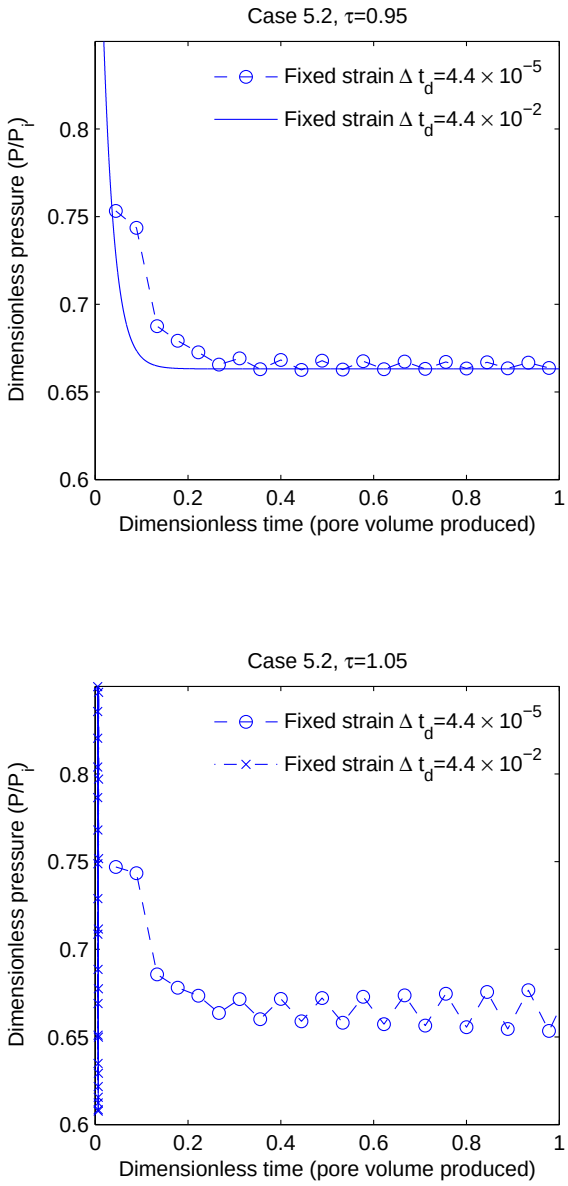

Figure 5.4: Case 5.2 (1D injection–production problem). Results are shown for the fixed-strain split, with two different coupling strengths: $\tau = 0.95$ (top), and $\tau = 1.05$ (bottom), and two very different time step sizes. The stability of the fixed-strain split is independent of time step size. The fixed-strain split is stable if $\tau < 1$ and unstable if $\tau > 1$, regardless of time step size.

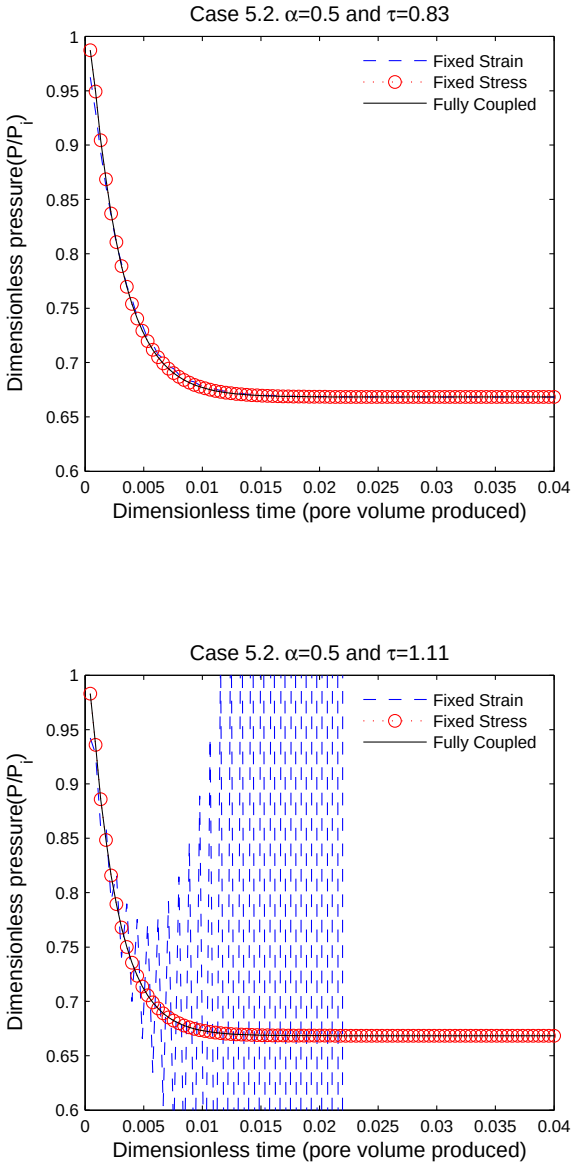

Figure 5.5: 1D problem with injection and production (Case 5.2). $K_{dr} = 1\ GPa$. $\alpha = 0.5$ for both flow and mechanics is considered. Top: $\tau = 0.83$. Bottom: $\tau = 1.11$.

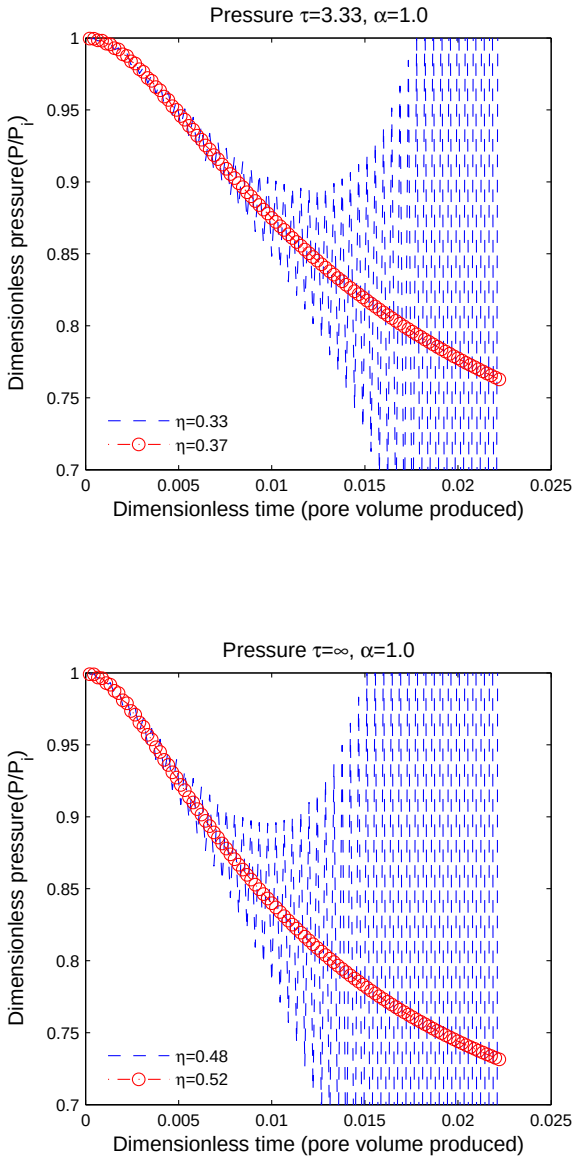

Figure 5.6: Stability behaviors of different η's and τ's. Top: pressure history at the observation well when $\tau = 3.33$. Bottom: pressure history at the observation well when $\tau = \infty$.

Behavior for high coupling strength

In this and the previous chapters, we have shown that, unlike the drained and fixed-strain splits, the undrained and fixed-stress splits are unconditionally stable. We have not addressed, however, the efficiency of the methods.

Figure 5.7 shows a comparison between the undrained and fixed-stress splits for Cases 5.1 and 5.2, at very high coupling strength. In these cases, the undrained split requires many iterations to match the fully coupled solution, while the fixed-stress split does so with only one iteration per time step. In particular, we have shown in Chapter 4 that the undrained split is not convergent for incompressibility of the fluid and the solid grains. On the other hand, the fixed-stress split takes only one iteration in Case 5.2 and two iterations in Case 5.1 in order to yield a virtually exact match with the fully coupled method. The flow problem for the first iteration in the Terzaghi problem (Case 5.1) is trivial, since the driving force is instantaneous loading from the mechanical problem.

This result implies that the fixed-stress split yields almost the same solution as the fully coupled method with one or two iterations. This behavior is consistent with the fact that the error amplification factor of the fixed-stress split is zero.

Case 5.3—The Mandel problem

Figure 5.8 indicates that the fixed-strain split (top) is stable for $\tau < 1$, while it is unstable when $\tau > 1$. Similar to the drained split, the fixed-strain split can yield the severe oscillations at early time. Due to the oscillations, the early time solution is not computed properly by the fixed-strain split, even though the late time solution converges to the analytical result. The fixed-stress split, on the other hand, is stable and non-oscillatory under all conditions as shown in Figure 5.8. The *Mandel–Cryer effect* can be also captured by the fixed-stress split showing good agreement with the analytical solution.

For the vertical and horizontal displacements, the fixed-strain split causes severe oscillations even though it is stable (the top of Figures 5.9 and 5.10). But, when the coupling strength is greater than one, the fixed-strain split is unstable (the bottom of Figures 5.9

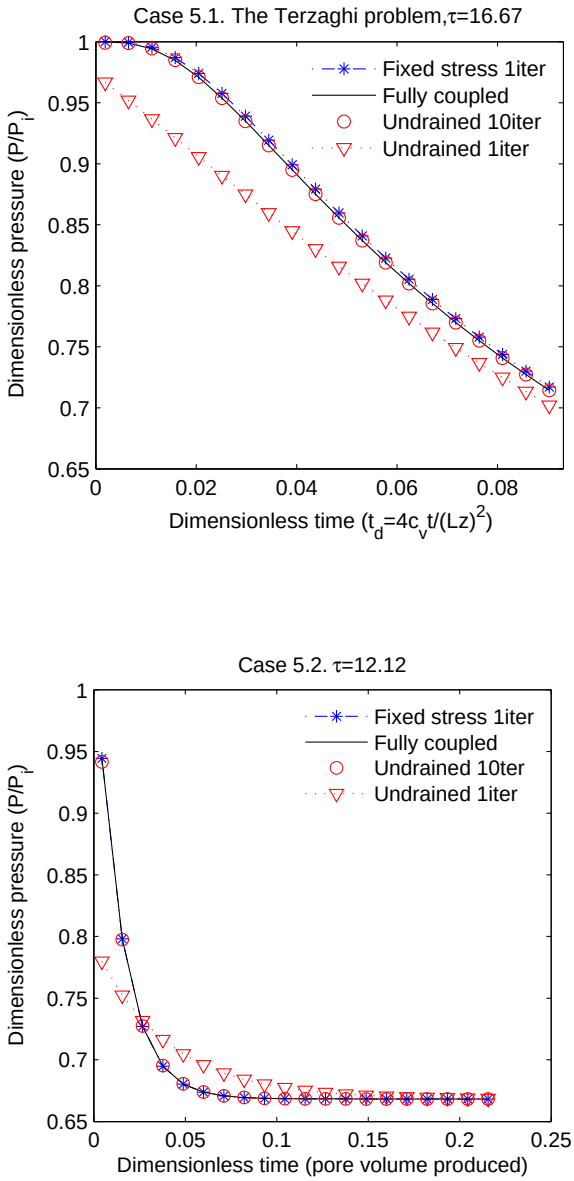

Figure 5.7: Behavior of the undrained and fixed-stress splits for cases with high coupling strength. Top: Case 5.1 with $\tau = 16.67$. Bottom: Case 5.2 with $\tau = 12.12$. In both cases, the fixed-stress split requires one single iteration per time step to match the fully coupled solution, while many iterations are required for the undrained split.

and 5.10). This behavior is the same as the drained split. However, the solutions from the fixed-stress split are stable regardless of the coupling strength, and they match the analytical solutions.

Case 5.4—Fluid production scenario in 2D with elastoplasticity

We consider a nonlinear poroelastoplastic problem using the staggered method, where the numerical stability is compared with a-priori stability estimates of the fixed-strain and fixed-stress splits. The modified Cam-clay model is used for plastic modeling (Borja and Lee, 1990; Borja, 1991). We adopt the associative plasticity formulation (Coussy, 1995; Simo, 1991; Simo and Hughes, 1998) for Case 5.4. We use the backward Euler time discretization. The input values for Case 5.4 are the same as Case 3.5.

In Case 5.4, compaction occurs because of production. As a result, subsidence occurs and the fluid pressure decreases. Figure 5.11 shows that the fixed-strain split becomes unstable when it enters the plastic regime, even though it is stable in the elastic regime. This is because plasticity increases the coupling strength beyond unity. The fixed-stress split is, however, stable in the plastic regime. Around $t_d = 0.018$, we observe some roughness in the pressure solution because we treat the relaxation term b^2/K_{dr} explicitly. The solution from fixed-stress split is slightly different from the fully coupled solution, since one iteration is performed. But, when two iterations are taken, the solutions by the fixed-stress split match those from the fully coupled method, as shown in Figure 5.11. That figure also shows that plasticity can slow down the rate of decline in the reservoir pressure.

Staggered Newton schemes for Case 5.4

We apply a staggered Newton scheme to Case 5.4. Figure 5.12 shows that the fixed-strain split is stable during the early-time elastic regime, which has a weak coupling strength ($\tau < 1$). However, when plasticity is reached, the solution by the fixed-strain method is no longer stable because the coupling strength increases beyond unity. The bottom of Figure 5.11 shows the variation of the coupling strength during the simulation. It is clear that when the coupling strength increases beyond unity, the solution by the fixed-strain

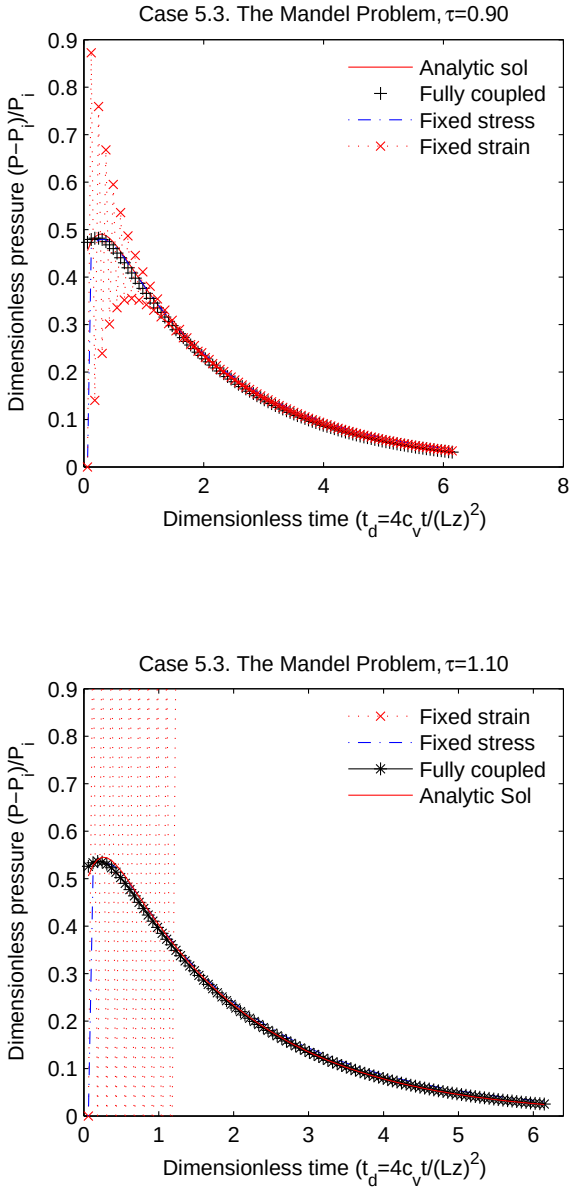

Figure 5.8: Case 5.3 (the Mandel problem). Evolution of the pressure at the observation well as a function of dimensionless time. Shown are the results for the fully coupled, fixed-strain, and fixed-stress split methods. Top: $\tau = 0.90$. Bottom: $\tau = 1.10$.

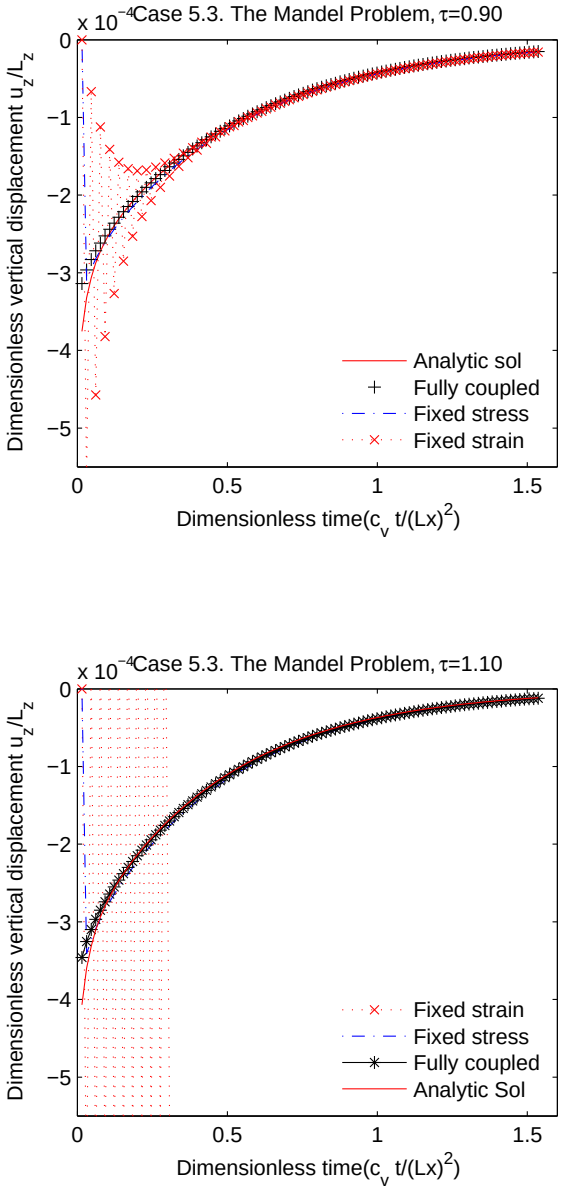

Figure 5.9: Case 5.3 (the Mandel problem). Evolution of the dimensionless vertical displacement on the top as a function of dimensionless time. Shown are the results for the fully coupled, fixed-strain, and fixed-stress split methods. Top: $\tau = 0.90$. Bottom: $\tau = 1.10$.

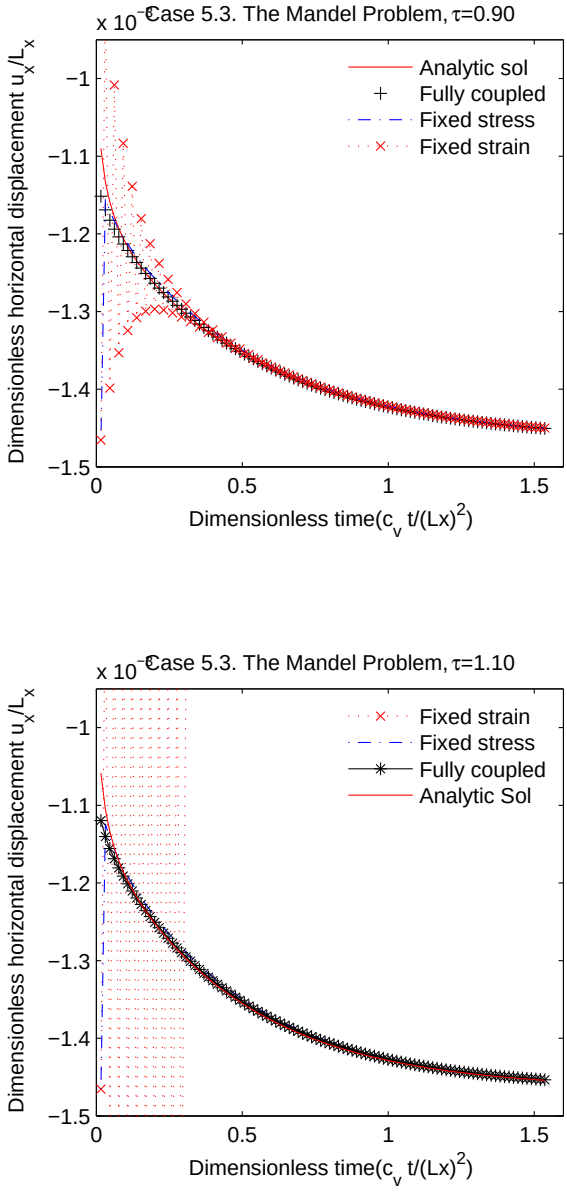

Figure 5.10: Case 5.3 (the Mandel problem). Evolution of the dimensionless horizontal displacement on the right side as a function of dimensionless time. Shown are the results for the fully coupled, fixed-strain, and fixed-stress split methods. Top: $\tau = 0.90$. Bottom: $\tau = 1.10$.

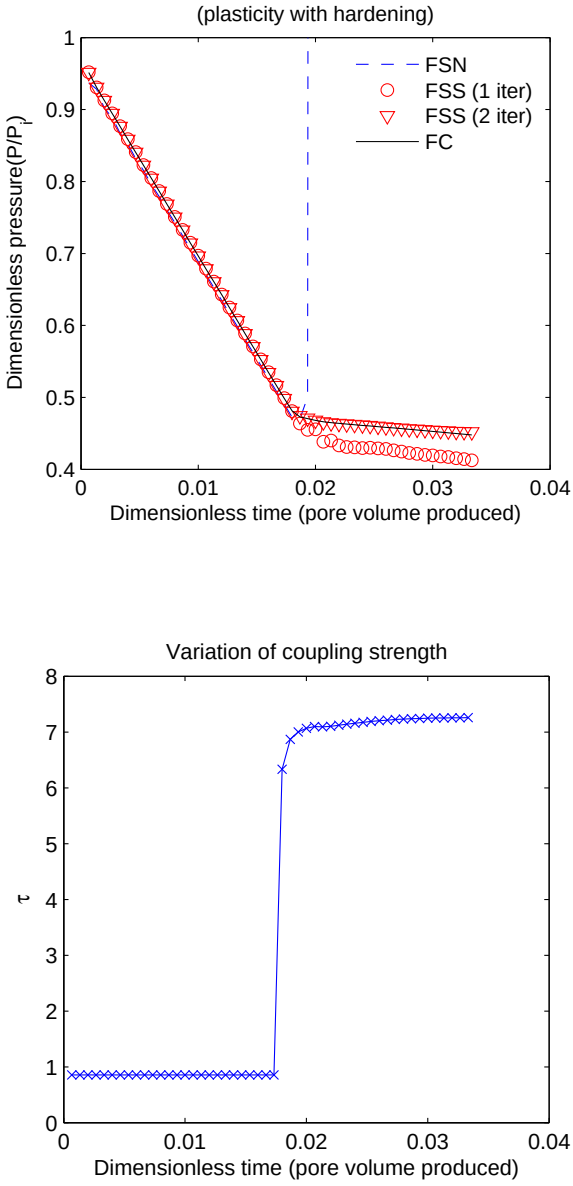

Figure 5.11: 2D problem with a production well (Case 5.4). Top: the history of pressure. Bottom: the history of the coupling strength. FSN and FSS indicate the fixed-strain and fixed-stress splits, respectively. The model enters the plastic regime at $t_d \approx 0.018$. Beyond this point, the fixed-strain split becomes unstable.

split becomes unstable during iterations (Figures 5.12). No solution by the fixed-strain split is possible after plasticity. On the other hand, the fully coupled and fixed-stress split methods provide stable results well into the plastic regime, as shown in Figure 5.12.

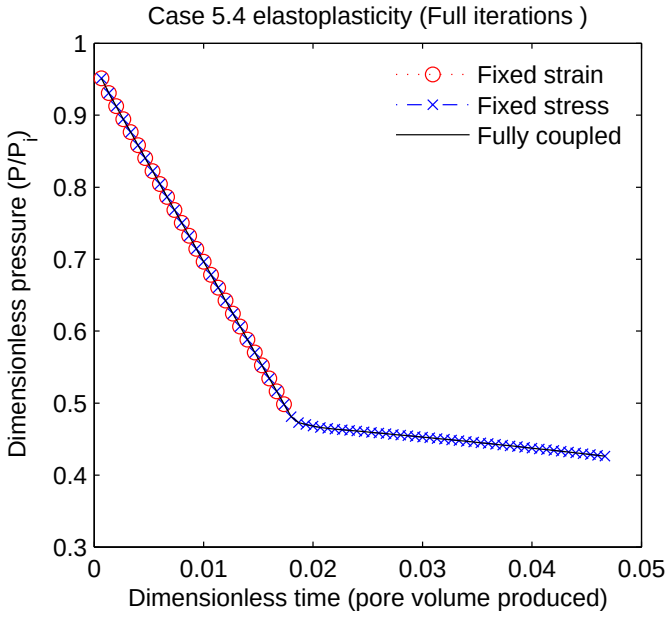

Figure 5.12: Case 5.4 (2D production problem in elastoplastic regime). Shown is the evolution of the dimensionless pressure at the observation well against dimensionless time (pore volume produced). Once the model enters the plastic regime, the fixed-strain split becomes unstable and fails to produce a solution at all.

5.6.2 Convergence

The Terzaghi problem (Case 5.1) - one-dimensional consolidation - is used for convergence analysis. The coupling strength τ is 0.95, and other input data are same as Case 5.1. We determine true solutions of pressure and displacement by the fully coupled method with very small time step sizes.

Figure 5.13 shows the errors between the true and numerical solutions using the fixed-strain, fixed-stress, and fully coupled methods with respect to time step size when a fixed number of iterations is performed. The errors in dimensionless pressure and displacement are measured by the L^2 norm.

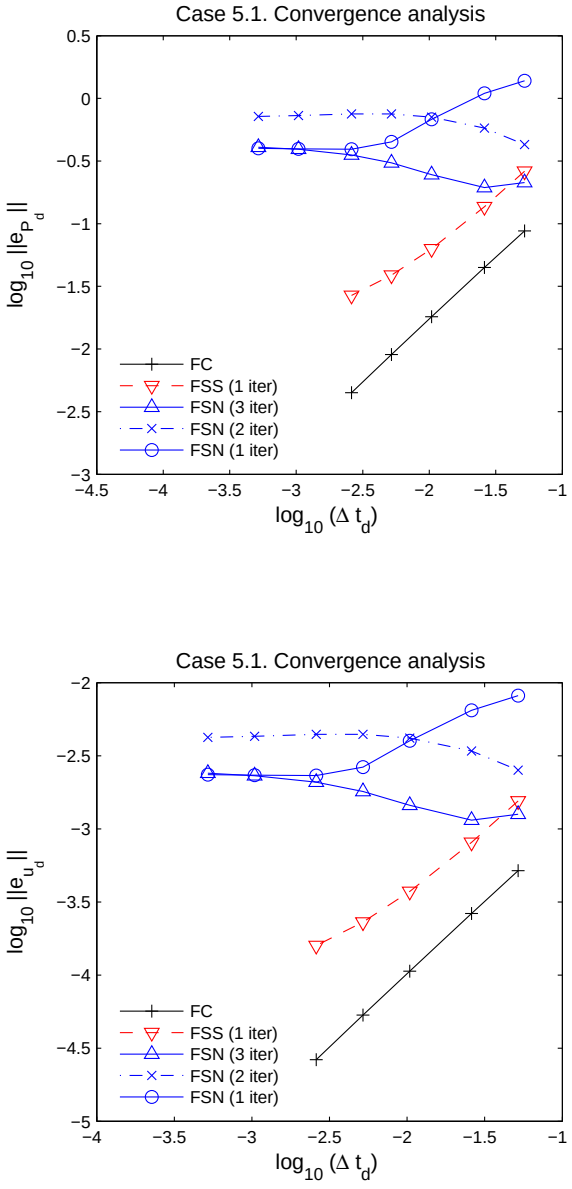

Figure 5.13: Convergence analysis of Case 5.1 on pressure (top) and displacement (bottom). $\Delta t_d = 4c_v \Delta t / {L_z}^2$. FC, FSS, and FSN indicate the fully coupled, fixed-stress, and fixed-strain split methods, respectively. The fixed-strain split shows zeroth-order accuracy. But, the fixed-stress split yields first-order accuracy.

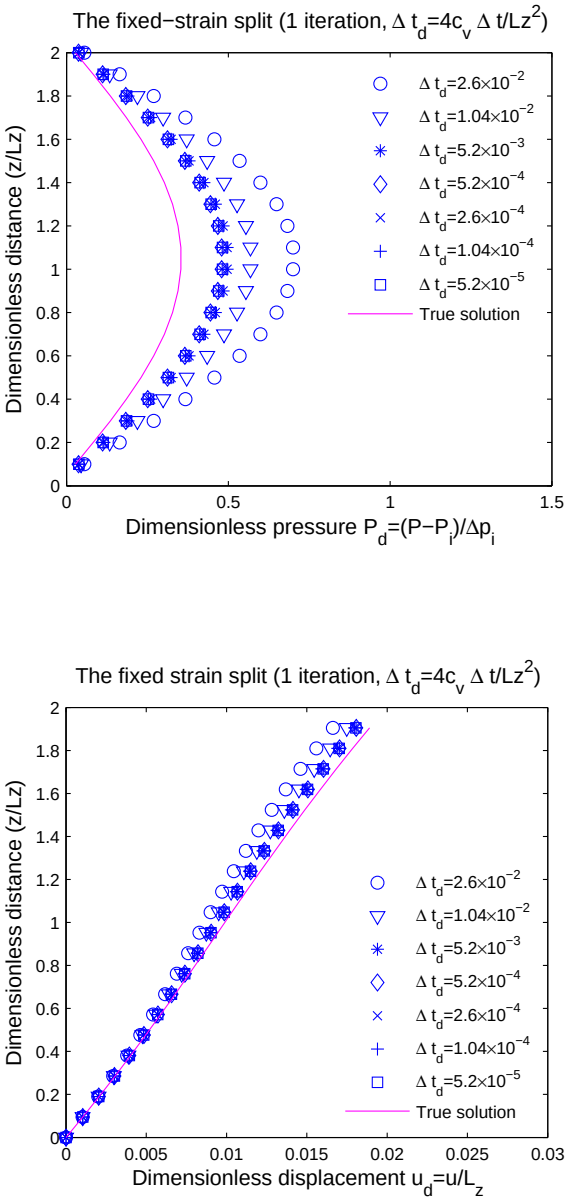

Figure 5.14: Non-convergence of the fixed-strain split with one iteration for Case 5.1: pressure (top) and displacement (bottom)

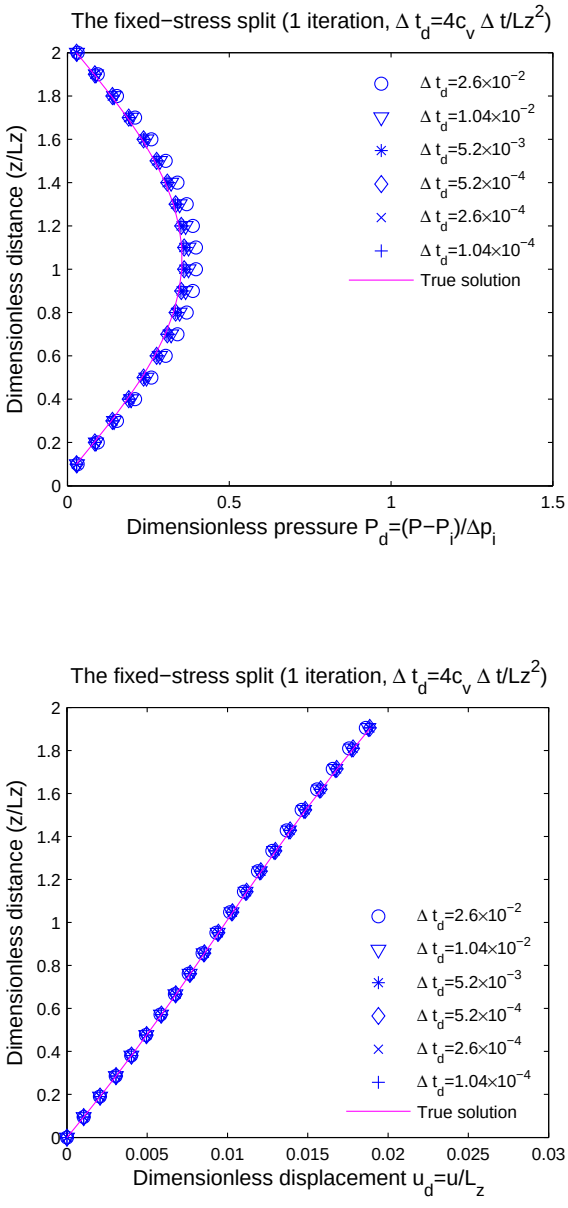

Figure 5.15: Convergence of the fixed-stress split with one iteration for Case 5.1: pressure (top) and displacement (bottom)

From Figure 5.13, the fixed-stress and fully coupled methods are convergent with one iteration, showing that the errors decrease as $O(\Delta t)$ as the time step size is refined. This also confirms that the fixed-stress and fully coupled methods have $O(\Delta t)$ error in time. However, the fixed-strain split does not show convergence, but yields zeroth-order accuracy ($O(1)$). Figures 5.14 and 5.15 show the spatial distributions of pressure and displacement by the fixed-strain and fixed-stress splits, respectively. As the time step size is refined, the fixed-strain split with one iteration does not converge to the true solution but to a different solution (Figure 5.14), whereas the fixed-stress spit with one iteration converges to the true solution (Figure 5.15). The numerical results for Case 5.1 support our a-priori error estimates of the fixed-strain and fixed-stress splits from Equations 5.67 and 5.76.

When full iterations are performed for Cases 5.1 and 5.4, the fixed-stress split takes a maximum of two iterations to converge to the solutions from the fully coupled method. Cases 5.2 and 5.4 take one and two iterations, respectively, to match the fully coupled method. These results are consistent with our a-priori estimates of the convergence rate of the fixed-stress split (i.e., $\mathbf{G}^2 = 0$ in Equation 5.77). Note that a few more iterations may be required in the presence of complex boundary conditions, even for elasticity because we do not have accurate estimates of the local K_{dr} in the flow problem.

5.6.3 Effect of the deviation factor η

Since the local K_{dr} is not known a-priori for complex boundary conditions and production scenarios, we investigate the effect of the deviation factor η on the fixed-stress split. We use two test cases adopting the backward Euler time discretization.

Case 5.5 Two dimensional consolidation problem with a constrained boundary (the left picture in Figure 5.16). This is equivalent to a half domain of the Terzaghi problem by symmetry. The true K_{dr} is K_{dr}^{1D}, and the porous medium is elastic.

Case 5.6 Two dimensional consolidation problem with a unconstrained boundary (the right picture in Figure 5.16). The true K_{dr} is close to K_{dr}^{2D}, and the porous medium is elastic.

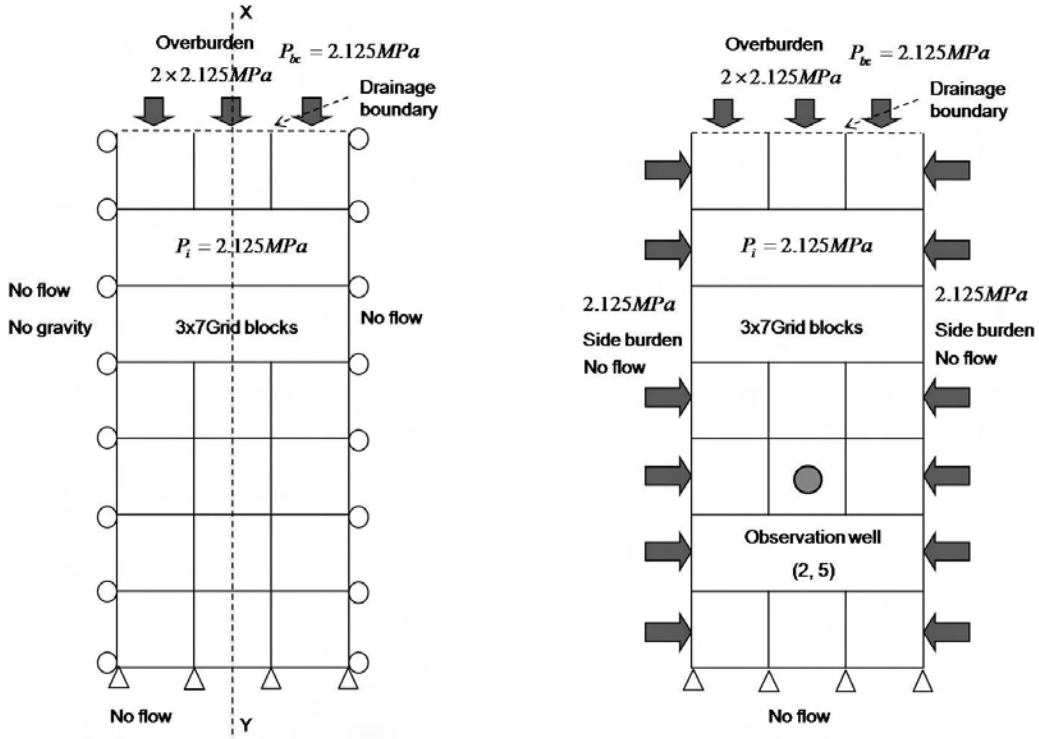

Figure 5.16: Two test cases to investigate the effect of different η's. Case 5.5: consolidation problem with constrained boundary (left picture). Case 5.6: consolidation problem with unconstrained boundary (right picture).

For Case 5.5, the dimension of the domain is $3\ m \times 14\ m$ with 3×7 grid blocks under the plane strain mechanical condition. The domain is homogeneous. Grid spacings, Δx and Δz are $1\ m$ and $2\ m$, respectively. The domain has an overburden $\bar{\sigma} = 2 \times 2.125\ MPa$ on the top, no horizontal displacement boundary on both sides, and no vertical or horizontal displacement at the bottom. The bulk density of the porous medium is $\rho_b = 2400\ kg\ m^{-1}$. Initial fluid pressure is $P_i = 2.125\ MPa$. The fluid density and viscosity are $\rho_{f,0} = 1000\ kg\ m^{-1}$ and $\mu = 1.0\ cp$, respectively. Permeability is $k_p = 50\ md$, and porosity is $\phi_0 = 0.3$. Young's modulus is $E = 500\ MPa$, and Poisson's ratio is $\nu = 0.0$. The Biot coefficient is $b = 1.0$. The observation well is located at (2,5). We have a drainage boundary for flow on the top, where the boundary fluid pressure is $P_{bc} = 2.125\ MPa$. No-flow boundary conditions are applied to both sides and the bottom. Gravity is neglected.

We investigate the convergence behavior of the fixed-stress split with $K_{dr}^{est} = K_{dr}^{3D}$ and $\tau = \infty$, where $M = \infty$. We assume a less stiff bulk modulus compared with the true bulk modulus. From $\nu = 0.0$, we obtain $\eta = 3.0$, which is the maximum deviation factor according to the dimension-based estimation of K_{dr}^{est}. Figure 5.17 shows the convergence behavior of pressure. On the top of Figure 5.17, we confirm first-order accuracy explained in Remark 5.4. The bottom of Figure 5.17 shows clearly that the pressure profile along the X-Y line in Figure 5.16 converges to the true solution by the fixed-stress split when $\eta = 3.0$.

For Case 5.6, the domain has a side burden $\bar{\sigma_h} = 2.125\ MPa$ on both sides instead of the no-horizontal displacement condition in Case 5.5. The other data are the same as Case 5.5. We take two stiffer and one less stiff bulk moduli for K_{dr}^{est} compared with the true bulk modulus. If we select K_{dr}^{1D} for K_{dr}^{est}, η is close to the stability limit of 0.5, because the true K_{dr} is close to K_{dr}^{2D}. For this reason, we consider $K_{dr}^{est} = 0.95 \times K_{dr}^{1D}$ and $K_{dr}^{est} = 1.05 \times K_{dr}^{1D}$, yielding $\eta \approx 0.48$ and $\eta \approx 0.52$, respectively. In Figure 5.18, $K_{dr}^{est} = 0.95 \times K_{dr}^{1D}$ provides stability, but with severe oscillations. Using $K_{dr}^{est} = 1.05 \times K_{dr}^{1D}$ causes instability. Figure 5.18 shows that using $K_{dr}^{est} = K_{dr}^{3D}$, we match the true solution, capturing the initial rise of pressure (Mandel-Cryer effect). Thus, it is better to take a less stiff bulk modulus when the true K_{dr} is not known a-priori. The fixed-stress split uses the dimension-based estimation for K_{dr}^{est}, which yields high accuracy without oscillations.

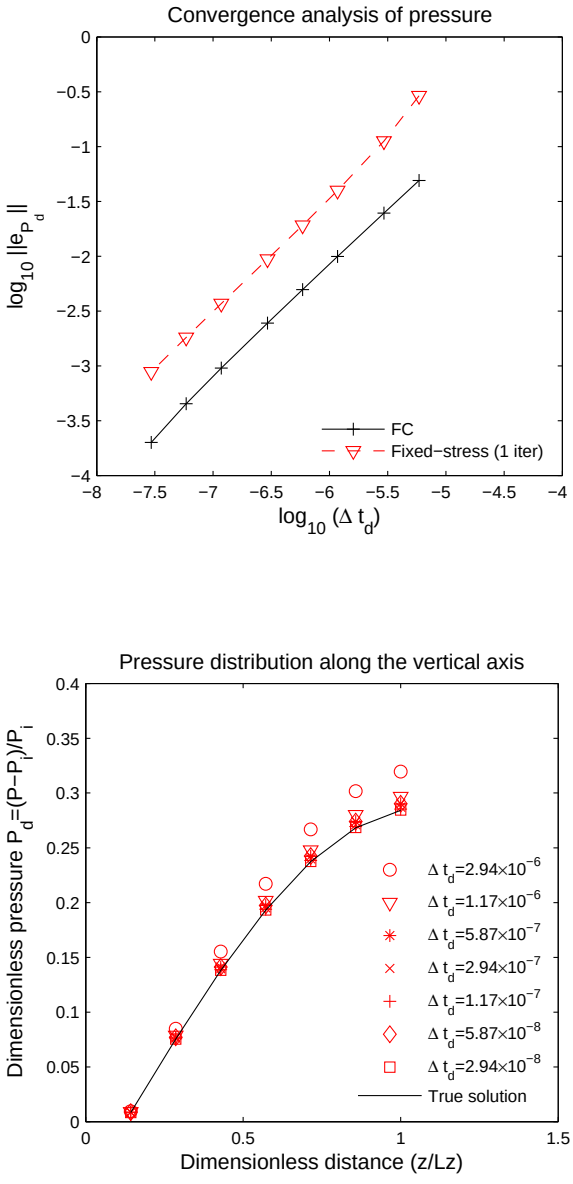

Figure 5.17: Convergence of the fixed-stress split for Case 5.5 when $K_{dr}^{est} = K_{dr}^{3D}$. Top: convergence of pressure. Bottom: pressure distribution along the vertical axis (X-Y section). $\Delta t_d = 4c_v\Delta t/L_xL_z$.

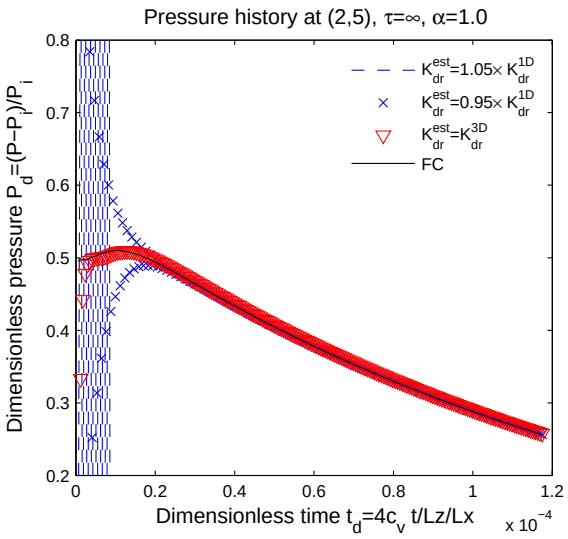

Figure 5.18: Pressure history at the observation well (2,5) for Case 5.6 with different deviation factors when $0.95 \times K_{dr}^{1D}$, $1.05 \times K_{dr}^{1D}$, and K_{dr}^{3D} are taken for K_{dr}^{est}.

Chapter 6

Coupled Multiphase Flow and Geomechanics

6.1 Sequential Methods for Multiphase Flow

Here, we analyze the stability and convergence of sequential implicit methods for multiphase flow. Let us denote by $\mathcal{A}^m$ the original operator of coupled multiphase flow and mechanics, shown in Equations 2.1 and 2.2 in Chapter 2. The superscript m in the operators, $(\cdot)^m$, means multiphase. Using the fully coupled method, the discrete approximation of $\mathcal{A}^m$ is written as:

$$\begin{bmatrix} \boldsymbol{u}^n \\ \boldsymbol{p}_J^n \end{bmatrix} \xrightarrow{\mathcal{A}_{fc}^m} \begin{bmatrix} \boldsymbol{u}^{n+1} \\ \boldsymbol{p}_J^{n+1} \end{bmatrix}, \quad \text{where} \quad \mathcal{A}_{fc}^m : \begin{cases} \operatorname{Div} \boldsymbol{\sigma} + \rho_b \boldsymbol{g} = \boldsymbol{0}, \\ \dot{m}_J + \operatorname{Div} \boldsymbol{w}_J = (\rho f)_J, \end{cases} \tag{6.1}$$

where we solve the coupled problem simultaneously using the Newton-Raphson method. Then the fully coupled method leads to the following system of Equations:

$$\underbrace{\begin{bmatrix} \boldsymbol{K}_m & -\boldsymbol{L}^T{}_m \\ \boldsymbol{L}_m & \boldsymbol{F}_m \end{bmatrix}}_{\boldsymbol{J}_{fc,m}} \begin{bmatrix} \delta \boldsymbol{u} \\ \delta \boldsymbol{p}_J \end{bmatrix}^{n+1,k} = - \begin{bmatrix} \boldsymbol{R}^u \\ \boldsymbol{R}_J^p \end{bmatrix}^{n+1,k}, \tag{6.2}$$

where $\boldsymbol{J}_{fc,m}$, $\boldsymbol{K}_m$, and $\boldsymbol{L}_m$ are the Jacobian, stiffness, and coupling matrices, respectively. $\boldsymbol{F}_m = \boldsymbol{Q}_m + \Delta t \boldsymbol{T}_m$ is the flow matrix, where $\boldsymbol{Q}_m$ is the compressibility matrix, and $\boldsymbol{T}_m$ is the transmissibility matrix. The subscript m, $(\cdot)_m$, implies multiphase.

Similar to our treatment of single-phase flow in the previous chapters, we split the original operator of coupled multiphase flow and mechanics. When only a single pass strategy is used, in which the two problems are solved implicitly and in sequence, we refer to the scheme as a staggered method.

We can also apply sequential methods to the fully coupled problem by adopting a staggered Newton scheme (Schrefler et al., 1997), where full iterations are performed as shown for single phase with elastoplasticity in Chapters 3 and 5. In this scheme, we linearize the governing equations first, and then we solve the linearized equations sequentially with full iterations. Then, $\boldsymbol{J}_{fc,m}$ is approximated by $\boldsymbol{J}_{sq,m}$, the Jacobian matrix of the sequential method of interest.

6.1.1 Drained split

In the drained split, we freeze the pressure of all the fluid phases when solving the mechanical problem. The drained split approximates the operator $\mathcal{A}^m$ as

$$\begin{bmatrix} \boldsymbol{u}^n \\ \boldsymbol{p}_J^n \end{bmatrix} \xrightarrow{\mathcal{A}_{dr}^{u,m}} \begin{bmatrix} \boldsymbol{u}^{n+1} \\ \boldsymbol{p}_J^n \end{bmatrix} \xrightarrow{\mathcal{A}_{dr}^{p,m}} \begin{bmatrix} \boldsymbol{u}^{n+1} \\ \boldsymbol{p}_J^{n+1} \end{bmatrix}, \quad \text{where} \quad \begin{cases} \mathcal{A}_{dr}^{u,m} : \operatorname{Div} \boldsymbol{\sigma} + \rho_b \boldsymbol{g} = \boldsymbol{0}, \ \delta p_J = 0 \\ \mathcal{A}_{dr}^{p,m} : \dot{m}_J + \operatorname{Div} \boldsymbol{w}_J = (\rho f)_J, \\ \qquad\qquad \dot{\boldsymbol{\varepsilon}} : \text{prescribed}, \end{cases} \tag{6.3}$$

where the variation of fluid pressure is frozen during the mechanics step (i.e. $\delta p_J = 0$). When a staggered Newton scheme is used with the drained split, the constraint $\delta p_J = 0$ for the linearized mechanical problem becomes $p_J^{k+1} = p_J^k$.

6.1.2 Undrained split

Similar to single-phase flow treatment, the undrained split decomposes the original operator $\mathcal{A}^m$ into

$$\begin{bmatrix} \boldsymbol{u}^n \\ \boldsymbol{p}_J^n \end{bmatrix} \xrightarrow{\mathcal{A}_{ud}^{u,m}} \begin{bmatrix} \boldsymbol{u}^{n+1} \\ \boldsymbol{p}_J^* \end{bmatrix} \xrightarrow{\mathcal{A}_{ud}^{p,m}} \begin{bmatrix} \boldsymbol{u}^{n+1} \\ \boldsymbol{p}_J^{n+1} \end{bmatrix}, \quad \text{where} \quad \begin{cases} \mathcal{A}_{ud}^{u,m} : \operatorname{Div} \boldsymbol{\sigma} + \rho_b \boldsymbol{g} = \mathbf{0}, \ \delta m_J = 0, \\ \mathcal{A}_{ud}^{p,m} : \dot{m}_J + \operatorname{Div} \boldsymbol{w}_J = (\rho f)_J, \\ \qquad \dot{\boldsymbol{\varepsilon}} : \text{prescribed}, \end{cases} \tag{6.4}$$

where we freeze all mass variation of the fluids when solving the mechanical problem (i.e. $\delta m_J = 0$). The intermediate pressure, p_J^*, is calculated locally and explicitly after we obtain the displacement, $\boldsymbol{u}^{n+1}$. Then, the intermediate pressure is used for the flow problem. When the undrained split is used with a staggered Newton method, the constraint $\delta m_J = 0$ for the linearized mechanical problem becomes $m_J^{k+1} = m_J^k$.

Remark 6.1. From Equations 2.44 – 2.46 in Chapter 2, the constraint $\delta m_J = 0$ yields

$$\mathbf{p}^* - \mathbf{p}^n = -\mathbf{N}^{-1}\mathbf{b}\left(\boldsymbol{\varepsilon}_v^{n+1} - \boldsymbol{\varepsilon}_v^n\right), \tag{6.5}$$

where $\mathbf{p} = \{p_J\}$. Equation 6.5 requires calculation of $\mathbf{N}^{-1}\mathbf{b}$ locally. $\mathbf{N}^{-1} = \mathbf{M}$ can be computed numerically or analytically (e.g., inversion of a 2×2 matrix for two phase flow). This additional computational cost is negligible compared with solving the global flow equation.

In the staggered Newton method, $m^{k+1} = m^k$ for the linearized mechanical problem yields

$$\mathbf{p}^* - \mathbf{p}^k = -\mathbf{N}^{-1}\mathbf{b}\left(\boldsymbol{\varepsilon}_v^{k+1} - \boldsymbol{\varepsilon}_v^k\right). \tag{6.6}$$

6.1.3 Fixed-strain split

Using the fixed-strain split, the original operator $\mathcal{A}^m$ is split as

$$\begin{bmatrix} \boldsymbol{u}^n \\ \boldsymbol{p}_J^n \end{bmatrix} \xrightarrow{\mathcal{A}_{sn}^{p,m}} \begin{bmatrix} \boldsymbol{u}^* \\ \boldsymbol{p}_J^{n+1} \end{bmatrix} \xrightarrow{\mathcal{A}_{sn}^{u,m}} \begin{bmatrix} \boldsymbol{u}^{n+1} \\ \boldsymbol{p}_J^{n+1} \end{bmatrix}, \quad \text{where} \quad \begin{cases} \mathcal{A}_{sn}^{p,m} : \dot{m}_J + \operatorname{Div} \boldsymbol{w}_J = (\rho f)_J, \ \delta\dot{\varepsilon}_v = 0 \\ \mathcal{A}_{sn}^{u,m} : \operatorname{Div} \boldsymbol{\sigma} + \rho_b \boldsymbol{g} = \boldsymbol{0}, \ p_J : \text{prescribed}, \end{cases} \tag{6.7}$$

where we freeze $\dot{\varepsilon}_v$ for the flow problem, $\delta\dot{\boldsymbol{\varepsilon}} = 0$, since the shear strain field does not affect the flow problem. In the staggered method, the constraint $\delta\dot{\varepsilon}_v = 0$ becomes

$$\varepsilon_v^{n+1} - \varepsilon_v^n = \varepsilon_v^n - \varepsilon_v^{n-1}. \tag{6.8}$$

In the staggered Newton method, the fixed-strain split has the constraint $\dot{\varepsilon}_v^{k+1} = \dot{\varepsilon}_v^k$ for the linearized flow problem, which yields

$$\varepsilon_v^{k+1} - \varepsilon_v^n = \varepsilon_v^k - \varepsilon_v^n. \tag{6.9}$$

6.1.4 Fixed-stress split

The fixed-stress approach splits the original operator $\mathcal{A}^m$ as follows:

$$\begin{bmatrix} \boldsymbol{u}^n \\ \boldsymbol{p}_J^n \end{bmatrix} \xrightarrow{\mathcal{A}_{ss}^{p,m}} \begin{bmatrix} \boldsymbol{u}^* \\ \boldsymbol{p}_J^{n+1} \end{bmatrix} \xrightarrow{\mathcal{A}_{ss}^{u,m}} \begin{bmatrix} \boldsymbol{u}^{n+1} \\ \boldsymbol{p}_J^{n+1} \end{bmatrix}, \quad \text{where} \quad \begin{cases} \mathcal{A}_{ss}^{p,m} : \dot{m}_J + \operatorname{Div} \boldsymbol{w}_J = (\rho f)_J, \ \delta\dot{\sigma}_v = 0, \\ \mathcal{A}_{ss}^{u,m} : \operatorname{Div} \boldsymbol{\sigma} + \rho_b \boldsymbol{g} = \boldsymbol{0}, \ p_J : \text{prescribed}, \end{cases} \tag{6.10}$$

where the initial condition of the flow problem, $\mathcal{A}_{ss}^p$, is determined from the original coupled problem satisfying

$$\operatorname{Div} \dot{\sigma}_{t=0} = 0\,, \quad \operatorname{Div} \sigma_{t=0} = 0, \tag{6.11}$$

which is the same as for single-phase flow. Since the flow problem does not affect the shear stress field, $\delta\dot{\sigma}_v = 0$ is equivalent to $\delta\dot{\boldsymbol{\sigma}} = 0$. In the staggered method, $\delta\dot{\sigma}_v = 0$ is written in

discrete form as

$$\sigma_v^{n+1} - \sigma_v^n = \sigma_v^n - \sigma_v^{n-1}. \tag{6.12}$$

With the staggered Newton method, for the linearized flow problem, $\delta\dot{\sigma}_v = 0$ is modified to

$$\sigma_v^{k+1} - \sigma_v^n = \sigma_v^k - \sigma_v^n. \tag{6.13}$$

6.2 Staggered Newton schemes for Multiphase Flow

In reservoir engineering, the most common solution algorithms for multiphase flow are the FIM (Fully Implicit Method) and the IMPES (IMplicit Pressure and Explicit Saturation). The FIM solves the multiphase flow equations simultaneously for the pressure and saturation fields. In the IMPES approach, the pressure field is obtained implicitly, and the saturation field is computed explicitly based on the updated pressure field. Thus, the FIM provides unconditional stability for the multiphase flow problem, but requires large systems and high computational cost. IMPES is only conditionally stable because the saturation field is obtained explicitly. But, IMPES yields small systems relative to FIM and saves computational resources.

In this chapter, we perform stability analysis of multiphase flow for staggered Newton schemes for the drained, undrained, fixed-strain, and fixed-stress splits. We first employ the Von Neumann method, since we linearize all the equations first for the Newton-Raphson method and solve the linearized equations sequentially. We take full iterations until the solutions are converged. We use the energy method for nonlinear stability analysis of staggered strategies.

6.2.1 Convergence of FIM

Oil pressure and water saturation are typically used as the primary variables for FIM in the case of oil-water flow. The Von Neumann method is applied to the linearized equations

of the four sequential methods. Capillarity is neglected here. The energy method, however, can account for capillarity, as shown later. For space discretization, we use the finite volume and finite element methods for flow and mechanics, respectively. For time discretization, we use the backward Euler method. The accumulation term in the flow problem for each phase is written as

$$\frac{\delta m_o}{\rho_{o,0}} = \underbrace{\left(\phi S_o \frac{1}{B_o} c_o + \frac{S_o}{B_o}\frac{b-\phi}{K_s}\right)}_{A_f^{oo}} \delta p_o + \underbrace{\left(-\phi \frac{1}{B_o}\right)}_{A_f^{ow}} \delta S_w + \underbrace{\frac{S_o}{B_o} b}_{A_u^o} \delta \varepsilon_v, \tag{6.14}$$

$$\frac{\delta m_w}{\rho_{w,0}} = \underbrace{\left(\phi S_w \frac{1}{B_w} c_w + \frac{S_w}{B_w}\frac{b-\phi}{K_s}\right)}_{A_f^{wo}} \delta p_o + \underbrace{\phi \frac{1}{B_w}}_{A_f^{ww}} \delta S_w + \underbrace{\frac{S_w}{B_w} b}_{A_u^w} \delta \varepsilon_v, \tag{6.15}$$

where B_J is the formation volume factor of phase J. Then the flow equation in one dimension reads as

$$\underbrace{\begin{pmatrix} A_f^{oo} & A_f^{ow} \\ A_f^{wo} & A_f^{ww} \end{pmatrix}}_{\mathbf{A}_f} \begin{pmatrix} \dot{p_o} \\ \dot{S_w} \end{pmatrix} + \underbrace{\begin{pmatrix} A_u^o \\ A_u^w \end{pmatrix}}_{\mathbf{A}_u} \dot{\varepsilon_v} = \begin{pmatrix} -\partial_x(\boldsymbol{w}_o/\rho_{o,0}) + (f/B)_o \\ -\partial_x(\boldsymbol{w}_w/\rho_{w,0}) + (f/B)_w \end{pmatrix}. \tag{6.16}$$

The mechanical problem in one-dimensional poroelasticity is expressed as

$$\frac{\partial}{\partial x}\left(K_{dr}\dot{\varepsilon_v} - b(S_w \dot{p_w} + S_o \dot{p_o})\right) = 0, \tag{6.17}$$

where we use the rate form of the mechanical problem because the constitutive relations are valid in incremental form. Let us assume that Equations 6.17 and 6.16 have no source terms or capillarity and homogeneous boundary conditions. Based on the given space and time discretizations, we obtain the residuals for mechanics and flow from Equations 6.17, and 6.16 as

$$R_u^m = -(\frac{K_{dr}}{h}\Delta U_{j-\frac{3}{2}}^{n+1} - 2\frac{K_{dr}}{h}\Delta U_{j-\frac{1}{2}}^{n+1} + \frac{K_{dr}}{h}\Delta U_{j+\frac{1}{2}}^{n+1}) - b(\Delta P_{o,j-1}^{n+1} - \Delta P_{o,j}^{n+1}), \tag{6.18}$$

$$\begin{aligned} R_o^m &= hA_f^{oo,n+1}\frac{\Delta P_{o,j}^n}{\Delta t} + hA_f^{ow,n+1}\frac{\Delta S_{w,j}^n}{\Delta t} + \frac{hA_u^{o,n+1}}{\Delta t}(-\frac{\Delta U_{j-\frac{1}{2}}^n - \Delta U_{j+\frac{1}{2}}^n}{h}) \\ &\quad -\frac{T_{o,j-\frac{1}{2}}^{n+1}}{h}\left(P_{o,j-1}^{n+1} - P_{o,j}^{n+1}\right) - \frac{T_{o,j+\frac{1}{2}}^{n+1}}{h}\left(P_{o,j+1}^{n+1} - P_{o,j}^{n+1}\right), \end{aligned} \tag{6.19}$$

$$\begin{aligned} R_w^m &= hA_f^{wo,n+1}\frac{\Delta P_{o,j}^n}{\Delta t} + hA_f^{ww,n+1}\frac{\Delta S_{w,j}^n}{\Delta t} + \frac{hA_u^{w,n+1}}{\Delta t}(-\frac{\Delta U_{j-\frac{1}{2}}^n - \Delta U_{j+\frac{1}{2}}^n}{h}) \\ &\quad -\frac{T_{w,j-\frac{1}{2}}^{n+1}}{h}\left(P_{o,j-1}^{n+1} - P_{o,j}^{n+1}\right) - \frac{T_{w,j+\frac{1}{2}}^{n+1}}{h}\left(P_{o,j+1}^{n+1} - P_{o,j}^{n+1}\right), \end{aligned} \tag{6.20}$$

where $T_J = (k_p/\mu)_J$. T_J/h is the transmissibility corresponding to phase J. R_u^m, R_o^m, and R_w^m are the residuals for mechanics, oil, and water flow, respectively. In order to investigate the convergence properties by the spectral method, we assume for simplicity small variation of the solutions with respect to time and space so that

$$\begin{aligned} & T_{J,i+1/2} \approx T_{J,i-1/2} \approx T_J, \\ & \left.\begin{aligned} \Delta P_o^n \tfrac{\partial A_f^{JK,k}}{\partial P_o}\Delta P_o^k \approx 0 \\ \Delta P_o^n \tfrac{\partial A_f^{JK,k}}{\partial S_w}\Delta S_w^k \approx 0 \end{aligned}\right\} \Rightarrow\ A_f^{JK,n+1} \approx A_f^{JK,k}, \\ & \left.\begin{aligned} \Delta S_w^n \tfrac{\partial A_u^{J,k}}{\partial P_o}\Delta P_o^k \approx 0 \\ \Delta S_w^n \tfrac{\partial A_u^{J,k}}{\partial S_w}\Delta S_w^k \approx 0 \end{aligned}\right\} \Rightarrow A_u^{J,n+1} \approx A_u^{J,k}, \\ & \left.\begin{aligned} \left(P_{o,j\pm1}^{n+1} - P_{o,j}^{n+1}\right)\tfrac{\partial T_J^k}{\partial P_o}\Delta P_o^k \approx 0 \\ \left(P_{o,j\pm1}^{n+1} - P_{o,j}^{n+1}\right)\tfrac{\partial T_J^k}{\partial S_w}\Delta S_w^k \approx 0 \end{aligned}\right\} \Rightarrow T_J^{n+1} \approx T_J^k, \end{aligned} \tag{6.21}$$

where $(\cdot)^k = (\cdot)^{n+1,k}$. The subscripts J and K denote the fluid phases. Equation 6.21 implies that the solutions at the kth iteration for the fully coupled or sequential methods are located near the solution of Equations 6.18 – 6.20, as illustrated in Figure 6.1.

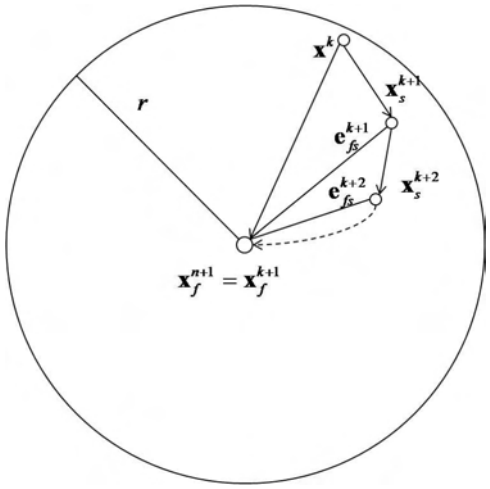

Figure 6.1: The region for the linear theory.

Using Equation 6.21 and applying the fully coupled method, we can linearize Equations 6.18 – 6.20, which can be written as

$$-(\frac{K_{dr}}{h}\left(U_{j-\frac{3}{2}}^{n+1}-U_{j-\frac{3}{2}}^{n}\right)-2\frac{K_{dr}}{h}\left(U_{j-\frac{1}{2}}^{n+1}-U_{j-\frac{1}{2}}^{n}\right)+\frac{K_{dr}}{h}\left(U_{j+\frac{1}{2}}^{n+1}-U_{j+\frac{1}{2}}^{n}\right))$$
$$-b\left((P_{o,j-1}^{n+1}-P_{o,j-1}^{n})-\left(P_{o,j}^{n+1}-P_{o,j}^{n})\right)\right)=0, \tag{6.22}$$

$$hA_f^{oo,k}\frac{P_{o,j}^{n+1}-P_{o,j}^{n}}{\Delta t}+hA_f^{ow,k}\frac{S_{w,j}^{n+1}-S_{w,j}^{n}}{\Delta t}+\frac{hA_u^{o,k}}{\Delta t}(-\frac{U_{j-\frac{1}{2}}^{n+1}-U_{j-\frac{1}{2}}^{n}}{h}+\frac{U_{j+\frac{1}{2}}^{n+1}-U_{j+\frac{1}{2}}^{n}}{h})$$
$$-\frac{T_o^k}{h}\left(P_{o,j-1}^{n+1}-2P_{o,j}^{n+1}+P_{o,j+1}^{n+1}\right)=0, \tag{6.23}$$
$$hA_f^{wo,k}\frac{P_{o,j}^{n+1}-P_{o,j}^{n}}{\Delta t}+hA_f^{ww,k}\frac{S_{w,j}^{n+1}-S_{w,j}^{n}}{\Delta t}+\frac{hA_u^{w,k}}{\Delta t}(-\frac{U_{j-\frac{1}{2}}^{n+1}-U_{j-\frac{1}{2}}^{n}}{h}+\frac{U_{j+\frac{1}{2}}^{n+1}-U_{j+\frac{1}{2}}^{n}}{h})$$
$$-\frac{T_w^k}{h}\left(\Delta P_{o,j-1}^{n+1}-\Delta P_{o,j}^{n+1}+\Delta P_{o,j+1}^{n+1}\right)=0, \tag{6.24}$$

where one iteration with the fully coupled method is required to obtain the converged

solution because the solution at the kth iteration is assumed to be within the linear region.

Our purpose is to analyze the convergence behavior of sequential methods during iterations. In the following sections, we study the propagation of the errors between the fully coupled and sequential methods as a function of iteration. We focus on the two phase flow (i.e., oil and water) with an elastic medium.

6.2.2 Drained split

When solving the mechanical problem, the drained split predicts P_o^{k+1} in Equation 6.22 as

$$P_o^{k+1} = P_o^k. \tag{6.25}$$

Let $e_{P_o}^k = {P_o}^{n+1} - {P_{o,s}}^k$, $e_{S_w}^k = {S_w}^{n+1} - {S_{w,s}}^k$, and $e_U^k = {U}^{n+1} - {U_s}^k$, where the subscript s, $(\cdot)_s$, denotes a sequential method. Similar to single-phase flow, we obtain the error equations for coupled multiphase flow and mechanics as

$$-(\frac{K_{dr}}{h}e_{U_{j-\frac{3}{2}}}^{k+1} - 2\frac{K_{dr}}{h}e_{U_{j-\frac{1}{2}}}^{k+1} + \frac{K_{dr}}{h}e_{U_{j+\frac{1}{2}}}^{k+1}) - b(e_{P_{o,j-1}}^k - e_{P_{o,j}}^k) = 0, \tag{6.26}$$

$$\begin{aligned} &hA_f^{oo,k}\frac{e_{P_{o,j}}^{k+1}}{\Delta t} + hA_f^{ow,k}\frac{e_{S_{w,j}}^{k+1}}{\Delta t} + \frac{hA_u^{o,k}}{\Delta t}(-\frac{e_{U_{j-\frac{1}{2}}}^{k+1} - e_{U_{j+\frac{1}{2}}}^{k+1}}{h}) \\ &-\frac{T_o^k}{h}\left(e_{P_{o,j-1}}^{k+1} - 2e_{P_{o,j}}^k + e_{P_{o,j+1}}^{k+1}\right) = 0, \end{aligned} \tag{6.27}$$

$$\begin{aligned} &hA_f^{wo,k}\frac{e_{P_{o,j}}^{k+1}}{\Delta t} + hA_f^{ww,k}\frac{e_{S_{w,j}}^{k+1}}{\Delta t} + \frac{hA_u^{w,k}}{\Delta t}(-\frac{e_{U_{j-\frac{1}{2}}}^{k+1} - e_{U_{j+\frac{1}{2}}}^{k+1}}{h}) \\ &-\frac{T_w^k}{h}\left(e_{P_{o,j-1}}^{k+1} - e_{P_{o,j}}^{k+1} + e_{P_{o,j+1}}^{k+1}\right) = 0. \end{aligned} \tag{6.28}$$

We introduce errors of the form $e_{U_j}^k = \gamma_e^k e^{i(j)\theta}\hat{U}$, $e_{P_{o,j}}^k = \gamma_e^k e^{i(j)\theta}\hat{P}_o$, and $e_{S_{w,j}}^k =$

$\gamma_e^k e^{i(j)\theta}\hat{S_w}$ to Equations 6.26 – 6.28, where γ_e is the error amplification factor. Following a similar procedure of the error analysis for single-phase flow, we obtain

$$\mathbf{B}_{dr}^m \begin{bmatrix} \hat{U} \\ \hat{P_o} \\ \hat{S_w} \end{bmatrix} = \begin{bmatrix} 0 \\ 0 \\ 0 \end{bmatrix}, \tag{6.29}$$

where

$$\mathbf{B}_{dr}^m = \begin{bmatrix} \frac{K_{dr}}{h} 2(1-\cos\theta)\gamma_e & b2i\sin\frac{\theta}{2} & 0 \\ A_u^{o,k} 2i\sin\frac{\theta}{2}\gamma_e & A_f^{oo,k} h\gamma_e + T_o^k \frac{\Delta t}{h} 2(1-\cos\theta)\gamma_e & A_f^{ow,k} h\gamma_e \\ A_u^{w,k} 2i\sin\frac{\theta}{2}\gamma_e & A_f^{wo,k} h\gamma_e + T_w^k \frac{\Delta t}{h} 2(1-\cos\theta)\gamma_e & A_f^{ww,k} h\gamma_e \end{bmatrix}.$$

From $\det(\mathbf{B}_{dr}^m) = 0$, we have

$$\gamma_e = 0, \ -\frac{b^2}{K_{dr}\left(\phi\left(c_o S_o + c_w S_w\right) + \frac{b-\phi}{K_s} + \left(B_o T_o^k + B_w T_w^k\right)\frac{\Delta t}{h^2} 2(1-\cos\theta)\right)}. \tag{6.30}$$

Convergence of the drained split is obtained when $\max|\gamma_e| < 1$ for all θ, yielding $\left\|\mathbf{e}_{fs}^{k+1}\right\| < \left\|\mathbf{e}_{fs}^{k}\right\|$. This condition is also used in Schrefler et al. (1997). $\left\|\mathbf{e}_{fs}^{k+1}\right\| < \left\|\mathbf{e}_{fs}^{k}\right\|$ indicates that $\mathbf{x}_s^{k+1}$ is closer to the converged solution $\mathbf{x}_f^{n+1}$, shown in Figure 6.1. The convergence condition, $\max|\gamma_e| < 1$ for all θ, yields

$$\tau \equiv \frac{b^2 M_{mp}}{K_{dr}} < 1, \tag{6.31}$$

$$\frac{1}{M_{mp}} = \phi\left(c_o S_o + c_w S_w\right) + \frac{b-\phi}{K_s}, \tag{6.32}$$

where we extend the definition of the coupling strength to two-phase flow, using the total fluid compressibility $c_f = c_o S_o + c_w S_w$. For three phase flow with capillarity, we can define the coupling strength as

$$\tau \equiv \frac{\mathbf{b}^t \mathbf{M} \mathbf{b}}{K_{dr}}. \tag{6.33}$$

The convergence estimate of the drained split for multiphase flow shows conditional convergence, where the coupling strength needs to be less than one. Thus, even though the drained split can be stable at the beginning when a compressible fluid is flowing, it can be unstable after we inject an incompressible fluid in later time due to an increase in the coupling strength. Water injection in an oil reservoir is an example of this situation, which will be shown in numerical experiments.

6.2.3 Undrained split

The undrained split predicts P_o^{k+1} in Equation 6.22 as

$$\begin{aligned} P^{k+1} &= P^k - (\varepsilon_v^{k+1} - \varepsilon_v^k)\mathbf{e}_1^t \mathbf{A}_f^{-1} \mathbf{A}_u \,, \\ &= P^k - bM_{mp}(\varepsilon_v^{k+1} - \varepsilon_v^k), \end{aligned} \tag{6.34}$$

where $\mathbf{e}_1^t = [1, 0]$. Then the error equation for mechanics is written as

$$\begin{aligned} &-(\frac{K_{ud}}{h} e^{k+1}_{U_{j-\frac{3}{2}}} - 2\frac{K_{ud}}{h} e^{k+1}_{U_{j-\frac{1}{2}}} + \frac{K_{ud}}{h} e^{k+1}_{U_{j+\frac{1}{2}}}) \\ &+(\frac{b^2 M_{mp}}{h} e^{k+1}_{U_{j-\frac{3}{2}}} - 2\frac{b^2 M_{mp}}{h} e^{k+1}_{U_{j-\frac{1}{2}}} + \frac{b^2 M_{mp}}{h} e^{k+1}_{U_{j+\frac{1}{2}}}) - b(e^k_{P_{o,j-1}} - e^k_{P_{o,j}}) = 0, \\ &K_{ud} = K_{dr} + b^2 M_{mp}. \end{aligned} \tag{6.35}$$

where K_{ud} is the undrained bulk modulus for multiphase flow. The error equations for flow in the undrained split remain the same as Equations 6.27 and 6.28. Taking the same

procedure as that for the drained split, we have

$$\mathbf{B}_{ud}^{m}\begin{bmatrix}\hat{U}\\ \hat{P}_o\\ \hat{S}_w\end{bmatrix}=\begin{bmatrix}0\\0\\0\end{bmatrix}, \tag{6.36}$$

where

$$\mathbf{B}_{ud}^{m}=\begin{bmatrix}\left(\frac{K_{ud}}{h}\gamma_e-\frac{b^2M_{mp}}{h}\right)2(1-\cos\theta) & b2i\sin\frac{\theta}{2} & 0\\ A_u^{o,k}2i\sin\frac{\theta}{2}\gamma_e & A_f^{oo,k}h\gamma_e+T_o^k\frac{\Delta t}{h}2(1-\cos\theta)\gamma_e & A_f^{ow,k}h\gamma_e\\ A_u^{w,k}2i\sin\frac{\theta}{2}\gamma_e & A_f^{wo,k}h\gamma_e+T_w^k\frac{\Delta t}{h}2(1-\cos\theta)\gamma_e & A_f^{ww,k}h\gamma_e\end{bmatrix}.$$

From $\det\left(\mathbf{B}_{ud}^{m}\right)=0$, the amplification factors of the error γ_e's are obtained as

$$\gamma_e=0,\ \ \frac{b^2M_{mp}\left(B_oT_o^k+B_wT_w^k\right)\frac{\Delta t}{h^2}2(1-\cos\theta)}{K_{ud}\left(\frac{1}{M_{mp}}+\left(B_oT_o^k+B_wT_w^k\right)\frac{\Delta t}{h^2}2(1-\cos\theta)\right)}. \tag{6.37}$$

Equation 6.37 yields unconditional convergence for the undrained split because $0\leq\gamma_e<1$. When both the fluid and solid grains are incompressible (i,e, $M_{mp}=\infty$), $\max|\gamma_e|=1$. Hence, we may face non-convergence when injecting an incompressible fluid that replaces a more compressible fluid.

6.2.4 Fixed-strain split

When we solve the flow problem first, the fixed-strain split predicts ε_v^{k+1} in Equations 6.23 and 6.24 as

$$\varepsilon_v^{k+1}=\varepsilon_v^{k}. \tag{6.38}$$

Based on Equation 6.38, we obtain the error equations for coupled multiphase flow and

mechanics as

$$
\begin{aligned}
&hA_f^{oo,k}\frac{e_{P_{o,j}}^{k+1}}{\Delta t}+hA_f^{ow,k}\frac{e_{S_{w,j}}^{k+1}}{\Delta t}+\frac{hA_u^{o,k}}{\Delta t}(-\frac{e_{U_{j-\frac{1}{2}}}^{k}-e_{U_{j+\frac{1}{2}}}^{k}}{h})\\
&-\frac{T_o^k}{h}\left(e_{P_{o,j-1}}^{k+1}-2e_{P_{o,j}}^{k}+e_{P_{o,j+1}}^{k+1}\right)=0, \qquad (6.39)\\
&hA_f^{wo,k}\frac{e_{P_{o,j}}^{k+1}}{\Delta t}+hA_f^{ww,k}\frac{e_{S_{w,j}}^{k+1}}{\Delta t}+\frac{hA_u^{w,k}}{\Delta t}(-\frac{e_{U_{j-\frac{1}{2}}}^{k}-e_{U_{j+\frac{1}{2}}}^{k}}{h})\\
&-\frac{T_w^k}{h}\left(e_{P_{o,j-1}}^{k+1}-e_{P_{o,j}}^{k+1}+e_{P_{o,j+1}}^{k+1}\right)=0. \qquad (6.40)
\end{aligned}
$$

$$
-(\frac{K_{dr}}{h}e_{U_{j-\frac{3}{2}}}^{k+1}-2\frac{K_{dr}}{h}e_{U_{j-\frac{1}{2}}}^{k+1}+\frac{K_{dr}}{h}e_{U_{j+\frac{1}{2}}}^{k+1})-b(e_{P_{o,j-1}}^{k+1}-e_{P_{o,j}}^{k+1})=0. \qquad (6.41)
$$

Introducing errors of the form $e_{U_j}^k=\gamma_e^k e^{i(j)\theta}\hat{U}$, $e_{P_{o,j}}^k=\gamma_e^k e^{i(j)\theta}\hat{P}_o$, and $e_{S_{w,j}}^k=\gamma_e^k e^{i(j)\theta}\hat{S_w}$ to Equations 6.39–6.41, we obtain

$$
\mathbf{B}_{sn}^m\begin{bmatrix}\hat{P}_o\\ \hat{S_w}\\ \hat{U}\end{bmatrix}=\begin{bmatrix}0\\0\\0\end{bmatrix}, \qquad (6.42)
$$

where

$$
\mathbf{B}_{sn}^m=\begin{bmatrix}
A_f^{oo,k}h\gamma_e+T_o^k\frac{\Delta t}{h}2(1-\cos\theta)\gamma_e & A_f^{ow,k}h\gamma_e & A_u^{o,k}2i\sin\frac{\theta}{2}\\
A_f^{wo,k}h\gamma_e+T_w^k\frac{\Delta t}{h}2(1-\cos\theta)\gamma_e & A_f^{ww,k}h\gamma_e & A_u^{w,k}2i\sin\frac{\theta}{2}\\
b2i\sin\frac{\theta}{2}\gamma_e & 0 & \frac{K_{dr}}{h}2(1-\cos\theta)\gamma_e
\end{bmatrix}.
$$

From $\det(\mathbf{B}_{sn}^m)=0$, the γ_e's are obtained as

$$
\gamma_e=0,\ -\frac{b^2}{K_{dr}\left(\phi\left(c_oS_o+c_wS_w\right)+\frac{b-\phi}{K_s}+\left(B_oT_o^k+B_wT_w^k\right)\frac{\Delta t}{h^2}2(1-\cos\theta)\right)}. \qquad (6.43)
$$

From Equation 6.43, the convergence for the fixed-strain split is obtained as long as

$$\tau \equiv \frac{b^2 M_{mp}}{K_{dr}} < 1, \tag{6.44}$$

which is identical to the convergence condition of the drained split.

6.2.5 Fixed-stress split

In contrast to the fixed-strain split, the fixed-stress split predicts ε_v^{n+1} in Equations 6.23 and 6.24 during the flow step as

$$\varepsilon_v^{k+1} = \varepsilon_v^k + \frac{b}{K_{dr}}\left(P_o^{k+1} - P_o^k\right). \tag{6.45}$$

Then the error equations for multiphase flow become

$$\begin{aligned} &hA_f^{oo,k}\frac{e_{P_{o,j}}^{k+1}}{\Delta t} + hA_f^{ow,k}\frac{e_{S_{w,j}}^{k+1}}{\Delta t} + \frac{hA_u^{o,k}}{\Delta t}(-\frac{e_{U_{j-\frac{1}{2}}}^k - e_{U_{j+\frac{1}{2}}}^k}{h}) \\ &-\frac{T_o^k}{h}\left(e_{P_{o,j-1}}^{k+1} - 2e_{P_{o,j}}^k + e_{P_{o,j+1}}^{k+1}\right) = 0, \end{aligned} \tag{6.46}$$

$$\begin{aligned} &hA_f^{wo,k}\frac{e_{P_{o,j}}^{k+1}}{\Delta t} + hA_f^{ww,k}\frac{e_{S_{w,j}}^{k+1}}{\Delta t} + \frac{hA_u^{w,k}}{\Delta t}(-\frac{e_{U_{j-\frac{1}{2}}}^k - e_{U_{j+\frac{1}{2}}}^k}{h}) \\ &-\frac{T_w^k}{h}\left(e_{P_{o,j-1}}^{k+1} - e_{P_{o,j}}^{k+1} + e_{P_{o,j+1}}^{k+1}\right) = 0. \end{aligned} \tag{6.47}$$

The equation for mechanics is the same as Equation 6.41. Introducing errors of the form $e_{U_j}^k = \gamma_e^k e^{i(j)\theta}\hat{U}$, $e_{P_{o,j}}^k = \gamma_e^k e^{i(j)\theta}\hat{P}_o$, and $e_{S_{w,j}}^k = \gamma_e^k e^{i(j)\theta}\hat{S}_w$, we have

$$\mathbf{B}_{ss}^m \begin{bmatrix} \hat{P}_o \\ \hat{S}_w \\ \hat{U} \end{bmatrix} = \begin{bmatrix} 0 \\ 0 \\ 0 \end{bmatrix}, \tag{6.48}$$

where $\mathbf{B}_{ss}^m =$

$$\begin{bmatrix} A_f^{oo,k} h\gamma_e + T_o^k \frac{\Delta t}{h} 2(1-\cos\theta)\gamma_e + \frac{b^2 S_o}{K_{dr} B_o}(\gamma_e - 1) & A_f^{ow,k} h\gamma_e & A_u^{o,k} 2i \sin\frac{\theta}{2} \\ A_f^{wo,k} h\gamma_e + T_w^k \frac{\Delta t}{h} 2(1-\cos\theta)\gamma_e + \frac{b^2 S_w}{K_{dr} B_w}(\gamma_e - 1) & A_f^{ww,k} h\gamma_e & A_u^{w,k} 2i \sin\frac{\theta}{2} \\ b2i \sin\frac{\theta}{2}\gamma_e & 0 & \frac{K_{dr}}{h} 2(1-\cos\theta)\gamma_e \end{bmatrix}.$$

From $\det(\mathbf{B}_{ss}^m) = 0$, the γ_e is

$$\gamma_e = 0, \tag{6.49}$$

which yields unconditional convergence.

6.3 Staggered Newton scheme with IMPES

From the one-dimensional flow equations, the IMPES pressure equation is expressed as

$$\begin{aligned} &\underbrace{\left(-\frac{A_f^{ww}}{A_f^{ow}} A_f^{oo} + A_f^{wo}\right)}_{A_p^s} \frac{dp_o}{dt} + \underbrace{\left(-\frac{A_f^{ww}}{A_f^{ow}} A_u^{o} + A_u^{w}\right)}_{A_u^s} \frac{d\varepsilon_v}{dt} \\ &= \frac{A_f^{ww}}{A_f^{ow}} \frac{\partial}{\partial x}\left(\frac{\mathbf{w}_o}{\rho_{o,0}}\right) - \frac{\partial}{\partial x}\left(\frac{\mathbf{w}_w}{\rho_{w,0}}\right) - \frac{A_f^{ww}}{A_f^{ow}}\left(\frac{f}{B}\right)_o + \left(\frac{f}{B}\right)_w, \end{aligned} \tag{6.50}$$

where all the coefficients and saturation values are explicit except for the pressure. Neglecting the source terms of Equation 6.50, we discretize Equation 6.50 based on the IMPES method, which produces

$$\begin{aligned} &hA_p^{s,n} \frac{\Delta P_{o,j}^n}{\Delta t} + \frac{hA_u^{s,n}}{\Delta t}\left(-\frac{\Delta U_{j-\frac{1}{2}}^n - \Delta U_{j+\frac{1}{2}}^n}{h}\right) \\ &-\frac{T_s^n}{h}\left(P_{o,j+1}^{n+1} - 2P_{o,j}^{n+1} + P_{o,j-1}^{n+1}\right) = 0, \end{aligned} \tag{6.51}$$

where $T_s = -\frac{A_f^{ww}}{A_f^{ow}} T_o + T_w$. The discretized equation for mechanics is the same as Equation 6.18. The flow problem is itself conditionally stable because we treat saturation and all the coefficients explicitly (Aziz and Settari, 1979). When the coupled problem is solved

sequentially, additional restriction to ensure convergence may be required, depending on the characteristics of the particular sequential method used.

6.3.1 Drained split

In the drained split, the predictor of pressure change in the mechanical problem is evaluated from the previous iteration, and the error equation for mechanics is the same as Equation 6.26. The the error equation for flow is

$$hA_p^{s,n}\frac{e_{P_{o,j}}^{k+1}}{\Delta t}+\frac{hA_u^{s,n}}{\Delta t}(-\frac{e_{U_{j-\frac{1}{2}}}^{k+1}-e_{U_{j+\frac{1}{2}}}^{k+1}}{h})-\frac{T_s^n}{h}\left(e_{P_{o,j+1}}^{k+1}-2e_{P_{o,j}}^{k+1}+e_{P_{o,j-1}}^{k+1}\right)=0. \tag{6.52}$$

Using the spectral method and introducing errors of the form $e_{U_j}^k=\gamma_e^k e^{i(j)\theta}\hat{U}$ and $e_{P_{o,j}}^k=\gamma_e^k e^{i(j)\theta}\hat{P}_o$, we obtain the matrix equation as

$$\underbrace{\begin{bmatrix}\frac{K_{dr}}{h}2\left(1-\cos\theta\right)\gamma_e & b2i\sin\frac{\theta}{2}\\ A_u^{s,n}2i\sin\frac{\theta}{2}\gamma_e & A_p^{s,n}h\gamma_e+T_s^n\frac{\Delta t}{h}2\left(1-\cos\theta\right)\gamma_e\end{bmatrix}}_{\mathbf{B}_{dr}^s}\begin{bmatrix}\hat{U}\\ \hat{P}_o\end{bmatrix}=\begin{bmatrix}0\\0\end{bmatrix}. \tag{6.53}$$

From $\det(\mathbf{B}_{dr}^s)=0$, we have

$$\gamma_e=0,\ -\frac{b^2}{K_{dr}\left(\frac{1}{M_{mp}}+\left(B_oT_o^n+B_wT_w^n\right)\frac{\Delta t}{h^2}2\left(1-\cos\theta\right)\right)}. \tag{6.54}$$

The convergence condition for the drained split with IMPES is obtained as

$$\tau\equiv\frac{b^2M_{mp}}{K_{dr}}<1, \tag{6.55}$$

which is the same as the drained split of FIM, as shown previously.

6.3.2 Undrained split

In the IMPES formulation, the undrained split yields the error equations for mechanics and flow as Equations 6.35 and 6.52, respectively. Using the spectral method, the matrix

equation is written as

$$\mathbf{B}^s_{ud}\begin{bmatrix}\hat{U}\\ \hat{P}_o\end{bmatrix}=\begin{bmatrix}0\\0\end{bmatrix}, \tag{6.56}$$

where

$$\mathbf{B}^s_{ud}=\begin{bmatrix}\left(\frac{K_{ud}}{h}\gamma_e-\frac{b^2M_{2p}}{h}\right)2(1-\cos\theta) & b2i\sin\frac{\theta}{2}\\ A^{s,n}_u 2i\sin\frac{\theta}{2}\gamma_e & A^{s,n}_p h\gamma_e+T^n_s\frac{\Delta t}{h}2\left(1-\cos\theta\right)\gamma_e\end{bmatrix}.$$

From $\det(\mathbf{B}^s_{ud})=0$, the error amplification factors are obtained as

$$\gamma_e=0,\ \frac{b^2M_{mp}\left(B_oT^n_o+B_wT^n_w\right)\frac{\Delta t}{h^2}2(1-\cos\theta)}{K_{ud}\left(\frac{1}{M_{mp}}+\left(B_oT^n_o+B_wT^n_w\right)\frac{\Delta t}{h^2}2(1-\cos\theta)\right)}. \tag{6.57}$$

Since $0\le\gamma_e<1$, the undrained split with IMPES has no additional restriction on convergence unless the fluids are incompressible.

6.3.3 Fixed-strain split

The fixed-strain split predicts the strain change of the flow problem from the previous iteration step as in Equation 6.38. Then the error equation for flow becomes

$$hA^{s,n}_p\frac{e^{k+1}_{P_{o,j}}}{\Delta t}+\frac{hA^{s,n}_u}{\Delta t}(-\frac{e^k_{U_{j-\frac{1}{2}}}-e^k_{U_{j+\frac{1}{2}}}}{h})-\frac{T^n_s}{h}\left(e^{k+1}_{P_{o,j+1}}-2e^{k+1}_{P_{o,j}}+e^{k+1}_{P_{o,j-1}}\right)=0. \tag{6.58}$$

The error equation for mechanics is the same as Equation 6.41. Using the spectral method, we obtain the matrix equation as

$$\underbrace{\begin{bmatrix}A^{s,n}_p h\gamma_e+T^n_s\frac{\Delta t}{h}2\left(1-\cos\theta\right)\gamma_e & A^{s,n}_u 2i\sin\frac{\theta}{2}\\ b2i\sin\frac{\theta}{2}\gamma_e & \frac{K_{dr}}{h}2\left(1-\cos\theta\right)\gamma_e\end{bmatrix}}_{\mathbf{B}^s_{sn}}\begin{bmatrix}\hat{P}_o\\ \hat{U}\end{bmatrix}=\begin{bmatrix}0\\0\end{bmatrix}. \tag{6.59}$$

From $\det(\mathbf{B}^s_{sn}) = 0$, we have

$$\gamma_e = 0,\ -\frac{b^2}{K_{dr}\left(\frac{1}{M_{mp}} + \left(B_o T_o^n + B_w T_w^n\right)\frac{\Delta t}{h^2} 2\left(1-\cos\theta\right)\right)}, \tag{6.60}$$

which yields the additional condition for convergence as

$$\tau \equiv \frac{b^2 M_{mp}}{K_{dr}} < 1. \tag{6.61}$$

6.3.4 Fixed-stress split

The fixed-stress split with IMPES predicts the strain change of the flow problem as Equation 6.45. Then, the error equation for flow is

$$\begin{aligned}&\left(hA_p^{s,n} + \frac{b^2}{K_{dr}B_w}\right)\frac{e^{k+1}_{P_{o,j}}}{\Delta t} - \frac{b^2}{K_{dr}B_w}\frac{e^{k}_{P_{o,j}}}{\Delta t} + \frac{hA_u^{s,n}}{\Delta t}(-\frac{e^k_{U_{j-\frac{1}{2}}} - e^k_{U_{j+\frac{1}{2}}}}{h})\\ &-\frac{T_s^n}{h}\left(e^{k+1}_{P_{o,j+1}} - 2e^{k+1}_{P_{o,j}} + e^{k+1}_{P_{o,j-1}}\right) = 0.\end{aligned} \tag{6.62}$$

The error equation for mechanics is the same as Equation 6.41. Using the spectral method, the matrix equation is written as

$$\mathbf{B}^s_{ss}\begin{bmatrix}\hat{P}_o\\ \hat{U}\end{bmatrix} = \begin{bmatrix}0\\0\end{bmatrix}, \tag{6.63}$$

where

$$\mathbf{B}^s_{ss} = \begin{bmatrix} A_p^{s,n}h\gamma_e + T_s^n\frac{\Delta t}{h}2\left(1-\cos\theta\right) + \frac{b^2}{K_{dr}B_w}\left(\gamma_e - 1\right) & A_u^{s,n}2i\sin\frac{\theta}{2}\gamma \\ b2i\sin\frac{\theta}{2}\gamma_e & \frac{K_{dr}}{h}2\left(1-\cos\theta\right)\gamma_e \end{bmatrix}.$$

From $\det(\mathbf{B}^s_{ss}) = 0$, we have

$$\gamma_e = 0\,, \tag{6.64}$$

which yields no additional restriction on convergence.

6.4 Stability Analysis via the Energy Method

6.4.1 Constitutive relations for multiphase flow and elastoplasticity

We showed the constitutive relations for elastic mechanics and multiphase flow in Chapter 2. Based on Coussy (1995)'s approach, we extend the constitutive relations for elasticity under isothermal conditions to those for poro-elasto-plasticity, which are written as

$$\delta\boldsymbol{\sigma} = \mathbf{C}_{dr} : (\delta\boldsymbol{\varepsilon} - \delta\boldsymbol{\varepsilon}_p) - b_J \delta p_J \mathbf{1}, \tag{6.65}$$

$$\delta p_J = M_{JK}\left(-b_K(\delta\varepsilon_v - \delta\varepsilon_{v,p}) + \left(\left(\frac{\delta m}{\rho}\right)_K - \delta\phi_{K,p}\right)\right), \tag{6.66}$$

where the variation of the elastic fluid content of phase J is

$$\left(\frac{\delta m}{\rho}\right)_{J,e} = \left(\frac{\delta m}{\rho}\right)_J - \delta\phi_{J,p}. \tag{6.67}$$

Repeated indices indicate summation, again. $(\cdot)_{J,e}$ and $(\cdot)_{J,p}$ mean elastic and plastic quantities for fluid phase J, respectively. The plastic porosity of phase J and plastic strain can be related to each other by assuming that $\dot{\phi}_{J,p} = \beta_J \dot{\varepsilon}_{p,v}$. Here, we assume that $\beta_J = b_J$, similar to single-phase flow, which yields

$$\delta\phi_{J,p} = b_J \delta\varepsilon_{p,v}. \tag{6.68}$$

For hardening, we can reuse the relation of the hardening variable ξ and force κ for single-phase flow, namely,

$$\delta\kappa = -\mathbf{H} \cdot \delta\xi. \tag{6.69}$$

6.4.2 Contractivity of multiphase flow

Similar to single-phase flow, we introduce the norm based on the complementary Helmholtz free energy to study the contractivity of coupled mechanics and multiphase flow, namely,

$$\begin{aligned} \|\zeta_m\|^2_{\mathcal{T}_m} &= \frac{1}{2}\int_\Omega \left(\boldsymbol{\sigma'} : \mathbf{C}_{dr}^{-1}\boldsymbol{\sigma'} + \kappa \cdot \mathbf{H}^{-1}\kappa + p_J N_{JK} p_K\right) d\Omega, \qquad (6.70) \\ \mathcal{T}_m &:= \left\{\zeta_m := (\boldsymbol{\sigma'}, \kappa, \mathbf{p}) \in \mathrm{S} \times \mathrm{R}^{\mathrm{n_{int}}} \times \mathrm{R}^{\mathrm{n_p}} : \sigma'_{ij} \in L^2(\Omega),\right. \\ &\quad \left. \kappa_i \in L^2(\Omega),\, p_J \in L^2(\Omega)\right\}, \qquad (6.71) \end{aligned}$$

where n_p is the number of fluid phases. $\mathbf{p} = \{p_J\}$. $\mathbf{N} = \{N_{JK}\}$ and $\mathbf{M} = \{M_{JK}\}$, where $\mathbf{M} = \mathbf{N}^{-1}$, as shown in Chapter 2.

Let $(\mathbf{u}_0,\ \mathbf{p}_0,\ \boldsymbol{\xi}_0)$ and $(\tilde{\mathbf{u}}_0,\ \tilde{\mathbf{p}}_0,\ \tilde{\xi}_0)$ be two arbitrary initial conditions. Let $(\mathbf{u},\ \mathbf{p},\ \xi)$ and $(\tilde{\mathbf{u}},\ \tilde{\mathbf{p}},\ \tilde{\xi})$ be the corresponding solutions, yielding $(\boldsymbol{\sigma'},\ \mathbf{m},\ \kappa,\ \boldsymbol{\varepsilon}_p)$ and $(\tilde{\boldsymbol{\sigma}}',\ \tilde{\mathbf{m}},\ \tilde{\kappa},\ \tilde{\boldsymbol{\varepsilon}_p})$, respectively, where $\mathbf{m} = \{m_J\}$. Denote the difference between the two solutions by $d(\cdot) = (\cdot) - \tilde{(\cdot)}$. Assume the corresponding solutions from two arbitrary initial conditions are close enough, such that they honor the incremental form of the constitutive relations which is given by

$$\begin{aligned} d\boldsymbol{\sigma} &= \mathbf{C}_{dr} : (d\boldsymbol{\varepsilon} - d\boldsymbol{\varepsilon}_p) - b_J dp_J \mathbf{1}, \qquad (6.72) \\ dp_J &= M_{JK}\left(-b_K(d\varepsilon_v - d\varepsilon_{v,p}) + \left(\left(\frac{dm}{\rho}\right)_K - d\phi_{K,p}\right)\right), \qquad (6.73) \\ d\kappa &= -\mathbf{H} \cdot d\xi. \qquad (6.74) \end{aligned}$$

Then Equations 6.72 – 6.74 yield

$$\begin{aligned}
\|d\zeta_m\|^2_{\mathcal{I}_m} &= \frac{1}{2}\int_\Omega \left(d\boldsymbol{\sigma}' : \mathbf{C}^{-1}_{dr} d\boldsymbol{\sigma}' + d\kappa \cdot \mathbf{H}^{-1} d\kappa + dp_J N_{JK} dp_K\right) d\Omega, \\
&= \frac{1}{2}\int_\Omega \Bigg(d\boldsymbol{\varepsilon}_e : \mathbf{C}_{dr} d\boldsymbol{\varepsilon}_e + d\xi \cdot \mathbf{H} d\xi \\
&\quad + \left(\left(\frac{dm}{\rho}\right)_{J,e} - b_J d\varepsilon_{e,v}\right) M_{JK} \left(\left(\frac{dm}{\rho}\right)_{K,e} - b_K d\varepsilon_{e,v}\right)\Bigg) d\Omega, \\
&= \|d\chi_m\|^2_{\mathcal{N}_m}, \qquad (6.75)
\end{aligned}$$

where we define the norm of $\|\chi_m\|_{\mathcal{N}_m}$ as

$$\begin{aligned}
\|\chi_m\|^2_{\mathcal{N}_m} &= \frac{1}{2}\int_\Omega \Bigg(\boldsymbol{\varepsilon}_e : \mathbf{C}_{dr} \boldsymbol{\varepsilon}_e + \xi \cdot \mathbf{H} \xi \\
&\quad + \left(\left(\frac{m}{\rho}\right)_{J,e} - b_J \varepsilon_{e,v}\right) M_{JK} \left(\left(\frac{m}{\rho}\right)_{K,e} - b_K \varepsilon_{e,v}\right)\Bigg) d\Omega, \qquad (6.76) \\
\mathcal{N}_m &:= \Big\{\chi := (\boldsymbol{\varepsilon_e}, \xi, m_{J,e}) \in \mathrm{S} \times \mathrm{R}^{\mathrm{n_{int}}} \times \mathrm{R}^{\mathrm{n_p}} : \varepsilon_{e_{ij}} \in L^2(\Omega), \\
&\quad \xi_i \in L^2(\Omega),\ m_{J,e} \in L^2(\Omega)\Big\}, \qquad (6.77)
\end{aligned}$$

which originates from the Helmholtz free energy (Coussy, 1995).

Since the corresponding solutions from two arbitrary initial conditions satisfy the governing equations and boundary conditions, the fully coupled method yields from Equation 6.1

$$\begin{bmatrix} d\boldsymbol{u}^n \\ dp^n_J \end{bmatrix} \xrightarrow{\mathcal{A}^m_{fc}} \begin{bmatrix} d\boldsymbol{u}^{n+1} \\ dp^{n+1}_J \end{bmatrix}, \quad \text{where} \quad \mathcal{A}^m_{fc} : \begin{cases} \mathrm{Div}\, d\boldsymbol{\sigma} = \mathbf{0}, \\ \dot{dm}_J + \mathrm{Div}\, d\boldsymbol{w}_J = 0, \end{cases} \qquad (6.78)$$

where maximum plastic dissipation is assumed for elasto-plasticity. Note that homogeneous boundary conditions are obtained. Then the coupled problem is contractive relative to the norms, $\|\cdot\|_{\mathcal{N}_m}$ and $\|\cdot\|_{\mathcal{I}_m}$. Specifically,

$$
\begin{aligned}
\frac{d\left\|d\chi_m\right\|^2_{\mathcal{N}_m}}{dt} &= \frac{\partial\|d\chi_m\|^2_{\mathcal{N}_m}}{\partial d\boldsymbol{\varepsilon}_e} : d\dot{\boldsymbol{\varepsilon}}_e + \frac{\partial\|d\chi_m\|^2_{\mathcal{N}_m}}{\partial d\xi}\cdot d\dot{\xi} + \frac{\partial\|d\chi_m\|^2_{\mathcal{N}_m}}{\partial dm_{J,e}} d\dot{m}_{J,e} \\
&= \int_\Omega \left(d\boldsymbol{\sigma}' : d\dot{\boldsymbol{\varepsilon}}_e - \left(\left(\frac{dm_e}{\rho} \right)_J - b_J d\varepsilon_{e,v} \right) M_{JK} b_K d\dot{\varepsilon}_{e,v} \right. \\
&\quad \left. - d\kappa \cdot d\dot{\xi} + \left(\left(\frac{dm_e}{\rho} \right)_J - b_J d\varepsilon_{e,v} \right) M_{JK} \left(\frac{d\dot{m}_e}{\rho} \right)_K \right) d\Omega \\
&= \int_\Omega \left(d\boldsymbol{\sigma} : d\dot{\boldsymbol{\varepsilon}} + \left(\frac{dp}{\rho} \right)_J d\dot{m}_J \right) d\Omega - \underbrace{\int_\Omega \left[d\boldsymbol{\sigma}' : d\dot{\boldsymbol{\varepsilon}}_p + d\kappa \cdot d\dot{\xi} \right] d\Omega}_{D_p^d} \\
&= \int_\Omega \left[d\boldsymbol{\sigma} : d\dot{\boldsymbol{\varepsilon}} - dp_J \operatorname{Div}(d\boldsymbol{v}_J) \right] d\Omega - D_p^d \ \ (\text{from Equation } 6.78_2) \\
&= -\int_\Omega d\boldsymbol{v}_J \cdot \mu \mathbf{k}^{-1}_{p,JK} d\boldsymbol{v}_K d\Omega - D_p^d \le 0, \qquad (6.79) \\
&\quad \left(\because \int_\Omega d\boldsymbol{\sigma} : d\dot{\boldsymbol{\varepsilon}} d\Omega = 0 \ \text{ from Equation } 6.78_1 \right)
\end{aligned}
$$

where $D_p^d \ge 0$ for maximum plastic dissipation, and the divergence theorem and Darcy's law are applied to the last equation. By Darcy's law in Chapter 2,

$$
\boldsymbol{v}_J = -\mathbf{k}_{p,JK} \, \mathbf{Grad}\, p_K, \quad v_{J,i} \in H\,(div, \Omega), \qquad (6.80)
$$

where $v_{J,i}$ is a component of $\boldsymbol{v}_J$. Note that $\mathbf{k}_{p,JK}$ includes viscosity effects, shown in Equation 2.11. Thus, Equation 6.79 yields

$$
\begin{aligned}
\left\|\chi_m(t) - \tilde{\chi}_m(t)\right\|_{\mathcal{N}_m} &\le \left\|\chi_{m0} - \tilde{\chi}_{m0}\right\|_{\mathcal{N}_m}, \\
\left\|\zeta_m(t) - \tilde{\zeta}_m(t)\right\|_{\mathcal{T}_m} &\le \left\|\zeta_{m0} - \tilde{\zeta}_{m0}\right\|_{\mathcal{T}_m}, \qquad (6.81)
\end{aligned}
$$

where $(\cdot)_0$ indicates a quantity at the initial (reference) condition. Therefore, coupled multiphase flow and geomechanics are contractive relative to the norms $\|\cdot\|_{\mathcal{N}_m}$ and $\|\cdot\|_{\mathcal{T}_m}$. Since the drained and fixed-strain splits are not contractive in single-phase flow, we exclude them for the investigation of contractivity properties for multiphase flow.

6.4.3 Contractivity of the undrained split

Similar to Equation 6.78 of the fully coupled method, Equation 6.4 gives

$$\begin{bmatrix} d\boldsymbol{u}^n \\ dp_J^n \end{bmatrix} \xrightarrow{\mathcal{A}_{ud}^{u,m}} \begin{bmatrix} d\boldsymbol{u}^{n+1} \\ dp_J^* \end{bmatrix} \xrightarrow{\mathcal{A}_{ud}^{p,m}} \begin{bmatrix} d\boldsymbol{u}^{n+1} \\ dp_J^{n+1} \end{bmatrix}, \quad \text{where} \quad \begin{cases} \mathcal{A}_{ud}^{u,m} : \operatorname{Div} d\boldsymbol{\sigma} = \mathbf{0},\ \delta dm_J = 0, \\ \mathcal{A}_{ud}^{p,m} : d\dot{m}_J + \operatorname{Div} d\boldsymbol{w}_J = 0, \\ d\dot{\boldsymbol{\varepsilon}} = \mathbf{0},\ d\dot{\boldsymbol{\varepsilon}}_p = \mathbf{0},\ d\dot{\boldsymbol{\xi}} = \mathbf{0}, \end{cases} \tag{6.82}$$

where maximum plastic dissipation is assumed for elastoplasticity. We have homogeneous boundary conditions. When solving the mechanical problem $\mathcal{A}_{ud}^{u,m}$ of Equation 6.82, we obtain

$$\begin{aligned} \frac{d\left\|d\chi_m\right\|_{\mathcal{N}_m}^2}{dt} &= \int_\Omega \left(d\boldsymbol{\sigma} : d\dot{\boldsymbol{\varepsilon}} + \left(\frac{dp}{\rho}\right)_J d\dot{m}_J \right) d\Omega - \underbrace{\int_\Omega \left(d\boldsymbol{\sigma}' : d\dot{\boldsymbol{\varepsilon}}_p + d\kappa \cdot d\dot{\xi} \right) d\Omega}_{D_p^d} \\ &= \int_\Omega d\boldsymbol{\sigma} : d\dot{\boldsymbol{\varepsilon}} d\Omega - D_p^d \\ &= -D_p^d \le 0 \quad (\text{from Equation } 6.82_1), \end{aligned} \tag{6.83}$$

which shows the contractivity property relative to the norm $\|\cdot\|_{\mathcal{N}_m}$.

Then when solving the flow problem $\mathcal{A}_{ud}^{p,m}$ of Equation 6.82,

$$\begin{aligned} \frac{d\left\|d\chi_m\right\|_{\mathcal{N}_m}^2}{dt} &= \int_\Omega \left(d\boldsymbol{\sigma} : d\dot{\boldsymbol{\varepsilon}} + \left(\frac{dp}{\rho}\right)_J d\dot{m}_J \right) d\Omega - \underbrace{\int_\Omega \left(d\boldsymbol{\sigma}' : d\dot{\boldsymbol{\varepsilon}}_p + d\kappa \cdot d\dot{\xi} \right) d\Omega}_{D_p^d} \\ &= \int_\Omega -dp_J \operatorname{Div}(d\boldsymbol{v}_J) d\Omega \quad \left(\because d\dot{\boldsymbol{\varepsilon}} = \mathbf{0},\ d\dot{\boldsymbol{\varepsilon}}_p = \mathbf{0},\ d\dot{\boldsymbol{\xi}} = \mathbf{0} \right) \\ &= -\int_\Omega d\boldsymbol{v}_J \cdot \mathbf{k}_{p,JK}^{-1} d\boldsymbol{v}_K d\Omega \le 0, \end{aligned} \tag{6.84}$$

which shows the contractivity property relative to the norm $\|\cdot\|_{\mathcal{N}_m}$. Therefore, the undrained split holds the contractivity property relative to the norms $\|\cdot\|_{\mathcal{N}_m}$ and $\|\cdot\|_{\mathcal{T}_m}$ for coupled

multiphase flow and mechanics.

6.4.4 Contractivity of the fixed-stress split

From Equation 6.10, the fixed-stress split has the form

$$\begin{bmatrix} d\boldsymbol{u}^n \\ dp_J^n \end{bmatrix} \xrightarrow{\mathcal{A}_{ss}^{p,m}} \begin{bmatrix} d\boldsymbol{u}^* \\ dp_J^{n+1} \end{bmatrix} \xrightarrow{\mathcal{A}_{ss}^{u,m}} \begin{bmatrix} d\boldsymbol{u}^{n+1} \\ dp_J^{n+1} \end{bmatrix}, \quad \text{where} \quad \begin{cases} \mathcal{A}_{ss}^{p,m} : d\dot{m}_J + \operatorname{Div} d\boldsymbol{w}_J = 0,\ \delta d\dot{\sigma}_v = 0, \\ \mathcal{A}_{ss}^{u,m} : \operatorname{Div} d\boldsymbol{\sigma} = \boldsymbol{0},\ dp_J = 0 \\ \quad \Rightarrow \quad \operatorname{Div} d\boldsymbol{\sigma}' = \boldsymbol{0}, \end{cases} \tag{6.85}$$

which has homogeneous boundary conditions. Note that the maximum plastic dissipation is applied implicitly to multiphase flow, just as it does for single-phase flow. The constraint $\delta d\dot{\sigma}_v = 0$ yields $\delta d\dot{\boldsymbol{\sigma}} = \boldsymbol{0}$ because the flow problem $\mathcal{A}_{ss}^{p,m}$ does not affect the shear stress field.

When we solve the flow problem, $\mathcal{A}_{ss}^{p,m}$, the initial conditions for the stress field (i.e., $\operatorname{Div} d\dot{\boldsymbol{\sigma}}_{t=0} = 0$ and $\operatorname{Div} d\boldsymbol{\sigma}_{t=0} = 0$) and $\delta d\dot{\boldsymbol{\sigma}} = \boldsymbol{0}$ yield

$$\operatorname{Div} d\boldsymbol{\sigma} = 0. \tag{6.86}$$

Then we obtain

$$\int_\Omega d\boldsymbol{\sigma} : d\dot{\boldsymbol{\varepsilon}} d\Omega = 0, \tag{6.87}$$

which is the same as the fixed-stress split for single-phase flow.

Hence, when solving the flow problem, we show the contractivity of the fixed-stress split as

$$\begin{aligned}\frac{d\left\|d\chi_m\right\|^2_{\mathcal{N}_m}}{dt} &= \int_\Omega \left(d\boldsymbol{\sigma} : \dot{d\boldsymbol{\varepsilon}} + \left(\frac{dp}{\rho}\right)_J \dot{dm}_J \right) d\Omega - \underbrace{\int_\Omega \left[d\boldsymbol{\sigma}' : \dot{d\boldsymbol{\varepsilon}}_p + d\kappa \cdot \dot{d\xi} \right] d\Omega}_{D_p^d} \\ &= -\int_\Omega \left(d\boldsymbol{v}_J \cdot \mathbf{k}^{-1}_{p,JK} \mu d\boldsymbol{v}_K \right) d\Omega - D_p^d \leq 0. \end{aligned} \tag{6.88}$$

When solving the mechanical problem $\mathcal{A}^{u,m}_{ss}$, we show the contractivity of the fixed-stress split as

$$\begin{aligned}\frac{d\left\|d\chi_m\right\|^2_{\mathcal{N}_m}}{dt} &= \int_\Omega \left(d\boldsymbol{\sigma} : \dot{d\boldsymbol{\varepsilon}} + \left(\frac{dp}{\rho}\right)_J \dot{dm}_J \right) d\Omega - \underbrace{\int_\Omega \left[d\boldsymbol{\sigma}' : \dot{d\boldsymbol{\varepsilon}}_p + d\kappa \cdot \dot{d\xi} \right] d\Omega}_{D_p^d} \\ &= \int_\Omega d\boldsymbol{\sigma}' : \dot{d\boldsymbol{\varepsilon}} d\Omega - D_p^d \\ &= -D_p^d \leq 0, \\ &\quad \left(\int_\Omega d\boldsymbol{\sigma}' : \dot{d\boldsymbol{\varepsilon}} d\Omega = 0 \text{ from Equation } 6.85_2 \right). \end{aligned} \tag{6.89}$$

Therefore, the fixed-stress split holds the contractivity property relative to the norms $\|\cdot\|_{\mathcal{N}_m}$ and $\|\cdot\|_{\mathcal{T}_m}$.

6.4.5 B-stability of the sequential methods

Since the undrained and fixed-stress splits are contractive, we study the two sequential schemes for discrete stability, B-stability relative to the norms $\|\cdot\|_{\mathcal{N}_m}$ or $\|\cdot\|_{\mathcal{T}_m}$, which is expressed as

$$\begin{aligned}\left\|d\chi_m{}^{n+1}\right\|_{\mathcal{N}_m} &\leq \left\|d\chi_m{}^{n}\right\|_{\mathcal{N}_m}, \\ \left\|d\zeta_m{}^{n+1}\right\|_{\mathcal{T}_m} &\leq \left\|d\zeta_m{}^{n}\right\|_{\mathcal{T}_m}. \end{aligned} \tag{6.90}$$

We use the generalized midpoint rule for time discretization. Thus, the return mapping

algorithm for elastoplasticity is also based on the generalized midpoint rule, which satisfies (Simo, 1991; Simo and Govindjee, 1991)

$$\ll \Sigma^{tr,n+\alpha} - \Sigma^{n+\alpha},\ \Pi - \Sigma^{n+\alpha} \gg \leq 0 \quad {}^{\forall}\Pi \in \mathcal{E}\,, \tag{6.91}$$

which follows the notation used in single-phase flow.

Same as single-phase flow, Equation 6.91 yields

$$\begin{aligned} &\ll d\Sigma^{n} - d\Sigma^{n+\alpha},\ -d\Sigma^{n+\alpha} \gg \\ &+ \ll (\alpha \mathbf{C}_{dr} \Delta d\varepsilon^{n}, 0),\ (-d\boldsymbol{\sigma}'^{n+\alpha}, -d\boldsymbol{\kappa}^{n+\alpha}) \gg \leq 0, \end{aligned} \tag{6.92}$$

which will be used for elastoplasticity.

6.4.6 B-stability of the undrained split

We show B-stability for two steps, mechanics and flow. When we solve the mechanical problem by the undrained split $\mathcal{A}_{ud}^{u,m}$, the discrete form of the mechanical problem is expressed as

$$\operatorname{Div} d\boldsymbol{\sigma}^{n+\alpha} = \mathbf{0}, \quad \Delta dm_J = 0. \tag{6.93}$$

When we solve the mechanical problem, Equation 6.92 is satisfied. The first term of Equation 6.92 can be written as

$$\begin{aligned} &\ll d\Sigma^{n} - d\Sigma^{n+\alpha},\ -d\Sigma^{n+\alpha} \gg \\ &= - \ll \alpha(d\Sigma^{n} - d\Sigma^{n+1}),\ d\Sigma^{n+1/2} + \left(\alpha - \frac{1}{2}\right)\left(d\Sigma^{n+1} - d\Sigma^{n}\right) \gg \\ &= \alpha\left(\left\|d\Sigma^{n+1}\right\|_{\mathcal{E}}^{2} - \left\|d\Sigma^{n}\right\|_{\mathcal{E}}^{2}\right) + \alpha\,(2\alpha - 1)\left\|d\Sigma^{n+1} - d\Sigma^{n}\right\|_{\mathcal{E}}^{2}. \end{aligned} \tag{6.94}$$

The second term of Equation 6.92 becomes

$$
\begin{aligned}
&\ll (\alpha \mathbf{C}_{dr} \Delta d\varepsilon^n, 0),\ (-d\boldsymbol{\sigma}'^{n+\alpha}, -d\kappa^{n+\alpha}) \gg \\
&= -\int_\Omega \alpha \Delta d\varepsilon^n : d\boldsymbol{\sigma}'^{n+\alpha} d\Omega \\
&= -\alpha \int_\Omega \Delta d\varepsilon^n : (d\boldsymbol{\sigma}^{n+\alpha} + b_J dp_J^{n+\alpha} \mathbf{1}) d\Omega \\
&= -\alpha \int_\Omega \Delta d\varepsilon^n : b_J dp_J^{n+\alpha} \mathbf{1} d\Omega \\
&\quad \left(\because \int_\Omega \Delta d\varepsilon^n : d\boldsymbol{\sigma}^{n+\alpha} d\Omega = 0 \text{ from Equation 6.93} \right) \\
&= \alpha \int_\Omega dp_J^{n+\alpha} N_{JK} (dp_K^{n+1} - dp_K^n) d\Omega \\
&\quad \left(\because b_J \Delta d\varepsilon^n : \mathbf{1} = -N_{JK} (dp_K^{n+1} - dp_K^n) \text{ from } \Delta dm_J = 0 \right) \\
&= \alpha \left(\left\| d\mathbf{p}^{n+1} \right\|_{\mathcal{M}}^2 - \left\| d\mathbf{p}^n \right\|_{\mathcal{M}}^2 \right) + \alpha (2\alpha - 1) \left\| d\mathbf{p}^{n+1} - d\mathbf{p}^n \right\|_{\mathcal{M}}^2 , \qquad (6.95)
\end{aligned}
$$

where $\|\cdot\|_{\mathcal{M}}$ is defined as

$$
\|\mathbf{p}\|_{\mathcal{M}}^2 = \frac{1}{2} \int_\Omega p_J N_{JK} p_K d\Omega. \qquad (6.96)
$$

Using Equation 6.92, Equations 6.94 and 6.95 yield

$$
\begin{aligned}
&\alpha \left(\left\| d\Sigma^{n+1} \right\|_{\mathcal{E}}^2 - \left\| d\Sigma^n \right\|_{\mathcal{E}}^2 + (\left\| d\mathbf{p}^{n+1} \right\|_{\mathcal{M}}^2 - \left\| d\mathbf{p}^n \right\|_{\mathcal{M}}^2) \right) \\
&+\alpha (2\alpha - 1) \left(\left\| d\Sigma^{n+1} - d\Sigma^n \right\|_{\mathcal{E}}^2 + \left\| d\mathbf{p}^{n+1} - d\mathbf{p}^n \right\|_{\mathcal{M}}^2 \right) \leq 0. \qquad (6.97)
\end{aligned}
$$

From Equation 6.97, when solving the mechanical problem, the undrained split shows

$$
\begin{aligned}
&\left\|d\chi_m{}^{n+1}\right\|^2_{\mathcal{N}_m} - \|d\chi_m{}^n\|^2_{\mathcal{N}_m} \\
&= \left\|d\zeta_m{}^{n+1}\right\|^2_{\mathcal{T}_m} - \|d\zeta_m{}^n\|^2_{\mathcal{T}_m} \\
&= \left\|d\Sigma^{n+1}\right\|^2_{\mathcal{E}} + \left\|d\mathbf{p}^{n+1}\right\|^2_{\mathcal{M}} - \|d\Sigma^n\|^2_{\mathcal{E}} - \|d\mathbf{p}^n\|^2_{\mathcal{M}} \\
&\leq -(2\alpha - 1)\left(\left\|d\Sigma^{n+1} - d\Sigma^n\right\|^2_{\mathcal{E}} + \left\|d\mathbf{p}^{n+1} - d\mathbf{p}^n\right\|^2_{\mathcal{M}}\right).
\end{aligned} \tag{6.98}
$$

From Equation 6.98, the undrained split has B-stability when we solve the mechanical problem if $0.5 \leq \alpha \leq 1$.

When we solve the flow problem $\mathcal{A}^{p,m}_{ud}$, Equation 6.82 produces the discrete form as

$$
N_{JK}\frac{dp_K^{n+1} - dp_K^n}{\Delta t} + b_J\frac{d\varepsilon_v^{n+1} - d\varepsilon_v^n}{\Delta t} + \mathrm{Div}(d\boldsymbol{v}_J^{n+\alpha}) = 0, \tag{6.99}
$$

$$
\Delta d\boldsymbol{\varepsilon} = \mathbf{0},\ \Delta d\boldsymbol{\varepsilon}_p = \mathbf{0},\ \Delta d\boldsymbol{\xi} = \mathbf{0}. \tag{6.100}
$$

Equations 6.99 and 6.100 yield with the Darcy law

$$
\begin{aligned}
&\int_\Omega dp_J^{n+\alpha} N_{JK}\frac{(dp_K^{n+1} - dp_K^n)}{\Delta t} d\Omega \\
&= \int_\Omega \mathbf{Grad}\, dp_J^{n+\alpha} d\boldsymbol{v}_J^{n+\alpha} d\Omega \\
&= -\int_\Omega d\boldsymbol{v}_J^{n+\alpha} \cdot \mathbf{k}^{-1}_{p,JK} d\boldsymbol{v}_K^{n+\alpha} d\Omega \\
&\quad \left(\because \mathbf{Grad}\, dp_J^{n+\alpha} = -\mathbf{k}^{-1}_{p,JK} d\boldsymbol{v}_K^{n+\alpha}\right).
\end{aligned} \tag{6.101}
$$

Equation 6.100 yields

$$
\left\|d\Sigma^{n+1}\right\|^2_{\mathcal{E}} = \|d\Sigma^n\|^2_{\mathcal{E}}. \tag{6.102}
$$

We introduce the following identity,

$$\int_{\Omega} dp_J^{n+\alpha} N_{JK} \left(dp_K^{n+1} - dp_K^n\right) d\Omega$$
$$= \left(\left\|d\mathbf{p}^{n+1}\right\|_{\mathcal{M}}^2 - \|d\mathbf{p}^n\|_{\mathcal{M}}^2\right) + (2\alpha - 1)\left\|d\mathbf{p}^{n+1} - d\mathbf{p}^n\right\|_{\mathcal{M}}^2. \tag{6.103}$$

From Equations 6.101 – 6.103, B-stability is achieved during the flow step, shown as

$$\begin{aligned}
&\left\|d{\chi_m}^{n+1}\right\|_{\mathcal{N}_m}^2 - \|d{\chi_m}^n\|_{\mathcal{N}_m}^2 \\
&= \left\|d{\zeta_m}^{n+1}\right\|_{\mathcal{T}_m}^2 - \|d{\zeta_m}^n\|_{\mathcal{T}_m}^2 \\
&= \left\|d\mathbf{p}^{n+1}\right\|_{\mathcal{M}}^2 - \|d\mathbf{p}^n\|_{\mathcal{M}}^2 \\
&= -(2\alpha - 1)\left\|d\mathbf{p}^{n+1} - d\mathbf{p}^n\right\|_{\mathcal{M}}^2 - \Delta t \int_{\Omega} d\boldsymbol{v}_J{}^{n+\alpha} \cdot \mathbf{k}_{p,JK}^{-1} d\boldsymbol{v}_K{}^{n+\alpha} d\Omega,
\end{aligned} \tag{6.104}$$

where the stability condition is $0.5 \leq \alpha \leq 1$. From Equations 6.98 and 6.104, the undrained split is B-stable if $0.5 \leq \alpha \leq 1$.

6.4.7 B-stability of the fixed-stress split

We show B-stability of the flow step first, followed by the mechanics step. When we solve the flow problem by the fixed-stress split, the discrete form of the flow problem is written as

$$N_{JK} \frac{dp_K^{n+1} - dp_K^n}{\Delta t} + b_J \frac{d\varepsilon_v^{n+1} - d\varepsilon_v^n}{\Delta t} + \mathrm{Div}(d\boldsymbol{v}_J^{n+\alpha}) = 0, \tag{6.105}$$
$$d\boldsymbol{\sigma}^{n+1} - d\boldsymbol{\sigma}^n = d\boldsymbol{\sigma}^n - d\boldsymbol{\sigma}^{n-1}, \tag{6.106}$$

where the initial conditions for the stress field satisfy

$$\mathrm{Div}\left(d\boldsymbol{\sigma}^1 - d\boldsymbol{\sigma}^0\right) = 0, \ \mathrm{Div}\, d\boldsymbol{\sigma}^0 = 0. \tag{6.107}$$

Same as for the single-phase flow case, Equations 6.106 and 6.107 provide

$$\mathrm{Div}\, d\boldsymbol{\sigma}^{n+\alpha} = 0, \tag{6.108}$$

which, when we solve the flow problem, yields

$$\int_\Omega d\boldsymbol{\sigma}^{n+\alpha} : \Delta d\boldsymbol{\varepsilon}^n d\Omega = 0. \tag{6.109}$$

Since maximum plastic dissipation is assumed for the flow problem, Equation 6.92 is satisfied. Note that Equation 6.94 is an identity. The second term of Equation 6.92 is calculated as

$$\begin{aligned}
&\ll (\alpha \mathbf{C}_{dr} \Delta d\varepsilon^n, 0),\ (-d\boldsymbol{\sigma}'^{n+\alpha}, -d\kappa^{n+\alpha}) \gg \\
&= -\int \alpha \Delta d\varepsilon^n : d\boldsymbol{\sigma}'^{n+\alpha} d\Omega \\
&= -\alpha \int \Delta d\varepsilon^n : (d\boldsymbol{\sigma}^{n+\alpha} + b_J dp_J^{n+\alpha} \mathbf{1}) d\Omega \\
&= -\alpha \int \Delta d\varepsilon_v^n b_J dp_J^{n+\alpha} d\Omega \quad \text{(from Equation 6.109)}.
\end{aligned} \tag{6.110}$$

From Equations 6.94 and 6.110, Equation 6.92 can be written as

$$\begin{aligned}
&\left(\left\| d\Sigma^{n+1} \right\|_{\mathcal{E}}^2 - \left\| d\Sigma^n \right\|_{\mathcal{E}}^2 \right) + (2\alpha - 1) \left\| d\Sigma^{n+1} - d\Sigma^n \right\|_{\mathcal{E}}^2 \\
&- \int \Delta d\varepsilon_v^n b_J dp_J^{n+\alpha} d\Omega \leq 0.
\end{aligned} \tag{6.111}$$

From Equation 6.105, the flow equation, $\mathcal{A}_{ss}^{p,m}$, has the following property

$$\int dp_J^{n+\alpha} \left(N_{JK} \frac{dp_K^{n+1} - dp_K^n}{\Delta t} + b \frac{d\varepsilon_v^{n+1} - d\varepsilon_v^n}{\Delta t} + \mathrm{Div}(d\boldsymbol{v}_J^{n+\alpha}) \right) d\Omega = 0. \tag{6.112}$$

Using the identity of Equation 6.103, Equation 6.112 with Darcy's law is written as

$$\begin{aligned}
&\left\|d\mathbf{p}^{n+1}\right\|_{\mathcal{M}}^2 - \|d\mathbf{p}^n\|_{\mathcal{M}}^2 \\
&= -(2\alpha-1)\left\|d\mathbf{p}^{n+1} - d\mathbf{p}^n\right\|_{\mathcal{M}}^2 - \int dp_J^{n+\alpha} b_J \Delta d\varepsilon_v^n d\Omega \\
&\quad -\Delta t \int d\boldsymbol{v}_J^{n+\alpha} \cdot \mathbf{k}_{p,JK}^{-1} d\boldsymbol{v}_K^{n+\alpha} d\Omega.
\end{aligned} \tag{6.113}$$

Thus, when we solve the flow problem by the fixed-stress split, we can show the evolution of the norm $\|\cdot\|_{\mathcal{N}_m}$ by adding Equations 6.111 and 6.113. So, we have

$$\begin{aligned}
&\left\|d{\chi_m}^{n+1}\right\|_{\mathcal{N}_m}^2 - \|d{\chi_m}^n\|_{\mathcal{N}_m}^2 \\
&= \left\|d{\zeta_m}^{n+1}\right\|_{\mathcal{T}_m}^2 - \|d{\zeta_m}^n\|_{\mathcal{T}_m}^2 \\
&= \left\|d\Sigma^{n+1}\right\|_{\mathcal{E}}^2 + \left\|d\mathbf{p}^{n+1}\right\|_{\mathcal{M}}^2 - \|d\Sigma^n\|_{\mathcal{E}}^2 - \|d\mathbf{p}^n\|_{\mathcal{M}}^2 \\
&\leq -(2\alpha-1)\left(\left\|d\Sigma^{n+1} - d\Sigma^n\right\|_{\mathcal{E}}^2 + \left\|d\mathbf{p}^{n+1} - d\mathbf{p}^n\right\|_{\mathcal{M}}^2\right) \\
&-\Delta t \int d\boldsymbol{v}_J^{n+\alpha} \cdot \mathbf{k}_{p,JK}^{-1} d\boldsymbol{v}_K^{n+\alpha} d\Omega.
\end{aligned} \tag{6.114}$$

From Equation 6.114, we obtain the condition for B-stability if $0.5 \leq \alpha \leq 1$ when we solve the flow problem.

After the flow step, we solve the mechanical problem. From Equation 6.85,

$$\mathrm{Div}\, d\boldsymbol{\sigma}'^{n+\alpha} = \mathbf{0}, d\mathbf{p}^{n+\alpha} = \mathbf{0}, \tag{6.115}$$

to which maximum plastic dissipation, Equation 6.92, is applied. The second term of Equation 6.92 is calculated as

$$\begin{aligned}
&\ll (\alpha \mathbf{C}_{dr} \Delta d\varepsilon^n, 0),\ (-d\boldsymbol{\sigma}'^{n+\alpha}, -d\kappa^{n+\alpha}) \gg \\
&= -\int \alpha \Delta d\varepsilon^n : d\boldsymbol{\sigma}'^{n+\alpha} d\Omega = 0.
\end{aligned} \tag{6.116}$$

Using Equations 6.94 and 6.116, Equation 6.92 becomes

$$\left(\left\| d\Sigma^{n+1} \right\|_{\mathcal{E}}^2 - \left\| d\Sigma^n \right\|_{\mathcal{E}}^2 \right) + (2\alpha - 1) \left\| d\Sigma^{n+1} - d\Sigma^n \right\|_{\mathcal{E}}^2 \leq 0. \tag{6.117}$$

Since $dp_J^{n+\alpha} = \mathbf{0}$, Equation 6.103 provides

$$\left\| d\mathbf{p}^{n+1} \right\|_{\mathcal{M}}^2 - \left\| d\mathbf{p}^n \right\|_{\mathcal{M}}^2 = -(2\alpha - 1) \left\| d\mathbf{p}^{n+1} - d\mathbf{p}^n \right\|_{\mathcal{M}}^2. \tag{6.118}$$

Then Equations 6.117 and 6.118 yield

$$\begin{aligned}
&\left\| d{\chi_m}^{n+1} \right\|_{\mathcal{N}_m}^2 - \left\| d{\chi_m}^n \right\|_{\mathcal{N}_m}^2 \\
&= \left\| d{\zeta_m}^{n+1} \right\|_{\mathcal{T}_m}^2 - \left\| d{\zeta_m}^n \right\|_{\mathcal{T}_m}^2 \\
&= \left\| d\Sigma^{n+1} \right\|_{\mathcal{E}}^2 - \left\| d\Sigma^n \right\|_{\mathcal{E}}^2 + \left\| d\mathbf{p}^{n+1} \right\|_{\mathcal{M}}^2 - \left\| d\mathbf{p}^n \right\|_{\mathcal{M}}^2 \\
&\leq -(2\alpha - 1) \left(\left\| d\Sigma^{n+1} - d\Sigma^n \right\|_{\mathcal{E}}^2 + \left\| d\mathbf{p}^{n+1} - d\mathbf{p}^n \right\|_{\mathcal{M}}^2 \right),
\end{aligned} \tag{6.119}$$

from which B-stability is achieved if $0.5 \leq \alpha \leq 1$ when we solve the mechanical problem, $A_{ss}^{u,m}$. Therefore, from Equations 6.114 and 6.119, the fixed-stress split has B-stability if $0.5 \leq \alpha \leq 1$.

6.5 Numerical Examples with the staggered Newton methods

We test the four sequential methods based on a staggered Newton approach. We use one and two dimensional oil production problems with water injection and overburden.

Case 6.1 Water injection and oil production in a 1D poroelastic medium. The driving force is due to injection, production, and an overburden (the left picture in Figure 6.2).

Case 6.2 Water injection and oil production in a 2D poroelastic medium. The compaction and dilation of the reservoir occur due to production of oil and injection of water, respectively (the right picture in Figure 6.2).

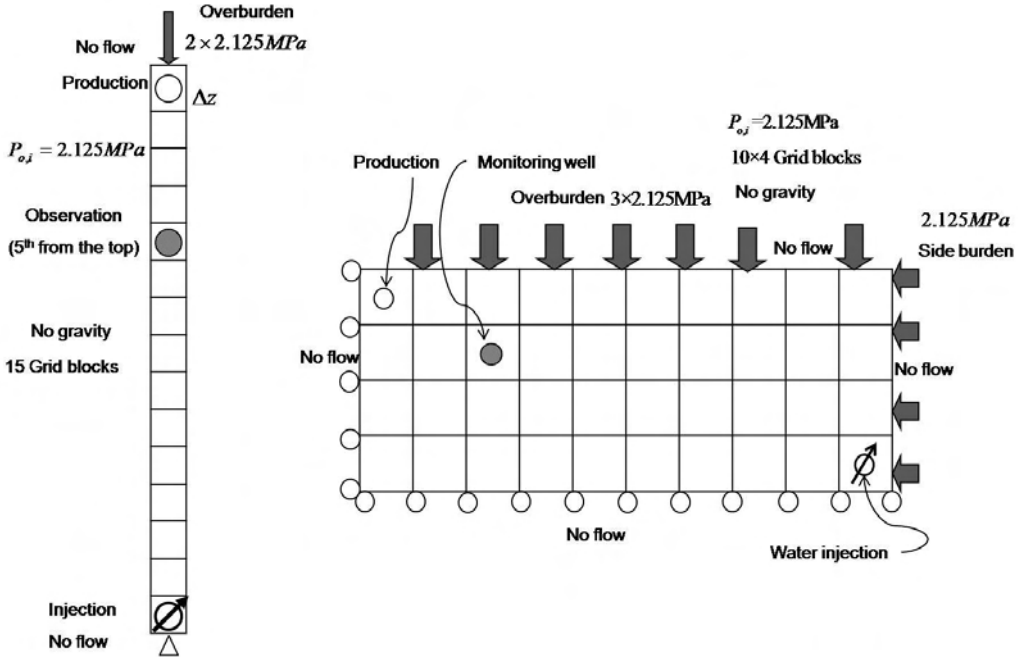

Figure 6.2: Water injection and oil production. Left: coupled multiphase flow and geomechanics in a 1D poroelastic medium with overburden. Right: coupled multiphase flow and geomechanics in a 2D poroelastic medium with overburden and side burden

6.5.1 Case 6.1—Water injection and oil production in the 1D poroelasticity

The schematic of this 1D problem is shown in the left plot of Figure 6.2. For Case 6.1, dilation and compaction occur around the injection and production wells, respectively. The water injection rate $Q_{w,inj} = 500\ kg\ day^{-1}$ is the same as the production rate $Q_{o,prod} = 500\ kg\ day^{-1}$. The domain is homogeneous with 15 grid blocks. The length of the domain is $L_z = 150\ m$ with grid spacing $\Delta z = 10\ m$. We have a constant overburden $\bar{\sigma} = 2 \times 2.125\ MPa$. A no-displacement boundary condition is maintained at the bottom of the domain. The bulk density of the porous medium is $\rho_b = 2400\ kg\ m^{-1}$. The initial oil pressure is $P_{o,i} = 2.125\ MPa$, where the formation is fully saturated with oil initially. The fluid densities and viscosities are $\rho_{o,0} = \rho_{w,0} = 1000\ kg\ m^{-1}$ and $\mu_o = \mu_w = 1.0\ cp$, respectively. Permeability is $k_p = 500\ md$, porosity is $\phi_0 = 0.3$, constrained modulus is $K_{dr} = 1\ GPa$, and the Biot coefficient is $b = 1.0$. Capillarity is ignored. A monitoring well is located at the fifth grid block from the top (1, 5). No-flow boundary conditions are applied at the top and bottom. Gravity is neglected. The oil and water compressibilities are similar, $c_o = 3.5 \times 10^{-9}\ Pa^{-1}$ and $c_w = 3.0 \times 10^{-9}\ Pa^{-1}$, respectively. These values yield $\tau = 0.95$ and $\tau = 1.05$ for single-phase flow, respectively. The residual oil and water saturations are zero. The parameter values for Case 6.1 are also given in Table 6.1.

Since the convergence behaviors of the drained and fixed-strain splits depend on the total fluid compressibility from Equations 6.31 and 6.44, water injection can cause non-convergence and instability during simulation.

We use a linear relative permeability of phase J, $k_{r,J}$, with respect to S_J, i.e.,

$$k_{r,J} = (S_J - S_{r,J}), \tag{6.120}$$

where $S_{r,J}$ is the residual saturation of J phase.

The top of Figure 6.3 shows the pressure history at the monitoring well during simulation. The pressure jumps at the initial time because of the excessive overburden and decreases with production. Then the pressure rises because the reservoir is being filled with

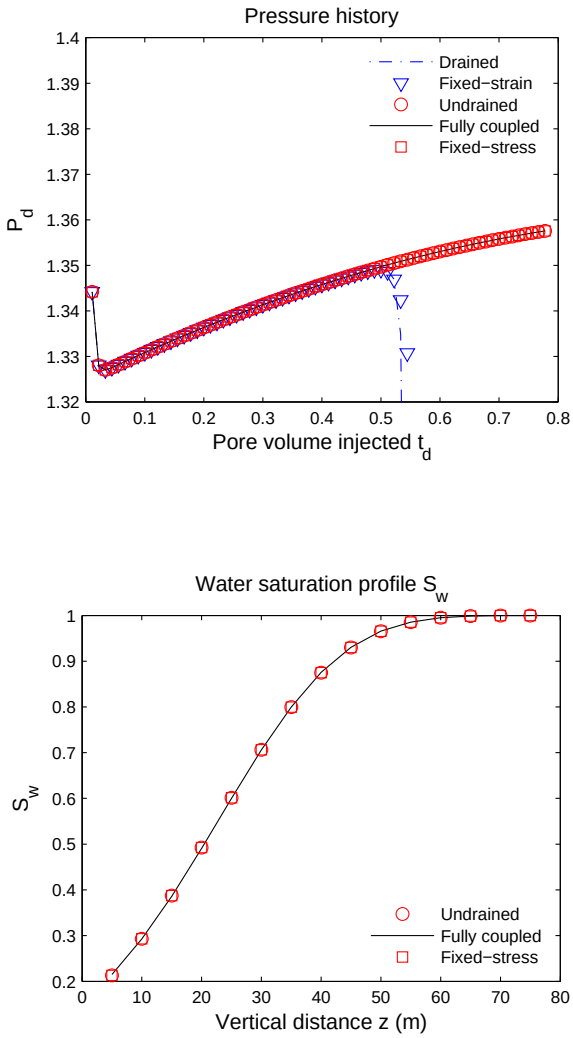

Figure 6.3: Top: pressure history at the monitoring well during simulation. Bottom: water saturation profile after simulation. $P_d = P/P_{o,i}$.

Table 6.1: Input data for Case 6.1

Property	Value
Permeability (k_p)	500 md
Porosity (ϕ_0)	0.3
Drained modulus (K_{dr})	1.0 GPa
Biot coefficient (b)	1.0
Bulk density (ρ_b)	2400 $\mathrm{kg\,m^{-3}}$
Oil compressibility (c_o)	3.5×10^{-9} $\mathrm{Pa^{-1}}$
Oil density ($\rho_{o,0}$)	1000 $\mathrm{kg\,m^{-3}}$
Oil viscosity (μ_o)	1.0 cp
Water compressibility (c_w)	3.0×10^{-9} $\mathrm{Pa^{-1}}$
Water density ($\rho_{w,0}$)	1000 $\mathrm{kg\,m^{-3}}$
Water viscosity (μ_w)	1.0 cp
Initial oil pressure ($P_{o,i}$)	2.125 MPa
Overburden ($\bar{\sigma}$)	2×2.125 MPa
Grid spacing (Δz)	10 m
Grid blocks	15
Water injection rate	500 $\mathrm{kg\,day^{-1}}$
Total liquid production rate	500 $\mathrm{kg\,day^{-1}}$
Residual oil saturation $S_{r,o}$	0
Residual water saturation $S_{r,w}$	0

a less compressible fluid, water. As oil is replaced by water, the total fluid compressibility decreases during simulation. The drained and fixed-strain splits violate the convergence conditions around $t_d = 0.5$ and suffer from severe instabilities. The bottom of Figure 6.3 shows the water saturation profile at the end of simulation $t_d = 0.78$. Water occupies significant portions of the reservoir, yielding a higher coupling strength compared with the initial condition where the medium was fully saturated by oil, which is more compressible than water.

Figure 6.4 shows the convergence behaviors with respect to the number of iterations at $t_d = 0.08$. The drained and fixed-strain splits show severe oscillations and very slow convergence, whereas the undrained and fixed-stress splits yield fast convergence. The fixed-stress split has the same convergence as the fully coupled method. This is consistent with the fact that the error amplification factor is zero ($\gamma_e = 0$), when we can estimate K_{dr} exactly. For the very first time step, we have errors from the boundary conditions. But,

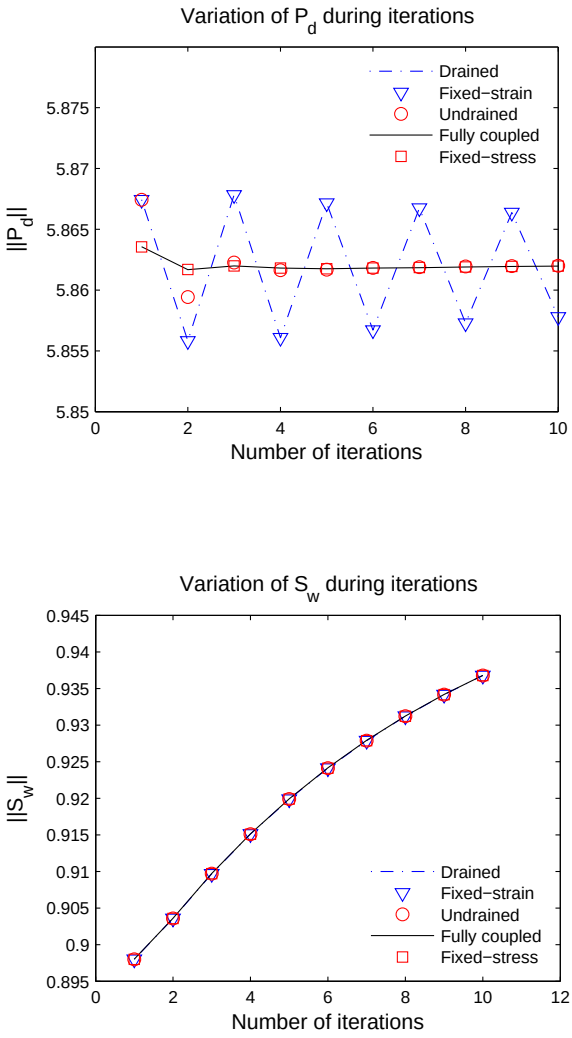

Figure 6.4: Convergence behaviors during iterations at $t_d = 0.08$. Top: pressure. Bottom: water saturation. $\|\cdot\|$ is the L^2 norm.

the error decreases rapidly with iterations. In contrast to pressure, all the schemes shows the same convergence behavior for saturation at $t_d = 0.08$.

6.5.2 Case 6.2—Water injection and oil production in 2D with poroelasticity

Figure 6.2 illustrates a 2D oil production problem. The injection and production wells are located at the right bottom and left top, respectively. The monitoring well is at (3,2) grid block. The input data for the 2D problem are shown in Table 6.2. The dimension of the domain is 100 $m \times 20$ m with 10×4 grid blocks under the plane strain mechanical condition. The water injection rate $Q_{w,inj} = 5000\ kg\ day^{-1}$ is the same as the production rate $Q_{o,prod} = 5000\ kg\ day^{-1}$. The domain is homogeneous. The domain has an overburden $\bar{\sigma} = 3 \times 2.125\ MPa$ on the top, no horizontal displacement on the left side, a side burden $\bar{\sigma_h} = 2.125\ MPa$ on the right side, and no vertical displacement at the bottom. The bulk density of the porous medium is $\rho_b = 2400\ kg\ m^{-1}$. Initial oil pressure is $P_{o,i} = 2.125\ MPa$, where oil fully saturates the formation. The density, viscosity and compressibility of water are $\rho_{w,0} = 1000\ kg\ m^{-1}$, $\mu_w = 1.0\ cp$, and $c_w = 3.5 \times 10^{-10}\ Pa^{-1}$, respectively. The density, viscosity, and compressibility of oil are $\rho_{o,0} = 1000\ kg\ m^{-1}$, $\mu_o = 1.0\ cp$, and $c_o = 3.5 \times 10^{-8}\ Pa^{-1}$, respectively. The permeability, k_p, is 500 md, and the porosity, ϕ_0, is 0.3. Young's modulus is $E = 300\ MPa$, and Poisson's ratio is $\nu = 0.35$. The Biot coefficient is $b = 1.0$. There is no capillarity. No-flow boundary conditions are applied at all sides. Gravity is neglected. The residual oil and water saturations are zero.

The oil and water compressibilities differ from each other by two orders of magnitude. It is anticipated that the drained and fixed-strain splits will face instability because of water injection. The relative permeability is the same as Equation 6.120. Figure 6.5 shows the distributions of pressure and water saturation at $t_d = 0.3$.

As shown in the top of Figure 6.6, the drained and fixed-strain splits deviate from the true solution around $t_d = 0.2$ and become unstable. From the pressure behaviors around $t_d = 0.22$, the solutions by the drained and fixed-strain splits are not reliable, even though they provide finite pressure values. In contrast to the drained and fixed-strain

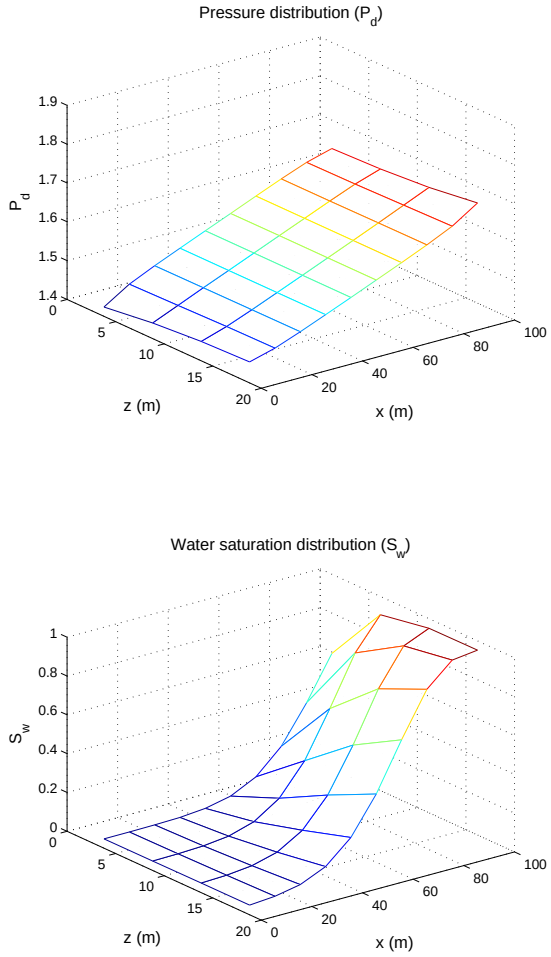

Figure 6.5: Pressure (top) and water saturation (bottom) distributions after simulation.

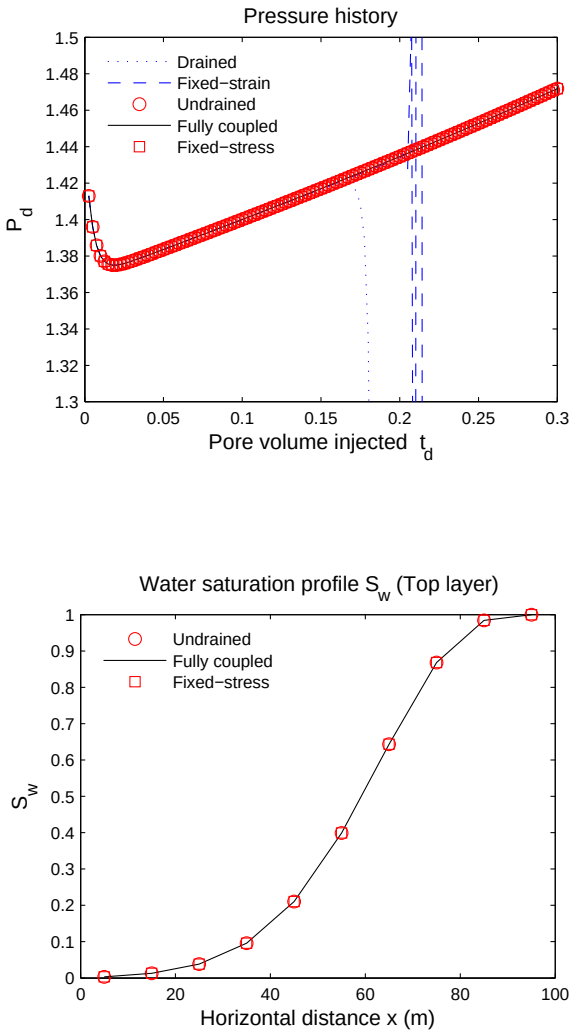

Figure 6.6: Top: pressure history at the monitoring well during simulation. Bottom: water saturation profile at the bottom layer after simulation.

Table 6.2: Input data for Case 6.2

Property	Value
Permeability (k_p)	500 md
Porosity (ϕ_0)	0.3
Young modulus (E)	300 MPa
Poisson ratio (ν)	0.35
Biot coefficient (b)	1.0
Bulk density (ρ_b)	2400 $\mathrm{kg\,m^{-3}}$
Oil compressibility (c_o)	3.5×10^{-8} $\mathrm{Pa^{-1}}$
Oil density ($\rho_{o,0}$)	1000 $\mathrm{kg\,m^{-3}}$
Oil viscosity (μ_o)	1.0 cp
Water compressibility (c_w)	3.5×10^{-10} $\mathrm{Pa^{-1}}$
Water density ($\rho_{w,0}$)	1000 $\mathrm{kg\,m^{-3}}$
Water viscosity (μ_w)	1.0 cp
Initial oil pressure ($P_{o,i}$)	2.125 MPa
Side burden	2.125 MPa
Overburden ($\bar{\sigma}$)	3×2.125 MPa
Grid spacing (Δx)	10 m
Grid spacing (Δz)	5 m
Grid	10×4
Water injection rate	5000 $\mathrm{kg\,day^{-1}}$
Total production rate	5000 $\mathrm{kg\,day^{-1}}$

splits, the undrained and fixed-stress splits yield stable and accurate solutions. The bottom of Figure 6.6 shows the water saturation profile for the bottom layer at $t_d = 0.3$. The high water saturation reduces the total fluid compressibility, and leads to violating the convergence conditions of the drained and fixed-strain splits.

To analyze the convergence of each scheme, we investigate the behaviors as a function of iterations, as shown in Figure 6.7. We choose the first time step for convergence behaviors because the effect of instantaneous loading is considerable for the first time step. The drained and fixed-strain splits show severe oscillations and slow convergence. The undrained split is monotonic and yields better convergence. The fixed-stress split is monotonic and yields the best convergence behavior. There is a large difference between the fixed-stress and fully coupled solutions for the first iteration of the first time step because the fixed-stress split does not capture the instantaneous loading. But, in the second iteration, the

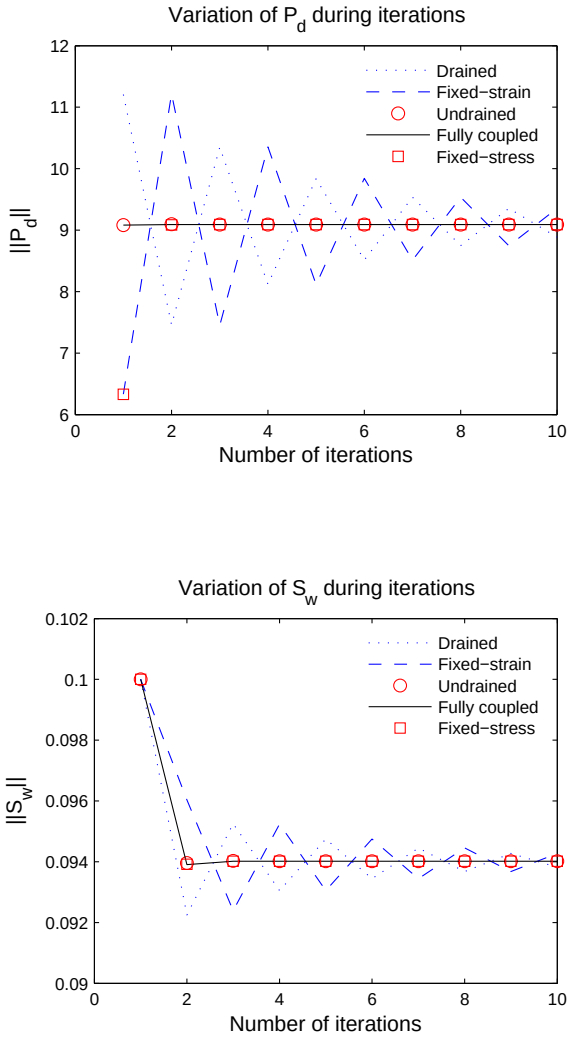

Figure 6.7: Convergence behaviors during iterations at the first time step. Top: pressure. Bottom: water saturation.

difference decreases significantly because the fixed-stress split uses updated information from the mechanical problem, capturing the effect of the instantaneous loading. After the second iteration, the fixed-stress shows the same convergence behavior as the fully coupled method.

6.6 Numerical Examples with the staggered method

We perform numerical simulation with the staggered method, reusing Case 6.2. The top of Figure 6.8 shows the results from the drained and fixed-strain splits. At early time, the two splits are stable because the coupling strength is below unity even though they have severe oscillation. However, the coupling strength increases during simulation because of injection of the less compressible fluid, namely, water. Then the solutions of the drained and fixed strain splits become unstable because the coupling strength exceeds unity eventually. On the other hand, the undrained and fixed-stress splits are stable for all time. The bottom of Figure 6.8 illustrates that the solutions of the undrained and fixed-stress splits are stable with good accuracy with one or two iterations.

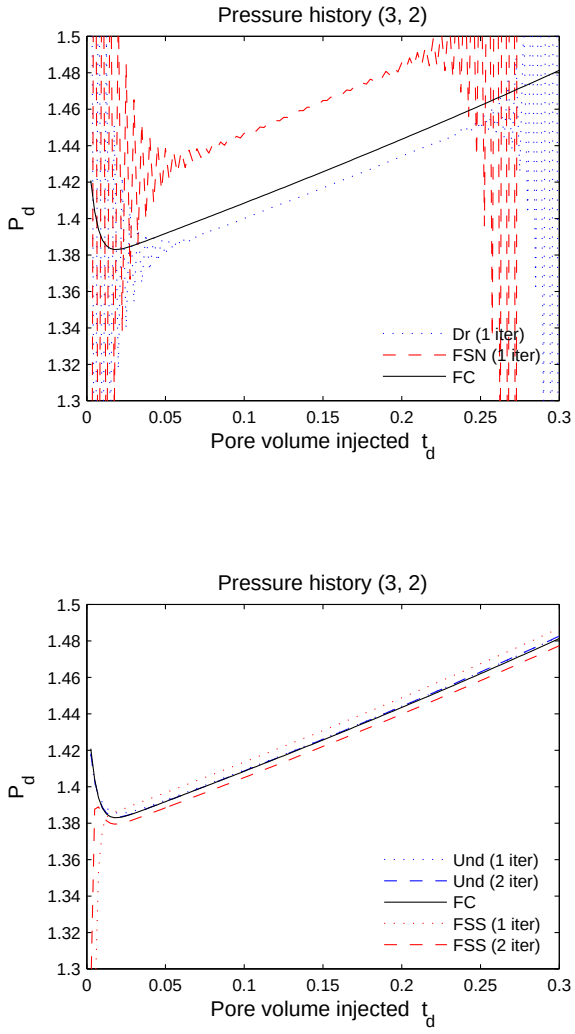

Figure 6.8: Pressure history at the monitoring well during simulation. Top: the drained and fixed-strain splits. Bottom: the undrained and fixed-stress splits. The drained and fixed-strain splits become unstable due to water injection whereas the undrained and fixed-stress splits yield stability with good accuracy.

Chapter 7

Conclusions

In this thesis, we analyzed the performance of four sequential methods for coupled flow and reservoir geomechanics. For numerical simulation, we adopt various time discretizations with the finite-volume and finite-element methods for flow and mechanics, respectively. We have also investigated constitutive relations for the coupling in conjunction with reservoir simulation.

7.1 Formulation of Coupled Flow and Mechanics

In Chapter 2, we reinvestigated the constitutive relations for coupled flow and mechanics based on thermodynamics principles. A linear set of constitutive relations applies for single-phase flow. However, we cannot simply extend the linear model of single-phase flow to nonlinear multiphase flow, since fluid saturations vary over a wide range and the fluid phases may have very different properties (e.g., compressibility). As a result, the incremental form of the constitutive relations are introduced for multiphase flow.

Based on the incremental formulation of the constitutive relations, reservoir simulation systems yield symmetric and positive definite Biot moduli, providing a well-posed problem that is thermodynamically stable.

7.2 Coupled Mechanics and Single-Phase flow

In Chapter 3–5, we limited our analysis to single-phase flow, but we accounted for both elastic and elasto-plastic material behaviors. The four sequential methods analyzed fall in two categories: those that solve the mechanical problem first (drained and undrained splits), and those that solve the flow problem first (fixed-strain and fixed-stress splits). The drained and fixed-strain splits are the obvious splits, as they freeze one of the state variables (pressure or displacement, respectively) in the sequential solution strategy. As we demonstrate quite clearly in this thesis, these obvious splits are not a good choice.

7.2.1 Stability

We have performed a thorough stability analysis using the Von Neumann and energy methods with the generalized midpoint rule for time integration. From the Von Neumann stability analysis, the coupling strength τ emerges as the key parameter. When we apply backward Euler time discretization (i.e., $\alpha = 1.0$), the drained and fixed-strain splits yield conditional stability, and this limit is independent of time step size and depends only on the coupling strength. This implies that stability of the drained and fixed-strain splits cannot be achieved by simply tuning the time step size. Therefore, physical problems with high coupling strength cannot be solved by the drained or fixed-strain splits, regardless of time step size. The stability criterion in one dimension is $\tau \leq 1$. This criterion can be applied, however, to multi-dimensional problems. From the Von Neumann stability analysis we also determine that the drained and fixed-strain splits can have negative amplification factors, which explain their oscillatory behaviors, even when they are stable.

When the midpoint rule $\alpha = 0.5$ is used, the drained split is unconditionally unstable, whereas the fixed-strain split is conditionally stable, where the stability condition is $\tau \leq 1$. But when we use a mixed time discretization, where $\alpha = 1.0$ for mechanics and $\alpha = 0.5$ for flow, the drained split yields the same stability behavior as the backward Euler time discretization.

On the other hand, the undrained and fixed-stress splits show unconditional stability for

both elasticity and elasto-plasticity. Using the Von Neumann method, the undrained and fixed-stress splits are unconditionally stable for $\alpha \geq 0.5$. Moreover, their error amplification factors are always positive for the backward Euler time discretization scheme; as a result, the undrained and fixed-stress numerical solutions do not exhibit oscillations in time. In particular, the fixed-stress split has the same amplification factors as those associated with the fully coupled method.

The undrained and fixed-stress splits can be applied safely to general poro-mechanical behaviors, such as compressible solid grains and plasticity with hardening. For operator splitting, the undrained and fixed-stress splits are contractive relative to the Helmholtz free-energy and the complementary Helmholtz free-energy norms, leading to well-posed problems. For algorithmic (discrete) stability, the undrained and fixed-stress splits yield B-stability relative to the two energy norms, when $\alpha \geq 0.5$.

7.2.2 Convergence

For convergence analysis, we estimated the error propagation for the sequential methods based on the backward Euler time discretization using matrix and spectral methods. One of the key results of this thesis is that the drained and fixed-strain splits with a fixed number of iterations are not convergent. That is, the drained and fixed-strain splits (with, say, a single iteration per time step) converge to a different (wrong) solution as $\Delta t \to 0$, even though they are numerically stable. This result is particularly relevant because the converged solution, even if incorrect, can appear to be physically plausible. We have illustrated this behavior with several test cases, including the Terzaghi problem. Clearly, for the drained and fixed-strain methods, taking more iterations per time step is a better strategy than cutting the time step size.

On the other hand, the undrained and fixed-stress methods are convergent for a compressible fluid with first-order accuracy in time, even if a staggered (one-pass) method is used. In the undrained and fixed-stress splits, reducing the time step size is a better strategy than taking more iterations.

7.2.3 Accuracy and Efficiency

Given that the undrained and the fixed-stress splits have similar (very favorable) stability and convergence properties, which strategy should be used? Here, we have shown that for problems of interest in reservoir engineering, the fixed-stress split converges significantly faster than the undrained split.

The fixed-stress split requires few iterations to match the fully coupled solution, even when the coupling strength is quite high, while the undrained split requires many iterations per time step to achieve similar accuracy. When the fluid is incompressible, or nearly incompressible, the undrained split loses first-order accuracy. On the other hand, the fixed-stress split preserves first-order accuracy regardless of the fluid type. For the rate of convergence, the fixed-stress split needs only two iterations to converge for linear problems, regardless of coupling strength and pressure diffusivity. This assumes that we can estimate the local bulk modulus, K_{dr}, exactly. One cannot estimate the exact local K_{dr} in the flow problem in the presence of complex boundary conditions for the mechanics problem. However, our dimension based estimation of K_{dr} provides stability and first-order accuracy in time for the fixed-stress split, which can be applied to an incompressible fluid.

The undrained split also requires a robust linear solver, due to the fact that a stiffer mechanical problem must be solved, since the undrained moduli are used. In contrast, the fixed-stress split yields a less stiff mechanical problem (drained moduli are used) and a less stiff flow problem as well, due to the added pore-compressibility term.

7.3 Coupled Mechanics and Multiphase Flow

In Chapter 6, we confirm that the fixed-stress split shows better numerical behaviors than the other sequential methods in the presence of multiple phases. In particular, we observed that the fixed-stress split with the staggered Newton scheme yields almost the same convergence rate as the fully coupled method. In fact, one or two iteration(s) with the fixed-stress split yield numerical solutions that match the fully coupled method. This implies that the

fixed-stress split can surpass the fully coupled method because it has comparable convergence rate to the fully coupled method, but it can lead to significant savings in computational cost and provide for flexible numerical schemes of the subproblems.

7.4 Finite-Volume and Finite-Element Methods

For space discretization, we adopt the finite-volume and finite-element methods for flow and mechanics, respectively. Reservoir simulation with the finite-volume method yields local mass conservation, while that with the finite element method does not honor local mass conservation. Use of piecewise constant approximation for the pressure eliminates the spatial oscillations at early time for consolidation.

7.5 Recommendation

In conclusion, we recommend the fixed-stress split with finite-volume and finite-element methods for flow and mechanics, respectively. The fixed-stress scheme is unconditionally stable and has convergence properties that are comparable to the fully coupled method.

Appendix A

Stability in Space

A.1 Background

Spurious numerical instability and inaccuracy in space at early time may result when nodal based finite element methods are employed to model consolidation problems. The instability comes from two parts: the incompressibility of both the fluid and the solid grains, and the discontinuity of pressure at the drainage boundary.

Since pressure diffusion is negligible at early time, the coupled flow-mechanics problem converges to a simple mechanical problem with undrained conditions. Hence, the LBB condition (Fortin and Brezzi, 1991) must be satisfied when both the fluid and the solid grains are incompressible. This is because, under these stiff conditions, the undrained bulk modulus is infinite. This numerical instability is obtained with equal-order approximations of pressure and displacement (e.g., piecewise continuous interpolation), which violates the LBB condition. Stable results are obtained using the elements satisfying the LBB condition (Murad and Loula, 1992; Wan, 2002).

However, the instability is still observed at the drainage boundary when the fluid is compressible even for the elements that satisfy the LBB condition (Vermeer and Verruijt, 1981; Murad and Loula, 1992; Wan, 2002; White and Borja, 2008). For a slightly compressible fluid, the coupled problem at early time reduces to a mechanical problem with a

compressible system, so the LBB condition is not required. This instability at early time is due to having a pressure jump at initial time by instantaneous loading, which causes a discontinuity of pressure at the drainage boundary.

Vermeer and Verruijt (1981) analyze the drainage-boundary instability for linear interpolation functions for pressure and displacement with the nodal based finite-element method in one-dimensional consolidation problems with single-phase flow (i.e., Terzaghi's problem). The flow equation is written as

$$\frac{\partial p}{\partial t} + \omega \frac{\partial \sigma}{\partial t} = c_v \frac{\partial^2 p}{\partial x^2}, \;\; c_v = \frac{k K_{dr}}{\mu}\omega, \;\; \omega = \frac{1/K_{dr}}{1/K_{dr} + \phi c_f}, \tag{A.1}$$

which is equivalent to Equation 3.12. When the initial pressure is zero, the resulting system of equations can be written as (Vermeer and Verruijt, 1981)

$$\begin{bmatrix} 1-2b^* & b^* & & & \\ b^* & 1-2b^* & b^* & & \\ & \cdots & \cdots & \cdots & \\ & & \cdots & \cdots & \cdots \\ & & & b^* & 1-2b^* \end{bmatrix} \begin{bmatrix} \Delta P_1 \\ \Delta P_2 \\ \cdots \\ \cdots \\ \Delta P_{n-1} \end{bmatrix} = \omega \Delta \sigma \begin{bmatrix} 1 \\ 1 \\ \cdots \\ \cdots \\ 1 \end{bmatrix}, \tag{A.2}$$

where

$$b^* = \frac{1}{6} - \alpha \frac{c_v \Delta t}{h^2}. \tag{A.3}$$

Here, α is a parameter from time discretization (e.g., $\alpha = 1.0$ for the backward Euler method). Then the necessary and sufficient conditions for stability in space is (Vermeer and Verruijt, 1981)

$$b^* \leq 0, \tag{A.4}$$

which yields

$$\Delta t \geq \frac{1}{6}\frac{h^2}{\alpha c_v}. \tag{A.5}$$

The lower bound on the time step size implies that enough pressure diffusion is required to obtain a pressure distribution that is smooth enough, such that it can be interpolated using piecewise polynomials. Ženišek (1984) shows the error estimates for the two dimensional consolidation problem with an incompressible fluid as

$$\|p - p_h\|_{l_2} + \|\mathbf{u}^m - \mathbf{u}_h^m\|_1 \leq C\left(h^n \Delta t^{-1/2} \left\|\mathbf{u}^0\right\|_{n+1} + h^n + \Delta t\right), \tag{A.6}$$

where $p \in H^n$, $\mathbf{u} \in [H^{n+1}]^2$, C is a constant independent of Δt and h, and $\mathbf{u}^m = \mathbf{u}(t = t_m)$. $\|\cdot\|_{l_2}$ and $\|\cdot\|_1$ are defined as

$$\|f\|_{l_2}^2 = \Delta t \sum_{i=1}^{m} \left\|f^i\right\|_0^2, \;\; \|f\|_k^2 = \sum_{a=k} \|D^a f\|_{L^2}^2, \tag{A.7}$$

where $D^a f$ is the ath order spatial derivative of f. From the first term of the right hand side in Equation A.6, we identify the lower bound on the time step size. The first term is only present during the first time step. The error estimate by Murad and Loula (1992) does not show a lower bound on the time step size, because $\|\mathbf{Grad}\, p\|_{L^2}$ is assumed to be bounded at initial time. A small oscillation is observed in the results by Murad and Loula (1992), even though the elements satisfy the LBB condition, and this is because $\|\mathbf{Grad}\, p\|_{L^2}$ is unbounded at the drainage boundary at initial time.

Even though there are two factors that cause the instability at early time, we can eliminate the instability completely by introducing a stabilization technique (Wan, 2002; White and Borja, 2008). The technique honors consistency in space and time, but it leads to a loss in local accuracy. Local accuracy is important in reservoir engineering applications. For example, the ability to saturation fronts of water accurately is considered (Wan, 2002).

A.2 Finite-Volume and Finite-Element Methods

In reservoir engineering, the finite-volume method (FVM) is widely used for flow in order to preserve local mass conservation, while in civil or mechanical engineering, the finite element method (FEM) is typically used for mechanics in order to accommodate the complex geometry. To make use of existing flow and mechanics simulators, the finite-volume and finite-element methods are a natural choice for coupled flow and mechanics. Another benefit is accuracy of solutions at early time for consolidation problems. In the finite-volume method for flow, pressure is in L^2 space, which allows for jumps in the pressure field. Hence, there is no spurious spatial instability around the drainage boundary. In Equation A.2, b^* by the finite-volume method for flow is obtained as

$$b^* = -\alpha \frac{c_v \Delta t}{h^2}, \tag{A.8}$$

which satisfies the Vermeer and Verruijt (1981) stability condition, Equation A.4.

A.3 Numerical Examples

We study two consolidation problems in order to investigate the solution behaviors at early time. This analysis is motivated by the spurious fluid pressure oscillations observed with nodal based finite-element methods near the drainage boundary when instantaneous loading is applied. We use the fully coupled method and backward Euler time discretization for the numerical solutions.

Case A.1 One dimensional consolidation problem in a 1D, linear poroelastic medium. This is Terzaghi's problem (the left picture in Figure A.1).

Case A.2 Two dimensional plain strain strip footing consolidation problem in a linear poroelastic medium (the right picture in Figure A.1).

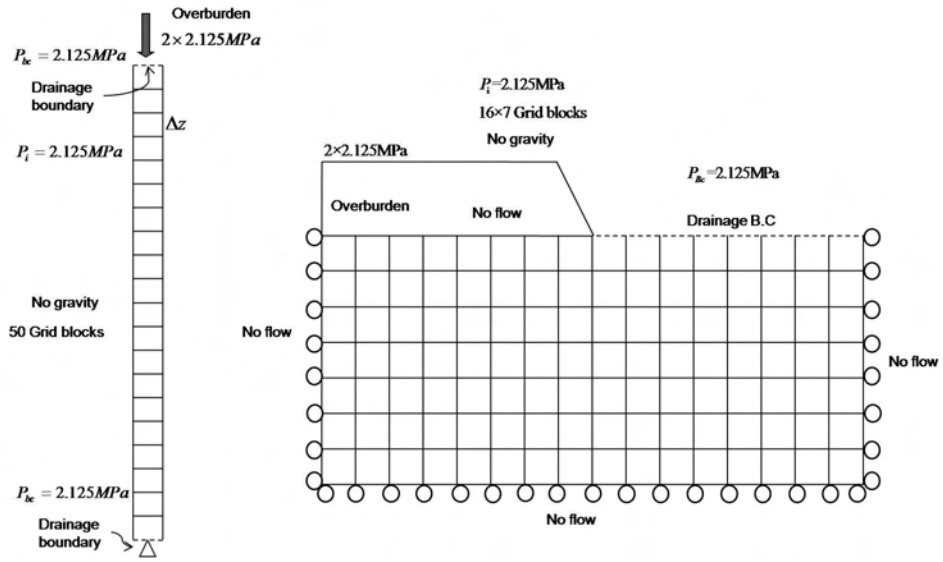

Figure A.1: Left: the Terzaghi problem. Right: the two dimensional plain strain strip footing consolidation problem.

A.3.1 Case A.1—Terzaghi's problem

We have a drainage boundary for flow on the top and at the bottom, where the boundary fluid pressure is $P_{bc} = 2.125\ MPa$. The overburden is $\bar{\sigma} = 2 \times 2.125\ MPa$ on the top, and a no-displacement boundary condition is applied to the bottom. The domain has 50 grid blocks. The length of the domain is $L_z = 100\ m$ with grid spacing $\Delta z = 2\ m$. The bulk density of the porous medium is $\rho_b = 2400\ kg\ m^{-1}$. Initial fluid pressure is $P_i = 2.125\ MPa$. The fluid density and viscosity are $\rho_{f,0} = 1000\ kg\ m^{-1}$ and $\mu = 1.0\ cp$, respectively. The fluid compressibility is $c_f = 1.0 \times 10^{-10}\ Pa^{-1}$. Permeability is $k_p = 100\ md$, porosity is $\phi_0 = 0.3$, the constrained modulus is $K_{dr} = 6\ GPa$, and the Biot coefficient is $b = 1.0$. There is no fluid production or injection of fluid and there is no gravity. The values for the input parameters are shown in Table A.1.

The top of Figure A.2 shows the pressure distributions at early and late time when the nodal based finite element methods are used with linear interpolation for pressure and displacement (Wan, 2002). At early time, this space discretization causes an unstable pressure solution, even though pressure becomes stable later in time. From Figure A.2, it

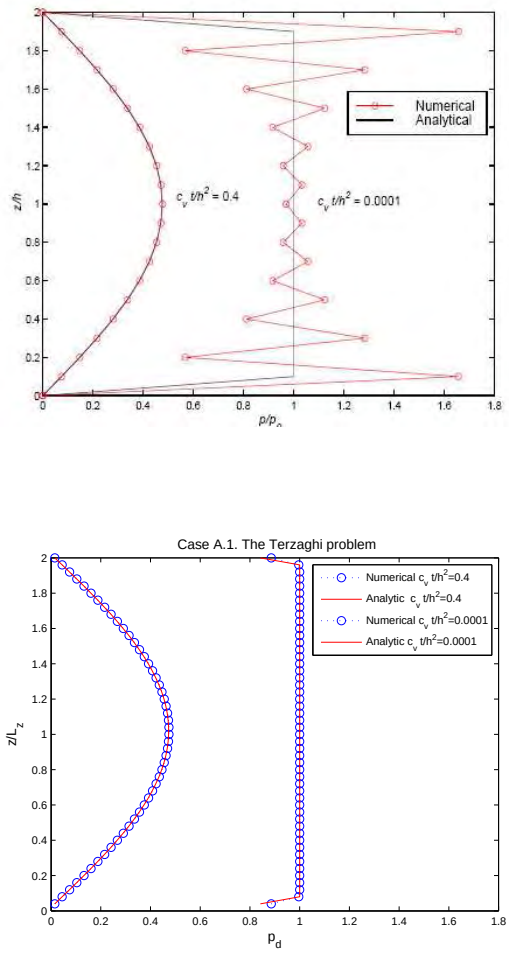

Figure A.2: Case A.1 Stability of pressure at early time for Terzaghi's problem. Top: pressure distributions at early and late time by the nodal based finite element method, where linear interpolation is used for pressure and displacement (Wan, 2002). Bottom: pressure distributions at early and late time by the combined finite-volume and finite-element approach.

Table A.1: Input data for Case A.1

Property	Value
Permeability (k_p)	100 md
Porosity (ϕ_0)	0.3
Drained modulus (K_{dr})	6 GPa
Bulk density (ρ_b)	2400 kg m^{-3}
Fluid density ($\rho_{f,0}$)	1000 kg m^{-3}
Fluid viscosity (μ)	1.0 cp
Initial pressure (P_i)	2.125 MPa
Boundary pressure (P_{bc})	2.125 MPa
Overburden ($\bar{\sigma}$)	2×2.125 MPa
Grid spacing (Δz)	2 m

is clear that the instability propagates from the drainage boundary to the interior domain. However, the combined finite-volume for flow and finite-elements for mechanics provide stable and accurate pressures at early time that match the analytical solution, as shown in the bottom of Figure A.2. For the combined finite-volume and finite-element method, Figure 4.4 shows that the fully coupled method yields first-order accuracy in time.

A.3.2 Case A.2—Two dimensional plain strain strip footing consolidation problem

At the top layer, the left part has an overburden, $\bar{\sigma} = 2 \times 2.125\ MPa$, and the right part is a the drainage boundary. The domain is 160 $m \times 70\ m$ with 16×7 grid blocks with a plane strain mechanical problem. The domain is homogeneous. The overburden at the drainage boundary is $\bar{\sigma} = 2.125\ MPa$. No-horizontal displacement boundary conditions are used on both sides and no-vertical displacement boundary condition is used at the bottom for mechanics. The bulk density of the porous medium is $\rho_b = 2400\ kg\ m^{-1}$. Initial fluid pressure is $P_i = 2.125\ MPa$. The fluid density and viscosity are $\rho_{f,0} = 1000\ kg\ m^{-1}$ and $\mu = 1.0\ cp$, respectively. The fluid compressibility is $c_f = 3.5 \times 10^{-8}\ Pa^{-1}$. Permeability is $k_p = 50\ md$, and porosity is $\phi_0 = 0.3$. Young's modulus is $E = 300\ MPa$, and Poisson's ratio is $\nu = 0.0$. The Biot coefficient is $b = 1.0$. A no-flow boundary condition is applied to the both sides, the bottom, and the left side of the top. No gravity is applied. The values

for the input parameters are also listed in Table A.2.

Table A.2: Input data for Case A.2

Property	Value
Permeability (k_p)	50 md
Porosity (ϕ_0)	0.3
Young modulus (E)	300 MPa
Poisson ratio (ν)	0
Biot coefficient (b)	1.0
Bulk density (ρ_b)	2400 $\mathrm{kg\,m^{-3}}$
Fluid density ($\rho_{f,0}$)	1000 $\mathrm{kg\,m^{-3}}$
Fluid viscosity (μ)	1.0 cp
Initial pressure (P_i)	2.125 MPa
Boundary pressure (P_{bc})	2.125 MPa
Left overburden ($\bar{\sigma}$)	2×2.125 MPa
Overburden at the drainage boundary ($\bar{\sigma}$)	2.125 MPa
Grid spacing (Δx)	10 m
Grid spacing (Δz)	10 m
Grid	16×7

The top of Figure A.3 shows that the fluid pressure is high at the left part, whereas it is low at the right part at early time, $t_d = 3.7 \times 10^{-19}$, where $t_d = 4\frac{c_v t}{LxLz}$. High pressure gradients occur around the central area. Large subsidence occurs under the left part on the top, where subsidence is positive (the bottom of Figures A.3 and A.4). But, the subsidence decreases at the drainage boundary, and there is a rebound of the surface showing negative displacements at the right part of the top layer because of dilation.

Figure A.5 shows the convergence behaviors of pressure and displacement with respect to time step size. These results confirm first-order accuracy in time for both pressure and displacement. The combined finite-volume and finite-element scheme yields stable and accurate solutions at early time.

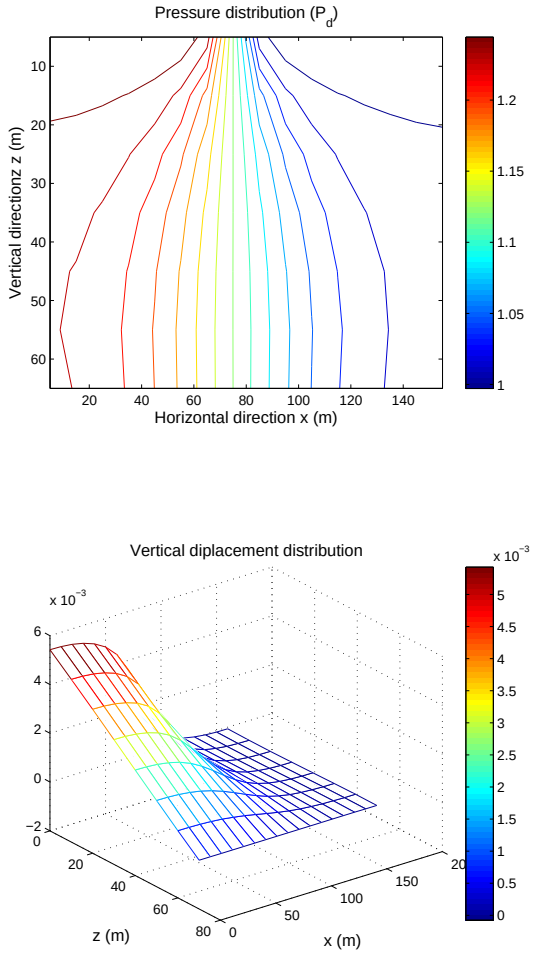

Figure A.3: Case A.2 Dimensionless pressure (top) and vertical displacement distributions (bottom) at early time, $t_d = 3.7 \times 10^{-19}$. Note that subsidence is positive.

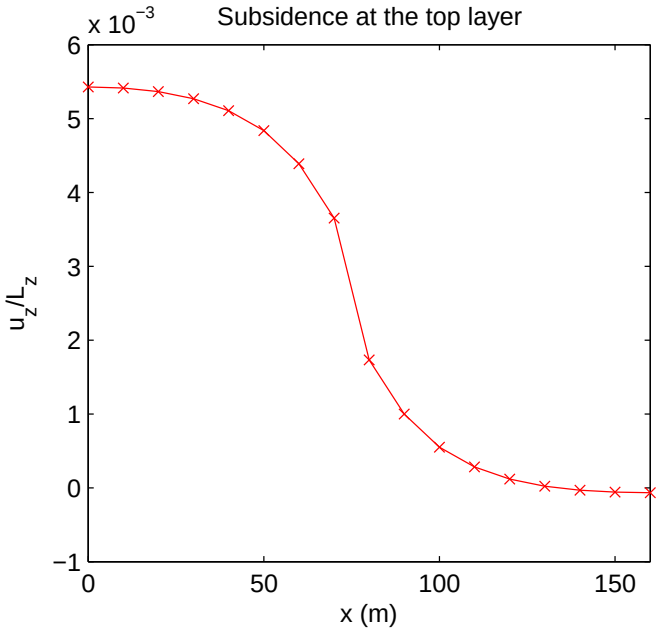

Figure A.4: Dimensionless vertical-displacement distribution of the top layer at early time, $t_d = 3.7 \times 10^{-19}$. The left part shows large subsidence, and the subsidence decreases along the right direction.

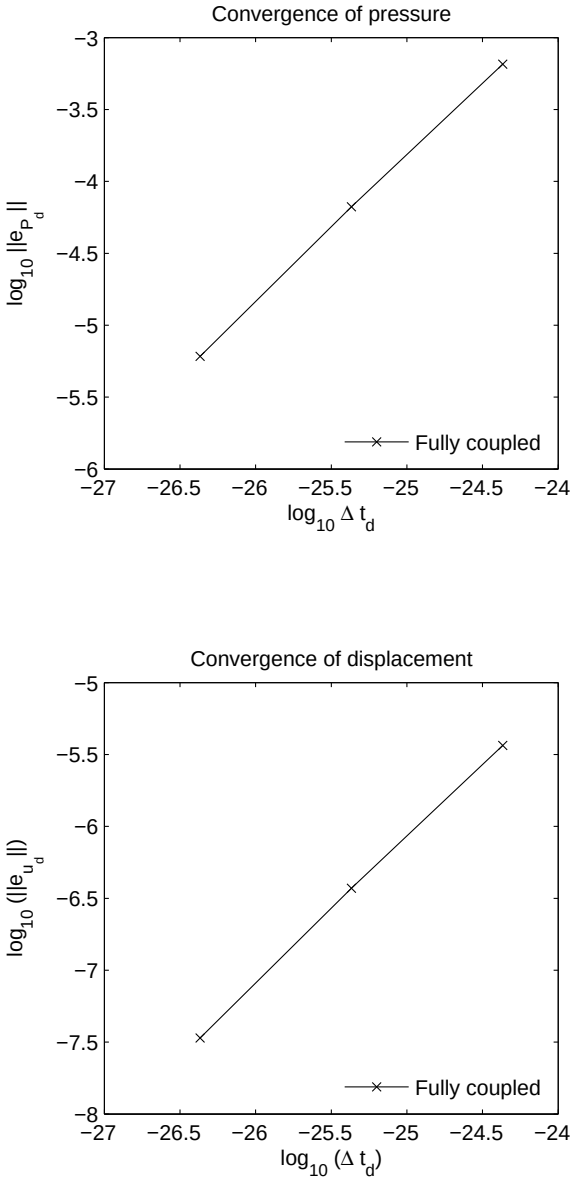

Figure A.5: Case A.2 Convergence of pressure (top) and displacement (bottom). First-order accuracy in time is observed for both pressure and displacement.

Appendix B

Miscellaneous Derivations

B.1 Positive-Definite Biot's Moduli, M

Here, we show that the Biot modulus matrix $\mathbf{M}$ is positive-definite. A positive-definite matrix $\mathbf{M}$ must satisfy

$$\mathbf{p}^t \mathbf{M} \mathbf{p} \geq 0, \quad \text{for all } \mathbf{p}, \tag{B.1}$$

where the equality is only permissible for $\mathbf{p} = \mathbf{0}$. Before proving the positive definiteness, we introduce a typical assumption for the capillary pressure relations, namely,

$$\frac{dp_{co}}{dS_w} < 0, \text{ and } \frac{dp_{cg}}{dS_g} > 0, \tag{B.2}$$

which are illustrated in Figure B.1.

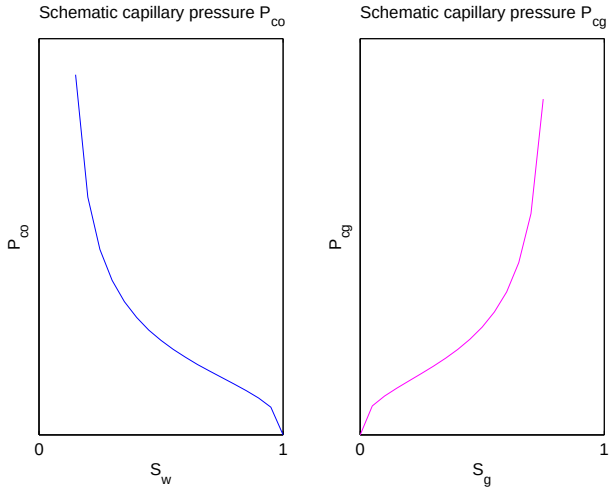

Figure B.1: Typical shapes of capillary pressure regarding wetting and non-wetting phases (e.g., S_w and S_g, respectively). $p_{co} = p_o - p_w$, and $p_{cg} = p_g - p_o$. The capillary pressure curves are drawn based on the work of Lenhard and Parker (1987)

Note from Chapter 2 that $\mathbf{N}^{-1} = \mathbf{M}$ and both $\mathbf{N}$ and $\mathbf{M}$ are symmetric. Then we obtain

$$\begin{aligned}
\mathbf{p}^t\mathbf{N}\mathbf{p} &= p_o^2 N_{oo} + p_w^2 N_{ww} + p_g^2 N_{gg} + 2N_{ow}p_o p_w + 2N_{og}p_o p_g + 2N_{wg}p_w p_g \\
&= \phi S_o c_o p_o^2 + \phi S_w c_w p_w^2 + \phi S_g c_g p_g^2 - \phi \frac{dS_w}{dp_{co}}\left(p_o^2 - 2p_o p_w + p_w^2\right) \\
&\quad + \phi \frac{dS_g}{dp_{cg}}\left(p_o^2 - 2p_o p_g + p_g^2\right) + \frac{b-\phi}{K_s}\left(S_o^2 p_o^2 + S_w^2 p_w^2 + S_g^2 p_g^2\right. \\
&\quad \left. + 2S_o S_w p_o p_w + 2S_o S_g p_o p_g + 2S_w S_g p_w p_g\right) \\
&= \phi\left(S_o c_o p_o^2 + S_w c_w p_w^2 + S_g c_g p_g^2\right) - \phi \frac{dS_w}{dp_{co}}\left(p_o - p_w\right)^2 + \phi \frac{dS_g}{dp_{cg}}\left(p_o - p_g\right)^2 \\
&\quad + \frac{b-\phi}{K_s}\left(S_o p_o + S_w p_w + S_g p_g\right)^2 \\
&\geq 0, \qquad \text{(B.3)}
\end{aligned}$$

where the equality is only satisfied with $\mathbf{p} = \mathbf{0}$. Hence, $\mathbf{N}$ is positive-definite, from which $\mathbf{M}$ is also positive-definite.

B.2 Accuracy of the Fully Coupled Method

The matrix form of the differential governing equations is written as

$$\underbrace{\begin{bmatrix} \mathbf{K} & -\mathbf{L^t} \\ \mathbf{0} & \mathbf{T} \end{bmatrix}}_{\mathbf{Z}} \underbrace{\begin{bmatrix} \mathbf{u}_{tr} \\ \mathbf{p}_{tr} \end{bmatrix}}_{\mathbf{x}_{tr}} - \underbrace{\begin{bmatrix} \mathbf{0} & \mathbf{0} \\ \mathbf{L} & \mathbf{Q} \end{bmatrix}}_{\mathbf{B}} \begin{bmatrix} \dot{\mathbf{u}}_{tr} \\ \dot{\mathbf{p}}_{tr} \end{bmatrix} = \underbrace{\begin{bmatrix} \mathbf{h_u} \\ \mathbf{h_p} \end{bmatrix}}_{\mathbf{h}}, \tag{B.4}$$

$$\mathbf{x} = [\mathbf{u}, \mathbf{p}]^t,$$

where $\mathbf{h}$ is the source-term vector. Consistency of the fully coupled method can be shown as follows. The matrix form of the difference equations for the fully coupled method yields

$$\underbrace{\begin{bmatrix} \mathbf{K} & -\mathbf{L^t} \\ \mathbf{L} & \mathbf{F} \end{bmatrix}}_{\mathbf{A}} \underbrace{\begin{bmatrix} \mathbf{u}_{tr} \\ \mathbf{p}_{tr} \end{bmatrix}}_{\mathbf{x}_{tr}}^{n+1} - \underbrace{\begin{bmatrix} \mathbf{0} & \mathbf{0} \\ \mathbf{L} & \mathbf{Q} \end{bmatrix}}_{\mathbf{B}} \begin{bmatrix} \mathbf{u}_{tr} \\ \mathbf{p}_{tr} \end{bmatrix}^n = \underbrace{\begin{bmatrix} \mathbf{f_u} \\ \mathbf{f_p} \end{bmatrix}}_{\mathbf{f}}^{n+1} + \Delta t \mathbf{R}^{n+1}, \tag{B.5}$$

$$\mathbf{R}^{n+1} = \left[\tfrac{1}{\Delta t}\mathbf{r_u}, \mathbf{r_p}\right]^t,$$

where $\mathbf{R}^{n+1}$ is the truncation-error vector for the mechanical ($\mathbf{r_u}$) and flow ($\mathbf{r_p}$) problems. $\mathbf{h_u} = \mathbf{f_u}$ and $\Delta t \mathbf{h_p} = \mathbf{f_p}$. Using a Taylor expansion,

$$\mathbf{x}_{tr}^n = \mathbf{x}_{tr}^{n+1} - \Delta t \frac{\partial \mathbf{x}_{tr}^{n+1}}{\partial t} + \frac{1}{2}\Delta t^2 \frac{\partial^2 \mathbf{x}_{tr}^{n+1}}{\partial t^2} + O(\Delta t^3) \cdots . \tag{B.6}$$

Combining Equations B.5 and B.6, we have

$$\mathbf{A}\mathbf{x}_{tr}^{n+1} - \mathbf{B}\left(\mathbf{x}_{tr}^{n+1} - \Delta t \frac{\partial \mathbf{x}_{tr}^{n+1}}{\partial t} + \frac{1}{2}\Delta t^2 \frac{\partial^2 \mathbf{x}_{tr}^{n+1}}{\partial t^2} + O(\Delta t^3)\right) = \mathbf{f}^{n+1} + \Delta t \mathbf{R}^{n+1}, \tag{B.7}$$

which yields

$$\mathbf{B}\frac{\partial \mathbf{x}_{tr}^{n+1}}{\partial t} + \frac{1}{\Delta t}(\mathbf{A} - \mathbf{B})\mathbf{x}_{tr}^{n+1} - \mathbf{B}\left(\frac{1}{2}\Delta t \frac{\partial^2 \mathbf{x}_{tr}^{n+1}}{\partial t^2} + O(\Delta t^2)\right) = \frac{1}{\Delta t}\mathbf{f}^{n+1} + \mathbf{R}^{n+1}. \tag{B.8}$$

From Equations B.4 and B.8, we obtain

$$\mathbf{R}^{n+1} = \mathbf{B}\left(\frac{1}{2}\Delta t \frac{\partial^2 \mathbf{x}_{tr}^{n+1}}{\partial t^2} + O(\Delta t^2)\right). \tag{B.9}$$

Therefore, the fully coupled method with the backward Euler time discretization is convergent with first-order accuracy in time, $O(\Delta t)$.

B.3 Drained Split in Coupled Flow and Dynamics

Imposing $max\,|\gamma_e| \leq 1$ for all θ, Equation 4.38 provides a necessary condition for stability of the drained split. Namely,

$$\frac{\Delta t^2 M b^2}{\rho_b h^2} 2(1-\cos\theta) \leq \left(1 + \frac{\Delta t^2 K_{dr}}{\rho_b h^2} 2(1-\cos\theta)\right)\left(1 + \frac{\Delta t M k_p}{\mu h^2} 2(1-\cos\theta)\right) \text{ for all } \theta, \tag{B.10}$$

which yields

$$4\frac{\Delta t^2 M b^2}{\rho_b h^2} \leq \left(1 + 4\frac{\Delta t^2 K_{dr}}{\rho_b h^2}\right)\left(1 + 4\frac{\Delta t M k_p}{\mu h^2}\right). \tag{B.11}$$

Since the undrained limit is $k_p = 0$, Equation B.11 reduces to Equation 4.45.

B.4 Non-Contractivity with Different Constitutive Relations

We investigate non-contractivity of the constitutive relations proposed by Lewis and Sukirman (1993) and Lewis and Schrefler (1998), which are slightly different from those by Coussy (1995). The relations for fluid pressure, total and effective stresses by Lewis and Sukirman

(1993) and Lewis and Schrefler (1998) are

$$\delta\boldsymbol{\sigma} = \mathbf{C}_{dr} : (\delta\boldsymbol{\varepsilon} - \delta\boldsymbol{\varepsilon}_p) - \left(b_J \delta p_J + \tilde{b_J}\delta S_J\right)\mathbf{1}, \tag{B.12}$$

$$\delta p_J = M_{JK}\left(-b_K(\delta\varepsilon_v - \delta\varepsilon_{v,p}) + \left(\left(\frac{\delta m}{\rho}\right)_K - \delta\phi_{K,p}\right)\right), \tag{B.13}$$

$$\delta\kappa = -\mathbf{H}\cdot\delta\xi, \tag{B.14}$$

where $\tilde{b_J} = b\,p_J$. Equation B.12 is different from Equation 6.72. Based on Equations B.12–B.14, we obtain

$$\begin{aligned}
\frac{d\,\|d\chi_m\|^2_{\mathcal{N}_m}}{dt} &= \frac{\partial\|d\chi_m\|^2_{\mathcal{N}_m}}{\partial d\boldsymbol{\varepsilon}_e} : \dot{d\boldsymbol{\varepsilon}_e} + \frac{\partial\|d\chi_m\|^2_{\mathcal{N}_m}}{\partial d\xi}\cdot\dot{d\xi} + \frac{\partial\|d\chi_m\|^2_{\mathcal{N}_m}}{\partial dm_{J,e}}\dot{dm}_{J,e} \\
&= \int_\Omega \Bigg(d\boldsymbol{\sigma}' : \dot{d\boldsymbol{\varepsilon}}_e - \left(\left(\frac{dm_e}{\rho}\right)_J - b_J d\varepsilon_{e,v}\right) M_{JK} b_K \dot{d\varepsilon}_{e,v} \\
&\quad -d\kappa\cdot\dot{d\xi} + \left(\left(\frac{dm_e}{\rho}\right)_J - b_J d\varepsilon_{e,v}\right) M_{JK}\left(\frac{\dot{dm}_e}{\rho}\right)_K \Bigg) d\Omega \\
&= \int_\Omega \left(d\boldsymbol{\sigma} : \dot{d\boldsymbol{\varepsilon}} + \left(\frac{dp}{\rho}\right)_J \dot{dm}_J \right) d\Omega - \underbrace{\int_\Omega \left[d\boldsymbol{\sigma}' : \dot{d\boldsymbol{\varepsilon}}_p + d\kappa\cdot\dot{d\xi}\right] d\Omega}_{D_p^d} \\
&\quad + \int_\Omega \tilde{b_J} dS_J \mathbf{1} : \dot{d\boldsymbol{\varepsilon}} d\Omega \\
&= \underbrace{\int_\Omega \tilde{b_J} dS_J \mathbf{1} : \dot{d\boldsymbol{\varepsilon}} d\Omega}_{\text{not always} \leq 0} - \int_\Omega d\boldsymbol{v}_J \cdot \mathbf{k}^{-1}_{p,JK} d\boldsymbol{v}_K d\Omega - D_p^d \not\leq 0,
\end{aligned} \tag{B.15}$$

where the first term in the last equation may be positive. Thus, Equations B.12– B.14 do not ensure contractivity relative to the Helmholtz free energy norm. As a result, well-posedness of the problem and thermodynamic stability are not guaranteed because the Helmholtz free energy may increase. Coussy (2004) points out that $p_t = S_J p_J$ is not appropriate when capillarity exists.

Remark D.1. When capillarity is ignored, $\tilde{b_J} dS_J = 0$. Equation B.12 is the same as Equation 6.72. Then, we recover contractivity with Equations B.12– B.14.

Remark D.2. Assume 1D oil-water flow with capillarity with $\dot{\sigma_v} = 0$ in order to study the properties of Equations B.12 – B.14 in a numerical sense. Using Equations B.12 – B.14, the governing equations become

$$\underbrace{\begin{bmatrix} N_{oo} & N_{ow} \\ N_{wo} & N_{ww} \end{bmatrix}}_{\mathbf{N}} \begin{bmatrix} \dot{p_o} \\ \dot{p_w} \end{bmatrix} + b \begin{bmatrix} S_o \\ S_w \end{bmatrix} \dot{\varepsilon_v} = \begin{bmatrix} -\operatorname{Div} \boldsymbol{v}_o + f_o \\ -\operatorname{Div} \boldsymbol{v}_w + f_w \end{bmatrix}, \tag{B.16}$$

$$\dot{\sigma_v} = K_{dr}\dot{\varepsilon_v} - \underbrace{b\left(S_o\dot{p_o} + S_w\dot{p_w}\right)}_{b_J\dot{p_J}} - \underbrace{\left(-bp_{co}\frac{dS_w}{dp_{co}}\left(\dot{p_o} - \dot{p_w}\right)\right)}_{\tilde{b_J}\dot{S_J}}, \tag{B.17}$$

where $\mathbf{N}$ is

$$\begin{bmatrix} N_{oo} & N_{ow} \\ N_{wo} & N_{ww} \end{bmatrix} = \begin{bmatrix} \phi S_o c_o - \phi\frac{dS_w}{dp_{co}} + S_o\frac{b-\phi}{K_s}S_o & \phi\frac{dS_w}{dp_{co}} + S_o\frac{b-\phi}{K_s}S_w \\ \phi\frac{dS_w}{dp_{co}} + S_w\frac{b-\phi}{K_s}S_o & \phi S_w c_w - \phi\frac{dS_w}{dp_{co}} + S_w\frac{b-\phi}{K_s}S_w \end{bmatrix}.$$

Then, substituting Equation B.17 into Equation B.16 and using $\dot{\sigma_v} = 0$, we obtain

$$\underbrace{\left(\underbrace{\begin{bmatrix} N_{oo} & N_{ow} \\ N_{wo} & N_{ww} \end{bmatrix}}_{\mathbf{N}} + \frac{b^2}{K_{dr}}\underbrace{\begin{bmatrix} S_o^2 & S_oS_w \\ S_wS_o & S_w^2 \end{bmatrix}}_{\tilde{\mathbf{S}}} - \frac{b^2}{K_{dr}}p_{co}\frac{dS_w}{dp_{co}}\underbrace{\begin{bmatrix} S_o & -S_o \\ S_w & -S_w \end{bmatrix}}_{\bar{\mathbf{S}}}\right)}_{\mathbf{W}} \begin{bmatrix} \dot{p_o} \\ \dot{p_w} \end{bmatrix}$$

$$= \begin{bmatrix} -\operatorname{Div} \boldsymbol{v}_o + f_o \\ -\operatorname{Div} \boldsymbol{v}_w + f_w \end{bmatrix}. \tag{B.18}$$

For the left terms of Equation B.18, the positive-definiteness of $\mathbf{W}$ is not guaranteed because $\bar{\mathbf{S}}$ is indefinite. This is the case even though $\mathbf{N}$ and $\tilde{\mathbf{S}}$ are positive-definite and positive-semidefinite, respectively. The eigenvalues of $\bar{\mathbf{S}}$ are 0, $S_o - S_w$. When $|p_{co}|$ and $|dS_w/dp_{co}|$ are large enough such $\mathbf{N}$ and $\tilde{\mathbf{S}}$ are ignored, we may face an ill-posed problem.

B.5 $\delta\phi$ for single-phase flow

We derive the expression of $\delta\phi$ based on Geertsma (1957)'s work, where p is the fluid tension. Note that p in this thesis is the fluid pressure. We denote by V_p and V_b the pore and bulk volumes, respectively. Then the change of V_p with respect to the movement of the solid skeleton is expressed as

$$\delta V_p = \left.\frac{\partial V_p}{\partial p}\right|_{\sigma_v} \delta p + \left.\frac{\partial V_p}{\partial \sigma_v}\right|_{p} \delta\sigma_v, \tag{B.19}$$

which yields

$$\frac{\delta V_p}{V_p} = \left(\frac{1}{V_p}\left.\frac{\partial V_p}{\partial p}\right|_{\sigma_v} - \frac{1}{V_p}\left.\frac{\partial V_p}{\partial \sigma_v}\right|_{p} \right) \delta p + \frac{1}{V_p}\left.\frac{\partial V_p}{\partial \sigma_v}\right|_{p} (\delta\sigma_v + \delta p)\,. \tag{B.20}$$

Similarly, the change of V_b with respect to the movement of the solid skeleton is described as

$$\delta V_b = \left.\frac{\partial V_b}{\partial p}\right|_{\sigma_v} \delta p + \left.\frac{\partial V_b}{\partial \sigma_v}\right|_{p} \delta\sigma_v, \tag{B.21}$$

which yields

$$\frac{\delta V_b}{V_b} = \left(\frac{1}{V_b}\left.\frac{\partial V_b}{\partial p}\right|_{\sigma_v} - \frac{1}{V_b}\left.\frac{\partial V_b}{\partial \sigma_v}\right|_{p} \right) \delta p + \frac{1}{V_b}\left.\frac{\partial V_b}{\partial \sigma_v}\right|_{p} (\delta\sigma_v + \delta p)\,. \tag{B.22}$$

Under the condition that $\delta\sigma_v + \delta p = 0$, we obtain for the dilation of the solid grains

$$\frac{\delta V_p}{V_p} = \frac{\delta V_b}{V_b} = -\frac{1}{K_s}\delta p = \frac{1}{K_s}\delta\sigma_v, \tag{B.23}$$

where K_s is the stiffness of the solid grains. Since the drained bulk modulus K_{dr} is defined as

$$\frac{1}{V_b}\left.\frac{\partial V_b}{\partial \sigma_v}\right|_{p} = \frac{1}{K_{dr}}, \tag{B.24}$$

using Equations B.23 and B.24, Equation B.22 is expressed as

$$\frac{\delta V_b}{V_b}\left(\equiv \delta\varepsilon_v\right) = -\frac{1}{K_s}\delta p + \frac{1}{K_{dr}}\left(\delta\sigma_v + \delta p\right), \tag{B.25}$$

which yields

$$\frac{1}{V_b}\frac{\partial V_b}{\partial p}\bigg|_{\sigma_v} = \frac{1}{K_{dr}} - \frac{1}{K_s}. \tag{B.26}$$

Equation B.25 also describes the constitutive relation between the total volumetric stress and pressure as

$$\delta\sigma_v = K_{dr}\delta\varepsilon_v - b\delta p. \tag{B.27}$$

We now introduce the reciprocal theorem of Betti and Rayleigh (Geertsma, 1957; Marsden and Hughes, 1983). The reciprocal theorem states that "the work done by the force of the first set ($\delta\sigma_v$) in the displacement caused by the second (δp) equals the work done by the the second in the displacement caused by the first." This theorem leads to

$$\delta\sigma_v \left.\frac{\partial V_b}{\partial p}\right|_{\sigma_v} \delta p = \delta p \left.\frac{\partial V_p}{\partial \sigma_v}\right|_{p} \delta\sigma_v, \tag{B.28}$$

which yields

$$\left.\frac{\partial V_b}{\partial p}\right|_{\sigma_v} = \left.\frac{\partial V_p}{\partial \sigma_v}\right|_{p}. \tag{B.29}$$

From Equations B.26 and B.29, we obtain

$$\frac{1}{V_p}\left.\frac{\partial V_p}{\partial \sigma_v}\right|_{p} = \frac{1}{\phi}\left(\frac{1}{K_{dr}} - \frac{1}{K_s}\right), \tag{B.30}$$

where $\phi = V_p/V_b$ by definition. Using Equations B.23 and B.30, Equation B.20 can be

rewritten as

$$\frac{\delta V_p}{V_p} = -\frac{1}{K_s}\delta p + \frac{1}{\phi}\left(\frac{1}{K_{dr}} - \frac{1}{K_s}\right)(\delta\sigma_v + \delta p)\,. \tag{B.31}$$

Then we can derive $\delta\phi$ as

$$\begin{aligned}
\delta\phi &= \delta\left(\frac{V_p}{V_b}\right) = \phi\left(\frac{\delta V_p}{V_p} - \frac{\delta V_b}{V_b}\right) \\
&= \phi\left(-\frac{1}{K_s}\delta p + \frac{1}{\phi}\left(\frac{1}{K_{dr}} - \frac{1}{K_s}\right)(\delta\sigma_v + \delta p) - \delta\varepsilon_v\right) \\
&= \phi\left(-\frac{1}{K_s}\delta p + \frac{1}{\phi}\left(\frac{1}{K_{dr}} - \frac{1}{K_s}\right)\underbrace{K_{dr}\left(\delta\varepsilon_v + \frac{1}{K_s}\delta p\right)}_{from\ \ Equation\ \ B.25} - \delta\varepsilon_v\right) \\
&= \frac{b-\phi}{K_s}\delta p + (b-\phi)\,\delta\varepsilon_v,
\end{aligned} \tag{B.32}$$

where we define the Biot coefficient b for single-phase flow as

$$b = 1 - \frac{K_{dr}}{K_s}. \tag{B.33}$$

Appendix C

Constitutive Relations in Reservoir Simulation

A standard black oil model for reservoir simulation is considered. There are two typical choices for the primary variables. One is p_o, p_w, and p_g, and the other is p_o, S_w, and S_g. The formation volume factor of phase J (i.e., $B_J = (\rho_0/\rho)_J$) and solution gas-oil ratio R_{so} are used for the standard black oil model, where R_{so} is the ratio of volume of gas in oil at the standard conditions and the volume of oil at the standard conditions (Aziz and Settari, 1979). The subscripts o, w, and g mean oil, water, and gas, respectively. Since the flux term is easily expressed in terms of fluid pressures using Darcy's law, we focus on the expression of the accumulation.

C.1 p_o, p_w, p_g formulation

For the oil pseudo-component, the accumulation term is written as

$$\begin{aligned} \frac{\delta m_o}{\rho_{o,0}} &= \delta\left(\frac{\phi S_o}{B_o}\right) + \left(\frac{S_o}{B_o}\right)\phi\delta\varepsilon_v \\ &= \phi\delta\left(\frac{S_o}{B_o}\right) + \left(\frac{S_o}{B_o}\right)\delta\phi + \left(\frac{S_o}{B_o}\right)\phi\delta\varepsilon_v. \end{aligned} \tag{C.1}$$

$\delta\left(S_o/B_o\right)$ can be expanded as

$$\begin{aligned}
\delta(\frac{S_o}{B_o}) &= S_o\delta(\frac{1}{B_o}) + \frac{1}{B_o}\delta S_o \\
&= S_o\frac{1}{B_o}c_o\delta p_o + \frac{1}{B_o}\delta S_o \\
&= S_o\frac{1}{B_o}c_o\delta p_o + \frac{1}{B_o}\left(-\delta S_w - \delta S_g\right) \\
&= S_o\frac{1}{B_o}c_o\delta p_o + \frac{1}{B_o}(-\frac{dS_w}{dp_{co}}\left(\delta p_o - \delta p_w\right) - \frac{dS_g}{dp_{cg}}\left(\delta p_g - \delta p_o\right)) \\
&= S_o\frac{1}{B_o}c_o\delta p_o + \frac{1}{B_o}\left[\left(-\frac{dS_w}{dp_{co}} + \frac{dS_g}{dp_{cg}}\right)\delta p_o + \frac{dS_w}{dp_{co}}\delta p_w - \frac{dS_g}{dp_{cg}}\delta p_g\right]. \qquad \text{(C.2)}
\end{aligned}$$

Then, from Equations 2.38 and C.2, $\delta m_o/\rho_{o,0}$ is expressed in terms of p_J as

$$\begin{aligned}
\frac{\delta m_o}{\rho_{o,0}} &= \phi\left(S_o\frac{1}{B_o}c_o\delta p_o + \frac{1}{B_o}\left[\left(-\frac{dS_w}{dp_{co}} + \frac{dS_g}{dp_{cg}}\right)\delta p_o + \frac{dS_w}{dp_{co}}\delta p_w - \frac{dS_g}{dp_{cg}}\delta p_g\right]\right) \\
&\quad + \frac{S_o}{B_o}\left(\frac{b-\phi}{K_s}\left[S_o\delta p_o + S_w\delta p_w + S_g\delta p_g\right] + b\delta\boldsymbol{\varepsilon_v}\right). \qquad \text{(C.3)}
\end{aligned}$$

Similarly, the accumulation term for water phase is written as

$$\begin{aligned}
\frac{\delta m_w}{\rho_{w,0}} &= \delta\left(\frac{\phi S_w}{B_w}\right) + \left(\frac{S_w}{B_w}\right)\phi\delta\varepsilon_v \\
&= \phi\delta\left(\frac{S_w}{B_w}\right) + \left(\frac{S_w}{B_w}\right)\delta\phi + \left(\frac{S_w}{B_w}\right)\phi\delta\varepsilon_v. \qquad \text{(C.4)}
\end{aligned}$$

$\delta\left(S_w/B_w\right)$ can be expanded as

$$\begin{aligned}
\delta(\frac{S_w}{B_w}) &= S_w\delta(\frac{1}{B_w}) + \frac{1}{B_w}\delta S_w \\
&= S_w\frac{1}{B_w}c_w\delta p_w + \frac{1}{B_w}\frac{dS_w}{dp_{co}}\left(\delta p_o - \delta p_w\right). \qquad \text{(C.5)}
\end{aligned}$$

From Equations 2.38 and C.5, we obtain

$$\begin{aligned}\frac{\delta m_w}{\rho_{w,0}} &= \phi\left(S_w\frac{1}{B_w}c_w\delta p_w+\frac{1}{B_w}\frac{dS_w}{dp_{co}}\left(\delta p_o-\delta p_w\right)\right)\\ &\quad+\frac{S_w}{B_w}\left(\frac{b-\phi}{K_s}\left[S_o\delta p_o+S_w\delta p_w+S_g\delta p_g\right]+b\delta\varepsilon_v\right).\end{aligned}\tag{C.6}$$

For the gas pseudo-component, the solution gas-oil ratio is introduced. Then the accumulation term becomes

$$\begin{aligned}\frac{\delta m_g}{\rho_{g,0}} &= \delta\left(\phi(\frac{S_g}{B_g}+\frac{R_{so}S_o}{B_o})\right)+\left(\frac{S_g}{B_g}+\frac{R_{so}S_o}{B_o}\right)\phi\delta\varepsilon_v\\ &= \phi\delta\left(\frac{S_g}{B_g}+\frac{R_{so}S_o}{B_o}\right)+\left(\frac{S_g}{B_g}+\frac{R_{so}S_o}{B_o}\right)\delta\phi+\left(\frac{S_g}{B_g}+\frac{R_{so}S_o}{B_o}\right)\phi\delta\varepsilon_v,\end{aligned}\tag{C.7}$$

where

$$\begin{aligned}\delta(\frac{S_g}{B_g}) &= S_g d(\frac{1}{B_g})+\frac{1}{B_g}\delta S_g\\ &= S_g\frac{1}{B_g}c_g\delta p_g+\frac{1}{B_g}\delta S_g\\ &= S_g\frac{1}{B_g}c_g\delta p_g+\frac{1}{B_g}\frac{dS_g}{dp_{cg}}\left(\delta p_g-\delta p_o\right),\end{aligned}\tag{C.8}$$

and

$$\begin{aligned}\delta(\frac{R_{so}S_o}{B_o}) &= R_{so}S_o\delta(\frac{1}{B_o})+\frac{S_o}{B_o}\delta R_{so}+\frac{R_{so}}{B_o}\delta S_o\\ &= R_{so}S_o\frac{1}{B_o}c_o\delta p_o+\frac{S_o}{B_o}\frac{dR_{so}}{dp_o}\delta p_o+\frac{R_{so}}{B_o}(-\delta S_w-\delta S_g)\\ &= R_{so}S_o\frac{1}{B_o}c_o\delta p_o+\frac{S_o}{B_o}\frac{dR_{so}}{dp_o}\delta p_o\\ &\quad+\frac{R_{so}}{B_o}\left[\left(-\frac{dS_w}{dp_{co}}+\frac{dS_g}{dp_{cg}}\right)\delta p_o+\frac{dS_w}{dp_{co}}\delta p_w-\frac{dS_g}{dp_{cg}}\delta p_g\right].\end{aligned}\tag{C.9}$$

Then Equations 2.38, C.7, C.8, and C.9 yield

$$\begin{aligned}\frac{\delta m_g}{\rho_{g,0}} &= \phi\left(S_g\frac{1}{B_g}c_g\delta p_g+\frac{1}{B_g}\frac{dS_g}{dp_{cg}}\left(\delta p_g-\delta p_o\right)\right)\\ &+\phi\left(R_{so}S_o\frac{1}{B_o}c_o\delta p_o+\frac{S_o}{B_o}\frac{dR_{so}}{dp_o}\delta p_o\right.\\ &\left.+\frac{R_{so}}{B_o}\left[\left(-\frac{dS_w}{dp_{co}}+\frac{dS_g}{dp_{cg}}\right)\delta p_o+\frac{dS_w}{dp_{co}}\delta p_w-\frac{dS_g}{dp_{cg}}\delta p_g\right]\right)\\ &+(\frac{S_g}{B_g}+\frac{R_{so}S_o}{B_o})\left(\frac{b-\phi}{K_s}\left[S_o\delta p_o+S_w\delta p_w+S_g\delta p_g\right]+b\delta\varepsilon_v\right). \qquad \text{(C.10)}\end{aligned}$$

Rearranging Equations C.3, C.6, and C.10, we have

$$\begin{aligned}\frac{\delta m_o}{\rho_{o,0}} &= \left(\phi S_o\frac{1}{B_o}c_o+\phi\frac{1}{B_o}\left(-\frac{dS_w}{dp_{co}}+\frac{dS_g}{dp_{cg}}\right)+\frac{S_o}{B_o}\frac{b-\phi}{K_s}S_o\right)\delta p_o\\ &+\left(\phi\frac{1}{B_o}\frac{dS_w}{dp_{co}}+\frac{S_o}{B_o}\frac{b-\phi}{K_s}S_w\right)\delta p_w\\ &+\left(\phi\frac{1}{B_o}\left(-\frac{dS_g}{dp_{cg}}\right)+\frac{S_o}{B_o}\frac{b-\phi}{K_s}S_g\right)\delta p_g+\frac{S_o}{B_o}b\delta\varepsilon_v, \qquad \text{(C.11)}\\ \frac{\delta m_w}{\rho_{w,0}} &= \left(\phi\frac{1}{B_w}\frac{dS_w}{dp_{co}}+\frac{S_w}{B_w}\frac{b-\phi}{K_s}S_o\right)\delta p_o+\left(\phi S_w\frac{1}{B_w}c_w-\phi\frac{1}{B_w}\frac{dS_w}{dp_{co}}+\frac{S_w}{B_w}\frac{b-\phi}{K_s}S_w\right)\delta p_w\\ &+\frac{S_w}{B_w}\frac{b-\phi}{K_s}S_g\delta p_g+\frac{S_w}{B_w}b\delta\varepsilon_v, \qquad \text{(C.12)}\\ \frac{\delta m_g}{\rho_{g,0}} &= \left(-\phi\frac{1}{B_g}\frac{dS_g}{dp_{cg}}+\phi\frac{R_{so}S_o}{B_o}c_o+\phi\frac{S_o}{B_o}\frac{dR_{so}}{dp_o}\right.\\ &\left.+\phi\frac{R_{so}}{B_o}\left(-\frac{dS_w}{dp_{co}}+\frac{dS_g}{dp_{cg}}\right)+\left(\frac{S_g}{B_g}+\frac{R_{so}S_o}{B_o}\right)\frac{b-\phi}{K_s}S_o\right)\delta p_o\\ &+\left(\phi\frac{R_{so}}{B_o}\frac{dS_w}{dp_{co}}+\left(\frac{S_g}{B_g}+\frac{R_{so}S_o}{B_o}\right)\frac{b-\phi}{K_s}S_w\right)\delta p_w\\ &+\left(\phi S_g\frac{1}{B_g}c_g dp_g+\phi\frac{1}{B_g}\frac{dS_g}{dp_{cg}}-\phi\frac{R_{so}}{B_o}\frac{dS_g}{dp_{cg}}+\left(\frac{S_g}{B_g}+\frac{R_{so}S_o}{B_o}\right)\frac{b-\phi}{K_s}S_g\right)\delta p_g\\ &+\left(\frac{S_g}{B_g}+\frac{R_{so}S_o}{B_o}\right)b\delta\varepsilon_v. \qquad \text{(C.13)}\end{aligned}$$

C.2 p_o, s_w, s_g formulation

Similarly to the p_o, p_w, p_g formulation, $\delta(S_o/B_o)$ for oil phase is written as

$$\begin{aligned}\delta(\frac{S_o}{B_o}) &= S_o\delta(\frac{1}{B_o}) + \frac{1}{B_o}\delta S_o \\ &= S_o\frac{1}{B_o}c_o\delta p_o + \frac{1}{B_o}\delta S_o \\ &= S_o\frac{1}{B_o}c_o\delta p_o + \frac{1}{B_o}(-\delta S_w - \delta S_g). \end{aligned} \tag{C.14}$$

Then, from Equations 2.38, C.1, and C.14, we obtain

$$\begin{aligned}\frac{\delta m_o}{\rho_{o,0}} &= \phi\left(S_o\frac{1}{B_o}c_o\delta p_o + \frac{1}{B_o}(-\delta S_w - \delta S_g)\right) \\ &\quad + \frac{S_o}{B_o}\left(\frac{b-\phi}{K_s}\left[\delta p_o - S_w\frac{dp_{co}}{dS_w}\delta S_w + S_g\frac{dp_{cg}}{dS_g}\delta S_g\right] + b\delta\varepsilon_v\right). \end{aligned} \tag{C.15}$$

For water phase, $\delta(S_w/B_w)$ is expanded as

$$\begin{aligned}\delta(\frac{S_w}{B_w}) &= S_w\delta(\frac{1}{B_w}) + \frac{1}{B_w}\delta S_w \\ &= S_w\frac{1}{B_w}c_w\delta p_w + \frac{1}{B_w}\delta S_w \\ &= S_w\frac{1}{B_w}c_w\delta(p_o - p_{co}) + \frac{1}{B_w}\delta S_w \\ &= S_w\frac{1}{B_w}c_w\delta p_o + (-S_w\frac{1}{B_w}c_w\frac{dp_{co}}{dS_w} + \frac{1}{B_w})\delta S_w. \end{aligned} \tag{C.16}$$

Then, from Equations 2.38, C.4, and C.16, we obtain

$$\begin{aligned}\frac{\delta m_w}{\rho_{w,0}} &= \phi\left(S_w\frac{1}{B_w}c_w\delta p_o + (-S_w\frac{1}{B_w}c_w\frac{dp_{co}}{dS_w} + \frac{1}{B_w})\delta S_w\right) \\ &\quad + \frac{S_w}{B_w}\left(\frac{b-\phi}{K_s}\left[\delta p_o - S_w\frac{dp_{co}}{dS_w}\delta S_w + S_g\frac{dp_{cg}}{dS_g}\delta S_g\right] + b\delta\varepsilon_v\right). \end{aligned} \tag{C.17}$$

For the gas phase, introducing the solution gas ratio,

$$\begin{aligned}
\delta(\frac{S_g}{B_g}) &= S_g\delta(\frac{1}{B_g}) + \frac{1}{B_g}\delta S_g \\
&= S_g\frac{1}{B_g}c_g\delta p_g + \frac{1}{B_g}\delta S_g \\
&= S_g\frac{1}{B_g}c_g\delta(p_o + p_{cg}) + \frac{1}{B_g}\delta S_g \\
&= S_g\frac{1}{B_g}c_g\delta p_o + (S_g\frac{1}{B_g}c_g\frac{dp_{cg}}{dS_g} + \frac{1}{B_g})\delta S_g, \qquad \text{(C.18)}
\end{aligned}$$

$$\begin{aligned}
\delta(\frac{R_{so}S_o}{B_o}) &= R_{so}S_o\delta(\frac{1}{B_o}) + \frac{S_o}{B_o}\delta R_{so} + \frac{R_{so}}{B_o}\delta S_o \\
&= R_{so}S_o\frac{1}{B_o}c_o\delta p_o + \frac{S_o}{B_o}\frac{dR_{so}}{dp_o}\delta p_o + \frac{R_{so}}{B_o}(-\delta S_w - \delta S_g) \\
&= \left(R_{so}S_o\frac{1}{B_o}c_o + \frac{S_o}{B_o}\frac{dR_{so}}{dp_o}\right)\delta p_o - \frac{R_{so}}{B_o}\delta S_w - \frac{R_{so}}{B_o}\delta S_g. \qquad \text{(C.19)}
\end{aligned}$$

Then, from Equations 2.38, C.7, C.18, and C.19, we have

$$\begin{aligned}
\frac{\delta m_g}{\rho_{g,0}} &= \phi\left(S_g\frac{1}{B_g}c_g\delta p_o + (S_g\frac{1}{B_g}c_g\frac{dp_{cg}}{dS_g} + \frac{1}{B_g})\delta S_g\right. \\
&\quad + \left(R_{so}S_o\frac{1}{B_o}c_o + \frac{S_o}{B_o}\frac{dR_{so}}{dp_o}\right)\delta p_o - \frac{R_{so}}{B_o}\delta S_w - \frac{R_{so}}{B_o}\delta S_g\Big) \\
&\quad + (\frac{S_g}{B_g} + \frac{R_{so}S_o}{B_o})\left(\frac{b-\phi}{K_s}\left[\delta p_o - S_w\frac{dp_{co}}{dS_w}\delta S_w + S_g\frac{dp_{cg}}{dS_g}\delta S_g\right] + b\delta\boldsymbol{\varepsilon}_v\right). \qquad \text{(C.20)}
\end{aligned}$$

Rearranging Equations C.15, C.17, and C.20, we have

$$\begin{aligned}
\frac{\delta m_o}{\rho_{o,0}} &= \left(\phi S_o\frac{1}{B_o}c_o + \frac{S_o}{B_o}\frac{b-\phi}{K_s}\right)\delta p_o + \left(-\phi\frac{1}{B_o} - \frac{S_o}{B_o}\frac{b-\phi}{K_s}S_w\frac{dp_{co}}{dS_w}\right)\delta S_w \\
&\quad + \left(-\phi\frac{1}{B_o} + \frac{S_o}{B_o}\frac{b-\phi}{K_s}S_g\frac{dp_{cg}}{dS_g}\right)\delta S_g + \frac{S_o}{B_o}b\delta\boldsymbol{\varepsilon}_v, \qquad \text{(C.21)}
\end{aligned}$$

$$\begin{aligned}
\frac{\delta m_w}{\rho_{w,0}} &= \left(\phi S_w \frac{1}{B_w} c_w + \frac{S_w}{B_w}\frac{b-\phi}{K_s}\right)\delta p_o \\
&+ \left(\phi(-S_w \frac{1}{B_w} c_w \frac{dp_{co}}{dS_w} + \frac{1}{B_w}) - \frac{S_w}{B_w}\frac{b-\phi}{K_s} S_w \frac{dp_{co}}{dS_w}\right)\delta S_w \\
&+ \frac{S_w}{B_w}\frac{b-\phi}{K_s} S_g \frac{dp_{cg}}{dS_g}\delta S_g + \frac{S_w}{B_w} b\delta\boldsymbol{\varepsilon}_v, \qquad \text{(C.22)} \\
\frac{\delta m_g}{\rho_{g,0}} &= \left(\phi S_g \frac{1}{B_g} c_g + \phi R_{so} S_o \frac{1}{B_o} c_o + \phi \frac{S_o}{B_o}\frac{dR_{so}}{dp_o} + (\frac{S_g}{B_g} + \frac{R_{so}S_o}{B_o})\frac{b-\phi}{K_s}\right)\delta p_o \\
&+ \left(-\phi\frac{R_{so}}{B_o} - (\frac{S_g}{B_g} + \frac{R_{so}S_o}{B_o})\frac{b-\phi}{K_s} S_w \frac{dp_{co}}{dS_w}\right)\delta S_w \\
&+ \left(\phi S_g \frac{1}{B_g} c_g \frac{dp_{cg}}{dS_g} + \phi\frac{1}{B_g} - \phi\frac{R_{so}}{B_o} + (\frac{S_g}{B_g} + \frac{R_{so}S_o}{B_o})\frac{b-\phi}{K_s} S_g \frac{dp_{cg}}{dS_g}\right)\delta S_g \\
&+ (\frac{S_g}{B_g} + \frac{R_{so}S_o}{B_o}) b\delta\boldsymbol{\varepsilon}_v. \qquad \text{(C.23)}
\end{aligned}$$

Bibliography

Aavatsmark I. 2002. An introduction to multipoint flux approximations for quadrilateral grids. *Comput Geosci* **6**: 405–432.

Abousleiman A., Cheng A., Detournay E., and Roegiers J. 1996. Mandel's problem revisited. *Geotechnique* **46**: 187–195.

Araújo A. 2004. A note on B-stability of splitting methods. *Comput Vasual Sci* **6**: 53–57.

Armero F. 1999. Formulation and finite element implementation of a multiplicative model of coupled poro-plasticity at finite strains under fully saturated conditions. *Comput Methods Appl Mech Eng* **171**: 205–241.

Armero F. and Simo J.C. 1992. A new unconditionally stable fractional step method for non-linear coupled thermomechanical problems. *Int J Numer Methods Eng* **35**: 737–766.

Armero F. and Simo J.C. 1993. A prior stability estimates and unconditionally stable product formula algorithms for nonlinear coupled thermoplasticity. *Int J Plasticity* **9**: 749–782.

Aziz K. and Settari A. 1979. *Petroleum Reservoir Simulation*. London: Elsevier.

Bevillon D. and Masson R. 2000. Stability and convergence analysis of partially coupled schemes for geomechanics reservoir simulations. Eur Conf Math Oil Recovery, Baveno, Italy.

Biot M.A. 1941. General theory of three-dimensional consolidation. *J Appl Phys* **12**: 155–164.

Biot M.A. and Willis D.G. 1957. The elastic coefficients of the theory of consolidation. *J Appl. Mech.* 594–601.

Borja R.I. 1991. Cam-Clay plasticity, Par II: Implicit integration of constitutive equation based on a nonlinear elastic stress predictor. *Comput Methods Appl Mech Eng* **88**: 225–240.

Borja R.I. 2006. On the mechanical energy and effective stress in saturated and unsaturated porous continua. *Int J Solid Struct* **12**: 1764–1786.

Borja R.I. and Alarcón E. 1995. A mathematical framework for finite strain elastoplastic consolidation Part 1: Balance laws, variational formulation, and linearization. *Comput Methods Appl*

Mech Eng **122**: 145–171.

Borja R.I. and Lee S.R. 1990. Cam-clay plasticity, Part I: Implicit integration of elasto-plastic constitutive relations. *Comput Methods Appl Mech Eng* **78**: 49–72.

Brenan K.E., Campbell S.L., and Petzold L.R. 1996. *Numerical Solution of Initial-value Problems in Differential-algebraic Equations*. Philadelphia: SIAM.

Chorin A., Hughes T.R., Mccraken M.F., and Marsden J.E. 1978. Product formulas and numerical algorithms. *Communications on Pure and Applied Mathematics,* 205–256.

Coussy O. 1995. *Mechanics of porous continua*. Chichester, England: John Wiley and Sons.

Coussy O. 2004. *Poromechanics*. Chichester, England: John Wiley and Sons.

Coussy O., Eymard R., and Lassabatére T. 1998. Constitutive modeling of unsaturated drying deformable materials. *J Eng. Mech.* 658–557.

Dean R.H., Gai S., Stone C.M., and Minkoff S.E. 2006. A comparison of techniques for coupling porous flow and geomechanics. *SPE J* **11**(1): 132–140.

Farhat C., Park K.C., and Dubois-Pelerin Y. 1991. An unconditionally stable staggered algorithm for transient finite element analysis of coupled thermoelastic problems. *Comput Methods Appl Mech Eng* **85**: 349–365.

Felippa C.A. and Park K.C. 1980. Staggered transient analysis procedures for coupled mechanical systems: formulation. *Comput Methods Appl Mech Eng* **24**: 61–111.

Fortin M. and Brezzi F. 1991. *Mixed and Hybrid Finite Element Methods*. Springer.

Gai X. 2004. A coupled geomechanics and reservoir flow model on parallel computers. Ph.D. Dissertation, University of Texas at Austin.

Geertsma J. 1957. The effect of fluid pressure decline on volumetric change of porous rocks. *Trans. AIME* **210**: 331–340.

Gutierrez M., Lewis R.W., and Masters I. 2001. Petroleum reservoir simulation coupling fluid flow and geomechanics. *SPE Res. Eval. Eng.* 164–172.

Hairer E. 1986. A- and B-stability for Runge-Kutta methods characterizations and equivalence. *Numer. Math* **48**: 383–389.

Hairer E. and T$'$urke H. 1984. The equivalence of B-stability and A-stability. *BIT* **24**: 520–528.

Huang M. and Zienkiewicz O.C. 1998. New unconditionally stable staggered solution procedures for coupled soil-pore fluid dynamic problems. *Int J Numer Methods Eng* **43**: 1029–1052.

Hughes T.J.R. 1987. *The Finite Element Method: Linear Static and Dynamic Finite Element Analysis*. Englewood Cliffs, NJ: Prentice-Hall.

Hundsdorfer W.H. and Splijer M.L. 1981. A note on B-stability of Runge-Kutta methods. *Numer. Math* **36**: 319–331.

Jean L., Mainguy M., Masson R., and Vidal-Gilbert S. 2007. Accelerating the convergence of coupled geomechanical-reservoir simulations. *Int J Numer Anal Meth Geomech* **31**: 1163–1181.

Jha B. and Juanes R. 2007. A locally conservative finite element framework for the simulation of coupled flow and reservoir geomechanics. *Acta Geotechnica* **2**: 139–153.

Kosloff D., Scott R., and Scranton J. 1980. Finite element simulation of Wilmington oil field subsidence: I. linear modelling. *Tectonophysics* **65**: 339–368.

Lapidus M.L. 1981. Generalization of the Trotter-Lie formula. *Integral Equations and Operator Theory* **4/3**: 366–413.

Lenhard R. and Parker J. 1987. Measurement and prediction of saturation-pressure relationships in three-phase porous media systems. *J Contami Hydro* 407–424.

Lewis R.W. and Schrefler B.A. 1998. *The finite element method in the static and dynamic deformation and consolidation of porous media*. Chichester, England: Wiley, 2nd edition.

Lewis R.W. and Sukirman Y. 1993. Finite element modelling of three-phase flow in deforming saturated oil reservoirs. *Int J Numer Anal Meth Geomech* **17**: 577–598.

Mainguy M. and Longuemare P. 2002. Coupling fluid flow and rock mechanics: formulations of the partial coupling between reservoir and geomechanics simulators. *Oil Gas Sci Tech* **57**: 355–367.

Marsden J.E. and Hughes T.J.R. 1983. *Mathematical Foundations of Elasticity*. Englewood Cliffs, NJ: Prentice-Hall.

Merle H.A., Kentie C.J.P., van Opstal G.H.C., and Schneider G.M.G. 1976. The Bachaquero Study - A composite analysis of the behavior of a compaction drive/solution gas drive reservoir. *JPT* 1107–1114.

Miga M.I., Paulsen K.D., and Kennedy F.E. 1998. Von Neumann stability analysis of Biot's general two dimensional theory of consolidation. *Int J Numer Methods Eng* **43**: 955–974.

Minkoff S.E., Stone C.M., Bryant S., Peszynska M., and Wheeler M.F. 2003. Coupled fluid flow and geomechanical deformation modeling. *J Petrol Sci Eng* **38**: 37–56.

Morris J. 2009a. *Injection and Reservoir Hazard Management: The Role of Injection-Induced Mechanical Deformation and Geochemical Alteration at In Salah CO2 Storage Project*. Lawrence Livermore National Laboratory.

Morris J.P. 2009b. Simulations of injection-induced mechanical deformation: A study of the In Salah CO2 storage project. SEG 2009 Summer Research Work CO2 Seq Geophy, Banff Canada, 23-27

Aug.

Murad M.A. and Loula A.F.D. 1992. Improved accuracy in finite element analysis of Biot's consolidation problem. *Comput Methods Appl Mech Eng* **95**: 359–382.

Murad M.A. and Loula A.F.D. 1994. On stability and convergence of finite element approximations of Biot's consolidation problem. *Comput Methods Appl Mech Eng* **37**: 645–667.

Ortiz M. and Popov E.P. 1985. Accuracy and stability of integration algorithms for elastoplastic constitutive relations. *Int J Numer Methods Eng* **21**: 1561–1576.

Pan F., Sepehrnoori K., and Chin L.Y. 2009. A new solution procedure for a fully coupled geomechanics and compositional reservoir simulator. SPE Res Simul Sym (SPE 119029), Woodland TX, 2-4 Feb.

Park K.C. 1983. Stabilization of partitioned solution procedure for pore fluid-soil interaction analysis. *Int J Numer Methods Eng* **19**(11): 1669–1673.

Phillips P.J. and Wheeler M.F. 2007a. A coupling of mixed and continuous Galerkin finite element methods for poroelasticity I: the continuous in time case. *Comput Geosci* **11**: 131–144.

Phillips P.J. and Wheeler M.F. 2007b. A coupling of mixed and continuous Galerkin finite element methods for poroelasticity II: the discrete-in-time case. *Comput Geosci* **11**: 145–158.

Prevost J.H. 1997. Partitioned solution procedure for simultaneous integration of coupled-field problems. *Commun. numer. meth. engng.* **13**: 239–247.

Richtmyer R.D. and Morton K.W. 1967. *Difference Methods for Initial Value Problems*. Chichester, England: John Wiley and Sons, second edition edition.

Samier P. and Gennaro S. 2007. A practical iterative scheme for coupling geomechanics with reservoir simulation. SPE Europec/EAGE (SPE 107077), London, 11-14 Jun.

Schrefler B.A. 2004. Multiphase flow in deforming porous material. *Int J Numer Methods Eng* **60**: 27–50.

Schrefler B.A., Simoni L., , and Turska E. 1997. Standard staggered and staggered Newton schemes in thermo-hydro-mechanical problems. *Comput Methods Appl Mech Eng* **144**: 93–109.

Settari A. and Mourits F. 1998. A coupled reservoir and geomechanical simulation system. *SPE J* **3**: 219–226.

Settari A. and Walters D.A. 2001. Advances in coupled geomechanical and reservoir modeling with applications to reservoir compaction. *SPE J* **6**(3): 334–342.

Simo J. 1991. Nonlinear stability of the time-discrete variational problem of evolution in nonlinear heat conduction, plasticity and viscoplasticity. *Comput Methods Appl Mech Eng* **88**: 111–131.

Simo J. and Govindjee S. 1991. Nonlinear B-stability and symmetry preserving return mapping algorithms for plasticity and viscoplasticity. *Comput Methods Appl Mech Eng* **31**: 151–176.

Simo J.C. and Hughes T.J.R. 1998. *Computational inelasticity*. Heidelberg: Springer.

Simo J.C. and Taylor R.L. 1986. A return mapping algorithm for plane stress elastoplasticity. *Int J Numer Methods Eng* **22**: 649–670.

Soares D.J. 2008. A time-domain FEM approach based implicit Green's functions for the dynamic analysis of the porous media. *Comput Methods Appl Mech Eng* **197**: 46454652.

Strang G. 1988. *Linear Algebra and Its Applications*. Brooks/Cole, third edition edition.

Strikwerda J.C. 2004. *Finite Difference Schemes and Partial Differential Equations*. Philadelphia: SIAM.

Tchonkova M., Peters J., and Sture S. 2008. A new mixed finite element method for poro-elasticity. *Int J Numer Anal Meth Geomech* **32**: 579–606.

Thomas L.K., Chin L.Y., Pierson R.G., and Sylte J.E. 2003. Coupled geomechanics and reservoir simulation. *SPE J* **8**(4): 350–358.

Thomée V. 2006. *Galerkin Finite Element Methods for Parabolic Problems*. Springer, 2nd edition.

Tran D., Nghiem L., and Buchanan L. 2005. Improved iterative coupling of geomechanics with reservoir simulation. SPE Res Simul Sym (SPE 93244), Houston, 31 Jan.-2 Feb.

Tran D., Settari A., and Nghiem L. 2004. New iterative coupling between a reservoir simulator and a geomechanics module. *SPE J* **9**(3): 362–369.

Truty A. and Zimmermann T. 2006. Stabilized mixed finite element formulations for materially nonlinear partially saturated two-phase media. *Comput Methods Appl Mech Eng* **195**: 1517–1546.

Turska E. and Schrefler B.A. 1993. On convergence condition of partitioned solution procedures for consolidation problems. *Comput Methods Appl Mech Eng* **106**: 51–63.

Turska E., Wisniewski K., and Schrefler B.A. 1994. Error propagation of staggered solution procedures for transient problems. *Comput Methods Appl Mech Eng* **114**: 177–188.

Vermeer P.A. and Verruijt A. 1981. An accuracy condition for consolidation by finite elements. *Int J Numer Anal Meth Geomech* **5**: 1–14.

Vijalapura P.K. and Govindjee S. 2005. An adaptive hybrid time-stepping scheme for highly nonlinear strongly coupled Problems. *Int J Numer Methods Eng* **64**: 819–848.

Vijalapura P.K., Strain J., and Govindjee S. 2005. Fractional step methods for index-1 differential-algebraic equations. *J Comput Physics* **203**: 305–320.

Ženišek A. 1984. The existence and uniqueness theorem in Biot's consolidation theory. *Apl. Mat* **29**: 194–210.

Wan J. 2002. Stabilized finite element methods for coupled geomechanics and multiphase flow. Ph.D. Dissertation, Stanford University.

Wan J., Durlofsky L.J., Hughes T.J.R., and Aziz K. 2003. Stabilized finite element methods for coupled geomechanicsreservoir flow simulations. SPE Res Simul Sym (SPE 79694), Houston, 3-5 Feb.

Wan J., Sarma P., Usadi A.K., and Beckner B.L. 2005. General stability criteria for compositional and black-oil models. SPE Res Simul Sym (SPE 93096), Houston, 31 Jan-2 Feb.

Wang H.F. 2000. *Theory of Linear Poroelasticity*. Princeton University Press.

Wheeler M.F. and Gai X. 2007. Iteratively coupled mixed and Galerkin finite element methods for poro-elasticity. *Numer Meth for PDEs* **23**: 785–797.

White A.J. and Borja R.I. 2008. Stabilized low-order finite elements for coupled solid-deformation/fluid-diffusion and their application to fault zone transients. *Comput Methods Appl Mech Eng* **197**: 43534366.

Zienkiewicz O.C., Paul D.K., and Chan A.H.C. 1988. Unconditionally stable staggered solution procedure for soil-pore fluid interaction problems. *Int J Numer Methods Eng* **26**(5): 1039–1055.

Zoback M.D. 2007. *Reservoir Geomechanics*. Cambridge, UK: Cambridge University Press.

Zuluaga E., Schmidt J.H., and Dean R.H. 2007. The use of a fully coupled geomechanics-reservoir simulator to evaluate the feasibility of a cavity completion. SPE Ann Tech Conf Exhib (SPE 109588), Anaheim CA, 11-14 Nov.